

Examining Incoherent UV Light as an Assistant to IR Laser on Texturing of CFRP Composites for Adhesive Joining

Ahmed Al-Mahdy

A thesis

submitted in partial fulfilment of the requirements of

Liverpool John Moores University

for the degree of

Doctor of Philosophy

February 2025

Abstract

Carbon Fibre Reinforced Polymers (CFRPs) are widely used in aerospace and automotive industries for their high strength-to-weight ratio, but joining their structures presents challenges. Adhesive bonding is preferred to maintain lightweight advantages, yet strong bonds require precise surface preparation. Laser surface processing, a contactless method, has widely been applied to surface preparation for various materials and extensively explored for CFRPs. This technique shows promise in improving adhesion by removing contaminants, adding surface texture to enhance mechanical interlocking, activating surface chemistry, or fully removing the matrix outer layer to expose carbon fibres for direct bonding. On the other hand, incoherent UV light treatment has been studied across a range of materials, including polymeric and non-polymeric substrates. It breaks down polymer or hydrocarbon bonds at the surface, activating surface chemistry and enhancing adhesion and bonding performance.

This research examines the effect of incoherent Ultraviolet (UV) light on enhancing the effectiveness of Infrared (IR) lasers in improving adhesive bonding in CFRP/CFRP structures. Two laser systems were used: a nanosecond (ns) pulsed Near-Infrared (NIR) fibre laser at 1064 nm and a Continuous-Wave (CW) Mid-Infrared (MIR) Carbon Dioxide (CO₂) laser at 10600 nm. The UV light was provided by a 46 W germicidal lamp emitting at 254 nm. The study optimised and evaluated the three surface treatment methods individually, followed by combining each laser with UV light to explore their effectiveness. Adhesive bonding was assessed using Single Lap Shear (SLS) tests, with mechanical abrading included for comparison. Various CFRP materials with woven and Unidirectional (UD) reinforcement were used. In comparison to as-received samples, NIR laser treatment with 200-nanosecond pulses enhanced bonding by over 60%. Shorter pulses posed a higher risk of fibre damage, resulting in significantly lower bonding improvement. Laser processing of woven CFRPs presented challenges due to the highly variable outer matrix thickness. CW CO₂ laser treatments resulted in slight bonding enhancement, with a risk of fibre-matrix debonding. UV treatment alone improved bonding by 75%, outperforming NIR laser treatments, with Cohesive Substrate Failure (CSF) mode indicating stronger adhesion than the material's interlaminar strength. Combining UV with laser treatments provided limited additional benefit. Mechanical abrading showed a 35% improvement in bonding, offering an industry-relevant comparison. Incoherent UV light treatment significantly enhanced bonding strength and offered a cost-effective alternative.

Declaration

I confirm that no part of the work presented in this thesis has been submitted for any other degree or qualification at this or any other university or educational institution.

Acknowledgements

First and foremost, I extend my deepest praises and thanks to God, the Almighty, for placing me at Liverpool John Moores University with this remarkable team and for His blessings throughout my research journey.

I wish to express my heartfelt gratitude to my exceptional supervision team. I could not have imagined having a better supervisory team for my study. I would like to express my deepest appreciation to Dr. Martin Sharp, who made this research opportunity possible, has provided invaluable guidance, support, and advice. His dynamism, vision, and motivation have deeply inspired me, and it has been a great privilege to work under his supervision. I am extremely grateful to Dr. Tahsin Opoz for his support and insightful feedback throughout my study. His patience during this period was instrumental in helping me overcome challenges. My sincere thanks also go to Dr. Hiren Kotadia for his invaluable support, suggestions, and guidance. His insightful feedback and expert advice have been essential in shaping this work. I would like to extend special thanks to Dr. Juan Ahuir Torres for his support, particularly in monitoring the practical aspects of this research, and for his insightful suggestions and constructive feedback. I am also thankful to Dr. Jack Mullett for his invaluable guidance and support.

I am deeply grateful to Prof. Richard Day of Wrexham Glyndwr University for his scientific advice and for facilitating access to the CFRP manufacturing facilities. My sincere thanks also go to Dr. Walter Perrie of the University of Liverpool for his scientific advice and assistance in measuring UV intensity.

Additionally, I would like to extend my appreciation to the technicians at Liverpool John Moores University, particularly Mr. Harvey Thompson, for their support, especially in conducting the mechanical tests during my PhD.

Finally, I wish to express my deepest thanks to my mother and my entire family for their unwavering support, patience, sacrifice, love, and encouragement in every aspect of my life. Their presence has been invaluable throughout this journey. I am especially grateful to my wife, Rafah, whose steadfast support, understanding, and belief in me have been a cornerstone of my success. Her sacrifices and dedication have given me the strength and motivation to persevere, and I am deeply thankful for her love and partnership. My heartfelt thanks also go to my two sons, Mustafa and Ali, for their patience and understanding during these years—you have been wonderful boys.

Publications and conferences

1. Al-Mahdy, A., et al., An investigation into the use of incoherent UV light to augment IR nanosecond pulsed laser texturing of CFRP composites for improved adhesion. *Optics & Laser Technology*, 2025. 181: p. 111626.
2. Al-Mahdy, A., et al., Effect of Surface Roughness on the Surface Texturing of 316 L Stainless Steel by Nanosecond Pulsed Laser. *Lasers in Manufacturing and Materials Processing*, 2023. 10(1): p. 141-164.
3. Al-Mahdy A, Öpöz TT, Kotadia HR, Ahuir-Torres JI, Sharp MC. Resin absorption and transmittance in CFRPs during CO2 laser surface preparation: Insights into matrix removal mechanisms. *Optics & Laser Technology*. 2025;186:112699.
4. Surface treatment of reinforced carbon fibre with woven reinforcement using nanosecond pulsed fibre laser. (ILAS March 2023 conference presentation)

Dedication

I dedicate this thesis

to

my late father, whose memory and influence continue to inspire me.

Table of Contents

| | |
|---|-------------|
| Abstract | II |
| Declaration | III |
| Acknowledgements | IV |
| Publications and conferences | V |
| <i>Dedication</i> | VI |
| 1. CHAPTER 1: Introduction and Thesis Structure | 1-1 |
| 1.1 Carbon Fibre Reinforced Polymers (CFRPs) | 1-1 |
| 1.2 Research motivation and the state of the art | 1-1 |
| 1.3 Research gaps and challenges | 1-3 |
| 1.4 Aim and objectives | 1-4 |
| 1.5. Thesis structure | 1-5 |
| 2. CHAPTER 2: Literature Review | 2-7 |
| 2.1. An overview of CFRP composites | 2-7 |
| 2.1.1. Composite materials | 2-7 |
| 2.1.2. Production of carbon fibres | 2-8 |
| 2.1.3. Sizing agent of CFs | 2-11 |
| 2.1.4. Properties of carbon fibre. | 2-12 |
| 2.1.5. Commercially available carbon fibre | 2-14 |
| 2.1.6. Matrix material | 2-15 |
| 2.1.7. Recycling of CFRP composites | 2-16 |
| 2.2. Joining of CFRP structures | 2-18 |
| 2.2.1. Mechanical fasteners | 2-19 |
| 2.2.2. Adhesive bonding of CFRP structures | 2-19 |
| 2.2.3. Adhesive and adhesion | 2-20 |
| 2.2.4. Evaluation of surface adhesivity | 2-22 |
| 2.2.4.1. Surface wettability | 2-22 |
| 2.2.4.2. Surface Free Energy (SFE) | 2-24 |
| 2.2.5. Surface preparation | 2-26 |
| 2.2.5.1. Traditional surface pretreatment techniques of CFRPs to improve adhesive bonding .. | 2-26 |
| 2.2.5.2. Laser surface treatment or texturing | 2-28 |
| 2.2.5.3. Surface treatment with incoherent UV light (non-laser) | 2-29 |
| 2.3. An overview of light and laser | 2-30 |
| 2.3.1. The electromagnetic wave and spectrum | 2-30 |
| 2.3.2. Laser fundamentals | 2-31 |
| 2.3.3. Common commercial lasers | 2-33 |
| 2.3.4. Laser structure | 2-34 |
| 2.3.5. Laser beam parameters | 2-36 |
| 2.3.5.1. Wavelength (λ) | 2-36 |

| | |
|--|------|
| 2.3.5.2. Beam quality (M^2 value)..... | 2-37 |
| 2.3.5.3. Laser power and intensity..... | 2-37 |
| 2.3.5.4. Laser spot size, focal length, and Rayleigh length | 2-38 |
| 2.3.5.5. Continuous wave and pulsed lasers..... | 2-39 |
| 2.3.6. Laser material interaction..... | 2-40 |
| 2.4. The state of the art: laser surface treatment of CFRP to improve adhesive bonding. | 2-43 |
| 2.5. Research gaps and challenges | 2-47 |
| 2.6. Hypotheses of the research | 2-49 |
| 3. CHAPTER 3: Experimental Methods..... | 3-54 |
| 3.1. Objectives..... | 3-54 |
| 3.2. Experimental equipment and instrumentation..... | 3-54 |
| 3.2.1. Nanosecond pulsed NIR fibre laser | 3-54 |
| 3.2.2. CW CO ₂ laser | 3-57 |
| 3.2.3. UV light equipment..... | 3-58 |
| 3.2.4. Surface, chemical, and topographical characterisation equipment | 3-60 |
| 3.3. Key experimental materials..... | 3-63 |
| 3.3.1. CFRP composites | 3-63 |
| 3.3.2 Bonding adhesives..... | 3-63 |
| 3.3.3. Epoxy resins..... | 3-64 |
| 3.4. Cross-section assessments of CFRP samples..... | 3-65 |
| 3.5. Adhesive bonding tests (Single Lap Shear (SLS) tests) | 3-65 |
| 3.6. Cutting and cleaning of the CFRP materials | 3-67 |
| 4. CHAPTER 4: Matrix Resin Absorption and Transmittance..... | 4-68 |
| 4.1. Introduction | 4-68 |
| 4.2. Objectives..... | 4-69 |
| 4.3. Transmittance to NIR laser (1064 nm)..... | 4-69 |
| 4.3.1. Methods (transmittance to NIR 1064 nm) | 4-69 |
| 4.3.2. Results and discussion (transmittance to NIR 1064 nm) | 4-71 |
| 4.4. Transmittance to MIR laser (10600 nm)..... | 4-74 |
| 4.4.1. Methods (transmittance to MIR 10600 nm) | 4-74 |
| 4.4.2. Results and discussion (transmittance to MIR 10600 nm) | 4-77 |
| 4.5. Conclusions | 4-79 |
| 5. CHAPTER 5: Laser Surface Processing of Woven Reinforced CFRP Composites to Improve Adhesive Bonding Using NIR ns Pulsed Fibre Laser. | 5-81 |
| 5.1. Introduction | 5-81 |
| 5.2. Objectives..... | 5-82 |
| 5.3. Experimental design and workflow | 5-82 |
| 5.4. Exploration trials..... | 5-83 |
| 5.5. The main study, laser surface treatment of woven reinforced CFRPs to improve adhesive bonding using a mask..... | 5-87 |
| 5.5.1. Methods..... | 5-88 |

| | |
|--|--------------|
| 5.5.1.1. CFRP material | 5-88 |
| 5.5.1.2 Surface treatment and the optimisation process of the laser variables | 5-89 |
| 5.5.1.3. Cross-section assessments | 5-91 |
| 5.5.1.4. Bonding strength /(SLS) tests | 5-91 |
| 5.5.2. Result and discussion | 5-92 |
| 5.5.2.1. Optimisation of the laser variables..... | 5-92 |
| 5.5.2.2. Optical profilometry assessment | 5-95 |
| 5.5.2.3 Cross-section assessment..... | 5-96 |
| 5.5.2.4 Wettability assessment | 5-97 |
| 5.5.2.5 Mechanical test of adhesively bonded coupons | 5-98 |
| 5.6 Conclusions | 5-102 |
| 6. CHAPTER 6: Laser Surface Processing of UD Reinforced CFRP Composites to Improve Adhesive Bonding Using NIR ns Pulsed Fibre Laser..... | 6-103 |
| 6.1. Introduction | 6-103 |
| 6.2. Objectives..... | 6-103 |
| 6.3. Experimental design and workflow | 6-104 |
| 6.4. CFRP material and laser equipment | 6-105 |
| 6.4.1 Cross-section assessment of the CFRP material..... | 6-105 |
| 6.5. First study: Investigating the effect of heat accumulated during laser processing..... | 6-107 |
| 6.5.1. Methods (First study) | 6-107 |
| 6.5.2. Results (First study)..... | 6-108 |
| 6.6. Second study: Understanding the pulse length and energy effects on the CFRP matrix ablation. ... | 6-110 |
| 6.6.1. Methods (Second study)..... | 6-110 |
| 6.6.2. Results (Second study) | 6-111 |
| 6.7. Third study: Understanding the effects of pulse length on wettability and adhesive bonding. ... | 6-119 |
| 6.7.1. Methods (Third study)..... | 6-119 |
| 6.7.1.1. Creation of separated dimples and measurements of the dimple's average lengths and widths..... | 6-119 |
| 6.7.1.2. Estimation of the hatch spacings and scanning speeds to be utilised for laser processing to fully expose the CFs for wettability assessment. | 6-120 |
| 6.7.1.3. Surface wettability | 6-121 |
| 6.7.1.4 Investigating the adhesive bonding strength | 6-123 |
| 6.7.2. Results (Third study) | 6-125 |
| 6.8. Fourth study: Understanding the effects of the adhesive's modulus of elasticity on the concentrated stresses in single lap joints..... | 6-134 |
| 6.8.1. Methods (Fourth study)..... | 6-134 |
| 6.8.2. Results (Fourth study) | 6-135 |
| 6.9. Conclusions | 6-138 |
| 7. CHAPTER 7: Surface Treatment of CFRP Composites Using Continues Wave Carbon Dioxide Laser | 7-140 |
| 7.1. Introduction | 7-140 |

| | |
|---|---------------|
| 7.2. Objectives..... | 7-141 |
| 7.3. Experimental design and workflow | 7-141 |
| 7.4. Experiments | 7-142 |
| 7.4.1 Understanding the effects of laser power and scanning speed on the ablation of the CFRP outer layer matrix. | 7-142 |
| 7.4.2 Understanding the effects of laser power and scanning speed on the ablation of pure epoxy resin..... | 7-148 |
| 7.4.3. Studying the effects of CW CO ₂ laser processing on the wettability and the adhesive strength of CFRP composite | 7-152 |
| 7.4.3.1 Surface wettability | 7-152 |
| 7.4.3.2. Adhesive bonding strength..... | 7-155 |
| 7.5. The ablation or removal mechanism of epoxy resin using CW CO ₂ laser..... | 7-159 |
| 7.6. FTIR spectroscopy | 7-160 |
| 7.7. Conclusion..... | 7-162 |
| 8. CHAPTER 8: Utilising Incoherent UV Light to Augment IR Lasers in Improving CFRP Composite for Adhesive Bonding | 8-163 |
| 8.1. Introduction | 8-163 |
| 8.2. Objectives..... | 8-164 |
| 8.3. Experimental design and workflow | 8-164 |
| 8.4. Main experiment | 8-165 |
| 8.4.1. Phase 1: Studying the effect of UV intensity and exposure period on the WCA. | 8-165 |
| 8.4.1.1. Methods | 8-165 |
| 8.4.1.2. Results and discussion | 8-167 |
| 8.4.2. Phase 2: Comparing the adhesive bonding of different surface treatment techniques | 8-170 |
| 8.4.2.1. Methods | 8-170 |
| 8.4.2.2. Results and discussion | 8-172 |
| 8.5. Supplementary experiment | 8-177 |
| 8.6. Conclusions | 8-179 |
| 9. CHAPTER 9: Conclusions and Future Works..... | 9-181 |
| 9.1. Conclusions | 9-181 |
| 9.2. Future works..... | 9-182 |
| 10. References | 10-185 |
| 11. Appendices | 11-202 |
| Appendix A, The UD reinforced prepreg datasheet..... | 11-202 |
| Appendix B, SEM images for UD CFRP material processed with different laser variables, see Table 7.3 or Table 7.6. | 11-203 |
| Appendix C, material properties and model types applied in SolidWorks..... | 11-204 |
| Appendix D, full SolidWorks modelling results of the two adhesives..... | 11-205 |

List of Figures

| | |
|--|------|
| Figure 2.1. Representation of carbon fibre reinforced polymer composite, adapted from [47]*. | 2-8 |
| Figure 2.2. Schematic of the wet spinning process, re-drawn from [61]*. | 2-10 |
| Figure 2.3. Production procedures for PAN-based carbon fibres. | 2-10 |
| Figure 2.4. SEM images of (a) unsized carbon fibre and (b) sized carbon fibre, adapted from [67]*, and (c) a schematic illustration of a cross-section of a sized carbon fibre. | 2-12 |
| Figure 2.5. Effect of elevated temperature on the strength of different organic fibres, adapted from [41]*. | 2-13 |
| Figure 2.6. Drawings of most common carbon fibre weave, [90]*. | 2-14 |
| Figure 2.7. Composites lay-ups with different orientations, a) unidirectional, b) plain weave, adapted from Bergant [93]*. | 2-15 |
| Figure 2.8. Overview of CFRP composites recycling and remanufacturing processes adapted from [97]*. | 2-18 |
| Figure 2.9. Illustration of good and poor wetting over irregular surface, adapted from Petrie [130]*. | 2-23 |
| Figure 2.10. Schematic illustration of hydrophobicity, hydrophilicity, super-hydrophobicity, and super-hydrophilicity. | 2-24 |
| Figure 2.11. The equilibrium state of a liquid droplet on a solid surface according to Young's equation adapted from [19]*. | 2-25 |
| Figure 2.12. Illustration of an electromagnetic wave, adapted from [205]*. | 2-30 |
| Figure 2.13. The electromagnetic spectrum and the corresponding photon energies, re-drawn based on Andrews and NASA [208, 209]. | 2-31 |
| Figure 2.14. Spontaneous and stimulated emission, adapted from [211]*. | 2-32 |
| Figure 2.15. Illustration of concepts of monochromatic and coherent light adapted from [213]*. | 2-33 |
| Figure 2.16. The irradiance distribution of the laser spot for various transverse modes adapted from Saleh [216]*. | 2-35 |
| Figure 2.17. A basic structure of a simple laser adapted from [233]*. | 2-36 |
| Figure 2.18. Real and pure Gaussian laser beam, adopted from Eichler [239]*. | 2-37 |
| Figure 2.19. The minimum spot size d_0 of a Gaussian beam and the Rayleigh length zR , adopted from [223]*. 2-39 | |
| Figure 2.20. Principles of pulsed and CW lasers. | 2-39 |
| Figure 2.21. The incident laser beam, the reflected and transmitted portions [228]*. | 2-40 |
| Figure 2.22. The penetration depth for different materials over a range of wavelengths, [248, 255]. | 2-42 |
| Figure 2.23. a) SEM image depicting cavities at the fibre-matrix interface in a sample treated with NIR laser. b) Darkfield microscopic image revealing fibres pulled out and adhered to the adhesive on the other coupon after bonding SLS test of a NIR laser-treated sample [27]*. | 2-45 |
| Figure 2.24. Absorption spectrum for a typical epoxy resin [35, 268]. | 2-47 |
| Figure 3.1. The NIR Laser equipment setup a) Schematic drawing and b) photograph. | 3-56 |
| Figure 3.2. Measured average power and pulse energy at PRF =25 kHz, τ =200 ns, and different power percentage setup. | 3-57 |
| Figure 3.3. a) A schematic drawing of the CO ₂ laser beam, b) a photograph of the equipment. | 3-58 |
| Figure 3.4. Measured average power at different power percentage setups. | 3-58 |
| Figure 3.5. UV lamp and the experimental setup: a) photograph and b) schematic drawing [279]*. | 3-59 |
| Figure 3.6. (a) Thermal imaging data captured by the IR camera for the lamp at 30 minutes, (b) graph representing the temperature over time for both the lamp and the sample. | 3-60 |
| Figure 3.7. a) Olympus BH2-UMA optical light microscope, b) VHX-7000 digital microscope, c) Bruker ContourGT-K optical profiler, d) SEM Hitachi TM4000Plus Tabletop Microscope, e) CAM 101 goniometer, and f) Cary 630 FTIR Spectrometer. | 3-62 |
| Figure 3.8. a) Optical microscopy of a woven CFRP sample processed with ns pulsed NIR laser, b) digital microscopy image of UD CFRP sample processed with CO ₂ laser, c) 3D profilometry image of a woven CFRP sample processed with CO ₂ laser, d) A SEM image of separated dimples were created with 30 ns pulse length NIR laser, e) Goniometer camera image of water droplet on a CFRP sample processed with CO ₂ laser, and f) FTIR spectra of an as received CFRP sample. | 3-62 |
| Figure 3.9. a) Buehler Metaserv Twin Grinder/Polisher, b) TegraPol 11 Struers Polisher. | 3-65 |
| Figure 3.10. Sample for SLS according to BS EN ISO 1465:2009 standard. | 3-66 |
| Figure 3.11. Bonding jig: (a) and (b) SolidWorks design, and (c) photograph of the manufactured jig. | 3-67 |
| Figure 3.12. Tinius Olsen 50 kN tensile testing machine. | 3-67 |
| Figure 4.1. Transmissivity of a 125 μ m thick layer of epoxy resin as a function of laser wavelength [37]*. | 4-69 |

| | |
|---|------|
| Figure 4.2. The moulded epoxy resins samples. | 4-70 |
| Figure 4.3. A scheme clarifies the experimental setup (transmittance to NIR 1064 nm). | 4-71 |
| Figure 4.4. Demonstration of the surface roughness assessment data. | 4-71 |
| Figure 4.5. The transmittance (T) for NIR 1064 nm laser as a function of the sample thickness (t) for SP115, EL2, and IN2 epoxies. | 4-72 |
| Figure 4.6. Camera images showing (a) multiple glass sheets utilised as moulds for epoxy films are compressed together using ratchet bar clamps, and (b) and (c) two pairs of glass mould with epoxy films before being released. | 4-74 |
| Figure 4.7. (a) camera image of an epoxy film intended to be 25 μm thick, (b) profilometry assessment indicating the thickness of 23.5 μm | 4-75 |
| Figure 4.8. A schematic drawing of the laser system and the experimental setup. | 4-76 |
| Figure 4.9. Perspex sample was positioned at the unfocused position and subjected to laser processing using laser power of 27 W and five different scanning speeds in order to estimate the laser spot size. | 4-77 |
| Figure 4.10. Epoxy films transmittance (T) for MIR (10600 nm) laser as a function of the film thickness (t). | 4-78 |
| Figure 4.11. (a) SEM images of cross-section of CFRP composites with a) UD and b) woven reinforcements. c) a magnified SEM image of CFRP with UD reinforcement showing the matrix outer layer thickness, and d) A plot illustrating absorbed, transmitted and reflected percentages of CO ₂ laser passing through resin film (0-25 μm thickness). | 4-79 |
| Figure 5.1. Flowchart simplifies the experimental design, steps, and phases. | 5-83 |
| Figure 5.2. a) CFRP material of the first trial under laser processing, optical microscopy images of b) an as-received sample, c) treated with the low pulse energy, d) treated with the high pulse energy. | 5-84 |
| Figure 5.3. (a) macro photograph of the CFRP specimen. (b), (c), (d), and (f) Optical microscopic images highlighting the degraded regions of the matrix or the carbon fibres. (e) Macro photograph indicating the degraded regions with arrows. | 5-86 |
| Figure 5.4. (a) 3D profilometric image of nine samples processed with a pulse energy of 0.1 mJ, stitched together. The hatch spacing and scanning speed are indicated at the top and the left side. (b) 3D profilometric image of a sample processed with a pulse energy of 0.1 mJ, a hatch spacing of 30 μm , and a scanning speed of 1000 mm/s. | 5-87 |
| Figure 5.5. (a and b), surface photos of the woven CFRP material captured with two different lighting angles show the carbon fibre weave pattern (8-Harness-Satin) and the production defects, (c) a macro photo shows the cross-section of CFRP sample embedded within epoxy mould, (d, e, and f) optical microscopy images show the variation in the outer layer matrix resin thickness. | 5-88 |
| Figure 5.6. Photos of a) the CFRP material and b) the cardboard mask illustrates the alignment of the mask holes within the elliptical shapes at the CFRP surface. | 5-90 |
| Figure 5.7. Macro photos of (a) a CFRP coupon undergoing laser partial treatment, (b) and (c) two CFRP coupons treated using partial and full laser surface treatment, d). mechanically abraded coupon. | 5-91 |
| Figure 5.8. Low magnified digital microscopy images and their ImageJ corresponded colour adjusted images of a) fully laser treated sample using $E_p = 0.124$ mJ, $S_{sc} = 600$ mm/s, $H = 25$ μm , b) fully laser treated sample using $E_p = 0.092$ mJ, $S_{sc} = 800$ mm/s, $H = 25$ μm , and c) partially treated samples using $E_p = 0.092$ mJ, $S_{sc} = 800$ mm/s, $H = 25$ μm | 5-92 |
| Figure 5.9. a) Low-magnification digital microscopy image of an as-received sample with arrows indicating the positions of the broken CFs and the degraded non-removed matrix on laser-treated samples. b-f) Optical microscopy images of samples treated using different processing parameters: b) $E_p = 0.124$ mJ, $v = 600$ mm/s, $H = 25$ μm , c) $E_p = 0.092$ mJ, $v = 600$ mm/s, $H = 25$ μm , d) $E_p = 0.124$ mJ, $v = 600$ mm/s, $H = 25$ μm , e) $E_p = 0.124$ mJ, $v = 1000$ mm/s, $H = 40$ μm , f) $E_p = 0.056$ mJ, $v = 1000$ mm/s, $H = 40$ μm . Note that the optical microscopy images may require to be unfocused to capture damaged fibres. | 5-93 |
| Figure 5.10. Digital microscopy images captured at different magnifications (a and b) for a fully laser-treated sample and (c and d) for a laser partially treated sample, utilising the optimised laser variables. | 5-94 |
| Figure 5.11. Optical microscopy images of a mechanically abraded CFRP sample with two different magnifications showing CF breakage. | 5-94 |
| Figure 5.12. 3D optical profilometric images of a) an as-received sample, b) and c) laser fully and partially treated samples, respectively, using $E_p = 0.092$ mJ, $v = 800$ mm/s, $H = 25$ μm . d), e), and f) laser fully treated sample using the same $v = 600$ mm/s and $H = 25$ μm but variable $E_p = 0.124$, 0.092, and 0.056 mJ, respectively. | 5-95 |
| Figure 5.13. Optical microscopy images of cross-section of a) and b) an as-received sample, c), d), e) and f) laser treated sample. The orientations of the samples align with those depicted in the images. | 5-96 |

| | |
|---|-------|
| Figure 5.14. SEM image of a) an as-received sample, b) and c) laser treated sample. The tops of the samples are positioned on the left side of the images..... | 5-97 |
| Figure 5.15. A mobile phone photo of a water droplet with two side-view images, captured through the goniometer (contact angle measuring equipment), showing significant variations in droplet shapes and CAs depending on the direction of view..... | 5-97 |
| Figure 5.16. The average failure strength and SD across the different treatment conditions. | 5-98 |
| Figure 5.17. Failure modes observed in a) as-received, b) sandpaper-treated, c) fully laser-scanned, and d) laser-treated with mask CFRP samples. | 5-99 |
| Figure 5.18. Fracture analysis clarifies the different failure modes associated with two laser processing techniques: a) and b) laser fully treated coupon, c) and d) laser partially treated coupon. | 5-100 |
| Figure 5.19. Elemental analysis reveals the presence of aluminium powder within the adhesive bonding. | 5-100 |
| Figure 5.20. Schematic diagram illustrates the different failure modes experienced in the current study..... | 5-101 |
| Figure 5.21. Schematic illustration explaining why partially scanned samples exhibit higher strength than fully laser-scanned samples..... | 5-101 |
| Figure 6.1. Flowchart simplifies the experimental design, steps, and phases. | 6-104 |
| Figure 6.2. (a) and (b) SEM images at two magnifications showing the cross-section of an as-received UD CFs CFRP sample, illustrating the distance from the surface to the fibres (adapted from Figure 4.11). | 6-106 |
| Figure 6.3. Optical microscopy images with different magnification of the cross-section of an as-received UD CFs CFRP sample..... | 6-106 |
| Figure 6.4. Illustration of the scanning pattern, the mark, and the jump, the distance between points a and á is equal to H, while the time the scanner takes to move from a to á is equal to δt | 6-108 |
| Figure 6.5. Optical microscopy images of samples processed using different processing variables, marked on them, each set of 2 processed with the same pulse length and energy and the same ratio of PRF to the scanning speed (v). | 6-109 |
| Figure 6.6. Two highly magnified optical microscopic images were taken at different positions of a single sample treated with 25 kHz, 0.09 mJ, 200 ns, and 1000 mm/s. | 6-110 |
| Figure 6.7. Clarification of the colour thresholding process using ImageJ to measure the dimple area. | 6-111 |
| Figure 6.8. Lines of separated dimples with five different pulse energies processed with a) 30 ns, b) 200 ns..... | 6-112 |
| Figure 6.9. The average dimple areas that were created with different pulse energy and pulse length. | 6-112 |
| Figure 6.10. SEM images of CFRP samples processed with a) 30 ns and b) 200 ns. For both images, the pulse energy in each line of dimples is as follows: 0.078, 0.065, 0.052, 0.041, 0.03 mJ from top to bottom. | 6-113 |
| Figure 6.11. SEM images of CFRP samples processed using a), c), and e) 30 ns, and b), d), and f) 200 ns. For all images, the pulse energy is 0.078 mJ..... | 6-113 |
| Figure 6.12. SEM images of CFRP samples processed using pulse length of 200 ns and pulse energy of 0.03 mJ. | 6-114 |
| Figure 6.13. The pulse instantaneous power versus time of the 30 and 200 ns pulse lengths was created based on the pulse amplitude profile obtained from the SPI laser manual. | 6-116 |
| Figure 6.14. 3D profilometric images with profiles of two dimples created with a pulse energy of 0.078 mJ and two different pulse lengths a) 30 ns and b) 200 ns..... | 6-117 |
| Figure 6.15. Optical profilometric images illustrating dimples and their profiles created with 30 ns (left) and 200 ns pulse length (right). Each profile is labelled with a letter representing each line of pulses, and the latter has specific pulse energy (0.078, 0.065, 0.052, 0.041, 0.03 mJ) from left to right. | 6-118 |
| Figure 6.16. The left image is an optical profilometric image illustrating the method used for estimating the dimple length and width. The other six images are optical microscopy images of the samples treated with different pulse lengths and energies, with the specific pulse length and energy marked on each microscopic image. | 6-120 |
| Figure 6.17. Macro photo of a CFRP coupon with the first nine samples. | 6-121 |
| Figure 6.18. The three WCA measurements and their averages for two samples as examples. | 6-122 |
| Figure 6.19. Photos extracted from a video record show the absorption of a water droplet with time. | 6-123 |
| Figure 6.20. (a), (b), and (c) show the laser-treated regions of the coupons with different laser processing sets specified respectively according to the pulse lengths used: 30 ns, 80 ns, and 200 ns; (d) depicts the bonding jig; and (e) presents the samples after curing, ready for the SLS test. | 6-124 |
| Figure 6.21. The average WCA vs time for the 18 samples which processed using different laser variables. For details on the laser processing variables for the different samples, see Table 6.3 | 6-125 |
| Figure 6.22. SEM images for a) sample 3, b) sample 9, c) sample 12, and d) sample 15..... | 6-127 |

| | |
|--|-------|
| Figure 6.23. SEM images with variable magnification of the cross-section of (on top) an as-received sample and (on bottom) a laser-treated sample with a pulse length of 200 ns..... | 6-128 |
| Figure 6.24. Bar chart showing the adhesive bonding strengths of CFRP samples with different surface conditions, adhesives, and curing methods..... | 6-129 |
| Figure 6.25. A schematic illustration of the various forces acting on a single CF when it is exposed at the surface and incorporated into an adhesively bonded joint. | 6-130 |
| Figure 6.26. Representation of the failure modes of a) and b) non-treated samples bonded using Loctite adhesive cured in an oven and at room temperature, respectively, c) non-treated sample bonded using Araldite adhesive, d), e), and f) samples treated with 30 ns, 80 ns, and 200 ns pulse lasers, respectively, and bonded with Loctite adhesive and cured in an oven..... | 6-131 |
| Figure 6.27. Failure modes of laser-treated samples bonded with Araldite adhesive, treated with a) 30 ns, b) 80 ns, and c) 200 ns pulse lengths. | 6-132 |
| Figure 6.28. Optical microscopy images of cross-section of fractured a) non-treated sample, b), c), and d) laser treated using 200 ns pulse length with different magnifications show fibres was torn from one coupon and adhered to the adhesive on the other coupon. | 6-133 |
| Figure 6.29. SEM images of the cross-sections of fractured laser-treated samples using pulse lengths of (a) 30 ns, (b) 200 ns, and (c) 200 ns, with high magnification focused on the CFRP-adhesive interface..... | 6-133 |
| Figure 6.30. Side view of a single lap joint derived from the SolidWorks model. | 6-134 |
| Figure 6.31. SolidWorks simulation results showing the x and z stress components of (a) and (b) the Loctite adhesive model, and (c) and (d) the Araldite adhesive model. | 6-136 |
| Figure 6.32. Peel stress distribution along the overlap of single lap joint using three different adhesives with variable modulus, adapted from [330]*..... | 6-136 |
| Figure 6.33. Shear stress distribution along the overlap of single lap joint using two different adhesives adapted from [332]*..... | 6-137 |
| Figure 7.1. Flowchart simplifies the experimental design and workflow. | 7-141 |
| Figure 7.2. a) scheme of the scanning pattern, and b) the laser-processed specimen. | 7-142 |
| Figure 7.3. Digital microscopy images of the laser processed CFRP samples, the sample number and the processing variables along with the LED are marked on top of each sample..... | 7-144 |
| Figure 7.4. The relationship between the LED and the matrix removal percentage. | 7-145 |
| Figure 7.5. An optical profilometry image with a surface profile shows the expansion of the laser-treated region compared to the non-treated region of sample 4, which was treated with a low LED (15 J/cm) CO ₂ laser. ... | 7-147 |
| Figure 7.6. Optical microscopy images of (a) as-received CFRP material, (b) laser-treated CFRP with low LED (non-removed matrix), (c) laser-treated with high LED (fully exposed fibres), and (d) laser-treated CFRP with low LED showed inflation of the matrix in regions where the CFs are close to the surface. | 7-147 |
| Figure 7.7. Schematic illustration of the epoxy resin moulding process (on the left), photo of the resin sample processed with laser (on the right). | 7-148 |
| Figure 7.8. Optical microscopy images of pure epoxy resin sample, each processed with a single CO ₂ laser scan utilising variable laser power and scanning speeds. | 7-150 |
| Figure 7.9. 2D optical profilometric images of grooves 8 and 14, along with their profiles represented at the bottom of the figure. | 7-150 |
| Figure 7.10. Top: 2D optical profilometric images of grooves 12 and 13. Bottom: profiles of grooves 1, 5, 6, 7, 12, and 13. | 7-151 |
| Figure 7.11. The influence of LED on groove depth and width. | 7-152 |
| Figure 7.12. A photo showing the surface of CFRP material 2. | 7-152 |
| Figure 7.13. WCAs for as received and laser treated samples (material 1). | 7-154 |
| Figure 7.14. UD-reinforced CFRP sample showing loose CFs after surface treatment using CO ₂ laser power of 6 W, scanning speed of 150 mm/s, and hatch spacing of 100 µm. The highlighted region revealed superhydrophobic behaviour. | 7-154 |
| Figure 7.15. Optical microscopy images with different magnifications of CFRP material 2 after laser processing: a) and b) with 6 W CO ₂ laser, c) and d) with 4 W CO ₂ laser. The scanning speeds and hatch spacing for both samples were 150 mm/s and 100 µm, respectively. | 7-155 |
| Figure 7.16. a) schematic and b) photo showing the scanning strategy. | 7-156 |
| Figure 7.17. The bonding strength for the different materials/surface conditions. | 7-156 |
| Figure 7.18. a) and b) photos of failed coupons of non-treated CFRP material 2 from two different angles, indicating NSSF. c) and d) optical microscopy images showing torn matrix..... | 7-157 |

| | |
|--|-------|
| Figure 7.19. Photos of failed coupons of CFRP: a) material 1 processed with 4 W, b) material 1 processed with 6 W, c) material 2 processed with 4 W, and d) material 2 processed with 6 W. | 7-158 |
| Figure 7.20. a) optical microscopy images of fibre-exposed CFRP material 2 after CO ₂ laser treatment with high LED, showing a high number of bubbles surrounding the fibres, b) an SEM image shows a bubble adhere to a CF. | 7-159 |
| Figure 7.21. Schematic of the CW laser ablation process of polymer material, illustrating bubble formation near the surface due to gas release from resin decomposition. | 7-160 |
| Figure 7.22. Comparison of FTIR spectra between CFRP Material 1 and Material 2. | 7-161 |
| Figure 7.23. Comparison of FTIR spectra among as-received and CO ₂ laser-treated samples with 4 W and 6 W. All of which are from CFRP Material 1. The scanning speed and hatch spacing for both laser-treated samples were 150 mm/s and 100 μm, respectively. | 7-161 |
| Figure 8.1. Flowchart Simplifies the experimental design and workflow. | 8-164 |
| Figure 8.2. UV lamp and the experimental setup: a) photograph and b) schematic drawing, [279]*. | 8-166 |
| Figure 8.3. Droplet shapes and WCAs at different UV fluence. | 8-167 |
| Figure 8.4. Typical time dependency for the reduction or stability of WCA of, a) laser textured, b) UV treated sample highest UV fluence. | 8-167 |
| Figure 8.5. Mean WCAs for CFRP samples treated with different UV intensities and exposure periods. | 8-168 |
| Figure 8.6. Mean WCAs for CFRP samples treated with different UV fluence. | 8-168 |
| Figure 8.7. Schemes show the UV intensity distribution over the width of samples exposed to a) 50 mW/cm ² , and b) 25 mW/cm ² | 8-169 |
| Figure 8.8. FTIR spectra comparison among as-received, UV-treated, and UV-treated and subsequently cleaned samples. | 8-170 |
| Figure 8.9. a) and b) optical microscopy images for sandpaper treated sample at various magnifications. ... | 8-172 |
| Figure 8.10. Comparison in CA for both water and diiodomethane among various surface treatment techniques. | 8-173 |
| Figure 8.11. Comparison of the bonding strength among different surface conditions. | 8-174 |
| Figure 8.12. The failure modes of a) UV treated, and b) sandpaper treated sample. | 8-174 |
| Figure 8.13. A macro photo showing a fractured UV-treated sample shows the fracture along the entire coupon. | 8-175 |
| Figure 8.14. Optical microscopy images of cross-sections of CFRP coupons treated with UV light after SLS test. | 8-175 |
| Figure 8.15. Scheme illustrating the load distribution in the tested CFRP material under the SLS test. | 8-177 |
| Figure 8.16. Photos of the five different CFRP materials investigated, with labels provided for each. | 8-177 |
| Figure 8.17. Comparison of WCA between non-treated and UV-treated samples of five different CFRP materials. | 8-178 |

List of Tables

| | |
|---|-------|
| Table 2.1. The mechanical characteristics of various types of carbon fibres [75-77]. | 2-13 |
| Table 2.2. Commercially available lasers, their characteristics and their primary application adopted from [203]*. | 2-34 |
| Table 3.1. The UV lamp characteristics [274]. | 3-59 |
| Table 3.2. UV intensities and distances from the lamp applied in the experimental work. | 3-59 |
| Table 3.3. The key characteristics of two bonding adhesives, Loctite 9394 and Araldite 420. | 3-64 |
| Table 3.4. Properties of SP115, EL2, and IN2 epoxy resins. | 3-64 |
| Table 4.1. The thickness, transmittance, surface roughness, and their standard deviations. | 4-72 |
| Table 4.2. The absorption coefficients α , penetration depths δ , and the reflection fractions R of the three epoxies for NIR laser 1064 nm. | 4-73 |
| Table 5.1. Pulse Energy and Hatch Spacing Levels of the first exploration trial. | 5-84 |
| Table 5.2. Pulse Energy, hatch Spacing, and scanning speed Levels of the second exploration trial. | 5-85 |
| Table 5.3. The factorial experimental design. | 5-89 |
| Table 5.4. The optimised laser parameters. | 5-89 |
| Table 6.1. The laser processing variables for the three experimental sets concern studying the effect of heat accumulated within the fibre. | 6-108 |
| Table 6.2. The laser processing variable for dimple creation. | 6-120 |
| Table 6.3. The laser processing variable for the different experimental runs. | 6-121 |
| Table 6.4. The laser processing variables utilised for the adhesive bonding tests. The sample numbers are initials from the previous optimisation step. | 6-123 |
| Table 6.5. The laser processing variables and the resultant WCAs at 25s after droplet deposition. | 6-126 |
| Table 7.1. The laser processing variables along with the calculated and resultant values for each sample. | 7-143 |
| Table 7.2. The laser processing variables along with the calculated and resultant depth and width of each groove. | 7-149 |
| Table 7.3. The laser variable utilised for wettability assessment. | 7-153 |
| Table 8.1. UV intensities and distances from the lamp applied in the project. | 8-166 |
| Table 8.2. UV intensities and exposure periods. | 8-166 |
| Table 8.3. The techniques implemented in the adhesive bonding strength comparison. | 8-171 |

Nomenclature

| Symbol | Description |
|----------------------|---|
| D | Laser beam diameter at the focusing lens |
| D' | Unfocused laser spot size |
| D_R | Raw laser beam diameter |
| d_o | Laser beam spot size |
| df | Defocus distance of a laser beam (distance away from focal point) |
| d_z | Laser beam diameter at a distance z from the focal point |
| E | Photon energy |
| E_p or E_{pulse} | Pulse energy |
| f | Lens focal length |
| h | Planck's constant |
| I | Light intensity |
| L | Resonator length |
| M^2 | Laser beam quality |
| P_{ave} | Average power |
| P_{peak} | Pulse power |
| T | Transmittance |
| v | Scanning speed |
| w | Radius of laser beam |
| w_o | Waist radius of laser beam |
| Z_R | Rayleigh length |
| α | Absorption coefficient |
| δ | Penetration depth |
| δt | The time interval between two adjacent laser marks (scans) |
| Δt | The time interval between two consecutive pulses |
| γ | Surface Free Energy |
| γ_l | Surface free energy of the liquid |
| γ_s | Surface free energy of the solid substrate |
| γ_{sl} | Solid-liquid interfacial free energy |
| γ^d | Dispersive component of Surface Free Energy |
| γ^p | Polar component of Surface Free Energy |
| θ & θ' | Gaussian and real divergence angles of laser beam |

| | |
|-----------|----------------------------|
| λ | Light Wavelength |
| ν | Pulse Repetition Frequency |
| τ | Pulse length |
| θ | Contact Angle |

List of abbreviations

| Notation | Decription |
|-----------------|---|
| 8-HS | 8-Harness Satin |
| AF | Adhesion Failure |
| ATR-FTIR | Attenuated Total Reflectance-Fourier Transform Infrared |
| CA | Contact Angle |
| CF | Carbon Fibre |
| CFRP | Carbon Fibre Reinforced Polymer |
| CO ₂ | Carbon Dioxide |
| CSF | Cohesive Substrate Failure |
| CW | Continuous-Wave |
| FRP | Fibre Reinforced Polymer |
| fs | Femtosecond |
| FTIR | Fourier Transform Infrared |
| SLS | Single Lap Shear |
| CSF | Cohesive Substrate Failure |
| FRP | Fibre Reinforced Polymer |
| GF | Glass Fibre |
| GP-grade | General-purpose grade |
| HAZ | Heat-Affected Zone |
| H | Hatch Spacing |
| HM | High modulus |
| HP-grade | High-performance grade |
| HT | High Strength |
| IR | Infrared |
| LED | Linear Energy Density |
| LFTF | Light Fibre Tear Failure |
| LIPSS | Laser Induced Periodic Surface Structures |
| MIR | Mid-Infrared |
| NIR | Near-Infrared |
| nm | Nanometre |
| ns | Nanosecond |
| NSSF | Near Surface Substrate Failure |

| | |
|------|---------------------------------|
| PAN | Polyacrylonitrile |
| PRF | Pulse Repetition Frequency |
| PTFE | Polytetrafluoroethylene |
| R | Reflection |
| SEM | Scanning Electron Microscopy |
| SFE | Surface Free Energy |
| SLS | Single Lap Shear |
| TEM | Transverse Electromagnetic Mode |
| UD | Unidirectional |
| UV | Ultraviolet |
| WCA | Water Contact Angle |

CHAPTER 1: Introduction and Thesis Structure

1.1 Carbon Fibre Reinforced Polymers (CFRPs)

A composite material is created by combining two or more distinct materials [1, 2], resulting in a new material with superior properties compared to its individual components. These enhanced properties include strength and stiffness, durability, and weight reduction [3, 4]. Moreover, composites are generally more resistant to fatigue compared to their metal counterparts [5]. Fibre Reinforced Polymers (FRPs) are composite materials consisting of a polymer matrix reinforced with fibres such as glass, aramid, and carbon fibre [6]. The fibre can be discontinuous (short) or continuous (long). Continuous-fibre composites are the most efficient from the point of view of stiffness and strength [4]. In advanced FRP composites, carbon fibre is the most used reinforcement, and epoxies are primarily used as the matrices in CFRP production [7]. CFRP composites, which have a higher specific strength than steel and lighter than aluminium [8], are being used across industries such as aerospace, wind energy, automotive, oil and gas, and sports equipment. Aircraft manufacturers are now using advanced composites more than metals in their structures [5]. They reduce weight and offer excellent fatigue strength, dimension stability, chemical resistance [3], and low thermal expansion coefficient [9]. From another point of view, the increasing demands to reduce fuel consumption and minimise carbon emissions encourage aircraft and automobile manufacturers to use CFRPs and other light composites in the fabrication of their product structures [10, 11].

1.2 Research motivation and the state of the art

Meeting the demanding requirements for lightweight construction can be effectively achieved using CFRP composites. However, one significant challenge remains: the joining technology. The fabrication of CFRP structures is complicated; large parts are often formed by assembling or joining several elements [12]. Mechanical joints, such as bolts and rivets, are widely used. These, however, have several drawbacks; they need holes to be drilled in the CFRP, and the abrasive and anisotropic properties of CFRPs lead to high tool wear and greater cutting forces while drilling and a harmful effect on the workpiece integrity. Delamination, cracks, and matrix thermal degradation are observed as a result of uncontrolled drilling [13]. Moreover, mechanical fasteners inevitably cause damage to the load-carrying fibres and create concentrated stress around the holes [14], which makes oversizing necessary [15]. Additionally, the fasteners themselves could be a significant source of increasing weight [16],

particularly in weight-sensitive structures such as aircraft. Adhesive bonding offers a promising approach to fully exploit the lightweight properties of CFRPs. It overcomes the mechanical fasteners' drawbacks and provides an excellent balance of fatigue strength and stiffness. Furthermore, adhesive joints are cost and weight-efficient [17]. Nevertheless, creating strong and durable adhesive joints is not straightforward. Surface pre-treatment is a crucial step before adhesive bonding to remove contaminants, enhance surface topography, and chemically activate the surface to ensure robust and durable joints. Release agent residues and other contaminants, such as dirt, oil, moisture, and weak layers, must be removed. Otherwise, the adhesive will bond to these weak boundaries rather than to the substrate [18]. In addition to the surface cleanliness, for a given adhesive and joint design, the main other factors governing adhesive joint strength are the surface wettability and roughness. The surface roughness increases the actual bonded interface area and adds mechanical interlocking between the substrate and the cured adhesive. The consequence of good wetting is a greater contact area between the adherents and the adhesive over which the forces of adhesion may act [19]. Some researchers have further proposed that exposing the Carbon Fibres (CFs) by removing the outer layer of the matrix, which allows direct load transfer into the fibres, is critical for strong bonding [14].

Currently, various techniques are used in the industry to improve CFRP surfaces for adhesive bonding, each with its own advantages and disadvantages. One popular technique in the aerospace industry is the peel-ply. This involves applying an extra layer of fabric material to the composite surface during curing, which is then peeled off before adhesive joining to create clean, textured surfaces [20]. However, peel ply manufacturers coat the surface with a release agent for easy removal after curing, but traces of contaminants like fluorine, nitrogen, or silicon negatively affect bonding. Post-treatments such as light sanding, grit blasting, or atmospheric plasma are necessary to eliminate these contaminants and improve adhesion [21], which increases the manufacturing complexity and cost [20]. Another common method is mechanical abrasion, which includes grinding and grit blasting. While these methods are easy to apply, they often produce additional surface contamination and have low efficiency and reproducibility, necessitating a subsequent cleaning process [22]. Chemical etching processes produce chemical wastes that pollute the environment [23].

In contrast, lasers, known for being non-contact, wear-free tools with the potential for robotic automation, show significant promise for the surface treatment of CFRPs. Recently, researchers have investigated various lasers to create effective and consistent surface

conditions. Some studies have demonstrated that laser surface processing can consistently achieve superior bond strengths compared to abraded specimens [15, 24-26]. Most previous studies have employed pulsed UV or IR lasers. These studies have generally shown improvements in joint strength, with particularly promising results observed with UV lasers [27-29]. IR lasers process materials through intense local heating that melts or vaporises parts of the material surface, which can damage surrounding areas. In contrast, UV laser treatment is considered a cold process that directly breaks down atomic bonds [27, 30]. However, UV lasers are associated with limited reliability, low processing speed, high power consumption, and high cost of ownership [31].

1.3 Research gaps and challenges

1. The potential benefits and mechanisms of using incoherent UV light alone or combined with IR lasers for treating CFRP surfaces have not been explored in existing literature. Previous studies [32, 33] have primarily focused on using incoherent UV light with ozone for treating various materials, but this method has drawbacks such as the need for specialised equipment and the toxic effects of ozone. Therefore, there is a significant research gap in understanding how incoherent UV light, independently or combined with IR lasers, can improve CFRP surfaces for adhesive bonding.
2. The interactions between NIR lasers and CFRP materials are not fully understood, with discrepancies in the literature about their effects on adhesive bonding and matrix removal. CFRP composites, composed of materials with differing thermal and optical properties, have a matrix that is highly transmissive to NIR lasers (1064 nm). This allows substantial laser energy to reach the underlying fibres, potentially causing fibre-matrix debonding. While some studies report significant improvements in bonding strength using pulsed NIR lasers, others reject the use of NIR lasers for CFRP surface treatment. Additionally, while the effects of NIR laser processing variables are well-documented, the variations in response due to different CFRP composites have not been thoroughly studied. The heterogeneity of CFRP often leads to uneven ablation results, with carbon fibres significantly influencing the outcome due to their high absorptivity and thermal conductivity. The fibre direction and the distance from the surface to the fibres in various CFRP composites can cause different responses to laser processing, underscoring the need for further research in this area.
3. There is a high discrepancy and limited data in the literature regarding the absorption and transmittance values of matrix resins, particularly to MIR (10,600 nm), such as CO₂

lasers. Some researchers [34, 35] have reported that the absorption of thermosetting matrices at 10.6 μm is very high (90-95%), with almost no transmittance. In contrast, other researchers have reported that a 6.5 μm epoxy film transmits 30% of the incident laser power [36] and a 125 μm epoxy film transmits 3% [37]. Moreover, the complexity of laser-material interactions is further increased due to the varying distances from the surface to the fibres. Notably, in UD-reinforced CFRPs, which exhibit less inhomogeneity than woven CFRPs, the distance from the surface to the fibre can vary from less than 1 μm to over 10 μm .

1.4 Aim and objectives

The aim of this research is to investigate the effectiveness of using a ns pulsed NIR fibre laser as well as a continuous-wave (CW) MIR laser, assisted by incoherent UV light, to improve the adhesive bonding of CFRP/CFRP structures.

To achieve this goal, the following objectives were established:

1. Understand the current industrial practices, techniques and standards concerning the preparation processes of CFRP composites for adhesive joining and align the research with these standards.
2. Review and evaluate existing research, comparing their methodologies, techniques, and results with the approaches and outcomes planned for this study.
3. Understand the laser material interaction, the transmittance and absorptivity, and the matrix removal mechanism.
4. Study the characteristics of different CFRP materials and their influences on laser treatment and adhesive bonding.
5. Understand the impact of adhesive properties on joint stresses and strength.
6. Optimise the processing parameters for each technique under investigation and analyse the impact of each processing variable on the response variables.
7. Compare the bonding strength among various processing techniques, including the ones investigated, combinations of them, and current industrial practices.
8. Assess and compare the outcomes of the different techniques used in this work in terms of efficiency, reliability, and cost with those currently used by industry.

1.5. Thesis structure

This thesis is structured into nine chapters, outlined as follows:

Chapter 1. Introduction and thesis structure

This chapter discusses the research motivation and current state of the art, identifies the research gaps and challenges, outlines the research aims and objectives, and specifies the thesis structure.

Chapter 2. Literature review

This chapter examines the essential role of adhesive bonding in CFRP structures and the necessity of surface preparation using existing literature. It reviews adhesion theories, surface preparation methods, and the potential of laser, emphasising laser fundamentals, and incoherent UV light as contactless tools for the surface treatment of CFRPs.

Chapter 3. Experimental methods

The main equipment and approaches used in the research project are discussed in this chapter, while other methods are detailed within the experimental sections of each respective experiment.

Chapter 4. Matrix resin absorption and transmittance.

An experimental investigation measuring the absorption coefficients of typical thermosetting matrix resins for both NIR and MIR lasers.

Chapter 5. Laser surface processing of woven reinforced CFRP composites to improve adhesive bonding using NIR ns pulsed fibre laser.

An experimental investigation focused on surface processing of woven, highly inhomogeneous CFRP composites using ns pulsed NIR fibre laser.

Chapter 6. Laser surface processing of UD reinforced CFRP composites to improve adhesive bonding using NIR ns pulsed fibre laser.

This chapter investigates the effects of different laser processing variables on the resultant responses through separated experiments.

Chapter 7. Surface treatment of CFRP using CW CO₂ laser.

This chapter presents an experimental study on the feasibility of using a CW CO₂ laser for surface treatment of CFRPs to improve adhesive bonding. The work includes processing bulk resin samples to further understand the ablation mechanism of the matrix.

Chapter 8. The use of incoherent UV light as assistant to IR lasers.

This chapter outlines the benefits of exposing CFRP composites to UV light (non-laser) emitting at 254 nm to improve adhesive bonding. The effects of UV light were investigated both separately and as an adjunct to IR lasers.

Chapter 9. Conclusions and future work

This chapter concludes the key findings of the experimental investigation presented in this thesis and outlines potential future research needed to further understand the role of laser and incoherent UV light treatments of CFRP treatment for adhesive bonding.

CHAPTER 2: Literature Review

2.1. An overview of CFRP composites

2.1.1. Composite materials

A material that consists of two or more different constituents on the macroscale with distinct boundaries is called a composite [1, 2]. A composite material typically has better properties compared to those of the individual components used alone. Carbon Fibre (CF), for example, exhibits exceptional tensile strength but is inherently brittle, lacking compressive strength and flexibility. Without a supporting matrix, CFs are prone to fracturing or splintering under compressive or bending loads [4]. The matrix not only binds the fibres together, enabling load distribution across them, but also protects the fibres from environmental factors like moisture and chemicals. Additionally, the matrix facilitates the arrangement of fibres into desired shapes and reduces weight and cost [3]. In contrast to metallic alloys, in composites each material maintains its distinct chemical, physical, and mechanical properties [3]. The concept composite, in its origin, is not a human invention; wood, bones, and teeth are examples of natural composites [38]. Compared with their constituents, composites generally have the potential to display enhancements in some properties, such as their strength, stiffness, durability, resistance to damage, wear, corrosion, fatigue, and thermal insulation [2]. Existing composites are classified into two main groups. The first is known as *filled materials*, where the basic or matrix material properties are improved by filling it with particles of one or more other material/(s). The second group involves composites that are called *reinforced materials*, also known as *advanced composites*. The main components of these composites are long, tiny fibres possessing high strength and stiffness embedded in a matrix whose volume fraction is usually less than 50% of the composite. In such composites, the fibres determine the strength and stiffness of the composite, while the matrix holds the fibres together [39]. The first type of fibre used in advanced composites was Glass Fibre (GF); it has about 40% of the stiffness of steel but is three times lighter. A substantial improvement in fibre's stiffness has been achieved with the introduction CFs. Modern high-modulus CFs have a modulus of up to five times that of steel [40], whereas its density is about four times lower [41]. Notably, commercial steel has a modulus of around 200 GPa [42], and a specific density of about 7.9 [43]. CFs as a reinforcement, are used with different matrices [44], including metals such as aluminium or titanium matrices [45], and for ultra-high-temperature applications with ceramics matrices [46]. However, the more common usage of CFs is with polymeric matrices (**Figure 2.1**), which

are known as CFRPs [44]. CFRPs, which hold significant importance due to their widespread use in various industries, are discussed in detail in this chapter, wherein their components, characteristics, varieties, applications, and manufacturing procedures are examined.

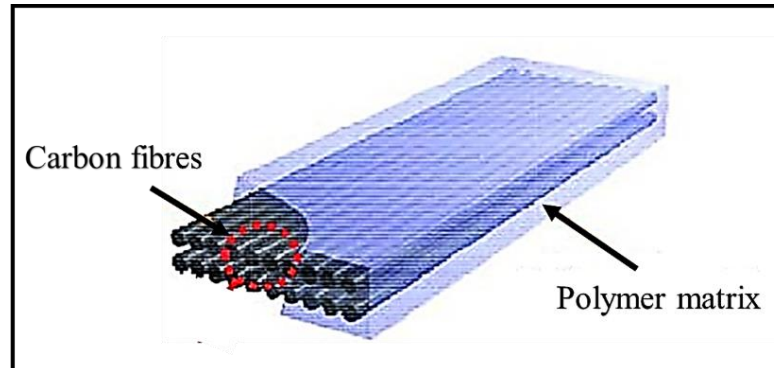


Figure 2.1. Representation of carbon fibre reinforced polymer composite, adapted from [47]*.

2.1.2. Production of carbon fibres

The production of carbon fibres started only in the early 1960s [48], and their properties were progressively improved over the last decades. Since then, carbon fibres have been extensively used in high-performance aerospace applications. Commercial aircraft, such as the Airbus A350 and the Boeing 787, have made extensive use of CFRPs in the airframe, with over 50 wt% [49] and in some helicopters such as the Boeing AH-66 the percentage is higher [50]. To date, carbon fibres are the strongest and stiffest fibrous reinforcement known [51, 52]. Moreover, they possess several other advantages over other reinforcing fibres including their light weight, low thermal expansion, and the superior chemical resistance [9].

In the 1990s and beyond, efforts to improve the production processes had led to further enhancement in the properties of CFRP and a reduction in the overall production cost [53]. Currently, CF market has been formed in many other industrial fields such as automotive, marine, wind energy and sports goods [48]. In 2021, the annual consumption of CFRPs was around 180 thousand tons, which is more than double its value in 2014 and expected to reach 285 thousand tons in 2025, largely credited to the rapid growth of non-aerospace sectors like the wind energy industry [49].

Carbon fibres are generally classified depending on the precursors being used, which are mainly either polyacrylonitrile (PAN) based or pitch-based [54, 55]. Such carbon fibre products can be obtained as continuous fibres with different morphologies such as monofilaments, tows of 1000-12,000 filaments, woven fabric, chopped fibres, and non-woven mats [56]. Theoretically, any fibrous material derived from a carbonaceous precursor could be utilised.

However, commercial carbon fibres are only produced from PAN, pitch, and rayon fibrous precursors [57]. Rayon-based carbon fibres were the first to be commercialised and remained dominant up to the early 1970s. Currently, PAN-based carbon fibre products represent the vast majority [48, 58, 59].

The production processes of PAN-based carbon fibres started with the spinning of the precursor. In this process, the powder or granular of the precursor is converted into continuous fibres. Almost all commercial fibres are produced by one of the three procedures: melt, wet, and dry spinning. Pure PAN has a glass transition temperature of around 120°C and tends to decompose before being melted. Thus, dry and wet spinning are the common methods for PAN-based fibres, and due to the processing cost, wet spinning is used in most commercial PAN-based CFs. In this process, the PAN precursor, constituting 10-30%, is dissolved in a polar solvent to reduce its viscosity to a level at which spinning becomes possible. The solution is first filtered and squeezed out of the spinneret into a coagulation bath. The latter can contain various solutions, such as dimethyl sulfoxide and water. The molecules are aligned during the spinning along the fibre axis, and the solvent diffuses out from the formed fibre. The concentration of the spinning solution and the coagulation bath solution, the bath temperature, and the circulation rate of the fluid in the coagulation bath all govern the final cross-sectional shape of the produced fibre and can affect its structure.[60]. A simplified schematic of the wet spinning process is re-drawn in **Figure 2.2** [61]. After the spinning process, there are three heat treatment steps. The first one is stabilization, where PAN filaments are stretched in an oxidation furnace at 400°C. The second step is carbonization in an inert gas medium between 1200-1400°C; in this stage, most elements of the stretched filaments other than carbon are removed or converted into carbon. The product from this stage has low tensile strength and modulus, around 1000 MPa and 100 GPa, respectively. It is classified as a general-purpose grade (GP-grade). The last step is graphitization, which involves heat treatment at a temperature reaching 3000°C. This process orients the carbon crystalline structure along the fibre's length, producing PAN-based carbon fibres with higher strength and modulus than that of the GP-grade. These are called high-performance grades (HP-grade). The latter is further classified into high-strength (HT) and high-modulus (HM) carbon fibres [41, 56, 62]. Toray, a prominent carbon fibre manufacturer, currently produces carbon fibres with a tensile modulus reaching 588 GPa (M60J) and tensile strength of 7000 MPa (T1100S and T1100G) [49].

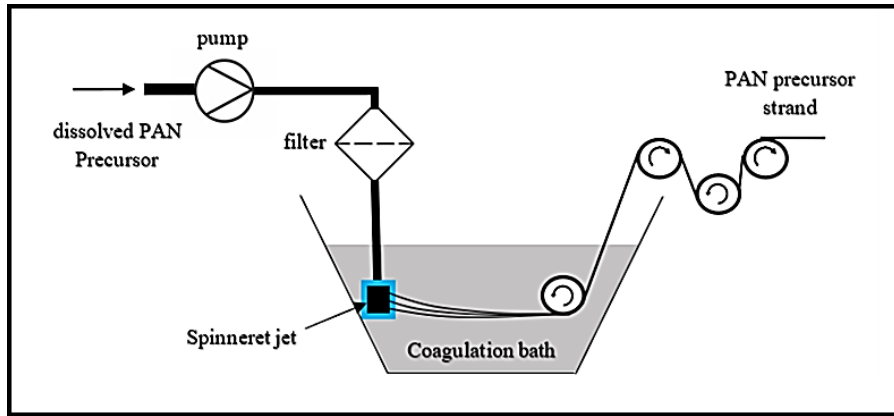


Figure 2.2. Schematic of the wet spinning process, re-drawn from [61]*.

Reviewing literature reveals variations in the production processes of carbon fibres. Moreover, it is important to note that due to industry confidentiality, the knowledge of proprietary practices has not been usually available in publicly accessible domains [56, 63]. The flowchart in **Figure 2.3** shows the main production steps for PAN-based carbon fibre simplified based on the description provided by some researchers [59, 60].

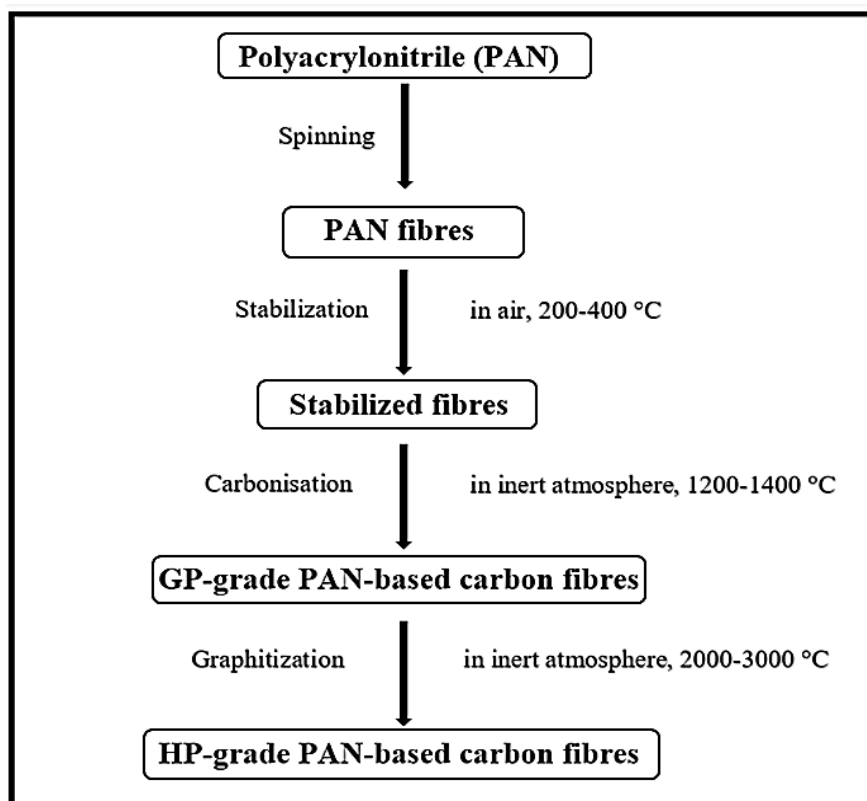


Figure 2.3. Production procedures for PAN-based carbon fibres.

2.1.3. Sizing agent of CFs

The surface of carbon fibre produced through wet spinning normally exhibits distributed grooves, where axial elongation and radial shrinkage of fibres occur simultaneously during the formation process. As the filament undergoes densification, its cross-section gradually decreases in imbalance, resulting in surface-folded wrinkles [64]. A sizing agent, a thin layer of a proprietary cocktail of ingredients, is applied to the fibre at the final production step, it typically ranges between 30–100 nm [65] or up to 500 nm, but irrespective of thickness, it usually between 0.5 – 1% by weight of the fibre [66]. This layer often plays a substantial role in enhancing carbon fibre surface properties. The mechanical properties of carbon fibres and the bonding strength between carbon fibres and the matrix are both crucial factors in achieving high-strength carbon fibre composites. The mechanical properties are mostly governed by the internal structure of the carbon fibre, including crystallinity, compactness, and defects, whereas the bonding performance is associated with the surface properties of the fibres [64]. It is widely reported that fibre-to-matrix adhesion is a critical parameter in any composite material and is substantial in determining the overall performance of the composite material [64, 67, 68]. The sizing makes the fibre tractable and aids in protecting the fibre from postprocessing, such as the transformation of fibres into woven materials by shielding the fibre surface from abrasion and preventing the fibre from breaking at contact points [66]. Moreover, it enhances interfacial adhesion between the fibre and the matrix. However, there is a large degree of conflicting results being reported in the literature over the past 4 decades regarding the latter point [66]. A study by Bascom et al. [69] have stated that the purpose of sizing agents is only for postprocessing and not to enhance fibre-matrix adhesion. Another study has concluded that the sizing itself reduces both fibre-matrix adhesion and the fibre tensile strength [70]. Similarly, with regards to the fibre surface roughness, which undoubtedly contributes to the Interfacial Shear Strength (IFSS) between the fibre and the matrix, there are contradictory findings in the literature about whether sizing increases or decreases fibre surface roughness [66], the vast majority have stated that sizing smoothens the fibre [71, 72]. **Figure 2.4** shows SEM of (a) unsized, (b) sized [73], and (c) a schematic representation of a sized fibre [64]. It seems that the sizing reduces the groove depths but does not eliminate them, resulting in a reduction in roughness. However, this depends on the thickness of the sizing layer and the fibre groove depth, which are both uncertain and possibly vary according to the production method and the producer.

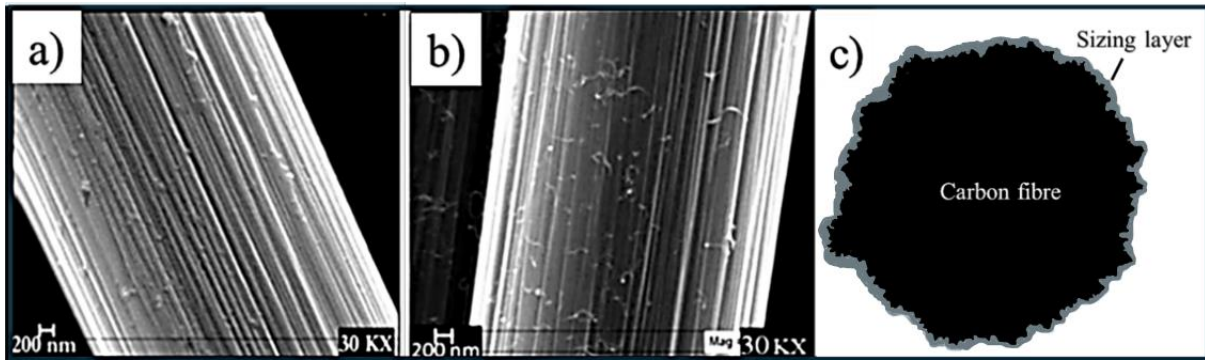


Figure 2.4. SEM images of (a) unsized carbon fibre and (b) sized carbon fibre, adapted from [67]*, and (c) a schematic illustration of a cross-section of a sized carbon fibre.

2.1.4. Properties of carbon fibre.

In addition to their exceptionally high strength and stiffness-to-weight ratios, which were mentioned earlier in this chapter, carbon fibres are anisotropic, brittle, and sensitive to damage. They exhibit no water absorption and maintain dimensional stability in humid conditions. Another important property of carbon fibres as components of advanced composites for engineering applications is their high strength stability under elevated temperatures. A comparison with other organic fibres is depicted in **Figure 2.5** [41]. Moreover, the high fatigue resistance is one of the key advantages of utilising carbon fibres in composite materials [74]. Additionally, carbon fibre is considered a good electrical and thermal conductive and chemically stable [75]. Currently, more than 50 types of carbon fibre are used across various industries, exhibiting a broad spectrum of properties and costs, and the evolution of carbon fibre technology is still ongoing [41]. **Table 2.1** presents the mechanical characteristics of various types of carbon fibres. Due to discrepancies found in the literature [59, 76], possibly attributed to the continuous improvement in carbon fibre properties; these data were sourced directly from recent datasheets provided by Toray and Solvay [77-79], international carbon fibre producers.

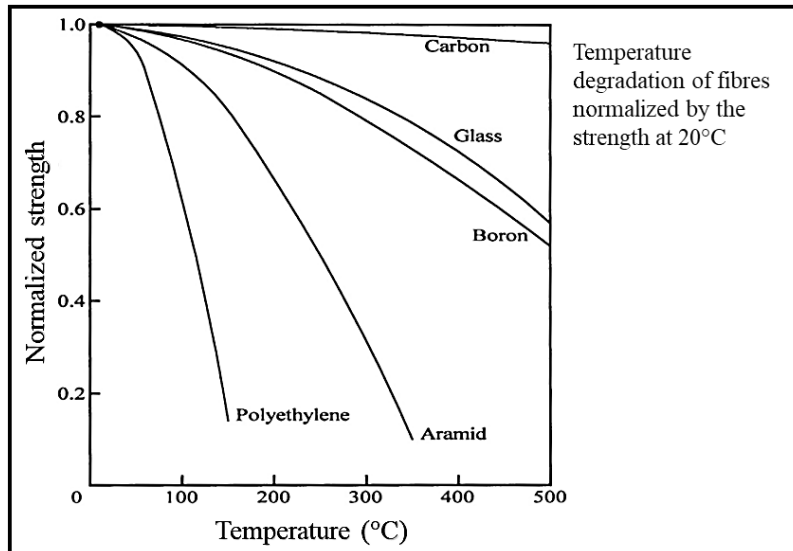


Figure 2.5. Effect of elevated temperature on the strength of different organic fibres, adapted from [41]*.

Table 2.1. The mechanical characteristics of various types of carbon fibres [77-79].

| Classification | CF | Modulus (GPa) | Tensile strength (GPa) | Thermal conductivity (W/m. K) | Density (g/cm ²) | Diameter (µm) |
|----------------|--------|---------------|------------------------|-------------------------------|------------------------------|---------------|
| PAN-based | T300 | 230 | 3.5 | 10.5 | 1.76 | 7 |
| | T700S | 240 | 4.9 | 9.6 | 1.8 | 7 |
| | T800S | 294 | 5.88 | 11.3 | 1.8 | 5 |
| | T1000G | 294 | 6.4 | - | 1.8 | 5 |
| | T1100G | 324 | 7 | 13 | 1.79 | 5 |
| Pitch-based | P25 | 160 | 1.56 | 36 | 1.9 | 11 |
| | P100 | 760 | 2.4 | 590 | 2.13 | 11 |

Nevertheless, carbon fibres have disadvantages as well. They exhibit low compressive strength, ranging from 10% to 60% of their tensile strength in the axial direction and significantly lower in the transverse direction [74, 80, 81]. Additionally, carbon fibre exhibits negative thermal expansion in the axial direction from room temperature up to above 500°C [74, 82, 83]. This is considered another disadvantage, especially for high-modulus carbon fibre when it is combined with matrices that typically have positive thermal expansion [74]. This expansion mismatch can induce residual stresses in the composite element. [83, 84]. However, this property also has benefits; it allows the manufacturing of composites with near-zero thermal expansion by appropriately controlling the fibre orientation [85, 86]. Moreover, carbon fibres have low impact resistance [87, 88], and at higher temperatures they suffer oxidation [74, 89].

2.1.5. Commercially available carbon fibre

Carbon fibres are provided in untwisted bundles of fibres known as tows. Tow sizes typically range from 1k fibres/tow to 12k fibres/tow, but sizes of up to over 200,000 fibres/tow are also available. The smaller 1k tow size is usually avoided due to its high cost. In aerospace structures, common tow sizes are 3k, 6k, 12k. For woven cloth, 3k and 6k tows are commonly used, and 12k is used for unidirectional tape. Woven fabrics are primarily constructed with two fibre orientations, 0° and 90° , by interlacing two perpendicular sets of yarns known as *warp* and *weft* [3, 90]. Weaves are classified by the interlacing pattern into plain, Twill, basket, satin, and many others. The three more common in industry are the plain, Twill and harness satin weaves [90]. In general, woven fabrics are used for complex geometries. Satin weaves are stronger than plain weaves, and because they have less crimp fraction than the other two types, they have better drapability, therefore they are used more for highly contoured parts [3, 90]. Besides the considerations related to the shape of the manufactured element, the desired mechanical properties govern the choice of a weave [3]. **Figure 2.6** represents draws of the three most common weave types [90].

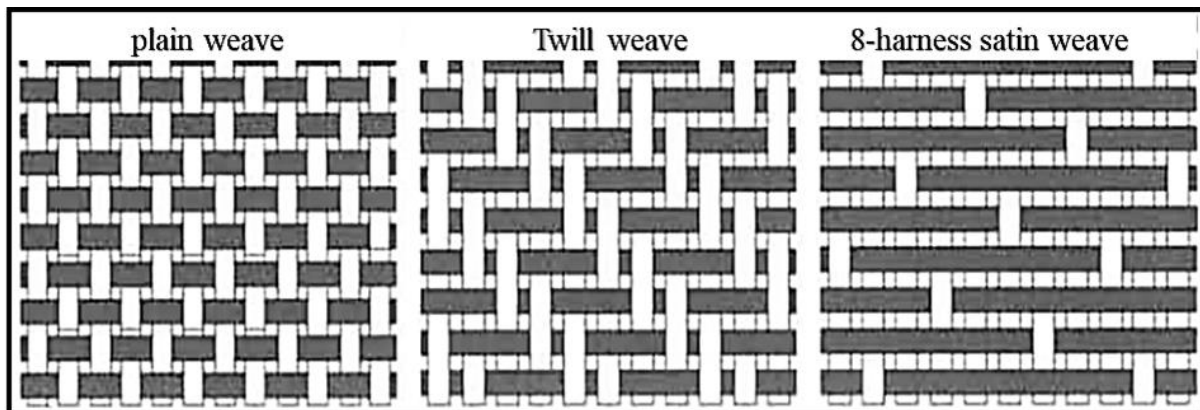


Figure 2.6. Drawings of most common carbon fibre weave, [90]*.

In addition to the dry woven fabric mentioned above, pre-impregnated (prepreg) carbon fibre's tows, weave, or unidirectional fibre tape with a known quantity of partially cured matrix resin are produced and typically used for high-performance composite structures such as aerospace and automotive. There are two commonly used techniques for thermosetting prepreg production: hot melt and solvent impregnation. In the hot melt process, carbon fibres are impregnated in a film of resin with controlled weight under heat and pressure. The solvent resin process involves immersing fibres in a resin-solvent solution until reaching the desired content, followed by heating to remove the solvent. Using prepregs is regarded as the most advanced

technology for composite fabrication. [91]. The resin in the prepreg materials is a tacky semisolid. The final prepreg products normally laid-up and autoclave cured under high pressure and a certain temperature cycle [3]. Unlike prepreg, for dry weaves, the resin is applied during the fabrication of the final element. Several different manufacturing processes are currently employed, each tailored to specific industrial priorities such as the complexity of the produced element, production rate, and cost. These methods include hand lay-up, resin transfer moulding, and compression moulding [87]. Carbon fibre composites exhibit high directionality; they are exceptionally strong in the direction of the fibres but comparatively very weak in the perpendicular direction [3, 45, 92]. Uniform unidirectional composites, where all fibres are oriented in the same direction, offer the highest properties for the composites in the direction of the fibres. Nevertheless, such composites are inherently anisotropic. Composites with less directionality, or quasi-isotropic composites, can be achieved by layering multiple plies, whether dry weave or prepreg, with varying orientations [3, 7]. See **Figure 2.7** [93].

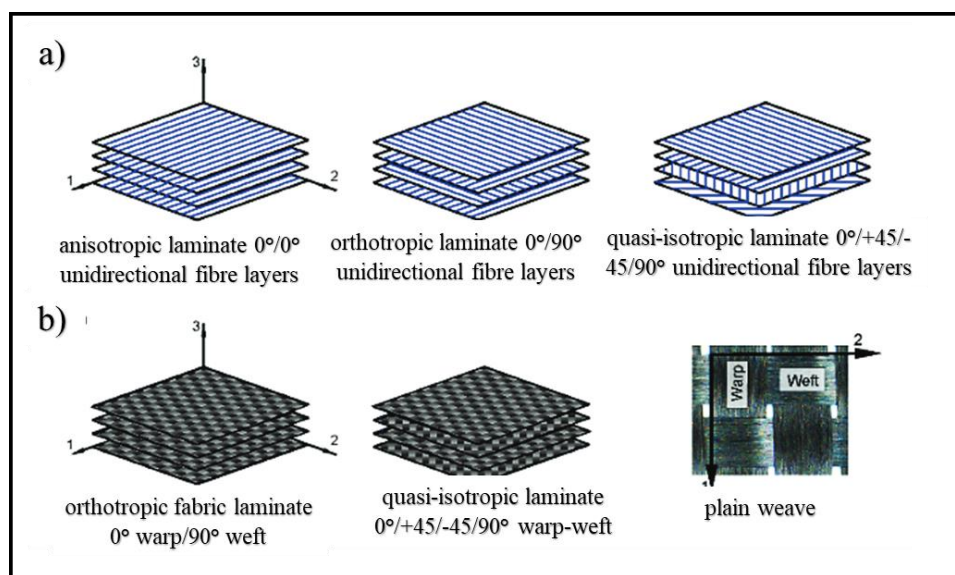


Figure 2.7. Composites lay-ups with different orientations, a) unidirectional, b) plain weave, adapted from Bergant [93]*.

2.1.6. Matrix material

In FRP composites, the fibres are embedded in a polymer or resin, referred to as the matrix. The matrix typically exhibits significantly lower strength and stiffness compared to the fibres; otherwise, there would be no necessity for the fibres [41]. The polymer matrix binds the fibres together and transfers the load between the fibres through shear stresses. This results in a better load distribution over the fibres in a composite compared to a dry fibre bundle, and because the matrix supports the fibres, it can undertake higher compressive loads [4][90]. However, for

high-performance composites, two critical conditions must be met: the stiffness of the matrix should match that of the fibres, and the adhesion strength between the fibres and matrix should be sufficiently high [5]. The matrix also protects the fibre from external factors such as moisture, chemicals, and UV light and often determines surface quality and fire safety [39]. For FRPs, matrices are typically classified into two main categories: thermoplastics and thermosets [90]. Thermoplastics melt or become formable upon heating and solidify upon cooling. They are not generally suitable for impregnation of fibre reinforcements unless high pressures and temperatures are applied. This is because of their high viscosity in liquid state, which prevents fibres from being adequately wetted. In contrast to thermoplastics, thermosets do not melt upon heating; instead, they ultimately disintegrate [4][90]. From a molecular perspective, thermosets are composed of relatively short chains, resulting in non-cured polymers with very low viscosity. The curing process involves a chemical reaction where the short chains form bonds and establish a three-dimensional cross-linked network. In fact, it is not always clear to distinguish between thermoplastics and thermosets. Polyesters, usually categorised as thermosets, display certain thermoplastic characteristics. Similarly, phenolic resins function as thermoplastics until they reach a specific temperature. The most common thermosets categories are polyesters, vinylesters and epoxies. The production of the first two is cheaper than epoxies, which have less shrinkage during the curing process and higher resistance to moisture [4]. Moreover, epoxies have good mechanical properties with high resistance to elevated temperatures and have very good adhesion to a wide variety of materials. However, they require longer polymerization time, are susceptible to cracking, and need higher safety considerations due to their harmful effects [94]. For CFRPs, thermosetting epoxies are the most used matrices [94-96].

2.1.7. Recycling of CFRP composites

As mentioned in a previous section, the annual global use of CFRP composite reached 180k tons in 2021, with an annual increase of 13%. CFRP composites are currently employed in an increasing variety of applications, with a growing presence in the majority of them. The aviation industry provides a notable example, with the new Boeing 787 and Airbus A350 having more than 50% of their weight composed of CFRPs [49]. The growing utilisation of CFRPs results in an increasing volume of CFRP waste; this includes expired prepregs, manufacturing cutoffs, testing materials, and end-of-life components. Recycling CFRP materials is challenging due to several parameters, including the complex composition of fibre-matrix-fillers (fillers in some of which), the cross-linked nature of the thermosetting matrix,

and the existence of other materials such as metal fixings or hybrid composites. The majority of CFRP waste is disposed of in landfills, which is environmentally and economically unsatisfactory [97]. Hence, the recycling of CFRP waste has received significant attention in the last two decades, with numerous studies that used various recycling techniques [98-102]. Depending on the main technique used, recycling processes are classified as mechanical or thermochemical. The mechanical involves breaking down the composite into powder through methods such as crushing, and milling [103]. Powder products from mechanical recycling can be classified into several types, such as coarse and fine or rich in resin and rich in fibres [104]. These are generally used as fillers in various products, such as asphalt and artificial woods [105]. Currently, mechanical recycling is mainly used as a pre-recycling process for other techniques [102]. Thermal and chemical recycling methods involve breaking down the matrix and recovering of the carbon fibres from the CFRP using thermal or chemical processes. The mechanical properties of recycled carbon fibres depend on the process used to break down the matrix. According to several studies, recycled fibres using thermal or chemical processes exhibit comparable properties to those of virgin carbon fibres [97, 98]; other studies, however, have reported that defects such as a drop in the properties of the recycled fibres or matrix residue at the carbon fibre surfaces [101, 102, 106]. **Figure 2.8** shows the most common CFRP recycling methods, the produced fibre characteristics, and the recycled fibre applications [97]. The value of recycled carbon fibres varies according to the method used. The mechanical recycling methods are simple, but their products, which range from powder to fibrous fragments, have limited applications. Chemical and thermal recycling techniques produce higher amounts of carbon fibres. However, each has its own drawbacks; for instance, chemical recycling using strong acids or solvents has severe environmental impacts [97, 102].

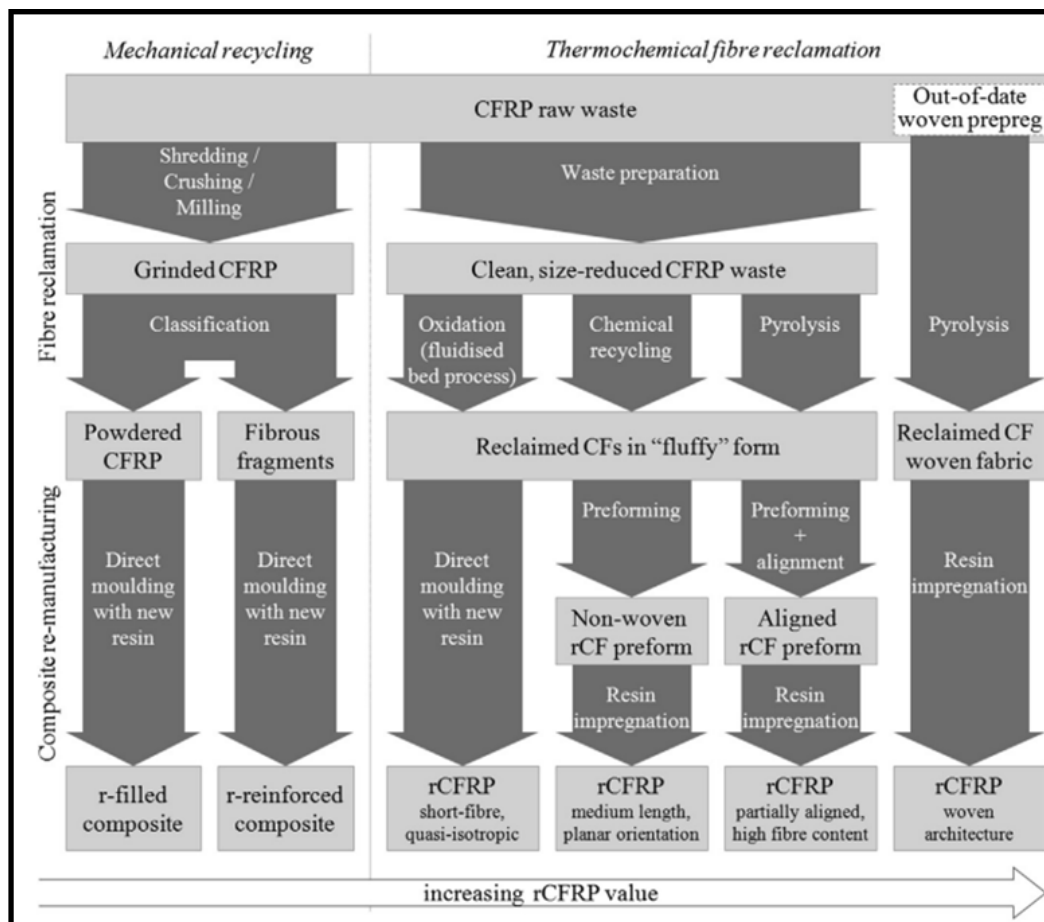


Figure 2.8. Overview of CFRP composites recycling and remanufacturing processes adapted from [97]*.

2.2. Joining of CFRP structures

The use of composite materials in different industries, such as aviation, has increased sharply in recent years. The methods used in the manufacturing of composite structures are somewhat similar to the casting of metals. Consequently, designs of structures, particularly large and complex ones, are usually simplified into several elements that are joined in another step [12, 107, 108]. Moreover, in most applications, CFRP elements require joining with metal frames to form complete structures [109]. Thus, the joining of CFRP elements to other CFRP or metal elements is unavoidable. The two main joining techniques used for thermosetting matrix composites are mechanical fastening and adhesive bonding [3]. Hybrid joining, incorporating both mentioned techniques (mechanical fasteners and adhesive joining), is also utilised [110, 111]. The main advantages and disadvantages of both techniques are summarised in the next sections, along with an overview of adhesion theories and surface preparation methods.

2.2.1. Mechanical fasteners

Mechanical fasteners, such as bolts and screws, offer significant advantages for joining CFRP composites. These include straightforward installation and convenient disassembly for maintenance or repair. Additionally, they exhibit lower sensitivity to peel stresses and residual stress effects [3]. Additionally, no need for surface preparation prior to the joining, which is crucial for strong durable adhesive bonding [26, 112]. However, mechanical fasteners have several disadvantages. They require holes to be cut through the composite, which can disrupt the load path and create concentrated stresses. As a result, adhesive bonding is often considered a more efficient method for load transfer [3, 109]. The abrasive and anisotropic nature of CFRPs leads to increased tool wear and higher cutting forces during drilling, which negatively impact the integrity of the workpiece. Uncontrolled tools can result in delamination, cracks, and thermal degradation of the matrix [13]. Moreover, mechanical fasteners increase the weight of the overall structures and have low sealing capacity. Additionally, the drilling process causes cracks in the composite structures [109], these cracks add additional concentrated stresses [113]. Furthermore, for thin composite structures, the bearing stress would be unacceptably high when mechanical fasteners are used [3, 114]. Inadequate hole preparation methods and inadequate shimming practices may cause delamination during assembly. In composite-metal joints, the use of mechanical fasteners poses an increased risk of galvanic corrosion in the metal during service [3, 115], and there is also a concern about the potential for fatigue cracking in metal components.

2.2.2. Adhesive bonding of CFRP structures

Adhesive bonding avoids the mentioned drawbacks and provides better fatigue strength and stiffness and good vibration and damping properties. It can join thin and dissimilar components, providing good sealing, low weight and manufacturing cost. Therefore, adhesive bonding is the preferred joining method in industries, especially those producing high-end products [17, 112, 116-119]. However, creating a strong, durable adhesive joint is not simple; surfaces require preparation prior to bonding [15, 112, 120, 121]. CFRP surfaces are typically contaminated with release agents due to the manufacturing process. Exposing their surface directly to the adhesive, without any release agents or other contaminants, is always preferable [26]. These contaminants could act as a barrier between the adhesive and the adherent surface. [122]. Nevertheless, surface cleaning alone is insufficient; most structural adhesives work because of the formation of chemical bonds. Thus, appropriate surface pre-treatments are

necessary to remove potential contaminants and introduce additional properties, such as enhancing surface energy, chemistry, and roughness [15, 117].

Although adhesive bonding is the preferred joining technique, it has some disadvantages. In addition to the essential surface preparation process, which is considered a drawback, bonded joints are typically permanent, making disassembly difficult and often resulting in damage to the adherents and surrounding structures. Moreover, adhesive bonding processes require clean rooms with temperature and humidity control [123].

2.2.3. Adhesive and adhesion

An adhesive is a material applied to the surfaces of two or more elements that is capable of forming bonds to each of the bonded elements to join them permanently and resist separation. The materials to be bonded are commonly referred to as substrates or adherends [122, 124]. The weight of the adhesive material is usually small compared to the weight of the final bonded structure [122]. With respect to adhesive and adhesion, it is important to differentiate between interface and interphase; an interface is the boundary between adherend and adhesive, which has no thickness. However, the boundary between two homogeneous phases is rarely an interface but is often comprised of a third phase called interphase [125]. An interphase is a thin region located between two phases and exists in many macrosystems, such as adhesive-adherend in an adhesive bond or fibre-matrix in fibre composites. The interphase is distinguished by its unique structure and properties compared to either of the two phases. This concept has garnered significant support among adhesion scientists [19, 125, 126]. Adhesives are commonly classified into structural and non-structural. Structural adhesives are described as high-strength adhesive materials; these are used when the adherends experience large stresses, which could be up their yield point without loss of structural integrity [122, 127]. Most structural adhesives are made from thermosetting polymers such as epoxy, urethane, acrylic, and silicone [127, 128]. Such high-strength adhesives are used extensively in aircraft manufacturing to bond metals and composite elements [129]. Non-structural adhesives, also known as holding adhesives, are typically employed to secure lightweight materials in place. Examples of these include packing tapes and packing adhesives [122]. Similar to the above classifications, adhesives can be classified as permanent or non-permanent adhesives [130].

The phenomenon, that allows the adhesive to resist separation and transfer a load from the adherend to the adhesive joint, is called adhesion [131]. In recent years, adhesion phenomena have become important in many scientific and technological areas. Adhesion is involved

whenever solids are brought into contact, for example, in coatings, paints, and composite materials. However, the main application of adhesion is adhesive bonding which is gradually replacing traditional mechanical joining methods such as bolting and riveting. Adhesive bonding reduces weight and offer better distribution of stresses over the bonded regions. Thus, it finds extensive use in various industries, including advanced sectors such as aviation, space, and automotive manufacturing. [132]. Adhesion is considered a complex phenomenon because it involves multidisciplinary knowledges including polymer and surface chemistry, mechanics of materials, fracture mechanics, rheology and other subjects [19]. However, the field of adhesion sciences has only found real interest about 60-70 years ago. Thus, it is still a subject in which empiricism is slightly ahead [132]. A thorough understanding of adhesion mechanisms is not yet developed with no single global theory or model that can explain all its phenomena or mechanisms [122, 133]. In the past, it was believed that mechanical interlocking, resulting from the adherend's surface irregularities, was the primary cause of adhesion. However, this theory faces a challenge when it comes to the effective creation of a robust adhesive bond on a smooth surface, like glass [124]. Surface roughness plays a critical role in adhesive bonding by increasing the available surface area for the adhesive to penetrate and form mechanical anchors within the microstructural features of the surface. This expanded contact area contributes to stronger bond formation. However, for optimal adhesion, the surface must also be sufficiently wetted by the adhesive, which depends on factors such as adherend cleanliness, its Surface Free Energy (SFE), and the adhesive's viscosity [3]. Beyond facilitating mechanical interlocking and increasing surface area, surface roughness influences the surface wettability and subsequently the SFE. The Wenzel model effectively explains the relationship between surface morphology and wettability, stating that surface roughness amplifies a surface inherent hydrophilic or hydrophobic behaviour. For hydrophilic surfaces, increased roughness enhances wettability, allowing adhesives to spread more effectively. Conversely, for hydrophobic surfaces, increased roughness diminishes wettability, causing adhesives to bead up and resist spreading [134]. It is widely reported that the wettability and SFE of solid surfaces can be adjusted by controlling surface morphology at micrometric and nanometric scales, rather than relying solely on altering the surface chemistry [134, 135]. The concept of adhesion remains debatable and a satisfactory definition for adhesion has not been agreed to date [122]. However, some researchers provide their definitions. Pocius explained adhesion as the phenomenon that enables the adhesive to transfer a load from one to another bonded adherend [133]. Other researchers [19, 130, 136] have defined adhesion as the attraction resulting between two different substances (adherend and adhesive) when they come into contact. Petrie

[130] has emphasised that the adhesion is primarily attributed to the molecular interactions between the adherend and the adhesive, and that chemical bonds, which represent cohesion feature, do occur in few adhesion instances. When referring to the molecular forces between the adhesive and the substrates, the term 'intrinsic adhesion' is often used to distinguish this phenomenon from the 'measured adhesion' or the measured strength of an adhesive joint [19]. In addition to the mechanical interlocking theory, which mentioned earlier, several other adhesion theories, of which the adsorption, diffusion, electrostatic, and the chemical bonding theory, were attempted to describe the phenomenon of adhesion, but the actual mechanism has not yet been clearly defined [130]. Each of these theories seems to be particularly accepted in explaining certain phenomena associated with adhesive bonding. It is often difficult to fully attribute adhesive bonding to an individual mechanism. Within a specific adhesive system, a combination of various mechanisms is most likely responsible for bonding. The significance of each mechanism's role may vary across different adhesion systems [18, 130]. The most common and accepted among researchers is adsorption theory, which also known as thermodynamic or wettability theory [19]. It states that to achieve strong bonding, the adhesive must effectively wet the surface to be bonded. [18, 19, 130, 137]. This theory has driven the development of adhesives with lower surface tension than that of the adherend, ensuring complete wetting of the adherend [19, 122]. Reviewing literature concerning the subject of improving the surface adhesivity of various materials and applications reveals particular importance in measuring surface wettability or SFE as initial criteria to evaluate the surface before testing the adhesive bond strength mechanically, typically performed through various destructive tests [138-140]. Comyn stated that an adhesive must fulfil two requirements. Firstly, it must wet the surfaces by spreading then harden to a cohesively strong solid [137]. Additionally, several other non-destructive techniques are commonly used to assess the surface physical or chemical characteristics such the surface roughness, morphology, functional groups, contaminants on substrate surface, these includes optical microscopy, profilometry, SEM, FTIR Spectroscopy [141].

2.2.4. Evaluation of surface adhesivity

2.2.4.1. Surface wettability

Wettability refers to a physical characteristic that defines how well a liquid droplet can maintain to or spread across a solid surface. It is often quantified using a surface Contact Angle (CA) (Θ). The latter is defined as the angle between the tangent to the surface plane of the droplet and the solid surface under equilibrium conditions, as outlined by Young's theory [142].

The process of creating continuous contact between the adhesive and the adherend is known as wetting. This process results from the interfacial forces between the substrate and the adhesive [19, 122, 130]. Early experimental studies revealed that every liquid exhibits a degree of wetting on any solid surface, that is the CA ranges between 0° - 180° [143]. Poor wetting means that the adhesive will bridge over the surface valleys and cracks on the substrate surface, or small air pockets will be formed along the interface. These defects result in a reduction of the actual contact area between the adhesive and the adherend, creating concentrated stresses and thereby reducing the adhesive bond strength. [122, 130, 133]. **Figure 2.9** illustrates good and poor wetting of a liquid droplet over an irregular surface [130].

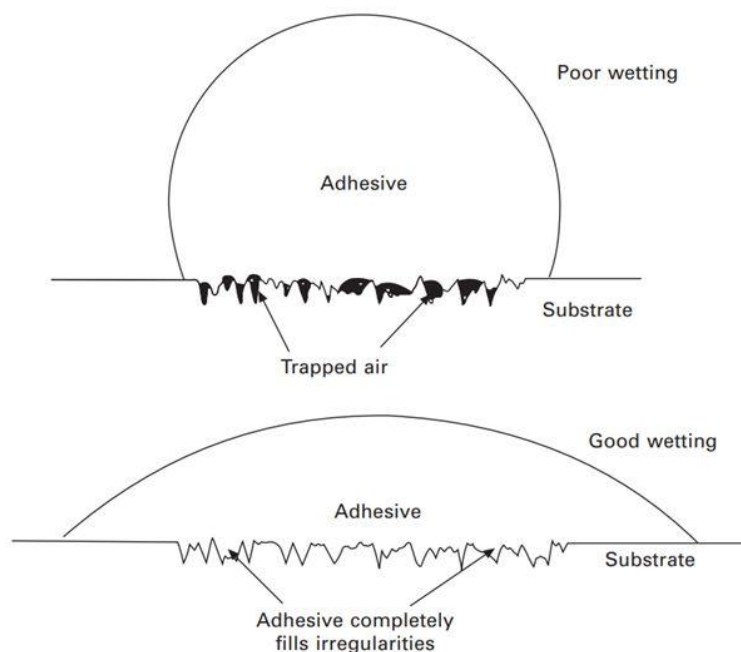


Figure 2.9. Illustration of good and poor wetting over irregular surface, adapted from Petrie [130]*.

As mentioned earlier, wettability is commonly determined by measuring the CA between the solid-liquid interface a drop of water or another liquid makes when placed on the substrate [144, 145]. There are two different types of CAs: static and dynamic [145, 146]. The static CA, commonly referred to as Young's angle of contact [146-148], is frequently employed due to its ease of measurement. Various methods are utilised to quantify the static CA, such as the surface tilting and the Wilhelmy balance method, with the sessile drop method being the most employed due to its conceptual and measurement simplicity [145, 149]. The process involves carefully dispensing a liquid droplet from a micro syringe onto a horizontal solid surface. Once the liquid droplet attains a stable state, its image is captured using a camera mounted on a goniometer. The tangential angle is determined by the equilibrium of surface tensions at the

solid-vapour, liquid-vapour, and solid-liquid interfaces [146]. This technique was used in this research project; **Chapter 3** provides further discussion about the instrument used.

The surface science community frequently employs the terms hydrophobicity and hydrophilicity. A surface is hydrophobic if its static Water Contact Angle (WCA) exceeds 90° , whereas it is considered hydrophilic when this angle is less than 90° [150, 151]. Furthermore, a surface is termed super-hydrophobic if its static water contact angle exceeds 150° and super-hydrophilic or super-wetted if its static water contact angle is zero or nearly zero [151]. Noting that the maximum WCA for all natural and man-made materials (except fluorinated materials/surfaces such as Polytetrafluoroethylene (PTFE)) is 120° [151, 152]. Higher WCA is achieved by manipulation of surface roughness, texture, and/or porosity [152-155]. It is important to note that the term "wettability" is employed in literature to characterise the wetting behaviour of a surface with any type of liquid. On the other hand, the terms "hydrophobicity" and "hydrophilicity," which are frequently encountered in literature, specifically denote the interaction between the surface and water [150]. Additionally, the terms "hydrophobic" and "hydrophilic" describe the Young contact angle for any liquid in the same manner as hydrophilic and hydrophobic but less commonly used [156]. The schematic provided in **Figure 2.10** offers clarification on these terms. Although the scientific community widely accepts that a surface is hydrophobic when its static water contact angle (Θ) exceeds 90° and hydrophilic when Θ is less than 90° , some researchers [150, 157] argue that there is little rationale for classifying a surface as hydrophobic or hydrophilic based on a slight 2° change from 89° to 91° . The same applies to super-hydrophobicity and super-hydrophilicity. [149]. WCA is the commonly used test in laboratories to determine the wettability of material surfaces.

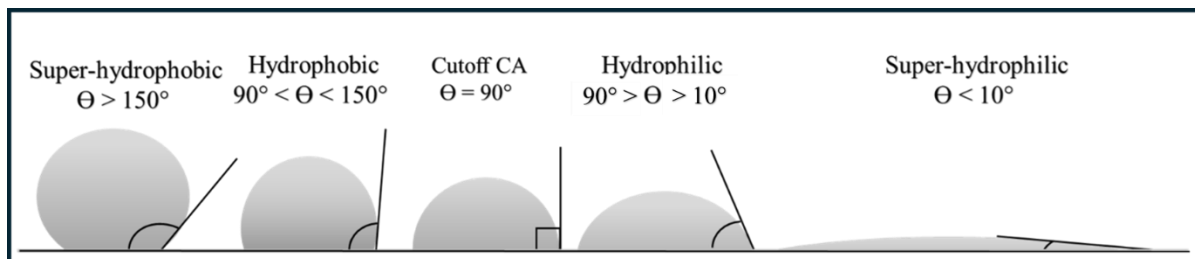


Figure 2.10. Schematic illustration of hydrophobicity, hydrophilicity, super-hydrophobicity, and super-hydrophilicity.

2.2.4.2. Surface Free Energy (SFE)

SFE (γ) is defined as the excess energy associated with the presence of a surface [19], or the amount of work needed to create a unit area of new surface [158]. For liquids, the SFE has the same value as the surface tension but different units [19, 137], for a solid surface, the same is

not true [159]. For an adhesive to wet a substrate surface sufficiently, it should have a lower surface tension than that of the substrate [18, 19, 130]. SFE arises from the intermolecular interactions occurring at the solid-liquid interface. These interactions encompass several types of forces: secondary bonds such as (i) van der Waals forces and (ii) hydrogen bonds; primary bonds including (i) covalent, (ii) ionic, and (iii) metallic bonds; and donor-acceptor interactions, which fall between secondary and primary bonds in strength, specifically acid-base interactions [19, 160]. When a liquid droplet reaches equilibrium on a solid surface, as illustrated in **Figure 2.11**, the relationship between the surface free energies and the CA (Θ) is expressed according to Young's equation (**Equation 2.1**) [19, 161].

$$\gamma_s = \gamma_{sl} + \gamma_l \cos(\Theta) \quad 2.1$$

where γ_s represents the SFE of the solid substrate (measured in mJ/m^2), γ_l denotes the SFE of the liquid drop (or the surface tension of the liquid, measured in mN/m), and γ_{sl} stands for the interfacial free energy between the solid substrate and the liquid droplet [19, 137].

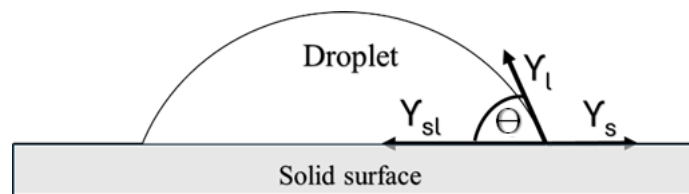


Figure 2.11. The equilibrium state of a liquid droplet on a solid surface according to Young's equation adapter from [19]*.

Numerous theories have been developed to explain and quantify the surface tension of materials, such as the Zisman approach, Owens-Wendt method, and Fowkes. Fowkes in his theory, which has been widely utilised in the literature [134, 137, 162-164], proposed that the SFE of a solid (γ_s) can be described as the summation of the dispersive (γ^d) and the polar components (γ^p), (**Equation 2.2**) [19, 165, 166].

$$\gamma_s = \gamma_s^d + \gamma_s^p \quad 2.2$$

Based on Fowkes method, if either the liquid or the solid possesses only a dispersive SFE component, then the dispersive part of the solid can be determined experimentally based on the known liquid SFE components and the contact angle (CA) using **Equation 2.3** [19].

$$\gamma_s^d = \frac{\gamma_l^d(1 + \cos\theta)^2}{4} \quad 2.3$$

To determine the polar SFE component of the solid, another liquid with known polar and dispersive SFE components must be utilised, applying **Equation 2.4** [19].

$$\sqrt{\gamma_l^d \cdot \gamma_s^d} + \sqrt{\gamma_l^p \cdot \gamma_s^p} = \frac{\gamma_l^d(1 + \cos\theta)}{2} \quad 2.4$$

2.2.5. Surface preparation

Surface preparation is a critical step in achieving high-quality adhesive bonds, influencing the joint's strength and durability. Structural adhesive bonding relies on mechanical interlocking and chemical bonding between the adhesive and adherend surfaces. To enhance bond strength and durability in different environments, surface pretreatment is essential before adhesive bonding. Various techniques alter substrate surfaces by increasing surface tension, roughness, or changing surface chemistry, as well as removing surface contaminants like release agents. These modifications create mechanical or chemical bonds, impacting the stability of the joint. Contaminants can lead to premature interfacial failures, underscoring the importance of proper surface preparation. [167, 168].

2.2.5.1. Traditional surface pretreatment techniques of CFRPs to improve adhesive bonding

Various surface treatment techniques have been utilised or investigated with varying degrees of success to eliminate contaminants and other weak boundary layers, enhance wettability and surface tension, modify surface roughness to increase the bonded area and add mechanical interlocking, and alter surface chemistry. These efforts aim to improve the bond strength and durability of adhesive joints in polymer composites. [121, 168]. These include mechanical abrading (sanding and grit blasting) and peel-ply, chemical treatment such as coupling agents,

acid and base etching, and solvents, and non-contact methods such as flame and plasma treatments and laser texturing.

Mechanical surface preparation processes (sanding and grit-blasting) are used primarily to produce macroscopically rough surfaces that increase the surface area to be bonded and to remove some of the existing contaminants and release agents [167]. However, secondary contaminants are widely reported to be created during the roughening process [15, 20, 119]. By cleaning with a solvent such as acetone following the abrasion process to remove secondary contaminants, some researchers consider sanding and grit-blasting as effective low-cost composite surface roughening methods [167, 169]. Other researchers, however, encourage dry wiping and discourage the use of solvents to remove residue after hand sanding or grit blasting due to the risk of re-contaminating the surface [3]. In addition to the secondary cleaning process, mechanical abrading is widely regarded to have significant drawbacks, including fibre fracture, fibre-matrix delamination, low reproducibility, and poor efficiency [15, 17, 20, 119, 123].

Another mechanical technique is the peel ply, which is an extra layer of nylon or polyester fabric integrated into the surface of the composite during manufacturing to maintain cleanliness and provide a textured surface matching the peel ply imprint. It is subsequently removed from the surface just before bonding occurs, ensuring optimal adhesion [118, 121]. The use of peel-ply for preparing CFRP surfaces is a common practice in the industry [20], originally intended to keep composite surfaces clean during storage [121]. This method gained wide acceptance as it minimises the human error present in mechanical abrading with good reproducibility [170, 171]. However, because silicone-based release agents are commonly used to facilitate the removal of the peel ply, silicone contaminants are often left on the surface [26, 121, 172]. Thus, additional hand sanding or light grit blasting is necessary to properly prepare the surface [118], which increases the manufacturing complexity and cost. Noting that silicone-based release agents have the capability to penetrate hundreds of nanometres into the CFRP matrices [173, 174]. Chemical treatments involving coupling agents and acid or base etchings are effective in roughening CFRP surfaces, thereby enhancing adhesive bonding. [175, 176]. These techniques often suffer from drawbacks such as unstable surface quality, low reproducibility, and inefficiency. Moreover, the agents used in chemical treatments pose environmental risks and potential health hazards to workers [170, 177]. One of the basic chemical treatment approaches to eliminating contaminants from a surface involves wiping it with a solvent. The success of this method relies on the type of contaminant and the solvent employed. Yet, there is a risk that

instead of removing the contaminants, this process may distribute them across the surface [121]. Moreover, it was reported that chemical treatments are generally difficult to be automated in an industrial scenario [170].

Non-contact treatment techniques include plasma, flame, and laser treatments. During plasma treatment, surfaces are exposed to ionised gases, typically generated using radio frequency energy within a low-pressure environment. This plasma region contains a high concentration of reactive species, such as ions and electrons, derived from the gas [121]. Various plasma-based treatment studies, including atmospheric pressure, low pressure, cold plasma, and plasma/oxygen treatments, have been investigated to improve the bonding strength of CFRPs. Plasma treatment involves the generation of free radicals, molecular interdiffusion, and chemical species on the surface, leading to an increase in surface energy [178, 179]. Research in this area has indicated improvements in both wettability and bonding strength as a result of plasma treatment [180-185]. Compared with the previously discussed surface treatment techniques, low-pressure plasma surface treatment has gained increasing attention due to its high efficiency and environmental friendliness. However, it requires special equipment, leading to additional costs for maintaining the vacuum in the treatment system. The size of the vacuum chamber posed limitations on the size and quantity of the pretreated CFRP structures.[35, 138, 184, 186-188]. Atmosphere plasma, on the other hand, has limited surface treatment effectiveness [35, 189] and rapid ageing due to the high reactivity of the treated surfaces [26, 179, 190-192].

2.2.5.2. Laser surface treatment or texturing

None of the pre-treatment technologies for adhesive bonding mentioned earlier, including plasma, grit-blasting, peel ply, corona, flame treatment, or mechanical abrasion, have been universally accepted as the primary pre-treatment process due to their individual drawbacks, particularly in reliably removing surface contaminations. Consequently, there is still a need for a new technology that can offer a robust treatment process with reproducible cleaning action and the potential for automation [28]. In recent years, laser technology has emerged as a promising solution to address the need for robust treatment processes with reproducible cleaning action and automation capabilities. Researchers have explored various lasers with different wavelengths to enhance the adhesiveness of CFRP surfaces. Regardless of the types of lasers explored, a review of the literature shows that the primary objective of surface treatment for CFRPs is to partially remove the outer matrix resin layer, thereby eliminating contaminants such as release agents, or completely removing it to expose the underlying load-

bearing carbon fibres with minimal damage, enabling a direct application of force to the reinforcements [15, 17, 26, 27, 29, 188, 191]. In laser processing, different processing parameters govern the ablation process of the matrix. The absorption of radiation, which varies with the laser wavelength, is the most critical parameter. It determines the amount of energy deposited within the material and the depth of penetration, thereby defining the ablation mechanism [15]. When compared to other industrial techniques, previous studies indicate that the bonding strength of CFRPs achieved with laser texturing is competitive or even higher. A comprehensive examination and critique of past research focused on laser surface treatment of CFRPs, highlighting its significant role in enhancing adhesive bonding, is reviewed in **Section 2.4**.

2.2.5.3. Surface treatment with incoherent UV light (non-laser)

Multiple researchers have explored alternative approaches, such as incoherent UV light treatments, aiming to enhance the surfaces of both polymeric and non-polymeric materials for adhesive bonding [32, 193-198]. These investigations predominantly involved the use of UV light in conjunction with ozone, either by directly applying ozone or employing UV sources emitting wavelengths below 240 nm, which generate ozone in the surrounding atmosphere. Studies have demonstrated the effectiveness of UV/ozone treatment in improving joint strength across a variety of materials, surpassing traditional methods like grit blasting and primers. However, implementing UV/ozone treatment necessitates specialised facilities with high resistance to ozone corrosion, which may prove impractical, particularly for larger structures. Furthermore, ozone is highly toxic [199].

UV light can impact polymer surfaces through two distinct mechanisms: direct photo-degradation and/or photo-crosslinking of polymer molecular bonds. The second mechanism, associated with wavelengths below 240 nm, involves the interaction of UV light with atmospheric oxygen to produce ozone, atomic oxygen, and oxygen radicals, which subsequently oxidise and modify the polymer surface [200, 201]. Generally, polymer photo-degradation occurs at depths of the order of micrometres or sub-micrometres from the surface, with the most pronounced effects observed near the surface. It is believed that an accumulated layer of degraded species near the surface absorbs UV irradiation more effectively, reducing the penetration of UV light into the inner regions of the polymers [202].

2.3. An overview of light and laser

One of the common definitions of visible light is “The natural agent that stimulates sight and makes things visible”. A more technical, scientific definition can be obtained from the ‘International Lighting Vocabulary (ILV): “Radiation that is considered from the point of view of its ability to excite the human visual system” [203]. The acronym "LASER" stands for Light Amplification by Stimulated Emission of Radiation. Laser light is a form of electromagnetic radiation. It is distinct from ordinary light because of its coherence, indicating that its photons share the same frequency, wavelength, and phase within the visible, IR, or UV parts of the electromagnetic spectrum [204].

2.3.1. The electromagnetic wave and spectrum

Visible light, which is perceptible to the human eye, comprises only a small segment of the electromagnetic spectrum, ranging from 0.37 to 0.75 μm [205]. The electromagnetic spectrum extends from gamma rays to radio waves [206]. Electromagnetic waves are characterised by electric and magnetic fields that oscillate perpendicular to each other and perpendicular to the direction of wave propagation [205], (**Figure 2.12**). From basic physics, it is well known that light is recognised to exhibit characteristics of both waves and particles. In other words, both wave and particle, known as photons, properties are required to entirely explain the behaviour of light.

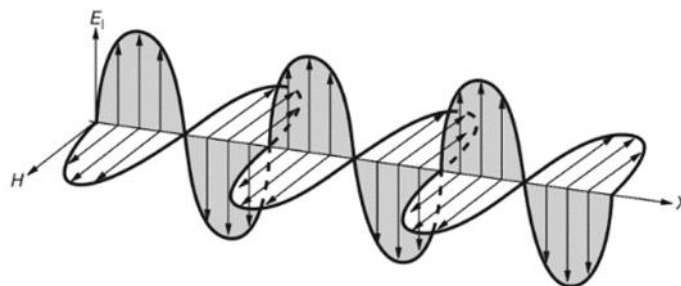


Figure 2.12. Illustration of an electromagnetic wave, adapted from [205]*.

The classification of light, along with other forms of electromagnetic radiation, is based on its wavelength. In the context of visible light, colour is determined by wavelength: Red light has wavelength around 650 nm, while blue light has a wavelength of approximately 450 nm. Photons of each specific wavelength have a unique energy, which can be calculated using **Equation 2.5**.

$$E = \frac{hc}{\lambda} \quad (2.5)$$

Where:

E: represents photon energy

h: Planck's constant (6.621×10^{-34} J.s)

c: is the speed of light which is about 300×10^6 m/s in vacuum, and

λ : is the wavelength in metres.

The photon energy is commonly expressed in electron volts (eV), where $1\text{eV} = 1.602 \times 10^{-19}$ J [207]. **Figure 2.12** represents the electromagnetic spectrum and the corresponding energies.

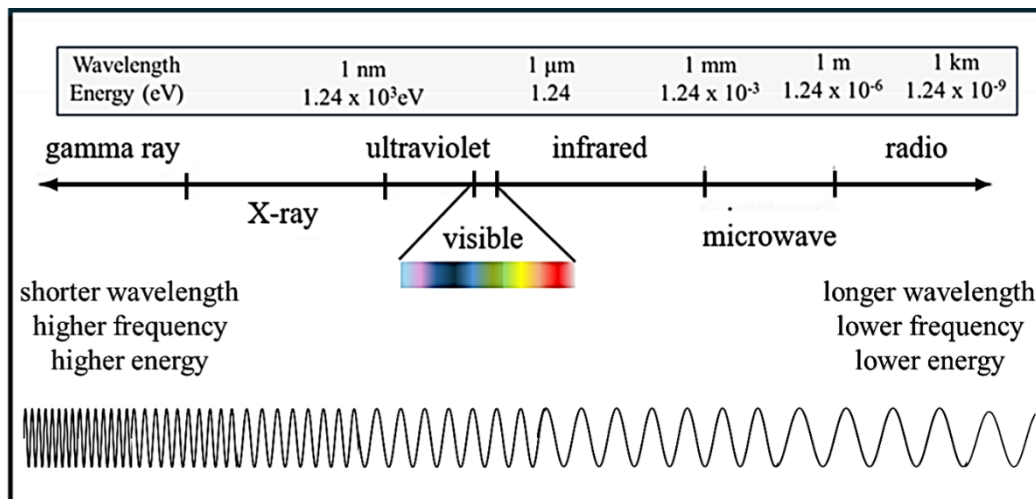


Figure 2.13. The electromagnetic spectrum and the corresponding photon energies, re-drawn based on Andrews and NASA [208, 209].

2.3.2. Laser fundamentals

Einstein laid the initial groundwork for laser theory, with Maiman inventing the first ruby laser in 1960, earning him the Nobel Prize. Since then, various types of CW and pulsed lasers,

including semiconductor, Nd:YAG, CO₂ gas, and dye lasers, have been developed with improved reliability and durability [210]. The principle of operation of a laser device relies on stimulated emission of radiation. Unlike ordinary light sources, such as sunlight, which emits photons spontaneously with varying wavelengths as various atoms or molecules release their excess energy, stimulated emission involves an atom or molecule with excess energy being stimulated by a previously emitted photon to release that energy as a photon with the same frequency and phase as that of the stimulating one [211], **Figure 2.14**. Therefore, laser beams demonstrate directionality, high power density, and superior focusing capabilities (typically in the range of a few micrometres), distinguishing them from regular light. Bulb light, for instance, could be monochromatic, meaning its photons share the same frequency and wavelength but have different phases (incoherent). Thus, coherent light is monochromatic, but not all monochromatic light is coherent [212]. **Figure 2.15** illustrates the concepts of monochromatic and coherent light. Lasers are generally considered monochromatic, but they are not exactly monochromatic; their bandwidth can be very narrow [205].

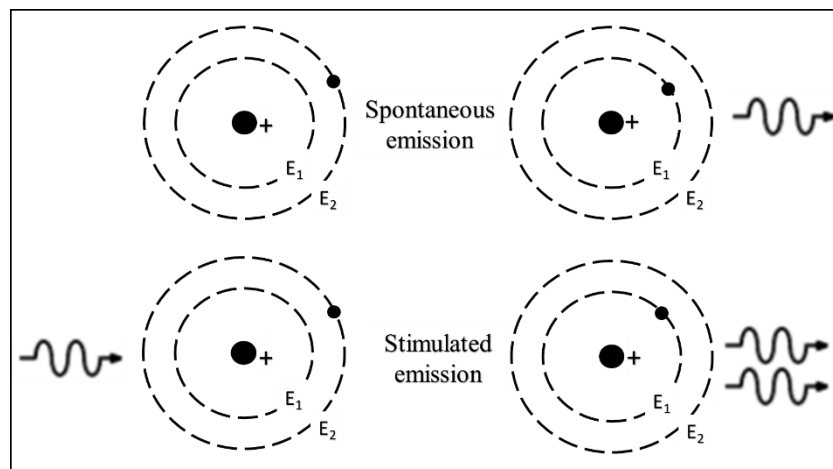


Figure 2.14. Spontaneous and stimulated emission, adapted from [211]*.

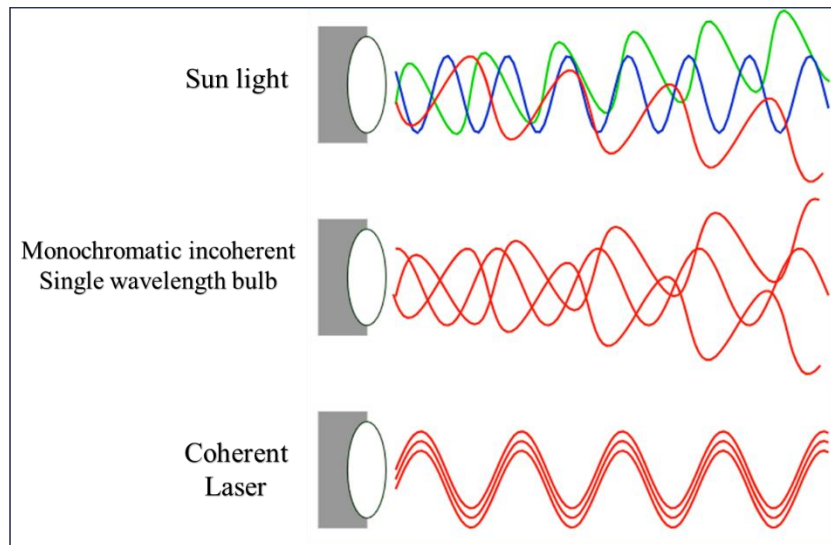


Figure 2.15. Illustration of concepts of monochromatic and coherent light adapted from [213]*.

The unique characteristics of laser beams, including monochromaticity, low divergence, directionality, high power density, and focusing capabilities, position them as potentially valuable tools for material processing [214]. Lasers offer the capability to precisely deliver substantial energy into confined areas of a material to achieve a specific desired outcome [215]. Laser applications span various fields, from industrial tasks like cutting and welding to medical procedures such as laser surgery and diagnostics [216]. They exhibit remarkable precision across diverse tasks, especially in material processing, encompassing cutting, drilling, heat treating, surface processing, and welding of various materials, including both metals and non-metals. Despite the generally low power efficiency of most lasers (apart from diode lasers), they enable faster, more cost-effective, and precise results with superior quality compared to traditional mechanical methods. Furthermore, lasers are highly compatible with robotics. Many major machine tool manufacturers provide fully automated laser processing solutions for industries [204].

2.3.3. Common commercial lasers

Lasers are typically categorised based on the state or the physical properties of their active medium, also known as the active lasing medium [210], which can be solid, liquid, or gaseous. Currently, a wide range of lasers are available, each tailored to specific applications and possessing unique characteristics. **Table 2.1** summarises the most common commercially available lasers, detailing their main characteristics [204].

Table 2.2. Commercially available lasers and their main characteristics, adapted from [204]*.

| Laser | Wavelength | Power range |
|-----------------------------------|-------------------|---------------------------------|
| Carbon dioxide (CO ₂) | 10.6 μm | milliwatts to tens of kilowatts |
| Nd: YAG | 1.06 μm | milliwatts to kilowatts |
| Nd: glass | 1.05 μm | Watts |
| Diodes | Visible and IR | milliwatts to kilowatts |
| Argon-ion | 514 nm and 488 nm | milliwatts to tens of watts |
| Fibre | Visible and IR | Watts to kilowatts |
| Excimer | UV | Watts to hundreds of watts |

2.3.4. Laser structure

The principal component of any laser system is the active medium, which is the region where the lasing action occurs. The active medium is contained within a closed volume known as the active cavity, placed between two parallel mirrors, known as the optical resonator. These mirrors are highly reflective, with one being partially transmissive [211, 217, 218]. The active medium governs the possible wavelengths emitted by the laser [211, 219-221]. This is related to the difference between energy levels within that material [211, 220]. Moreover, the gain or the amplification factor of a laser, which represents the extent to which the laser medium can stimulate emission, depends on the medium and its length; the longer the medium, the greater the stimulation [207, 211]. However, for the stimulated and stimulating photons to be all in phase, the resonator length should satisfy **Equation 2.6** [211, 222].

$$L = n \frac{\lambda}{2} \quad (2.6)$$

Where L is the resonator length, λ is the wavelength, and n is an integer.

Many other measures are typically implemented for shaping the laser cavity or the resonator. The objective of a laser designer is to direct most laser photons in a specific direction to generate a highly directional beam. Achieving this involves elongating the gain medium significantly in one axis compared to the other two directions [222]. Moreover, the occurrence of undesired longitudinal and transverse modes, which can happen due to the gain bandwidth of the laser, the longitudinal are typically controlled by shaping the cavity [211, 222], for the transverse modes, by controlling both the cavity shape and the mirror curvature [216]. The transverse modes are more significant as they indicate the irradiance distribution of the laser beam in the plane perpendicular to the direction of propagation [211]. The structure of the transverse mode is described using TEM_{mn}, where the subscripts m and n represent the number

of nodes along the two mentioned orthogonal axes. **Figure 2.16** shows the irradiance distribution of the laser spot for various transverses modes. The lowest order mode TEM_{00} , also known as the fundamental mode, has a cylindrical Gaussian irradiance distribution. This mode has the minimum divergence angle and experiences the minimum possible diffraction loss that makes it possible to be focused to the smallest spot. Although Higher-order modes exhibit a wider spread and suffer greater diffraction losses, lasers are often optimised to produce maximum output power and operate at one or more higher order modes. [211, 222].

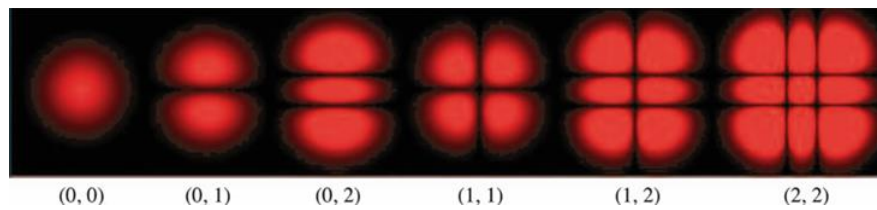


Figure 2.16. The irradiance distribution of the laser spot for various transverse modes adapted from Saleh [216]*. The effectiveness of nearly all laser applications relies predominantly on the power density distributions within specific areas of the laser beam, typically in the focal region [223]. A pure Gaussian laser beam (TEM_{00}) exhibits a symmetrical intensity distribution around its axis, decreasing as the distance from the axis increases. The intensity at point (z, r) of the laser beam is calculated using **Equation 2.7** [224, 225].

$$I(z, r) = I_0(z) \exp\left(-\frac{2r^2}{w_z^2}\right) \quad (2.7)$$

Where z is a point in the laser beam propagation axis, (r) is a radial distance from the axis, $I(z, r)$ is the intensity at the point (z, r) , $I_0(z)$ the maximum intensity at the plane (z) , and (w_z) is the radius of the beam at the plane (z) .

At the beam boundary, where the radius is (w_z) , the intensity of a Gaussian beam falls to $1/e^2$, approximately 13.5%, of the maximum intensity at the plane (z) [226-228].

In addition to the active medium and the resonator, a basic laser system includes an excitation device (pumping source) to pump energy for the active medium [229, 230]. Any form of energy can serve, with typical options including flash lamps emitting incoherent light [229]. The objective of the two mirrors is to allow for the electromagnetic wave to undergo multiple reflections within the resonator, that increases the travelled distance thereby causing further stimulated emission to amplify the light. A small number of photons then escape from the

partially reflective mirror in the form of a very intense beam of laser light [231, 232]. **Figure 2.17** shows a basic structure of a simple laser [230, 233].

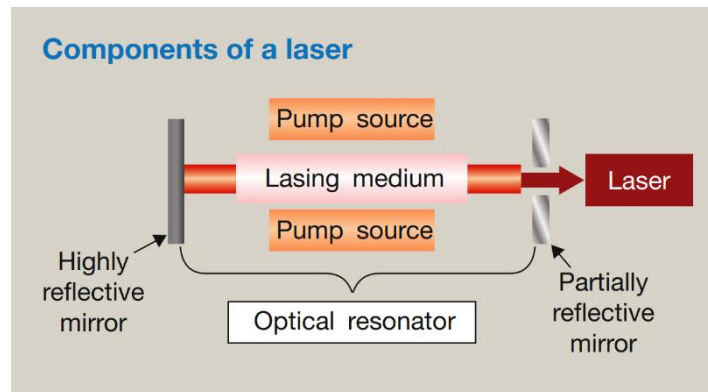


Figure 2.17. A basic structure of a simple laser adapted from [233]*.

Laser systems may include additional elements such as cooling mechanisms for mirrors and optical delivery systems, including beam guidance, such as mirror or optical fibre, and target manipulation, which are essential for effective material processing [210].

2.3.5. Laser beam parameters

In addition to the active medium discussed previously, lasers are typically identified by their maximum average power and the emitted wavelength. However, in many laser applications, such as laser processing of materials, relying solely on wavelength and power is insufficient to determine whether a particular laser is suitable for specific applications [234, 235]. Hence, it is essential to consider various other parameters of the laser beam. These include the spot size, the focal length, Rayleigh length, and the beam quality (M^2 value) for both CW and pulsed lasers, and peak power, pulse energy, pulse length, pulse frequency, and duty cycle for pulsed lasers [215].

2.3.5.1. Wavelength (λ)

The wavelength is a fundamental characteristic of a laser, normally remaining fixed for a given laser, unlike other laser beam parameters, which are often adjustable [236]. The wavelength influences the capability of focusing the beam into a small spot size, which is wavelength-dependent. Generally, shorter wavelengths allow for achieving smaller spot sizes [229, 237], and as a consequent higher intensity. Laser material interaction heavily relies on the wavelength as the absorption coefficient for each material varies with different wavelengths, where each material has a unique absorption spectrum [238]. Shorter wavelengths result in photons with higher energy levels, thereby increasing absorptivity [229].

2.3.5.2. Beam quality (M^2 value)

The beam quality, M^2 value, is the ratio of divergence of the real laser beam to the pure Gaussian laser beam. In other words, the beam quality describes how close to pure-Gaussian a laser beam is [211, 239]. **Figure 2.18** illustrates the difference between real and pure Gaussian laser beams.

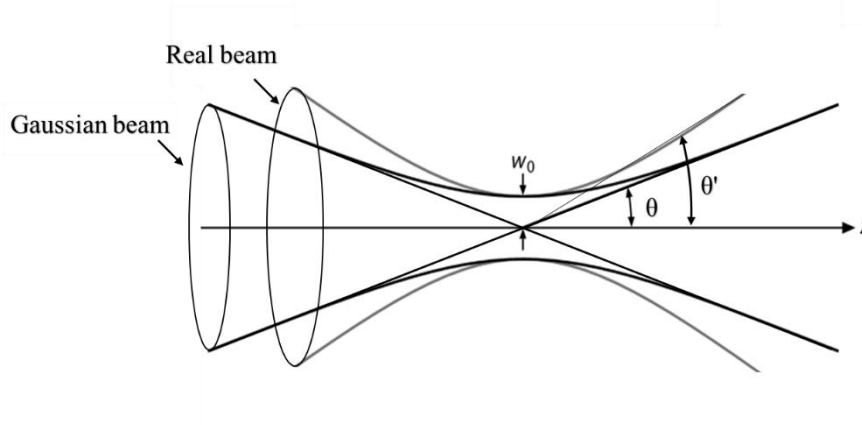


Figure 2.18. Real and pure Gaussian laser beam, adopted from Eichler [239]*.

The divergence for a pure Gaussian laser beam is calculated using **Equation 2.8**, and the real divergence is calculated with **Equation 2.9**. Where w_0 is the waist radius of beam, θ and θ' are divergence angles of pure Gaussian and real laser beam, and M^2 is the beam quality [211, 239].

$$\theta = \frac{\lambda}{\pi w_0} \quad (2.8)$$

$$\theta' = M^2 \frac{\lambda}{\pi w_0} \quad (2.9)$$

2.3.5.3. Laser power and intensity

Despite the wide selection of lasers available, ensuring an adequate power level is essential for laser-based material processing. This necessity considerably narrows down the suitable options to only a few specific types [229, 240]. One of the main technical aims of laser manufacturers is to generate lasers with high powers [223]. The laser power refers to the energy emitted per unit time (W), while the intensity of the laser beam is defined as the power per unit area, commonly expressed in (W/cm^2). For laser processing of material applications, achieving high

beam intensities is crucial. For a particular laser, it typically accomplished by focusing the laser beam into a small spot size [241]. It is well known that laser power and intensity have direct influences on the material interaction and processing speed. Reviewing literature on various laser material processing techniques revealed that laser power has also significant effects on the cost and quality of processing [234, 240, 242].

2.3.5.4. Laser spot size, focal length, and Rayleigh length

In the majority of laser material processing applications, laser beams are focused into small spot sizes to attain high intensity on the workpiece. The spot size (d_0) of a laser beam is the minimum possible laser beam diameter that can be achieved, it depends on the wavelength (λ), the lens focal length (f), and the beam diameter at the focusing lens (D), for an ideal Gaussian beam it calculated using **Equation 2.10** [225].

$$d_0 = \frac{4f\lambda}{\pi D} \quad (2.10)$$

In the case of real beam, the spot size is M^2 times the ideal spot size [211], thus **Equation 2.10** is revised to **Equation 2.10a** below.

$$d_0 = \frac{4M^2 f \lambda}{\pi D} \quad (2.10a)$$

At a distance z from the focal point, the spot size (d_z) is calculated with **Equation 2.11** [223, 226, 243].

$$d_z = d_0 \sqrt{1 + \left(\frac{z - z_0}{z_R}\right)^2} \quad (2.11)$$

where d_0 is the minimum possible spot size, z_0 is the position of d_0 , and z_R is the Rayleigh length (**Figure 2.19**), defined as the distance from the minimum spot size to the point where the spot size is multiplied by $\sqrt{2}$, the Rayleigh length is determined with **Equation 2.12** [226, 243, 244].

$$z_R = \frac{\pi d_0^2}{4\lambda M^2} \quad (2.12)$$

At large distances ($z \gg z_R$), the spot size increases linearly with z [226, 243], and can be determined using the divergence angle **Equation 2.9**.

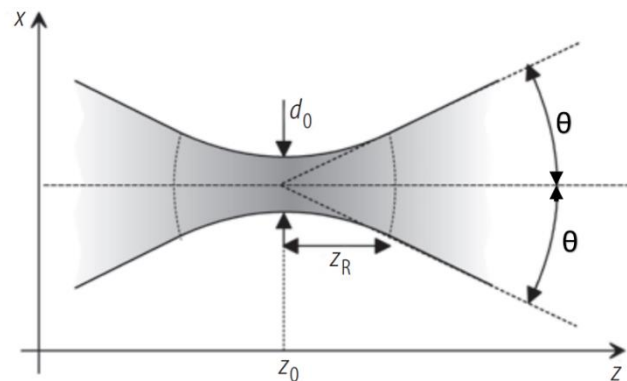


Figure 2.19. The minimum spot size d_0 of a Gaussian beam and the Rayleigh length z_R , adopted from [223]*.

2.3.5.5. Continuous wave and pulsed lasers.

A laser beam that maintains a constant output power over time is referred to as operating in Continuous Wave (CW) mode. On the other hand, pulsed lasers include any laser that does not operate in CW mode, delivering optical power in pulses with varying durations and repetition rates. Pulsed lasers are classified based on their pulse length, such as nanosecond, picosecond, and femtosecond lasers [245]. **Figure 2.20** clarifies the principles of pulsed and CW lasers.

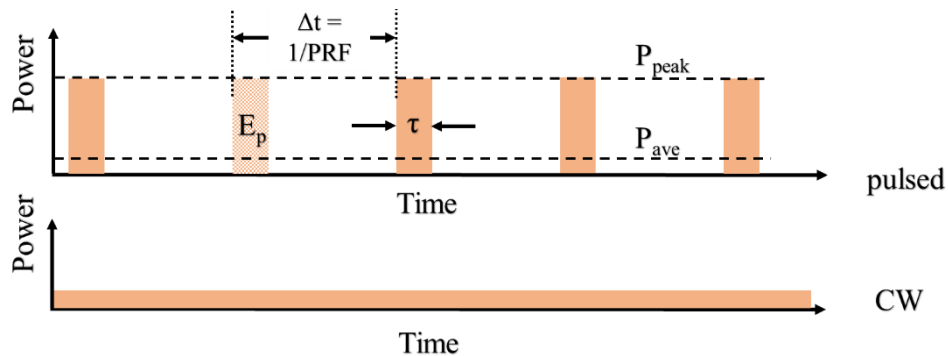


Figure 2.20. Principles of pulsed and CW lasers.

Where:

τ is the pulse length, PRF is the Pulse Repetition Frequency, Δt is the cycle period, E_p is the pulse energy, and P_{peak} is the peak power (pulse power), and P_{ave} is the average power. These variables are calculated using **Equations 2.13, 2.14, and 2.15** [246].

$$\Delta t = \frac{1}{PRF} \quad (2.13)$$

$$P_{peak} = \frac{E_p}{\tau} \quad (2.14)$$

$$P_{ave} = E_p * PRF \quad (2.15)$$

In pulsed lasers, the pulse length and consequently the peak power are particularly crucial. The pulse length indicates how long the laser beam stays active in each pulse. It has a significant impact on how the material interacts with the laser and its ablation threshold [245], which is defined as the minimum fluence or energy required to cause ablation in a certain material [245, 247]. Typically, shorter pulse durations lead to lower ablation thresholds, enabling efficient material removal at lower energy levels. This feature is especially beneficial when dealing with heat-sensitive materials, as it reduces the risk of thermal damage. Additionally, shorter pulse lengths enable processing at higher precision and with finer detail. When laser energy is delivered in ultrashort pulses, it allows for precise positioning and reduces thermal diffusion. This results in sharper edges and well-defined machined features [245].

2.3.6. Laser material interaction

When laser beam encounters a surface, it travels as illustrated in **Figure 2.21**. Part of the radiation is reflected, some is absorbed, and the rest is transmitted.

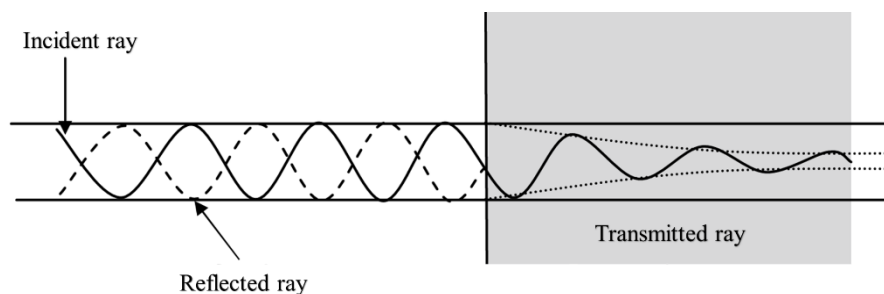


Figure 2.21. The incident laser beam, the reflected and transmitted portions [228]*.

As light passes the material, it undergoes absorption, leading to a reduction in intensity with depth at a rate determined by the material absorption coefficient (α), which varies based on wavelength and temperature. When the absorption coefficient is constant, the decrease in intensity follows the Beer-Lambert law, **Equation 2.16** [15, 228, 248-250].

$$I(z) = I_0 e^{-\alpha z} \quad (2.16)$$

Where I_0 represents the incident laser intensity (at the surface with consideration of the reflection losses), and $I(z)$ is the laser intensity at depth z .

The fraction of incident light reflected from the surface, denoted by R , depends on various parameters. These include the polarization and angle of incidence of the light, as well as the indices of refraction of both the atmosphere and the material [248, 251, 252]. For constant reflection (R), the Beer-Lambert law can be formulated in terms of the total laser intensity (I) as **Equation 2.17** [253].

$$I(z) = (1 - R) I e^{-\alpha z} \quad (2.17)$$

The optical behaviour of materials is commonly described in the literature using terms such as transmittance, absorption, and optical penetration or absorption depth [15, 34, 35, 227, 248]. The transmittance, as indicated by **Equation 2.18**, derived from **Equation 2.16**, represents the percentage of incident light that passes through a material with a thickness (L) without being absorbed or scattered. Meanwhile, absorption represents the percentage of light absorbed by the material, expressed as $(1 - \text{Transmittance})$ for non-scattered materials.

$$\text{Transmittance } (T)\% = \frac{I(L)}{I_0} = e^{-\alpha L} \quad (2.18)$$

The optical penetration depth (δ), **Equation 2.19**, is a measure of how far light can travel within a material before it decreases to only $(1/e)$, about one-third, of its original intensity [248].

$$\text{Penetration depth } (\delta) = \frac{1}{\alpha} \quad (2.19)$$

At a specific wavelength, the penetration depth depends on the absorption coefficient (α). In the case of UV light, the penetration depth (δ) may be on the nanometre scale for most materials, particularly metals [227, 248], and up to few micrometres for some polymers [254]. In the NIR range, polymers typically display high transmittance, with epoxies demonstrating penetration depths of around 1 meter at 1064 nm [15]. **Figure 3.22** shows the penetration depth for different materials over a range of wavelength [248].

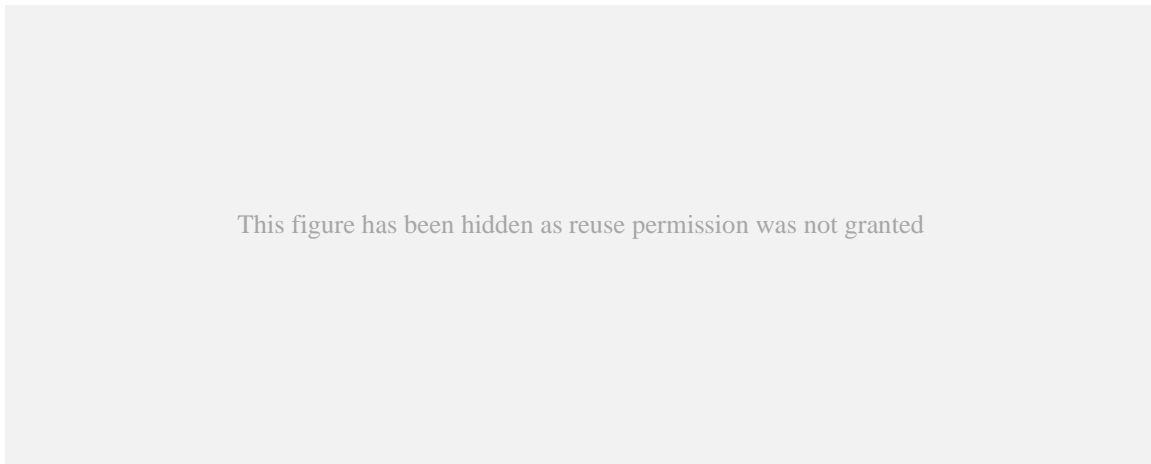


Figure 2.22. The penetration depth for different materials over a range of wavelengths, [248, 255].

The process of light absorption can be photothermal or photochemical. Exposing polymers to short-wavelength radiation, where the energy of photons is comparable to the energy of chemical bonds, demonstrates photochemical processing. In metals and semiconductors, optical absorption is primarily governed by free electrons, which means direct photochemical bond breaking does not typically occur. Instead, the laser energy causes electrons to become excited, subsequently transferring their energy into heat and phonons (vibrational waves). If the laser pulse length is shorter than the electron thermalisation time (ranging from approximately 10^{-10} to 10^{-12} seconds for metals), the ablation process is classified as photochemical. In a purely photochemical reaction, the temperature of the system generally remains constant [248, 256, 257]. Regardless of whether the reaction is photothermal or photochemical, the material response to laser processes can be categorised into three types: laser surface heating, surface melting, and ablation. Surface heating, also called surface activated processes, occurs with fluences below the melting threshold, while fluences exceeding this threshold can create temporary pools of molten material on the surface. Laser ablation, typically associated with pulsed lasers but can also occur with continuous wave (CW) lasers, involves the removal of material from a substrate [248]. Material removal can occur due to various mechanisms depending on the specific material system and laser processing parameters [248, 258]. At low fluence levels, laser ablation can be as result of evaporation or

sublimation. As the fluence levels increase, vapour bubbles and subsequent boiling can be initiated. If the material heats up rapidly enough, it can reach a critical temperature, resulting in explosive boiling and the expulsion of solid and liquid fragments. In metals and semiconductors, ultrafast pulses in the range of picosecond and femtosecond, which can achieve high power intensity, can induce the ejection of multiple electrons from the surface upon interaction, leading to the creation of a highly ionised region that undergoes explosion. This phenomenon, which involves nonlinear absorption [259], referred to as the Coulomb explosion [260, 261], represents a form of non-thermal photochemical ablation. Photochemical ablation of polymers can also occur using short-wavelength lasers [248, 262].

2.4. The state of the art: laser surface treatment of CFRP to improve adhesive bonding.

One of the significant advantages of lasers in material processing is their ability to precisely control energy deposition within the material. This precision is achieved by carefully selecting laser processing parameters to achieve the desired modifications in the material. Laser surface processing encompasses various applications such as laser surface hardening, annealing, cladding, cleaning, and texturing. Among these, laser surface texturing is considered one of the most important processes, particularly for improving the adhesive bonding of different materials [248].

Silicone-based mould release agents, which are frequently employed in the fabrication of CFRP parts, are known to cause adhesion problems when CFRP structures are adhesively joined. These agents typically penetrate several hundred nanometres into the CFRP matrix. Therefore, surface pre-treatment is essential before bonding to ensure proper adhesion [10, 28, 263]. As mentioned earlier in this chapter, various techniques have been utilised to pre-treat CFRPs for adhesive bonding, each with its own limitations. There remains a demand for a novel technology capable of providing a reliable treatment process with consistent results and potential for automation. Consequently, numerous studies have been directed towards enhancing CFRP surfaces for adhesive bonding through laser texturing. These investigations have explored the use of both CW and pulsed lasers across different wavelengths, ranging from UV to MIR. Given the objective of this research to contribute to this specific research domain, this section provides a thorough review of the most significant studies conducted in this field.

The study by Fischer et al. [15] represents a significant contribution to the exploration of laser surface texturing of CFRPs for adhesive bonding. While many previous studies have explored

the use of lasers for machining and drilling of polymers and CFRPs [264-267], Fischer et al. [15] were among the pioneering researchers in this specific area. They conducted a comparative study using SLS tests to evaluate three different surface treatment techniques: laser surface texturing with two different ns pulsed lasers (UV emitting at 355 nm and CO₂ emitting at 10600 nm), and mechanical abrasion. The results showed that the bonding strengths achieved with all three techniques were competitive, with a slight preference for the UV laser. However, it was noted that texturing with the UV laser was approximately 10 times slower than with the CO₂ laser, attributed to the lower average power of the UV laser. The study emphasised the importance of absorption depth, which is wavelength-dependent, on the ablation mechanism of the outer layer matrix resin. They noted that unlike UV and CO₂ lasers, which have low absorption depth, using a NIR laser (1064 nm), which shows a significantly greater absorption depth, most of the light would pass through the matrix and be absorbed by the underlying CFs. Consequently, the ablation process of the matrix material involves heating the underlying fibres and spallation away the top matrix layer due to thermal stresses. This presents a risk of thermal degradation of the CFs.

Oliveira et al. [17] explored the surface treatment of CFRP composites using laser ablation with a femtosecond NIR laser emitting 1064 radiation with a pulse duration of 550 fs. They pointed out that by employing the right processing parameters, it's possible to selectively remove the epoxy resin and expose the carbon fibres. Additionally, they observed the formation of sub-micron laser-induced periodic surface structures (LIPSS) on the surface of the carbon fibres. They suggested, but did not investigate, that these structures could potentially enhance the adhesion between the fibres and the matrix in adhesive bonds between CFRP parts.

Yokozeski et al. highlighted in their investigation [25] that surface treatment of CFRPs using a pulsed TEA CO₂ laser can achieve adhesive strength comparable to sandpaper treatment. This suggests the potential for laser treatment to serve as a viable alternative to traditional abrasive paper treatment methods for CFRPs.

For the same purpose, Schweizer et al, [26] compared UV and NIR lasers emitting at 355 nm and 1064 nm, respectively. They investigated various processing parameters, focusing particularly on pulse lengths, for each laser system. For the NIR laser, the pulse lengths were set at two significantly different values: 200 ns and 30 ns. Mechanical tests on the bonded coupons demonstrated that all processing parameters resulted in higher bonding strength compared to samples prepared by grinding. However, despite samples treated with shorter

pulse lengths showing higher bonding strength, cross-section assessment revealed damage at the fibre-matrix interface with the short pulse (30 ns) NIR laser.

A study with laser systems and processing parameters similar to those of Schweizer's was conducted by Reitz et al. [27], focusing on aluminium/CFRP joints using two different types of CFRP materials, labelled as A and B. SLS tests were performed to compare laser-treated samples with untreated ones, the latter being cleaned with acetone. The mechanical tests revealed an enhancement in the bonding strength of CFRP type A after laser treatment, with no significant variation observed among different laser processing parameters. In contrast, for CFRP type B, laser treatment led to a reduction in bonding strength. Moreover, Reitz et al. highlighted the impact of NIR laser processing on the integrity of the matrix-fibre interface. Their findings revealed that NIR laser treatment of CFRP surfaces often led to the formation of cavities between the fibres and the matrix, as illustrated in **Figure 2.23** (a). Consequently, during mechanical testing, the top fibres, primarily affected by this process, were pulled out and adhered to the adhesive on the other coupon, as illustrated in **Figure 2.23** (b).

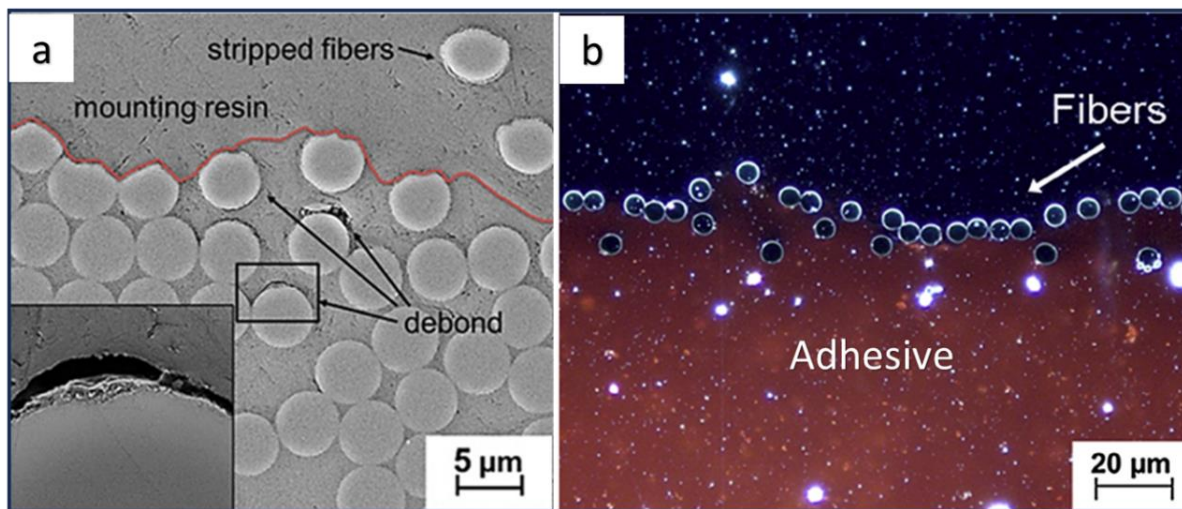


Figure 2.23. a) SEM image depicting cavities at the fibre-matrix interface in a sample treated with NIR laser. b) Darkfield microscopic image revealing fibres pulled out and adhered to the adhesive on the other coupon after bonding SLS test of a NIR laser-treated sample [27]*.

See et al. [138] explored the use of a 15 ns pulsed Excimer laser with a wavelength of 248 nm to enhance paint adhesion on CFRP surfaces. Their goal was to remove contaminants, roughen the surface using a mask, and improve wettability. They observed significant enhancements in paint adhesion compared to untreated samples and those treated with sandpaper. They pointed out that the improvement was mainly attributed to the elimination of surface contaminants and an increase in surface-active functional groups, with a minor contribution from surface

roughness. Similarly, Rauth et al. [28] utilised a UV ns pulsed laser emitting at 266 nm for surface cleaning of an Aerospace CFRP material. Their findings revealed a remarkable improvement of over 100% in bonding strength. However, they noted that despite the matrix resin absorbing most of the UV 266 nm light, UV-vis spectroscopy showed that a 6 μm silicon release agent layer absorbed less than 10% of the light in the wavelength range between 200 and 1000 nm. Considering that the actual thickness of the residues on the CFRP surface is approximately 40 nm [28], the absorption by the release agent can be considered negligible. Consequently, most of the light is transmitted through the release agent layer and enters the epoxy resin. As a result, the cleaning mechanism is based on chipping and peeling of the release agent layer.

It is mostly agreed [15, 26-28] that due to their high absorption and short penetration depth, UV lasers, particularly those with shorter wavelengths, induce direct depolymerisation reactions in the uppermost layer of the matrix resin and effectively remove epoxide material without causing damage to the fibres or compromising the integrity of the fibre-matrix structure. Consequently, contaminated and excess epoxide material can be eliminated from the surface, enhancing bonding performance. However, high-power UV-based lasers are expensive [26] and suffer from various other problems, such as low power stability due to vibration [31]. On the other hand, NIR lasers that emit around 1 μm have a significant transmission coefficient for epoxy [15, 31], allowing most of the energy to penetrate the polymer surface and be absorbed by the underlying carbon fibres, see the absorption spectrum in **Figure 2.24**. This absorption can lead to fibre-induced overheating at the fibre-matrix interface, followed by evaporation, resulting in unintended recoil pressure and the potential for matrix blasting or spalling [27, 31]. Some researchers stated that the matrix removal mechanism is based on the difference in thermal elongation between the fibres and the resin [15, 35]. Consequently, some researchers rejected the use of NIR lasers for surface treatment of CFRPs [15, 27]. Nevertheless, certain studies propose that fibres stripped by NIR radiation may enhance bonding strength by interlocking with the bonding adhesive. Additionally, exposure of fibres through laser-induced partial graphite fibre oxidation may improve wetting properties and increase the concentration of covalent bonds at the interface between the adhesive and substrate [27]. Despite the high absorption in epoxy to MIR lasers, such as CO₂ lasers that emit at 10600 nm, some researchers stated that the low photon energy can lead to thermal ablation, causing delamination effects [35].

This figure has been hidden as reuse permission was not granted

Figure 2.24. Absorption spectrum for a typical epoxy resin [35, 268].

Several other research efforts have been conducted in the field of laser surface texturing of CFRPs for adhesive bonding, mostly utilising UV, NIR, or MIR lasers [9, 29, 139, 191, 269-271]. These studies generally show improvement in bonding strength, with some preference for UV laser treatment. Unlike the previously mentioned studies, which were mostly based on the removal of the outer layer matrix partially or totally and exposing the load-carrying fibres undamaged, a non-typical laser surface treatment approach was found in two studies conducted by Coban et al. [20] and Loutas et al. [272]. They investigated the effect of micro-machining, creating surface structures in the range of 10-100 μm to enhance mechanical interlocking and, consequently, the resultant bonding strength. Coban utilised a pulsed CO_2 laser, while Loutas employed a green pulsed laser. Both studies demonstrated improvements in bonding strength, which were attributed to the mechanical interlocking they achieved.

2.5. Research gaps and challenges

The fundamental interactions between IR lasers and CFRP materials are not yet fully understood, and there exist significant discrepancies in the literature regarding their effects on adhesive bonding and the mechanisms of matrix removal. CFRP composites are composed of two distinct materials: carbon fibres and a thermosetting matrix, which possess vastly different thermal and optical properties. At NIR wavelengths, specifically at 1064 nm, the matrix material exhibits high transmittance. This high transmittance allows nearly 100% of the laser energy to penetrate through the matrix and reach the underlying carbon fibres, which can potentially lead to fibre-matrix debonding [27, 188]. Several researchers have reported that by optimising the laser processing inputs, using ns or shorter pulsed NIR lasers can significantly enhance the bonding strength by effectively removing the outer matrix layer and exposing the

carbon fibres [17, 26, 27, 188]. However, another researcher has rejected the use of NIR lasers for surface treatment of CFRP composites due to the high transmittance of matrix [15]. Additionally, while the effects of NIR laser processing variables have been extensively documented, there is a notable lack of thorough investigation into how geometrical variations, such as the fibre distribution within the matrix, affect laser processing outcomes. It has been reported that the heterogeneity of CFRP often leads to inhomogeneous ablation results [34]. The distance between the surface and the fibres, which can vary from less than 1 μm to over 10 μm in unidirectional CFRPs [28], introduces further variability that affects the efficiency of laser-material interactions. This variability can be even more pronounced in woven CFRPs, where the complex weave pattern introduces additional inhomogeneities. Understanding these variations is crucial for optimising laser processing techniques to achieve consistent and effective surface treatments across different CFRP structures. Further research is needed to explore how these structural differences influence laser processing and to develop methods that account for these variations to improve the effectiveness of laser-based surface treatments.

In the context of MIR lasers, particularly CO_2 lasers operating at 10,600 nm, there is a significant discrepancy and a lack of comprehensive data regarding the absorption and transmittance properties of matrix resins. Existing literature reveals a broad range of findings on how matrix resins interact with MIR 10,600 nm wavelength. For instance, some studies using FTIR have documented extremely high absorption rates of 90% to 95% for thermosetting matrix resins at 10.6 μm , indicating that most of the incident laser energy is absorbed with no or minimal transmission through the resin [34, 35]. Conversely, other researchers have reported that a 6.5 μm epoxy film transmits 30% of the incident laser power [36] and a 125 μm epoxy film transmits 3% [37]. This discrepancy highlights the complex nature of laser-material interactions and the need for more precise measurements and a deeper understanding of how matrix resins absorb and transmit MIR laser wavelengths. The variabilities in resin properties and fibre/matrix distribution add another layer of complexity to this issue. In unidirectional CFRPs, the distance between the surface and the fibres can vary from less than 1 μm to over 10 μm [28], and this variability is even greater in woven CFRPs, where the weave pattern introduces additional inhomogeneities. These factors affect laser penetration depth and the matrix removal process, further complicating the understanding of MIR laser interactions with CFRP materials.

Lastly, there is a significant research gap regarding the use of incoherent UV light for enhancing CFRP surfaces for adhesive bonding or as a complementary technique to IR laser

texturing. While some studies have explored the application of incoherent UV light for surface treatment across various materials, including both polymeric and non-polymeric substrates [32, 33], these investigations have largely focused on UV light used in conjunction with ozone. UV/ozone treatment has been effective but comes with notable drawbacks, such as the need for specialised equipment and the hazardous nature of ozone, which poses health risks and increases process complexity and costs. This presents a clear opportunity for research into the potential advantages of using incoherent UV light independently or in combination with IR lasers for CFRP surface treatment. Investigating this approach could offer a simpler, safer, and more cost-effective alternative to existing techniques, potentially leading to innovative advancements in CFRP surface preparation for adhesive bonding and other applications.

This divergence in findings highlights critical research gaps and underscores the need for more detailed and comprehensive studies. By exploring the fundamental interactions between IR lasers and CFRP materials, examining the variability in CFRP composite, and investigating alternative surface treatment methods such as incoherent UV light, this research aims to develop more effective and reliable techniques for improving CFRP bonded joints. These efforts are essential for enhancing the performance, durability, and applicability of CFRP composites in a range of industrial applications.

2.6. Hypotheses of the research

Despite significant advancements in the field of laser processing of CFRP composites, there remain several critical research gaps that hinder the optimization of laser-based surface treatments for CFRP composites. This study aims to address these gaps by formulating hypotheses that investigate the fundamental interactions between IR lasers and CFRP materials, the impact of composite heterogeneity on laser processing outcomes, and the potential benefits of incoherent UV light treatments. The following hypotheses are developed to guide this research.

➤ Chapter 4: Matrix resin absorption and transmittance

There is a significant discrepancy and limited data regarding the absorption and transmittance properties of matrix resins at MIR 10600 nm wavelengths.

- **Hypothesis 1:** The transmittance of thin resin films, with thicknesses varying from 15 μm to 105 μm , was precisely measured during exposure to an unfocused CO₂ laser beam using a laser power meter. The Beer-Lambert law was then applied to calculate the absorption coefficient and the reflection percentage, with reflection assumed to be constant for all samples. This study aims to provide a more accurate understanding of

MIR laser interactions with epoxy resin and CFRP materials, ultimately leading to improved laser processing strategies. A similar investigation was carried out for NIR 1064 nm wavelengths, examining samples with thicknesses ranging from 1 mm to 43 mm.

➤ **Chapter 5: Laser surface processing of woven reinforced CFRP composites to improve adhesive bonding using NIR ns pulsed fibre laser**

- **Hypothesis 2:** Variations in CFRP composite structures, particularly the heterogeneity introduced by different reinforcement patterns and fibre distributions, significantly influence the outcomes of laser processing. When processing woven reinforced CFRPs with a NIR 1064 nm pulsed laser, periodic non-ablated matrix resin structures appear due to matrix-rich zones resulting from the wavy nature of the reinforcement. These laser-affected non-ablated matrix zones are believed to negatively impact adhesive bonding. To address this, a masking technique was employed to cover matrix-rich zones while exposing only regions with shallow resin to the laser. Adhesive bonding tests were conducted to compare different surface conditions, including fully laser-scanned and partially scanned using a mask. Prior to this, a factorial experiment with different laser processing variables was conducted to optimise the laser settings to expose as many CFs as possible without causing noticeable damage.

➤ **Chapter 6: Laser surface processing of UD reinforced CFRP composites to improve adhesive bonding using NIR ns pulsed fibre laser**

The interactions between ns pulsed NIR lasers and CFRP materials remain inadequately understood, with significant discrepancies in the existing literature concerning their effects on adhesive bonding and matrix removal mechanisms. To address these gaps, this chapter employs a series of experiments designed to explore the effects of various laser parameters on CFRP surface treatment. The experiments are structured to be cost-effective while providing comprehensive insights. Unidirectional (UD) fibre-reinforced CFRP is selected for the study due to its lower inhomogeneity compared to woven CFRPs, which facilitates more straightforward and consistent comparisons of laser processing responses. The hypotheses tested in this chapter are designed to advance our understanding of these interactions and to optimise laser treatment techniques for better bonding strength and surface quality. The hypotheses explored are outlined below.

- **Hypothesis 3:** The effect of heat accumulated during laser processing. Literature has revealed that laser scanning in the direction of the fibre orientation can result in damage

to the CFs due to heat accumulation within the fibres from preceding pulses. This was further proven experimentally in this research project. However, to the best of current knowledge, there are no clear experimental or simulation studies in the literature showing whether there is any effect of accumulated heat between consecutive marks (adjacent laser scans) when the scanning is perpendicular to the CFs. To check whether there is any effect of heat accumulation on the laser treatment, a laser processing experiment was conducted using several sets with variable (high and low) scanning speeds and pulse frequencies, keeping the ratio of scanning speed to frequency and all other processing variables fixed for each set.

- **Hypothesis 4:** The pulse length and energy effects on the CFRP's matrix ablation, the surface wettability, and the adhesive bonding. At first, a factorial experiment was conducted utilising variable pulse length and energy to assess the impact of single pulses by creating separated dimples. The average ablated area of the dimples for each laser processing set was measured using the colour thresholding feature of ImageJ software. A similar factorial experiment was then performed to estimate the average length and width of the dimples. Based on the latter findings, for each variable set (pulse length and pulse energy), the scanning speed and hatch spacing were estimated with the aim of fully scanning CFRP samples (to fully expose the CFs). WCA assessment was then conducted for the fully scanned samples to identify the optimal variable set for each pulse length, followed by adhesive bonding tests to compare and evaluate the effectiveness of the optimal laser processing sets.
- **Hypothesis 5:** In line with the literature, utilising different bonding adhesives with varying mechanical properties, particularly the modulus of elasticity, results in significant variability in peeling stresses at the bond line ends. Modelling was conducted using SolidWorks software to compare two bonding adhesives under SLS test. The samples were modelled based on the mechanical properties provided by the suppliers of the adhesives and the UD reinforced CFRP material.

➤ **Chapter 7: Surface treatment of CFRP composites using continues wave carbon dioxide laser.**

Surface treatment of CFRP composites using a CW CO₂ laser has not been extensively studied. To the best of the available knowledge, only a single study exists, which highlights several findings but leaves gaps in understanding, particularly regarding the matrix removal mechanism. The effectiveness of CW CO₂ laser surface processing of CFRPs in improving

adhesive bonding is investigated through a series of experiments. These experiments involve laser surface processing of CFRP materials and pure epoxy resin samples. Moreover, surface wettability assessment and adhesive bonding tests were performed. Based on the findings from these experiments, a theory for the matrix removal mechanism was proposed. This research aims to fill the existing knowledge gaps by providing a comprehensive understanding of the effects of CW CO₂ laser surface treatment on CFRP composites and the underlying mechanisms involved. The hypotheses explored are outlined below.

- **Hypothesis 6:** Understanding the effects of laser power and scanning speed on the removal of CFRP's outer layer matrix and the ablation of pure epoxy material. For CFRP material, laser scanning of CFRP material was conducted using varying scanning speeds and laser powers, with hatch spacing wider than the laser spot size. For each laser processing set, multiple scans (laser marks or lines) were created. The percentage of the ablated area (fibres exposed regions) for each sample was then measured using ImageJ. A relationship between the ablation percentage and the Linear Energy Density (LED) was then identified. For pure epoxy resin material, the same hypothesis was tested, but instead of multiple scans, a single scan was processed for each set of laser power and scanning speed. The depth and width of the laser-created grooves were then measured, and their relationships with the LED were determined.
- **Hypothesis 7:** For surface wettability and adhesive bonding assessments, CFRP samples were processed utilising three different laser powers while all other processing inputs were the same. The surface wettability was evaluated using contact angle (CA) assessments, and bonding strength was then compared among different surface conditions.

➤ **Chapter 8: Surface treatment of CFRP composites using incoherent UV light to assist IR laser in improving CFRP surface for adhesive bonding.**

The potential of using incoherent UV light, either alone or in combination with IR lasers, to improve CFRP surfaces for adhesive bonding. This would offer a simpler and more cost-effective alternative.

- **Hypothesis 8:** This hypothesis investigates the effectiveness of UV treatment and its synergy with IR lasers. Initially, UV treatment was performed on CFRP materials using a UV lamp emitting at 254 nm at three different intensities, achieved by varying the distance of the CFRP samples from the lamp. Various UV exposure periods were tested,

and CA assessments were conducted to evaluate surface wettability. Based on the CA assessment, the optimised processing variables were applied for bonding tests. The bonding tests included several sample groups: UV treatment only, NIR laser followed by UV treatment, UV treatment followed by NIR laser, and CO₂ laser followed by UV treatment. Furthermore, mechanically abraded and as-received samples were adhesively bonded and tested as references. This comprehensive approach aims to determine the most effective method for enhancing adhesive bonding of CFRP surfaces using incoherent UV light alone or in combination with IR lasers.

CHAPTER 3: Experimental Methods

3.1. Objectives

To improve understanding of the thesis overall methodology and structure, this chapter provides an in-depth analysis of the primary methods, equipment, and materials utilised across the thesis, with a particular focus on those employed in multiple experiments. While these core aspects are emphasised, supplementary materials, methods, and equipment are discussed within the specific contexts of individual experiments, which are reviewed in subsequent chapters. The main objectives of this chapter are:

- To offer a detailed examination of the key methods, equipment, and materials used across multiple experiments.
- To reduce redundancy in the description of methods across different experimental sections.

3.2. Experimental equipment and instrumentation

The primary equipment used in this experimental work includes various lasers, a UV light source, and surface analysis and chemical characterization instruments. The main laser system utilised was a ns pulsed NIR fibre laser, with a CW CO₂ laser used to a lesser extent. UV light equipment was also employed for specific treatments, and a range of surface and chemical characterization tools were used to analyse the samples. The following descriptions provide detailed information about the equipment and instruments used in the experimental work.

3.2.1. Nanosecond pulsed NIR fibre laser

The NIR fibre laser system comprises an IR fibre laser, a beam delivery system, and an automated three-axis table. Specifically, the laser utilised is a SPI Laser (UK) G3 20 W ns pulsed fibre laser. The laser operates at a wavelength (λ) of 1064 \pm 5 nm, exhibiting a near TEM₀₀ mode, and has a beam quality factor $M^2 = 2.1$. It offers adjustable pulse lengths (τ) ranging from 9 to 200 ns and pulse repetition rates (PRF) from 1 to 500 kHz.

The beam delivery system comprises the following components:

- a) A manually adjustable 1064 nm beam expander (Linos (Qioptiq) 2-8x) was set to give a raw beam diameter (DR) of 5.7 mm as measured by taking a beam print of the beam on exposed photographic paper.

- b) Four silver mirrors (Thorlabs) guide the laser beam from the beam expander to a scanning galvanometer.
- c) A galvanometric scanner (Nutfield Extreme15-YAG) has scanning field of (50 mm x 50 mm) and controlled using SAMLight v3.05 software (SCAPS GmbH). It operates within a scanning speed range from 0.00001 m/s to 20 m/s. The galvanometric scanner is fitted with an f-theta lens (Linor Ronar F-Theta) with a focal length (f) of 100 mm. The theoretical laser beam diameter at the focal point ($d_{o(Theo)}$) was around 51 μm , calculated using **Equation 2.10a**, (from **Section 2.3.5.4/Chapter 2**) which is valid for Gaussian and near-Gaussian beams [273-275].

$$d_{o(Theo)} = \frac{4 f \lambda M^2}{\pi D_R} \quad (2.10a)$$

The three-axis computer-controlled table was supplied by Aerotech Limited (UK). In all experiments conducted using this laser system within the research project, the galvanometric scanner was responsible for scanning the laser beam across the sample surfaces. The three-axis table held the sample in place and was utilised to adjust the focal length. **Figure 3.1** depicts a schematic drawing and photograph of this equipment.

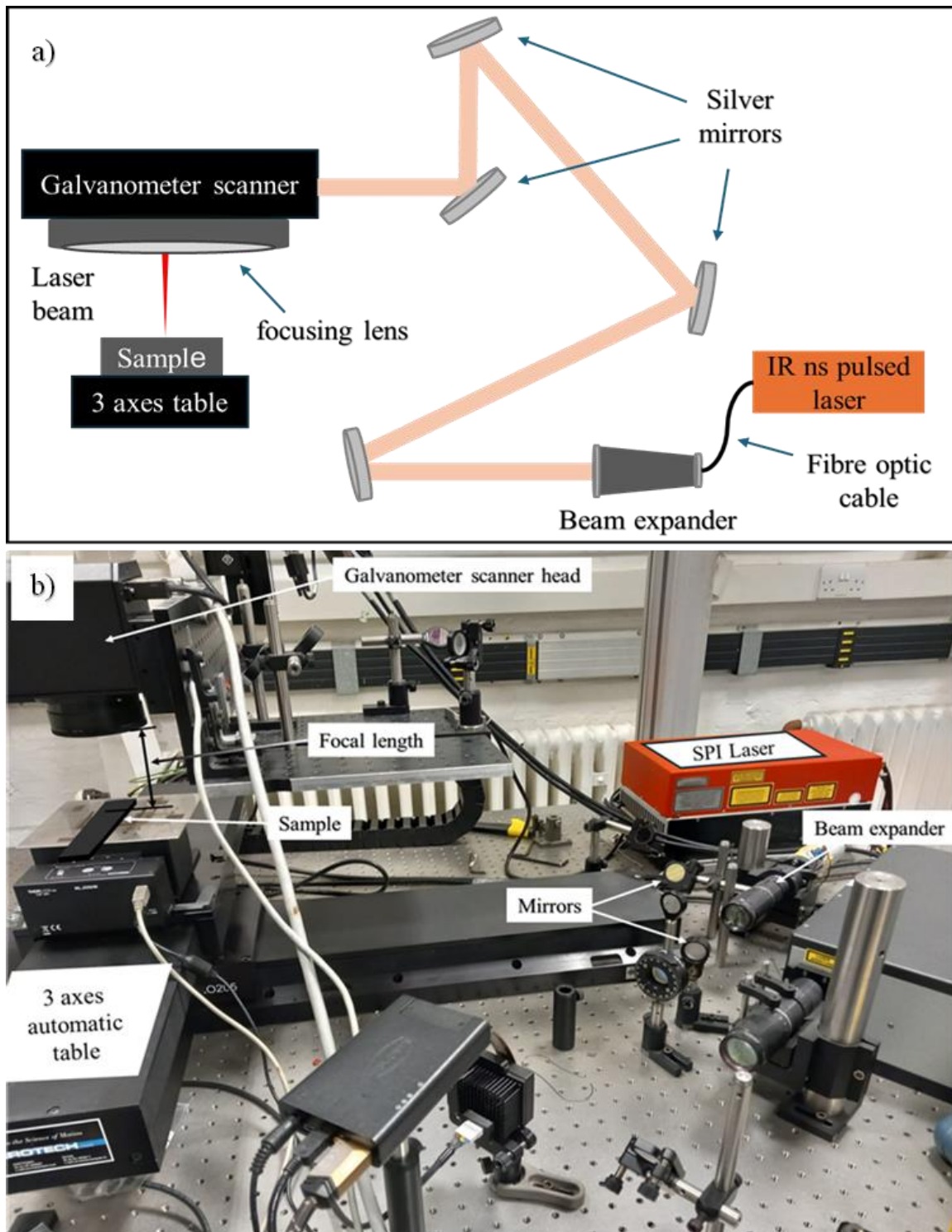


Figure 3.1. The NIR Laser equipment setup a) Schematic drawing and b) photograph.

Due to the optical system losses and the nonlinear behaviour of the output power with the setup percentages, the laser average power (P_{ave}) after the galvanometric scanner was measured for each experimental setup. This was achieved using a laser power meter calibration system consists of a *30A-N-SH ROHS* head and *Nova II display* software (Ophir). Power measurements

were conducted over a duration of 60 seconds. The pulse energy (E_p) is calculated using **Equation 3.1** [276] (derived from **Equation 2.15**). Where (PRF) is pulse repetition rate. **Figure 3.2** shows the measured average power and pulse energy for $PRF = 25$ kHz and $\tau = 200$ ns at different percentage setups. The same was done for all other sets of pulse lengths and repetition rates that were utilised in this thesis.

$$E_p = \frac{P_{ave}}{PRF} \quad (3.1)$$

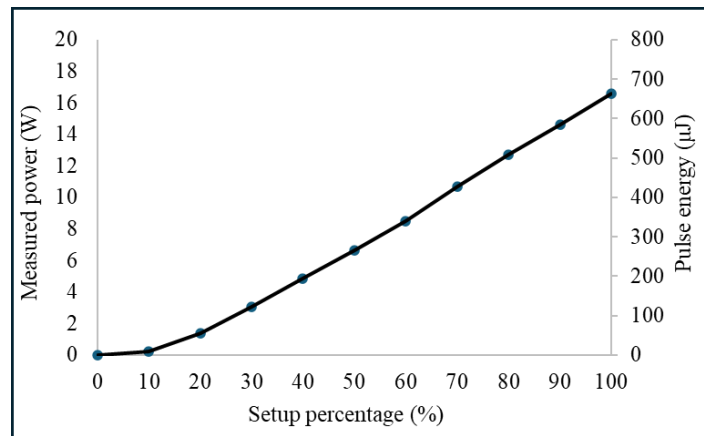


Figure 3.2. Measured average power and pulse energy at $PRF = 25$ kHz, $\tau = 200$ ns, and different power percentage setup.

3.2.2. CW CO₂ laser

A Lotus Laser System LL10600 was fitted with a CW CO₂ laser. According to the specification provided by the manufacturer, it has a maximum power of 30 W, wavelength ($\lambda = 10600$ nm), raw beam diameter of 3.5 mm with full angle beam divergence of 4 mrad, $M^2 < 1.2$, and mode quality near TEM₀₀. The beam was delivered by gold coated mirrors to a 40 mm focal length ZnSe lens. The spot size at the focal point is 185 μm, calculated using **Equation 2.10a**, and the Rayleigh Length is 2.113 mm, calculated using **Equations 2.12**. The laser is equipped with a built-in XY scanning system, offering a scanning field measuring 1000 mm x 600 mm and a scanning speed range from 0.0001 to 0.3 m/s. Manual adjustment of the focal point is achieved by altering the Z position of the sample bed. **Figure 3.3** represents a schematic drawing of the beam delivery system and a photograph of the equipment. The power out of the focusing lens was calibrated using the same method described for the fibre laser in **Section 3.2.1**. The graph in **Figure 3.4** represents the measured average power at different power percentage setup. All experiments were conducted under ambient conditions without the use of assisted gases.

Furthermore, the laser beam was at focus for all experiments unless otherwise specified, such as in Chapter 4, where it was in a non-focused position.

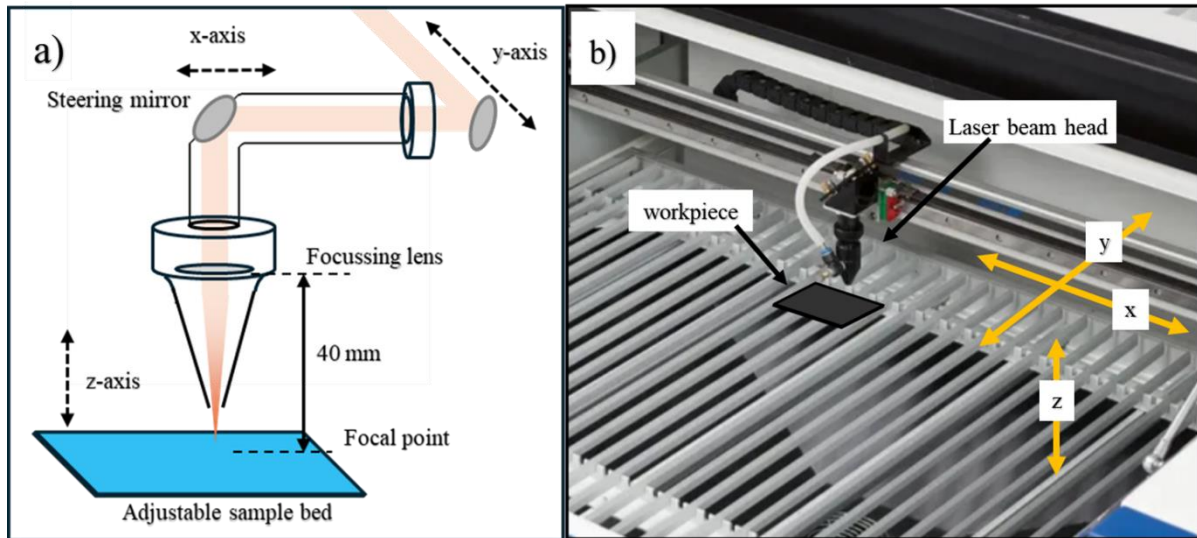


Figure 3.3. a) A schematic drawing of the CO₂ laser beam, b) a photograph of the equipment.

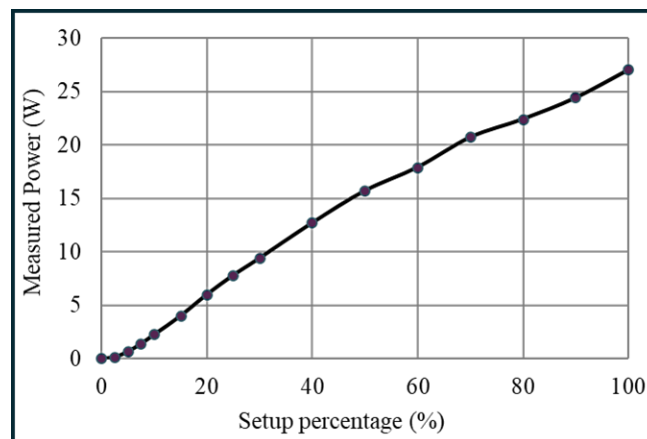


Figure 3.4. Measured average power at different power percentage setups.

3.2.3. UV light equipment

A Germicidal UV lamp (TUV Amalgam T6 130W XPT SE G10.2q) from Philips UK Ltd [277]. was utilised in this study (Fig. 1a). Over 95% of the light emitted by the lamp is at 254 nm. The lamp characterisations are detailed in **Table 3.1**. The lamp's illumination was assumed to be uniform, and the UV intensity at a sample placed at a distance (r) from the centre of the lamp was calculated by dividing the lamp's output power by the cylindrical area. The light intensity at a distance r from the axis of a long cylindrical source is inversely proportional to r [278]. **Table 3.2** presents the UV intensities and the corresponding distances of the samples from the lamp used in the experimental work. This table provides the necessary data for

understanding the relationship between UV intensity and distance, which is essential for evaluating the effectiveness of the UV exposure conditions.

Table 3.1. The UV lamp characteristics [277].

| Parameter | Value |
|---------------------------|-------|
| Power input (W) | 130 |
| UV output power (W) | 46 |
| Wavelength λ (nm) | 254 |
| Lamp length (mm) | 740 |
| Lamp diameter (mm) | 19 |

Table 3.2. UV intensities and distances from the lamp applied in the experimental work.

| Distance from the lamp centre (mm) | UV intensity (mW/cm ²) |
|------------------------------------|------------------------------------|
| 19.8 | 50 |
| 39.6 | 25 |
| 79.2 | 12.5 |

The lamp was housed within a sealed wooden enclosure. **Figure 3.5** shows a photograph and a schematic drawing of the UV lamp, and the experimental setup used in the experimental work.

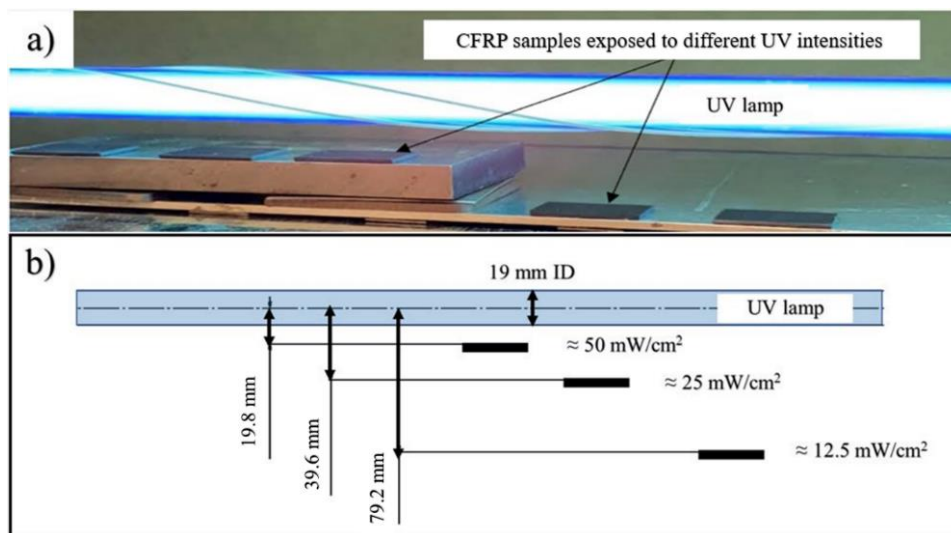


Figure 3.5. UV lamp and the experimental setup: a) photograph and b) schematic drawing [279]*.

To mitigate potential thermal influences and as a safety measure, a cooling fan with a flow rate of 0.55 m³/min was installed to maintain near-ambient temperature. Thermal changes on the sample surfaces were monitored using a thermal IR camera (thermoIMAGER TIM) from Micro-Epsilon UK, with temperature readings taken at one-minute intervals over 30 minutes using TIMConnect software. The lamp's temperature rose and then stabilised at 85°C after about 5 minutes. For the CFRP sample with the highest UV intensity, positioned approximately 10 mm below the lamp, stabilization occurred after 15 minutes at 37°C, which was 14°C above ambient temperature, **Figure 3.6**.

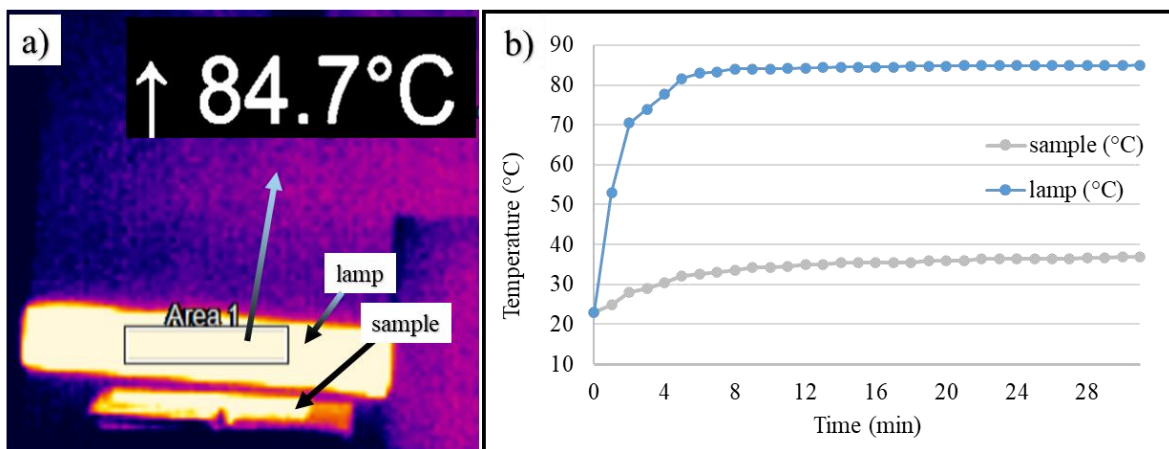


Figure 3.6. (a) Thermal imaging data captured by the IR camera for the lamp at 30 minutes, (b) graph representing the temperature over time for both the lamp and the sample.

Additionally, an assessment was conducted to determine if the elevated temperature affected surface wettability. The results indicated no significant change in the measurements.

3.2.4. Surface, chemical, and topographical characterisation equipment

Different surface characterisation equipment and techniques were utilised, the following are description of each of these equipment, **Figure 3.7**. Sample images from each of the instruments are presented in **Figure 3.8**.

- **Optical microscopy:** Olympus BH2-UMA optical light microscope, equipped with five objective lenses: 5x, 10x, 20x, 50x, and 100x. Calibration for each objective lens was performed using a stage micrometer and ImageJ software. A Dino-Lite digital camera is attached to one of the microscope's eyepieces and is used in conjunction with DinoCapture 2.0 software.

- **Digital microscopy:** VHX-7000 digital microscope from KEYENCE UK with magnification capabilities of up to 500x. This system integrates advanced image processing software for enhanced visualisation and precise measurement.
- **Optical profilometry:** Bruker Contour GT-K optical profiler, integrated with Vision64 software. The system features variable magnification and multiple operating modes, allowing for precise surface topography and roughness measurements. Green light was used for all evaluations. Both Vertical Scanning Interferometry (VSI) and Vertical eXtended Interferometry (VXI) modes were utilised, with VXI offering superior resolution for analysing light-transmitting epoxy resin and generally better details. However, it is a slow process because it captures every frame of data and is only useful for a scan range of less than 50 μm .
- **Scanning Electron Microscopy (SEM):** The primary SEM equipment used was Hitachi TM4000Plus Tabletop Microscope. Additionally, Thermofisher Inspect S model was utilised for certain assessments. Both instruments provided backscattered electron (BSE) and secondary electron (SE) imaging at various magnifications.
- **Goniometer:** The CAM 101 from KSV Instruments Ltd (UK) is an optical contact angle meter designed to measure contact angles and drop shapes of various liquids. In this experimental work, CAM 101 was used to assess surface wettability by measuring the contact angles (CAs) of both treated and non-treated samples using water and diiodomethane. For all assessments, the diameter of the liquid droplet from the syringe was 1.5 mm, corresponding to a volume of approximately 1.77 mm^3 . For non-laser treated samples, 100 frames at 16 ms intervals were captured. For laser-treated CFRP materials with exposed fibres, a longer period was used (100 frames at 16 ms plus an additional 100 frames at 1 s intervals).
- **Infrared spectrometer:** The Cary 630 FTIR Spectrometer from Agilent Technologies is a compact, Attenuated Total Reflectance (ATR) Fourier Transform Infrared (FTIR) instrument designed for rapid and reliable analysis across a broad range of samples. It was used to assess chemical variations in treated and non-treated CFRP samples. The spectrometer employs the ATR single-reflection sampling technique, utilising a diamond crystal with a 1 mm diameter sampling surface and a 200 μm active area. This setup enables approximately 2 μm depth of penetration for infrared energy at a wavenumber of 1700 cm^{-1} . It's important to note that the penetration depth is

wavelength-dependent, typically ranging from about 100 nm to several micrometres [280].

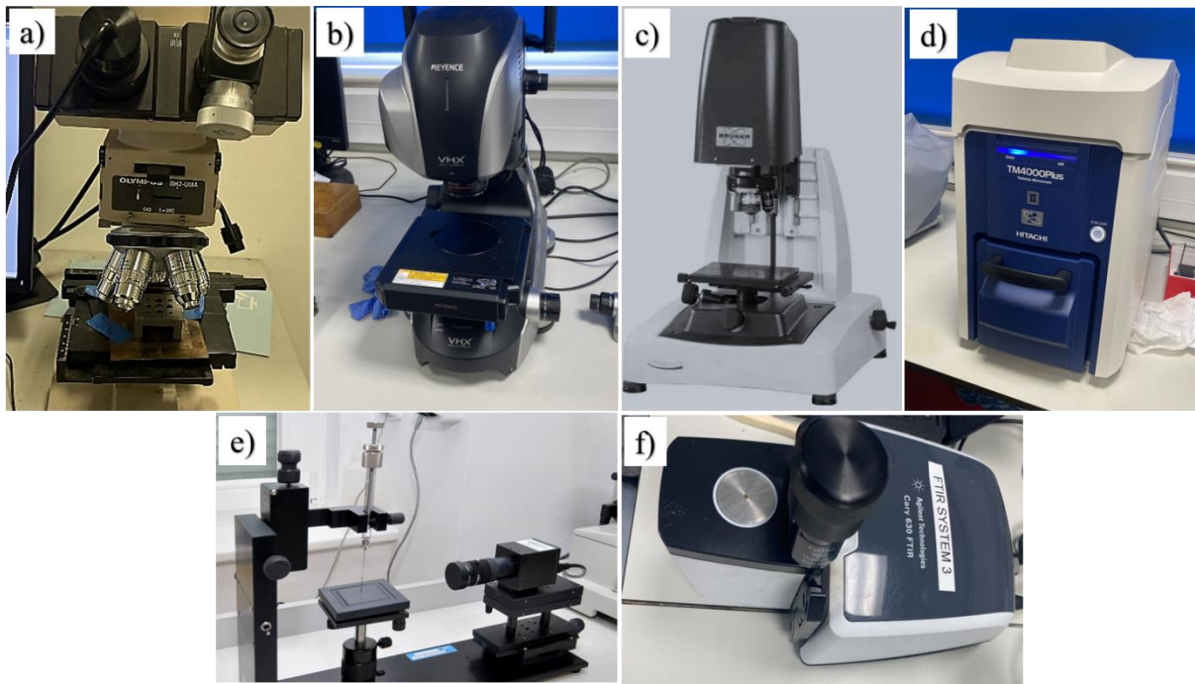


Figure 3.7. a) Olympus BH2-UMA optical light microscope, b) VHX-7000 digital microscope, c) Bruker ContourGT-K optical profiler, d) SEM Hitachi TM4000Plus Tabletop Microscope, e) CAM 101 goniometer, and f) Cary 630 FTIR Spectrometer.

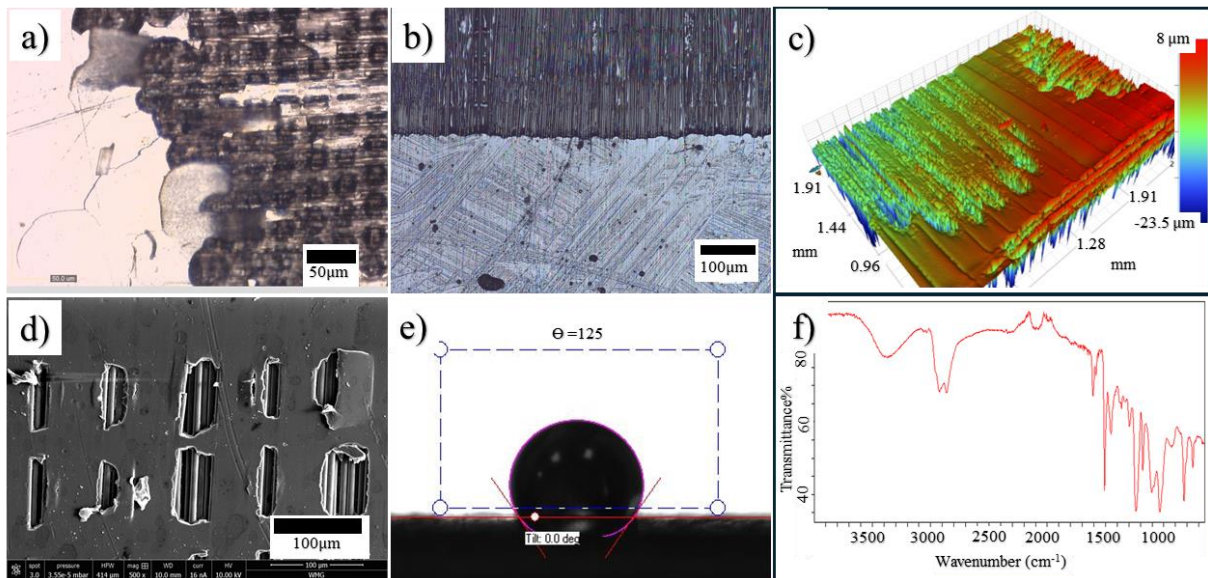


Figure 3.8. a) Optical microscopy of a woven CFRP sample processed with ns pulsed NIR laser, b) digital microscopy image of UD CFRP sample processed with CO₂ laser, c) 3D profilometry image of a woven CFRP sample processed with CO₂ laser, d) A SEM image of separated dimples were created with 30 ns pulse length NIR laser, e) Goniometer camera image of water droplet on a CFRP sample processed with CO₂ laser, and f) FTIR spectra of an as received CFRP sample.

3.3. Key experimental materials

3.3.1. CFRP composites

In this research project, various types of CFRP composites were utilised. Some materials that were readily available were employed in preliminary exploration trials and supplementary experiments. Other CFRP materials were specifically ordered to meet the experimental requirements. The primary CFRP material used consisted of five layers of unidirectional (UD) fibre prepreg, which was applied in several experiments throughout this research project. Detailed descriptions of each main CFRP material and their specific properties are provided in the relevant chapters of this thesis. Additionally, to supplement the information provided by the suppliers or manufacturers, investigations such as cross-section assessments and tensile strength tests were conducted on some of these materials before their implementation in the main experiments.

3.3.2 Bonding adhesives

Two bonding adhesives were used to evaluate the bonding strength of different surface-treated CFRPs: Loctite EA 9394 AERO Epoxy from Henkel, and Araldite 420 Epoxy from Huntsman Advanced Materials. Both adhesives are two-part paste structural adhesives but have distinct physical properties. Initial investigations with Loctite EA 9394 showed significant sensitivity to curing conditions, with strength varying greatly between oven and ambient curing. This variability is likely due to the effect of curing temperature on molecular diffusion between the adhesive and the CFRP matrix resin. Additionally, the pre-oven time (the duration from mixing the adhesive to placing the bonded coupons in the oven) might have further influenced curing, leading to inconsistent results. Consequently, curing was performed at ambient temperature, and Araldite 420 was employed for subsequent tests. Araldite 420 was chosen over Loctite EA 9394 for two main reasons. First, Araldite 420 has a lower modulus of elasticity, which reduces peeling stresses at the bondline ends. Second, its lower viscosity allows better penetration into the porous laser-treated CFRPs. This made it more suitable for the specific requirements of this experimental work. Moreover, for one of the experiments, comparative tests were conducted with both adhesives under various curing conditions to analyse the results comprehensively. **Table 3.3** provides the key specifications of both adhesives based on their data sheets [281, 282].

Table 3.3. The key characteristics of two bonding adhesives, Loctite 9394 and Araldite 420.

| Property | Loctite EA 9394 Epoxy (Henkel) | Araldite 420 Epoxy (Huntsman) |
|-----------------------------|----------------------------------|------------------------------------|
| Mix ratio (by weight) | 100:17 | 100:40 |
| Curing | 3-5 days @ 25°C or 1 hour @ 66°C | 1-2 weeks @ 25°C or 1 hour @ 120°C |
| Pot life @ 25°C (min) | 90 | 60-120 |
| Tensile strength (MPa) | 46 | 29 |
| Shear strength (MPa) | 29 | 35 |
| Modulus of elasticity (MPa) | 4237 | 1495 |
| Shear Modulus (MPa) | 1360 | 730 |
| Elongation at break (%) | 1.7 | 4.6 |
| Viscosity @ 25°C (Pa·s) | 160 | 35-45 |
| Shelf life (month) | 12 | 36 |

3.3.3. Epoxy resins

Three different epoxy resins—SP115 from Etsy UK, along with EL2 and IN2 from Easy Composites UK—were utilised to manufacture bulk resin samples and films for this experimental work. These two-part epoxy systems were employed to assess transmittance in **Chapter 4** and CO₂ laser processing of bulk epoxy resin in **Chapter 7**. Known for their clarity, low viscosity, and high strength, these resins are particularly suitable for a wide range of composite applications, especially in fibre-reinforced polymer composites. Given that the resin system compositions used by most CFRP manufacturers are proprietary, these three epoxy resin systems were selected to evaluate if there are significant differences in absorption and transmittance. **Table 3.4** presents a detailed comparison of the key specifications of these resins, highlighting their unique attributes and suitability for various applications [283-285].

Table 3.4. Properties of SP115, EL2, and IN2 epoxy resins.

| Property | SP115 (Etsy UK) | EL2 (Easy Composites UK) | IN2 (Easy Composites UK) |
|-------------------------|----------------------------------|---|--|
| Mix ratio (by weight) | 3:1 | 10:3 | 10:3 |
| Curing | 14 days | 14 days | 14 days |
| Viscosity (Pa·s) @ 20°C | 0.86 | 1.0-1.4 | 0.2-0.45 |
| Pot life (min) @ 25°C | 10 | 12-17 | 10-14 |
| Main applications | Laminating, casting, and coating | High-performance laminating applications particularly with carbon fibre | Infusion and vacuum bagging processes, ideal for large or complex shapes |

3.4. Cross-section assessments of CFRP samples

Cross-section assessments were conducted at various stages of this thesis. Some assessments focused on evaluating the thickness of the matrix outer layer, defined as the distance from the outer surface of the CFRP sample through the outermost resin layer to the surface of the carbon fibres, for the as-received CFRP samples. Other assessments analysed laser-treated samples and examined the fracture characteristics of CFRP coupons after bonding tests. Regardless of the sample conditions, the method was the same, with only the sample dimensions differing. For as-received or laser-treated materials, the samples measured 15 mm x 15 mm, whereas for fractured coupons, the samples measured 25 mm x 6 mm, with the coupons cut at the midpoint of the bondline. The samples were mounted vertically in an epoxy resin mould (VersoCit-2 by Struers), then ground and polished. Grinding was conducted using a Buehler Metaserv Twin Grinder/Polisher from Specrographic UK, while polishing was performed using a TegraPol 11 from Struers (**Figure 3.9**). The grinding process used SiC abrasive paper grades of 80, 120, 240, 400, 600, 1200, and 2400 consecutively. In the first grinding process (with paper grade 80), more than 1 mm of material was removed to eliminate the cut-affected edge. Polishing was performed in three stages: two with diamond grit sizes of 3 μm and 1 μm , and a final stage using a solution of distilled water and colloidal silica gel (50/50 by volume) with a grain size of 40 nm. All polishing consumables were procured from Struers. The polished cross-sections were then studied using optical microscopy and SEM.

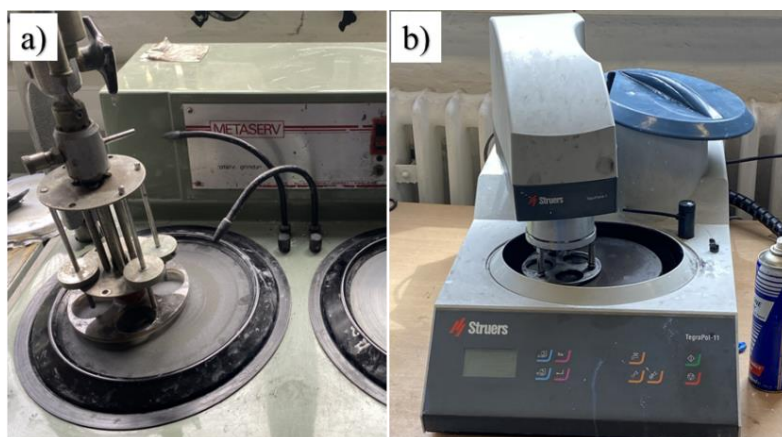


Figure 3.9. a) Buehler Metaserv Twin Grinder/Polisher, b) TegraPol 11 Struers Polisher.

3.5. Adhesive bonding tests (Single Lap Shear (SLS) tests)

SLS tests were selected to evaluate the adhesive bonding strength following various surface treatments across the whole research project. BS EN ISO 1465:2009 standard [286], a widely

used guideline for adhesive joining tests, was utilised [15, 26, 27]. To ensure symmetry and minimise load path eccentricity, which can lead to out-of-plane bending moments, aluminium shims of the same thickness as the CFRP were bonded to the ends of the samples [287]. The sample dimensions are illustrated in **Figure 3.10**.

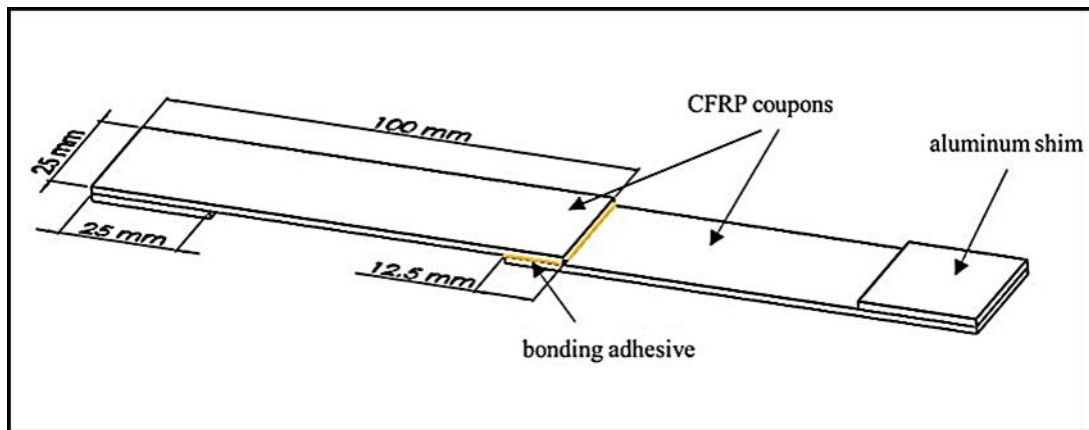


Figure 3.10. Sample for SLS according to BS EN ISO 1465:2009 standard.

For each surface condition, six coupons were prepared to form three test pairs. These coupons were adhesively joined using a special jig designed in SolidWorks, which could join up to six pairs simultaneously. The jig was adjustable according to the CFRP material thickness and was manufactured from a 6 mm thick aluminium plate. A milling machine was used to create six (1 mm deep x 26 mm wide) grooves in the jig to ensure alignment of the bonded coupons. For the bonded pairs, the bondline thickness was maintained at 0.2 mm by incorporating chopped pieces of copper wire (0.5 mm length x 0.2 mm diameter) into the adhesive. For the same purpose, glass beads were used in a previous study [288]. The upper coupons were then positioned, and steel compression springs (as shown in **Figure 3.11**), each with a spring constant of 2.3 N/mm, were compressed by 5 mm to exert a compression force of approximately 11.5 N. This force was sufficient to uniformly distribute the adhesive layers across all samples, following the method used by Bregar et al. [289]. Excess adhesive was removed with a small spatula. The adhesive was cured under varying conditions across different experiments. In some cases, oven curing was used, while in others, curing occurred at ambient conditions (20-23 °C). Following the curing process, the samples were tested using a Tinius Olsen 50 kN tensile testing machine at a loading rate of 1 mm/min, **Figure 3.12**.

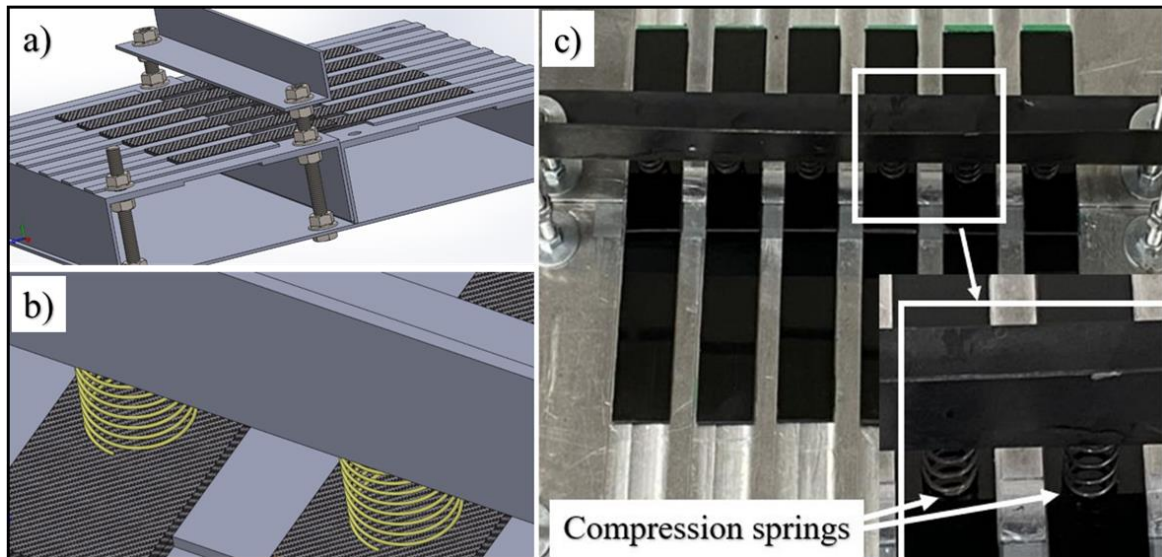


Figure 3.11. Bonding jig: (a) and (b) SolidWorks design, and (c) photograph of the manufactured jig.



Figure 3.12. Tinius Olsen 50 kN tensile testing machine.

3.6. Cutting and cleaning of the CFRP materials

The as-received CFRP panels, each measuring 500 mm x 500 mm, were cut into coupons (25 mm x 100 mm) or smaller samples based on the experiment requirements using a water-cooled cut-off saw (Erbauer 750W) with a diamond cutting blade. The resulting samples were immediately cleaned through a multi-step process: first with a detergent solution, followed by distilled water, then sprayed with isopropanol, and finally cleaned in an ultrasonic bath of isopropanol. The same cleaning process was repeated prior to any surface treatment, wettability assessment, and adhesive bonding for both non-treated coupons and those subjected to mechanical sanding.

CHAPTER 4: Matrix Resin Absorption and Transmittance

4.1. Introduction

Understanding the ablation mechanism of the matrix through laser surface processing of CFRPs depends on several factors, with wavelength being the key parameter. Firstly, it defines the photon energy and subsequently categorises the laser-material interaction into photothermal or photochemical processes. Short wavelengths in the UV range have high photon energy that directly breaks down polymer molecular bonds, while longer wavelengths in the IR range have low photon energy and are said to interact photothermally. Secondly, the laser wavelength determines the absorption coefficient of a particular material and, consequently, the absorptivity and the transmittance. As discussed in **Chapter 2/Section 2.3.6**, when a laser beam passes through a material, its illumination decays exponentially with the travelled distance according to the Beer-Lambert law. Epoxy resins are recognised for their low absorption coefficients under NIR light at 1064 nm, whereas at the MIR wavelength of 10600 nm, their absorption coefficients are notably higher. Despite this recognition, limited studies have provided specific values for absorption coefficients and penetration depths, revealing significant variability in the available data and highlighting gaps in the understanding of their optical properties. Fischer et al. [15] reported a high penetration depth of up to 900 mm for 1064 nm light while not specifying a specific value for 10600 nm light. Zarei et al. [290] indicated depths of only 150 μm for 1064 nm and 20 μm for 10600 nm. It's worth noting that Zarei et al. [290] referenced Kalms et al. [291], who provided only a qualitative representation of the transmission spectrum of an epoxy layer without specific values. Firbank et al. [292] also provided an absorption coefficient spectrum for epoxy resin, suggesting a penetration depth of around 200 mm at 1064 nm. Additionally, Mckie and Addison [37] noted that a 0.005 inch (125 μm) epoxy layer transmitted about 93% of 1064 nm laser intensity, while less than 3% of 10600 nm laser was transmitted, **Figure 4.1**. Some other researchers reported, using Fourier Transform Infrared Spectroscopy (FTIR), the absorption of epoxies at 10.6 μm is very high (90-95%), with almost no transmittance [34, 35].

This chapter explores the absorptivity and transmissivity of epoxy matrix resin to NIR, ($\lambda=1064$ nm) and MIR ($\lambda=10600$ nm) lasers through two distinct experiments.

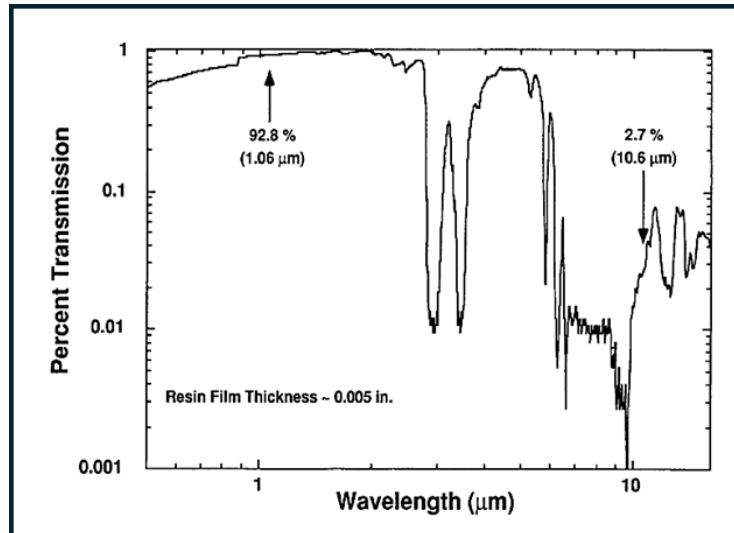


Figure 4.1. Transmissivity of a 125 μm thick layer of epoxy resin as a function of laser wavelength [37]*.

4.2. Objectives

The objective is to systematically measure the transmittance, absorption coefficient, and reflection of a representative thermosetting epoxy matrix when exposed to a fibre laser (1064 nm) and a CO₂ laser (10600 nm), thereby enhancing the understanding of the matrix removal mechanism. Additionally, this study aims to address gaps and variability in existing data on the absorption coefficients and penetration depths of thermosetting epoxies, particularly at 10600 nm, by providing comprehensive measurements and insights.

4.3. Transmittance to NIR laser (1064 nm)

4.3.1. Methods (transmittance to NIR 1064 nm)

Three different epoxy resins (SP115 from Etsy UK, EL2, and IN2 from Easycomposites UK) were tested. These epoxies have low viscosity and are typically used as matrices in FRPs. Each consists of a main resin material and hardener with a particular mix ratio. Further specifications about the three resins are available in **Chapter 3**. For the first two epoxies (SP115 and EL2), six samples were moulded, with thicknesses ranging between 0.8 mm up to ≈ 10 mm. For the IN2 epoxy, an additional four samples were created with thicknesses ranging between 20 mm to 43 mm. SP115 and EL2 epoxies were found to be difficult to be mould into thick samples (over 10 mm), and even at lower thicknesses, mixing the main material with the hardener was performed slowly to avoid creating bubbles. After being fully cured for 14 days at room temperature, all samples were polished from both sides with sandpapers (80, 220, 400, 600, 1200, and 2400), respectively. The polishing process was performed manually and was

repeated across several samples for two main purposes. Firstly, to achieve flat surfaces, ensuring that the thickness variation within each polished sample remained within ± 0.02 mm. Secondly, to minimise variation in roughness among all samples. However, due to the manual nature of the process, achieving uniform thicknesses across the three different resin materials posed a challenge. The thickness of the samples was measured using a two decimal places digital calliper. The thicknesses of the SP115 samples are (0.8, 1.5, 2.75, 3, 5, and 9.75 mm), for EL2 samples (1.95, 2.95, 3.9, 4.35, 5.3, and 10.2 mm) and for the IN2 samples (0.9, 1.85, 2.8, 3.75, 4.4, 9.6, 19, 25.5, 37, 42.7 mm). **Figure 4.2** shows the polished samples.

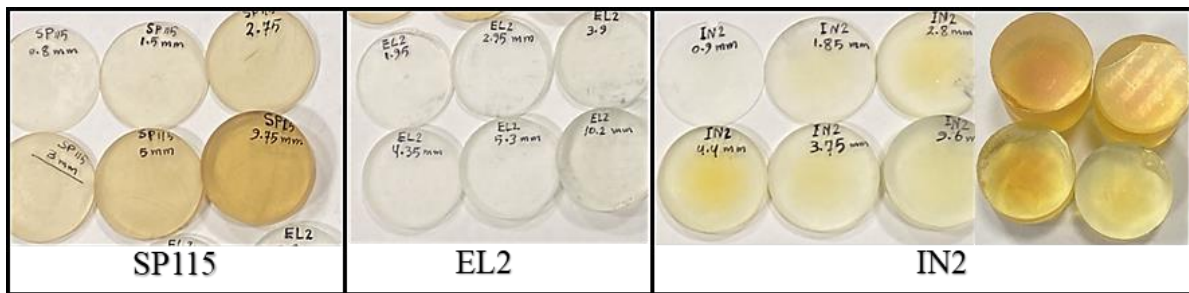


Figure 4.2. The moulded epoxy resins samples.

The areal surface roughness (S_a) of the samples was assessed using optical profilometry (Bruker). For the Bruker setup, a green light with VXI mode was utilised. Six measurements were taken for each sample, with three from each side, covering an area of 1 mm x 1.3 mm. The average S_a for each sample and Standard Deviation (SD) were subsequently calculated. The Ophir laser power meter, described in **Chapter /Section 3.2.1**, was employed to assess the transmittance of the resin samples by measuring the laser power both with and without a sample. The laser system utilised was the NIR SPI ns pulsed fibre laser. Details of the laser system are available in **Chapter 3**. The laser power was set to 3 W, and the power meter indicated fluctuations within a ± 0.01 W range around this set value. These fluctuations could be attributed to either unstable laser power or potential errors in the power meter itself. The detector of the power meter was positioned 50 mm above the focal point, while a resin sample was placed above the detector, as illustrated in **Figure 4.3**. The purpose of using an unfocused laser beam was to prevent potential damage to the power meter detector at high laser intensities and to eliminate the potential impact of sample partial evaporation on the laser beam, which could occur due to laser interactions with the generated gases. The transmitted power from each sample was then measured at five different positions.

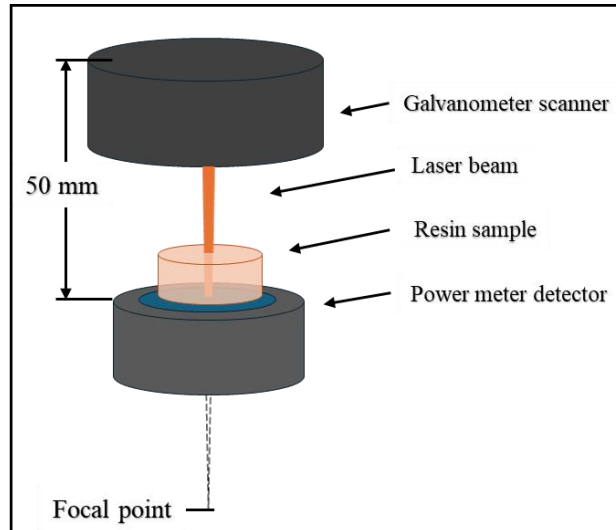


Figure 4.3. A scheme clarifies the experimental setup (transmittance to NIR 1064 nm).

4.3.2. Results and discussion (transmittance to NIR 1064 nm)

The surface roughness of most samples was maintained within a narrow range of 0.2-0.35 μm . Achieving this consistency required repeating some or all of the polishing processes, but it was challenging to achieve similar results due to the manual processing, as mentioned earlier.

Figure 4.4 demonstrates an example of the surface roughness assessment data. From the transmittance data collected, the average transmittance (T) and the SD were calculated for each sample.

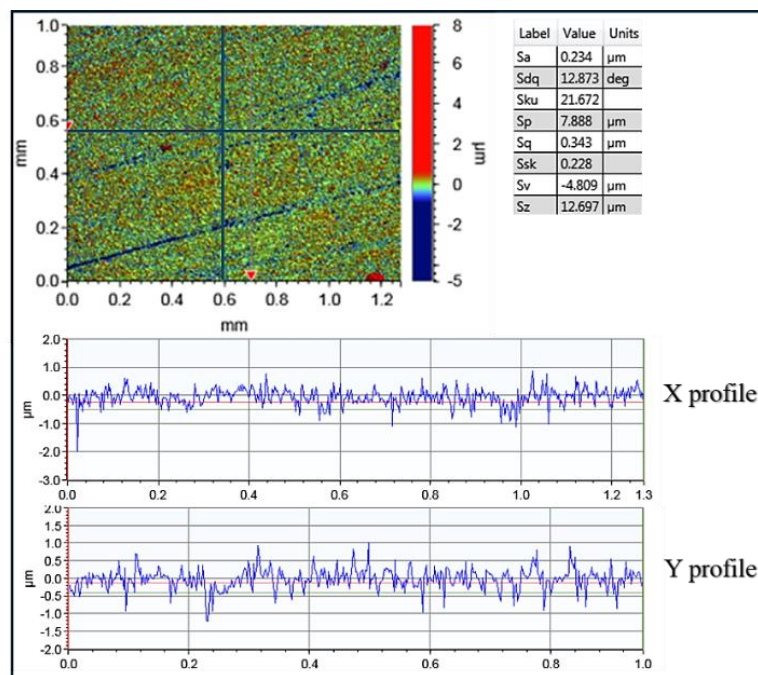


Figure 4.4. Demonstration of the surface roughness assessment data.

The average roughness (Sa), transmittance and the SD for both transmittance and roughness of the different samples are presented in **Table 4.1**.

Table 4.1. The thickness, transmittance, surface roughness, and their SD.

| SP115 | | | | | EL2 | | | | | IN2 | | | | |
|-------|------|-----------------|------|------------------|------|------|-----------------|------|------------------|------|------|-----------------|------|------------------|
| t | T | SD _T | Sa | SD _{Sa} | t | T | SD _T | Sa | SD _{Sa} | t | T | SD _T | Sa | SD _{Sa} |
| (mm) | % | % | (μm) | (μm) | (mm) | % | % | (μm) | (μm) | (mm) | % | % | (μm) | (μm) |
| 0.8 | 86.5 | 2 | 0.54 | 0.097 | 1.5 | 86.2 | 0.8 | 0.25 | 0.013 | 0.9 | 85.1 | 1.7 | 0.41 | 0.090 |
| 1.5 | 87.3 | 1.6 | 0.31 | 0.016 | 2.95 | 86.3 | 0.1 | 0.18 | 0.002 | 1.85 | 85.9 | 0.3 | 0.25 | 0.018 |
| 2.75 | 86.8 | 0.4 | 0.19 | 0.013 | 3.9 | 83.8 | 0.3 | 0.28 | 0.017 | 2.8 | 86.4 | 0.7 | 0.29 | 0.031 |
| 3 | 86.6 | 0.7 | 0.27 | 0.043 | 4.35 | 84.1 | 0.4 | 0.18 | 0.009 | 3.75 | 84.2 | 1.2 | 0.24 | 0.006 |
| 5 | 82.7 | 0.2 | 0.24 | 0.005 | 5.3 | 84.6 | 0.4 | 0.22 | 0.043 | 4.4 | 83.5 | 1.2 | 0.21 | 0.019 |
| 9.75 | 79.3 | 0.3 | 0.41 | 0.058 | 10.2 | 81.1 | 0.8 | 0.26 | 0.021 | 9.6 | 80 | 0.3 | 0.26 | 0.014 |
| | | | | | | | | | | 19 | 74.3 | 0.4 | 0.19 | 0.006 |
| | | | | | | | | | | 25.5 | 72.7 | 0.3 | 0.06 | 0.003 |
| | | | | | | | | | | 37 | 66.2 | 0.3 | 0.15 | 0.005 |
| | | | | | | | | | | 42.7 | 64.2 | 0.2 | 0.18 | 0.010 |

The graphs in **Figure 4.5** were created to illustrate the relationship between transmittance (T) and the sample thickness (t) for each of the three different epoxies.

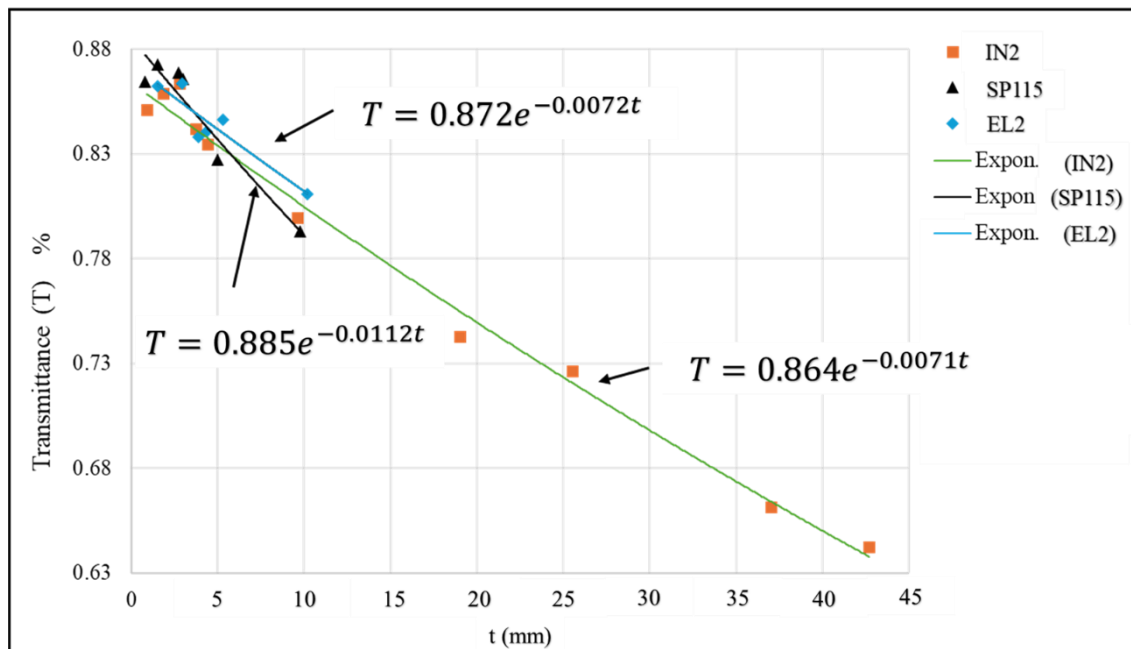


Figure 4.5. The transmittance (T) for NIR 1064 nm laser as a function of the sample thickness (t) for SP115, EL2, and IN2 epoxies.

Assuming the reflection remains constant across all samples and considering that the resin exhibits minimal scattering to the laser beam while attenuation primarily occurs through exponential absorption, the absorption coefficient (α) and reflection (R), **Table 4.2**, are calculated by substituting the exponential fit of the T-t graphs with the Beer-Lambert law **Equation 2.14** [253]. The penetration depth (δ) was also calculated using **Equation 2.15** [248].

$$\text{Transmittance } (T)\% = \frac{I(t)}{I} = (1 - R) \cdot e^{-\alpha t} \quad (2.14)$$

$$\text{Penetration depth } (\delta) = \frac{1}{\alpha} \quad (2.15)$$

Where I represent the laser power without a sample, I(t) denoted the transmitted laser power through a sample has a thickness t, R is the reflected fraction of the light, and α is the absorption coefficient.

Table 4.2. The absorption coefficients α , penetration depths δ , and the reflection fractions R of the three epoxies for NIR laser 1064 nm.

| | SP115 | EL2 | IN2 |
|------------------------|---------|--------|---------|
| α (mm^{-1}) | 0.01123 | 0.0072 | 0.00711 |
| δ (mm) | 89 | 140 | 141 |
| R (%) | 11.5 | 12.8 | 13.6 |

The results show a close exponential trend for the EL2 and IN2 epoxies. However, the SP115 epoxy, which exhibits lower transmission to visible light (seems darker than other two epoxies), also demonstrates lower transmission to the NIR laser. The deviations in the transmittance data around the averages, as well as fluctuations in the average values around the exponential trend both are mostly within the range of $\pm 2\%$ or less, as seen in **Figure 4.5**. These deviations and fluctuations can be attributed to three main factors. Firstly, the reflection fraction, which was assumed to be constant among the different samples, varies because of the variation in thickness and surface roughness. The reflection, encompassing reflectance from both the top and the bottom surfaces, depends not only on roughness and sample thickness but also on other parameters such as the laser wavelength [293]. It seems that samples with higher roughness (S_a) exhibit transmittance below the exponential trend, and vice versa. However, the

relationship between the reflection and surface roughness is complex, and no exact general theory is available [294]. Secondly, the potential error or inconsistency in sample thickness. Thirdly, the unstable laser power. The first two factors are linked to the manual polishing processes. For this reason, the deviation or fluctuation appears to be more obvious for thinner (< 2 mm) samples due to the challenges associated with handling them.

4.4. Transmittance to MIR laser (10600 nm)

4.4.1. Methods (transmittance to MIR 10600 nm)

For this experiment, IN2 epoxy resin, described in **Chapter 3/ Section 3.3.3**, was used to fabricate resin films (20 resin films in total) with thicknesses ranging from 15 to 110 μm . This was accomplished by moulding the resin between two toughened glass sheets measuring 120 mm by 100 mm by 6 mm, which were compressed together using ratchet bar clamps. Aluminium foil sheets with variable thickness were used as shims to control the thicknesses of the produced films, see **Figure 4.6**. Before applying the resin, the glass sheets were wiped with a lint-free cloth soaked in CR1 Easy-Lease, a volatile chemical release agent from Easycomposites UK, and allowed to evaporate for about 60 seconds. The moulds were then left for seven days at room temperature to be fully cured.

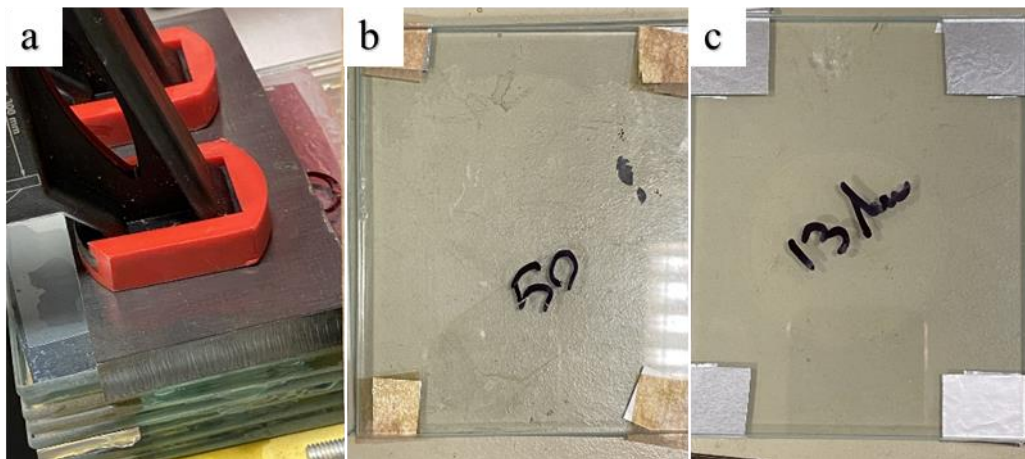


Figure 4.6. Camera images showing (a) multiple glass sheets utilised as moulds for epoxy films are compressed together using ratchet bar clamps, and (b) and (c) two pairs of glass mould with epoxy films before being released.

For accuracy, the thicknesses of the produced epoxy films were measured using optical profilometry (Bruker Contour GT-K 3D white light interferometer). This was achieved by measuring the thickness of a 5 mm by 5 mm piece from each sample, which was taken from a location very close to the laser-exposed regions. As illustrated in **Figure 4.7**, an epoxy film intended to be 25 μm thick was found to have an actual thickness of 23.5 μm according to the

profilometry. Additionally, several profilometry measurements verified that the release agent layer was less than 0.1 μm thick, and therefore, it was considered to have a minimal impact.

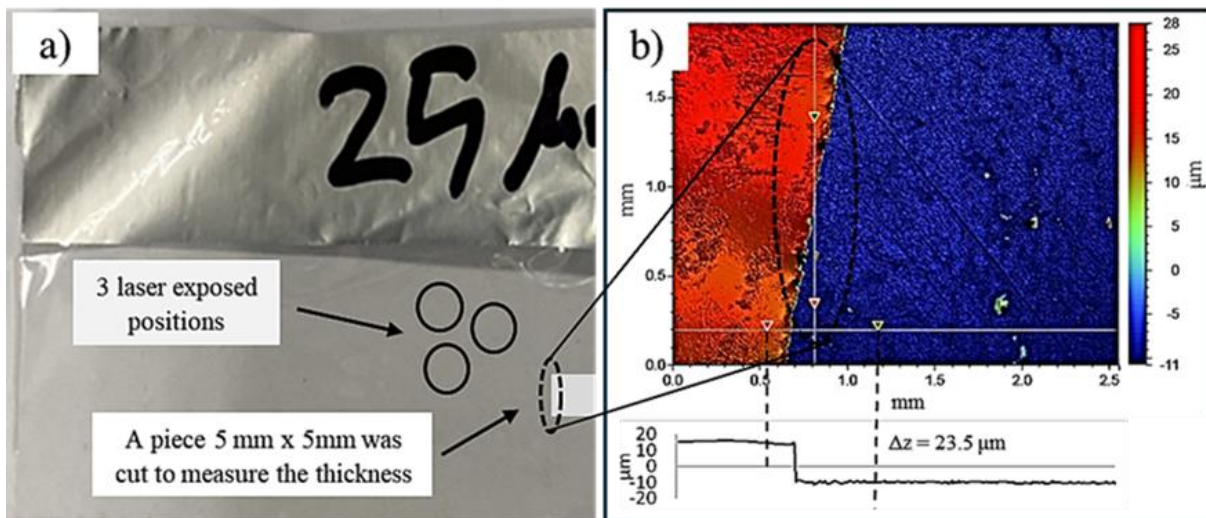


Figure 4.7. (a) camera image of an epoxy film intended to be 25 μm thick, (b) profilometry assessment indicating the thickness of 23.5 μm .

It is worth noting that since these resin films were created by moulding using smooth glass sheets, there was no need for roughness assessment. They are all considered to have the same surface finish, which is almost a mirror surface finish.

The laser utilised to assess the transmittance of the epoxy resin films was the Lotus Laser Systems LL10600, a 30 CW CO_2 laser, which has been extensively described in **Chapter 3/ Section 3.2.2**. The epoxy films were placed 70 mm below the focal point as shown in **Figure 4.8**. As the distance from focus significantly exceeds the Rayleigh length, the beam diameter $d(z)$ increases linearly with the distance, **Equation 4.1** [226, 295].

$$W(z) = z \cdot \theta \quad (4.1)$$

Where $W(z)$ is the beam width at a distance z from the focal point, which is equal to $d(z)/2$, and θ is beam divergence angle.

Accordingly, the unfocused laser spot size (D') was estimated to be 6.1 mm using **Equation 4.1a** which is driven from **Equation 4.1**, where (df) is the defocus distance, (D) is the beam diameter at the lens, (f) is the focal length of the lens.

$$D' = D (df/f) \quad (4.1a)$$

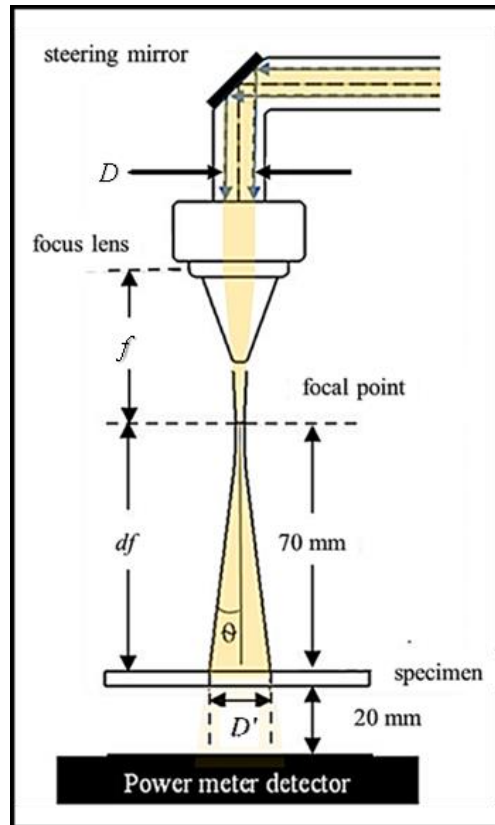


Figure 4.8. A schematic drawing of the laser system and the experimental setup.

The power of the laser beam was measured using the Ophir laser power meter, described in **Section 3.2.1** both with and without a sample, and it was recorded as 0.65 ± 0.02 W when no sample was present.

To experimentally verify the spot size estimation, a Perspex sample was placed at the unfocused position and subjected to laser processing using the full laser power (27 W) at five different scanning speeds (5, 10, 20, 30, and 40 mm/s). The maximum width of the laser traces, approximately 6 mm, was achieved at a scanning speed of 10 mm/s. Slower scanning speeds yielded similar trace widths but were surrounded by a Heat-Affected Zone (HAZ), as depicted in **Figure 4.9** below. The low power and large spot size used in the experiment ensured the resin film did not degrade.

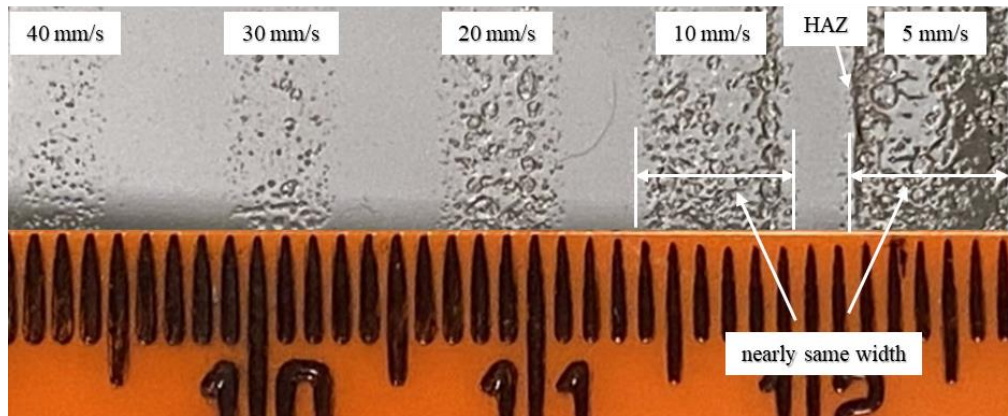


Figure 4.9. Perspex sample was positioned at the unfocused position and subjected to laser processing using laser power of 27 W and five different scanning speeds in order to estimate the laser spot size.

The power emitted from each resin film was recorded after scanning the laser beam for about 10 seconds (a circle 3 mm in diameter was processed at a speed of 1 mm/s). Each epoxy resin film was exposed to the laser at three distinct but closely spaced positions. Additionally, profilometry samples were taken from areas near the laser-exposed positions. Readings from at least two repeated measurements were found to be matched, and these were then considered.

To measure the thickness of the outer layer matrix resin of CFRPs, different CFRP samples were analysed using SEM (*Inspect S model, Thermofisher*). The method employed for this purpose was secondary electron imaging. The sample was embedded within epoxy and polished to a mirror finish before undergoing SEM assessment. Both the polishing and SEM methods are thoroughly described in **Chapter 3**.

4.4.2. Results and discussion (transmittance to MIR 10600 nm)

The results indicated that a 15 μm film transmitted approximately 55% of the laser power, whereas less than 5% of the power was transmitted through an 86 μm film. A plot (**Figure 4.10**) was generated to represent the resulting transmittance values $I(t)/I$ as a function of the film thickness (t), where (I) represents the measured laser power without a sample, and $I(t)$ is the power transmitted through a resin film has thickness (t).

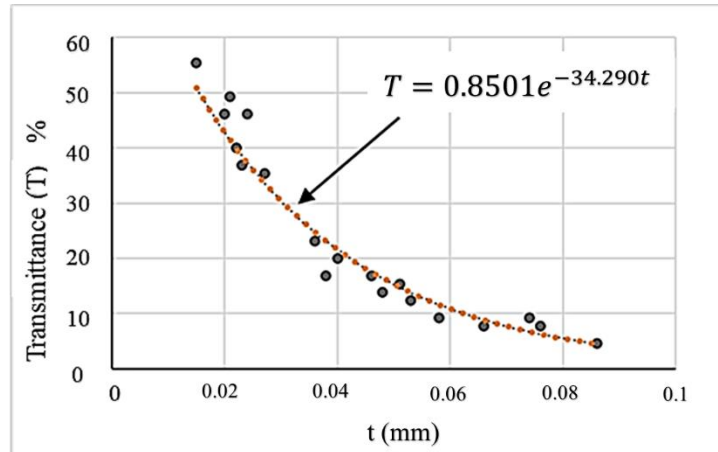


Figure 4.10. Epoxy films transmittance (T) for MIR (10600 nm) laser as a function of the film thickness (t).

The 110 μm resin film displayed no detectable transparency with the power used, and thus it was excluded from the plot. This limitation arose from the power meter's ability to measure only up to two decimal places. Consequently, any power less than 0.01 W would be displayed as zero. The data points closely fit an exponential decay relation [$T=0.851\exp(-34290t)$] representing the relationship between transmittance and film thickness. By assuming constant reflection for all the samples, no scattering, and that the beam is attenuated exponentially by absorption, the absorption coefficient (α) and the reflectivity (R) are determined by substituting the above relation with Beer-Bouguer-Lambert law **Equation 2.14**. The penetration depth is also calculated using **Equation 2.15**.

$R = 15\%$, $\alpha = 34.3 \text{ mm}^{-1}$, and $\delta \approx 0.00029 \text{ mm}$ or $29 \mu\text{m}$.

Examination of the CFRP cross-sectional using SEM revealed that the thickness of the epoxy matrix outer layer varies. This variability depends on the distribution of the fibre reinforcements. In CFRPs reinforced with unidirectional carbon fibres, the thickness ranged from 1 to 25 μm , with an estimated average of approximately 10 μm , as shown in **Figure 4.11** (a) and (c). In CFRPs with woven reinforcement, the variation is more pronounced, especially at the fibre tow intersections, where the thickness is significantly greater **Figure 4.11** (b). The plot in **Figure 4.11** (d), based on the Beer-Bouguer-Lambert law, illustrates the absorption, transmittance, and reflected percentages of a CO_2 laser beam passing through a matrix resin film with a thickness ranging from 0 to 25 μm . For a 10 μm resin layer, typical of the average outer layer matrix of unidirectional CFRP material, around 60% of the light intensity is transmitted through the matrix and absorbed by the underlying CFs, while less than 25% is absorbed by the matrix layer itself, with the remaining portion (15%) being reflected.

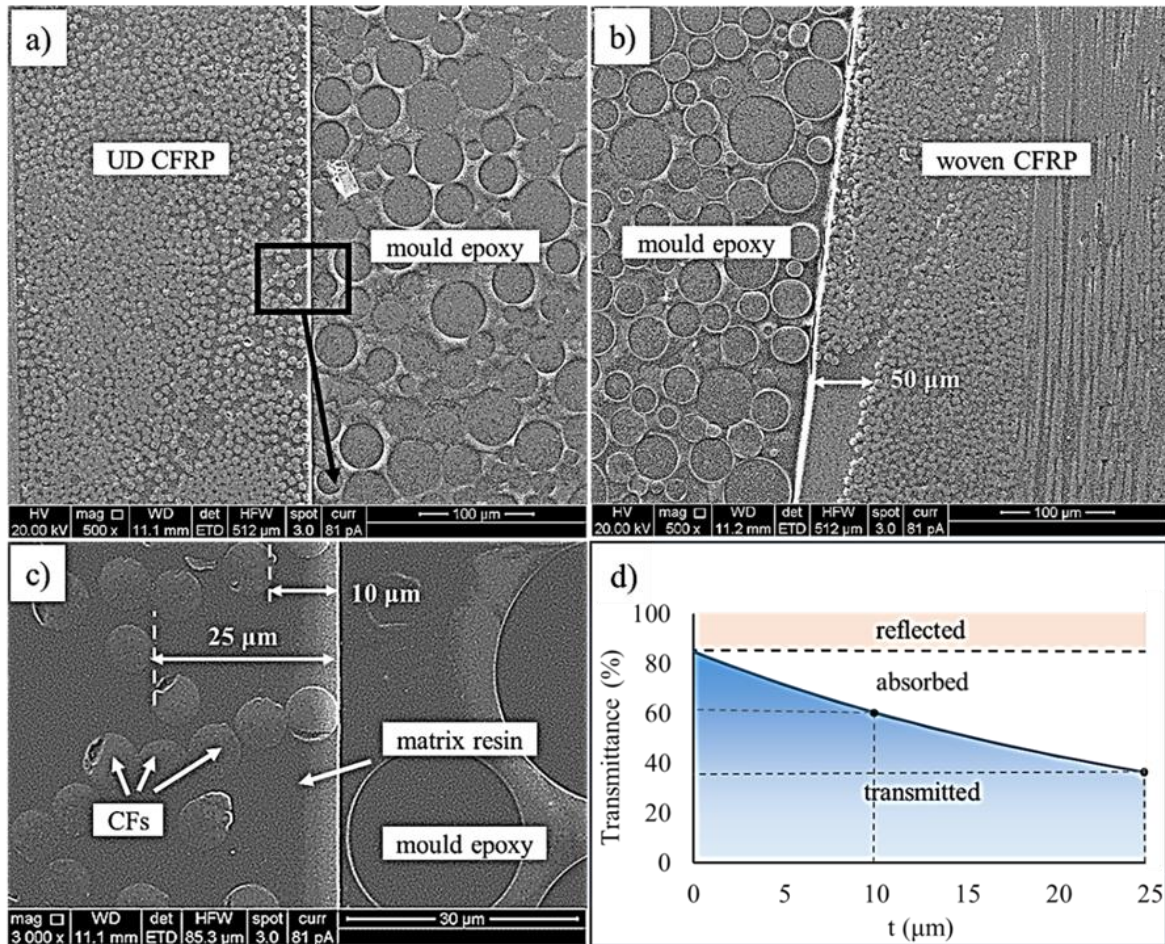


Figure 4.11. (a) SEM images of cross-section of CFRP composites with a) UD and b) woven reinforcements. c) a magnified SEM image of CFRP with UD reinforcement showing the matrix outer layer thickness, and d) A plot illustrating absorbed, transmitted and reflected percentages of CO₂ laser passing through resin film (0-25 μm thickness).

4.5. Conclusions

In this experimental investigation, the transmittance of thermosetting resins to both NIR (1064 nm) and MIR (10600 nm) lasers was examined. For the 1064 nm laser, three different epoxies were tested, revealing penetration depths ranging from 90 to 140 mm and reflection fractions between 11.5% and 13.6%. For the MIR 10600 nm laser, an epoxy resin layer of 15 μm thickness transmits approximately 55% of the laser intensity, while a thickness of 86 μm results in only 5% transmittance. These findings are agreed with some previous research, particularly McKie and Addison's investigation [37]. For NIR laser surface processing of CFRPs, the dominant hypothesis, widely supported by researchers, suggests that the majority of incident light penetrates the outer layer matrix, being absorbed by the underlying fibres, thus inducing matrix removal through heat conduction from the laser-induced fibres. Conversely, for MIR laser processing, previous studies primarily assumed that MIR laser is absorbed by the epoxies

at the surface. However, our investigation suggests a different mechanism. It is proposed that approximately 60% of the light is transmitted and absorbed by the fibres. This results in matrix ablation through a combination of direct evaporation of the matrix and heat conduction at the fibre-matrix interface via the laser-induced fibres.

CHAPTER 5: Laser Surface Processing of Woven Reinforced CFRP Composites to Improve Adhesive Bonding Using NIR ns Pulsed Fibre Laser.

5.1. Introduction

Laser surface treatment is widely recognised as a promising technique for enhancing the adhesive strength of CFRP joints. It offers several advantages, including a dry, non-contact process that can be precisely controlled at high speeds. Fibre lasers, which typically emit in the NIR range, particularly around 1µm wavelength, hold a specific advantage over other types of lasers. This advantage stems from their delivery mechanism, where the laser beam is transmitted via a typical fibre optic cable, eliminating the need for a lot of mirrors to guide the laser beam. This feature makes fibre lasers more easily adaptable for implementation in robotic machines and automated systems [296, 297]. Some researchers have rejected the use of NIR lasers for surface treatment of CFRPs due to difficulties arising from the high transmittance of the matrix resin at wavelengths around 1 µm [15]. These difficulties increase when treating woven reinforced CFRPs due to the variation in outer layer matrix thickness. However, the surface treatment of CFRPs using NIR lasers remains a subject of extensive research [17, 26, 27, 29, 298-300].

This chapter outlines an investigation utilising a NIR ns pulsed fibre laser for surface treatment of woven reinforced CFRP materials to enhance adhesive bonding. A mask made from cardboard was utilised to prevent thick matrix areas from being exposed to the laser radiation. Prior to this investigation, initial exploratory trials were conducted to establish a foundational knowledge base, complemented by a review of the literature serving as a starting point for subsequent experiments.

Laser surface treatment for improving adhesive bonding is often termed "texturing" in the literature [271, 298, 299, 301, 302], involving selective laser ablation of the material at the surface and the creation of micro or nano-scale dimples, grooves, or texture using laser beams [303, 304]. However, using NIR lasers for CFRP treatment typically removes the entire outer matrix layer. Thus, "treatment" seems to fit better than "texturing," as it refers to the process of exposing CFs rather than creating patterns in the matrix.

5.2. Objectives

- **Understanding the Effect of NIR ns Pulsed Laser Treatment:** Investigate the impact of NIR ns pulsed laser treatment of woven reinforced CFRPs and analyse how different processing variables affect the resulting responses.
- **Optimising processing variables to maximise the area of exposed fibres while ensuring minimal damage to the fibres.**
- **Utilising Masking Techniques:** Employ masking techniques to selectively expose shallow matrix regions to the laser while protecting rich matrix regions from laser radiation and compare the adhesive bonding strength among different surface conditions, including laser treatments with and without masking.

5.3. Experimental design and workflow

Investigations into laser processing of materials typically involve multiple stages of parameter optimisation, such as adjusting pulse variables and scanning strategies based on the outcomes of previous stages. Moreover, factorial experimental designs are used to study multiple variables simultaneously, enhancing understanding of their interactions and improving the reliability and accuracy of results. This approach also reduces the number of trials [305], and accordingly the experimental time and cost.

The study in this chapter involves two main experimental parts. In the first part, a factorial experiment with multiple processing variables was utilised to optimise the input variables, followed by various surface assessments. Removal of matrix resin at the surface and exposing as much as possible CFs with minimal damage was used as a standard for the optimisation process of the laser inputs. Different techniques and equipment were used for surface assessment. The second part involves mechanical testing of the adhesive bonding strength. In this phase, a masking technique was employed, and the adhesive bonding was compared among different surface conditions. Prior to the main experiment, several exploratory trials were conducted, two of which are detailed in the following section. These trials, along with insights from the literature, particularly the studies by Schweizer et al. [26] and Reitz et al. [27], who utilized laser systems with similar characteristics (wavelength, pulse frequency, and pulse length) to those used in this study—provided a foundational starting point. The experimental design and stages of these investigations are summarised in the flow chart presented in **Figure 5.1**.

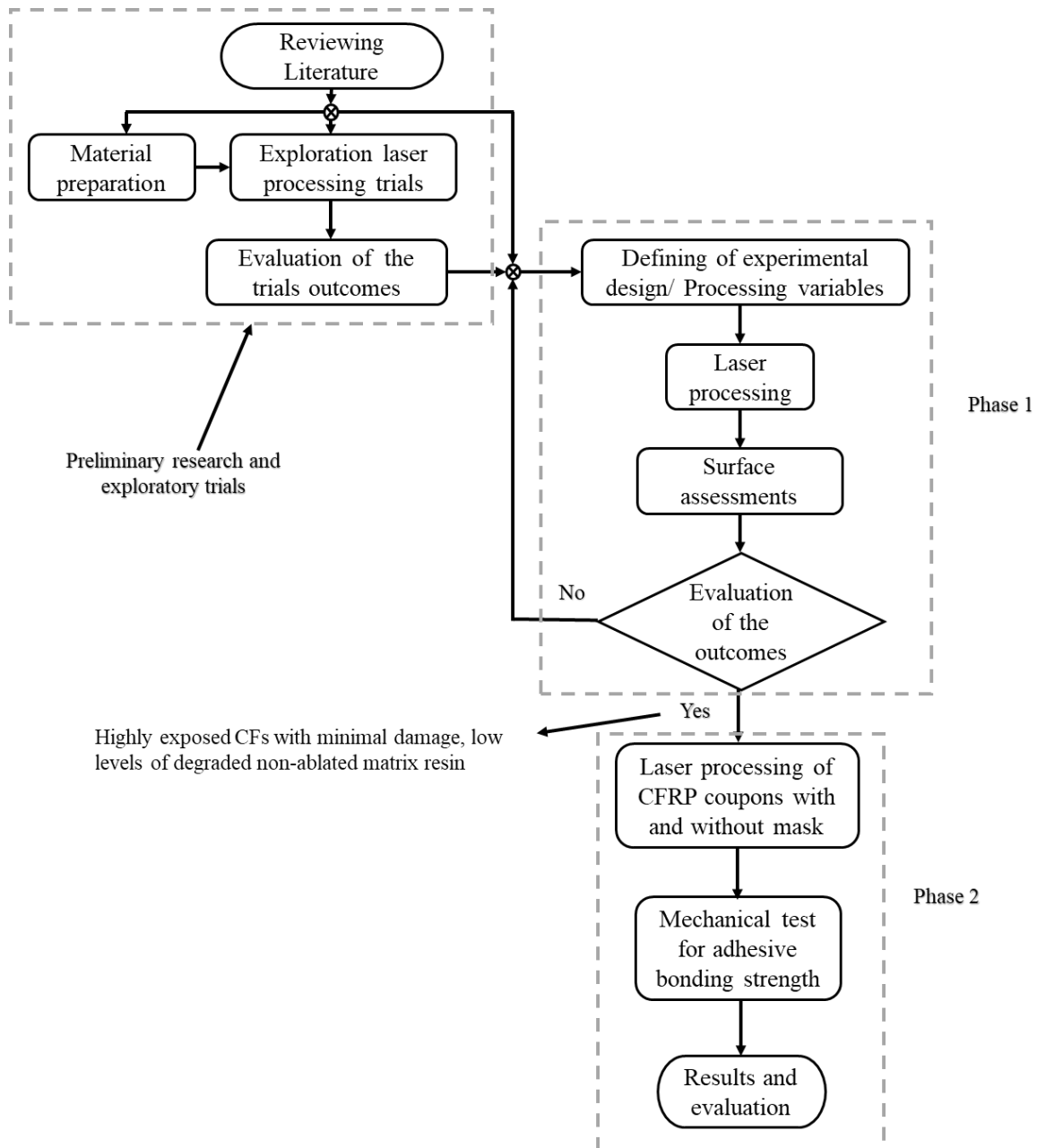


Figure 5.1. Flowchart simplifies the experimental design, steps, and phases

5.4. Exploration trials

Several exploratory trials of laser surface treatment of CFRPs were conducted before the main experiments. The SPI ns pulsed NIR fibre laser was employed, and various CFRP materials were tested. The details and main outcomes of two of these trials are briefly outlined below.

For the first trial, the CFRP material was reinforced with bidirectional woven CFs. Four samples were subjected to laser processing using a (2 factors x 2 levels) factorial experiment. The pulse energy (E_p) and the hatch spacing (H) were varied at two levels as depicted in **Table 5.1**.

Table 5.1. Pulse Energy and Hatch Spacing Levels of the first exploration trial.

| Level | E_p (mJ) | H (μm) |
|-------|------------|---------------------|
| 1 | 0.1 | 30 |
| 2 | 0.4 | 50 |

The pulse length (τ) and the PRF were 200 ns and 25 kHz respectively, the scanning speed (v) was 1000 mm/s and was unidirectional scanning. **Figure 5.2** (a) shows a macro photo of the CFRP sample during laser processing. **Figures 5.2** (b), (c), and (d) represent optical microscopy images of the sample in its original state and after laser treatment with low and high pulse energies, respectively. Note that for both laser-treated samples in **Figure 5.2**, the hatch spacing was 30 μm .

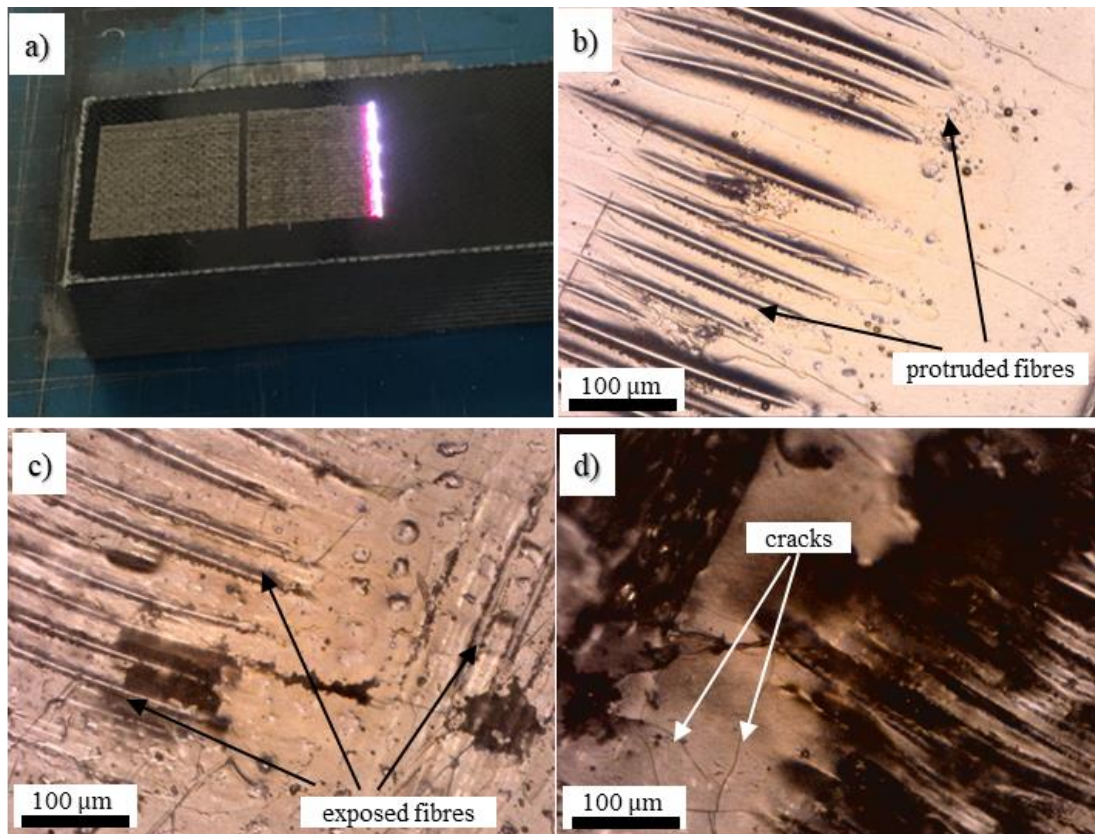


Figure 5.2. a) CFRP material of the first trial under laser processing, optical microscopy images of b) an as-received sample, c) treated with the low pulse energy, d) treated with the high pulse energy.

From this trial, it was concluded that utilising low pulse energy with this material can only ablate the shallow matrix covering the protruded fibres, **Figure 5.2** (c). Conversely, high pulse energy induced significant changes in the surface, as depicted in **Figure 5.2** (d), although thick matrix regions remained intact, exhibiting only cracking. Regardless of the matrix thickness, the laser radiation is absorbed by the underlying carbon fibres due to the high transmittance, as

discussed in **Chapter 4/ Section 4.3**. However, the thicker matrix likely resists the removal process (spalling or chipping). Moreover, no significant changes were observed between the two different hatch spacings utilised.

The second laser exploratory trial employed a (3 factors x 3 levels) factorial design. The CFRP material has a glossy face and was reinforced with 4 Harness Satin (4HS) weave CFs. In a 4HS weave, a warp passes over 3 wefts, while the 4th weft passes over the warp. On the CFRP surfaces, this results in the creation of elliptical shapes (similar to rice grains), representing the warp segments passing above the 3 wefts, and circular shapes, representing the weft segments intersecting above the warp.

The pulse length (τ) and pulse repetition rate (PRF) were 200 ns and 25kHz, respectively, whereas the pulse energy (E_p), the hatch spacing (H), and the scanning speed (v) were varied at 3 levels. The scanning was unidirectionally, aligned with the dominant fibre tows (warp).

Table 5.2 represent the three varied parameters and their levels.

Table 5.2. Pulse Energy, hatch Spacing, and scanning speed Levels of the second exploration trial.

| Level | E_p (mJ) | H (μm) | v (mm/s) |
|-------|------------|---------------------|----------|
| 1 | 0.1 | 30 | 600 |
| 2 | 0.13 | 40 | 800 |
| 3 | 0.17 | 50 | 1000 |

The 27 processing conditions were all conducted on a single CFRP specimen, each is 8 mm x 8 mm as depicted in **Figure 5.3** (a). The samples were assessed using optical microscopy and optical profilometry. Moreover, a wettability assessment using WCA was conducted.

The results indicate that for all processed samples, approximately between 60-80% of the carbon fibres (CFs) at the surface were exposed. This exposure was primarily observed in the elliptical and circular shapes, where the thickness of the outer layer matrix was thin. However, near the intersections between the warps and wefts (at the tips of the ellipses), the matrix layer was much thicker. As a result, it exhibited degradation, cracking, and potential loss of integrity with the fibres, although it was not removed. Samples processed with higher laser mean fluence (achieved through higher pulse energy and/or lower speed or hatch) exhibit wider fibre exposed areas within the ellipses (rice grains), accompanied by larger regions of degraded (cracked) non-removed matrix and damaged (breakage) CFs, particularly at the tips of the ellipses (**Figure 5.3** c, d, and f). The macro photo in **Figure 5.3** (e) highlights the degraded regions with arrows. Samples processed with the lowest scanning speed and hatch (600 mm/s and 30

μm , respectively) show severe carbon fibre damage. In general, matrix damage or cracking and fibre breakage were observed to be significantly higher in areas where the fibre orientation aligns with the direction of the laser scanning. This is likely due to the higher heat input to the CFs [26]. For this reason, scanning in the direction of the CFs is avoided in some previous studies [26, 27]. The WCA assessment for all laser-treated samples was less informative, as the water droplets were confined by the degraded matrix or fibres at the boundary of the fibre-exposed regions, limiting their spreading, see **Figure 5.3** (b).

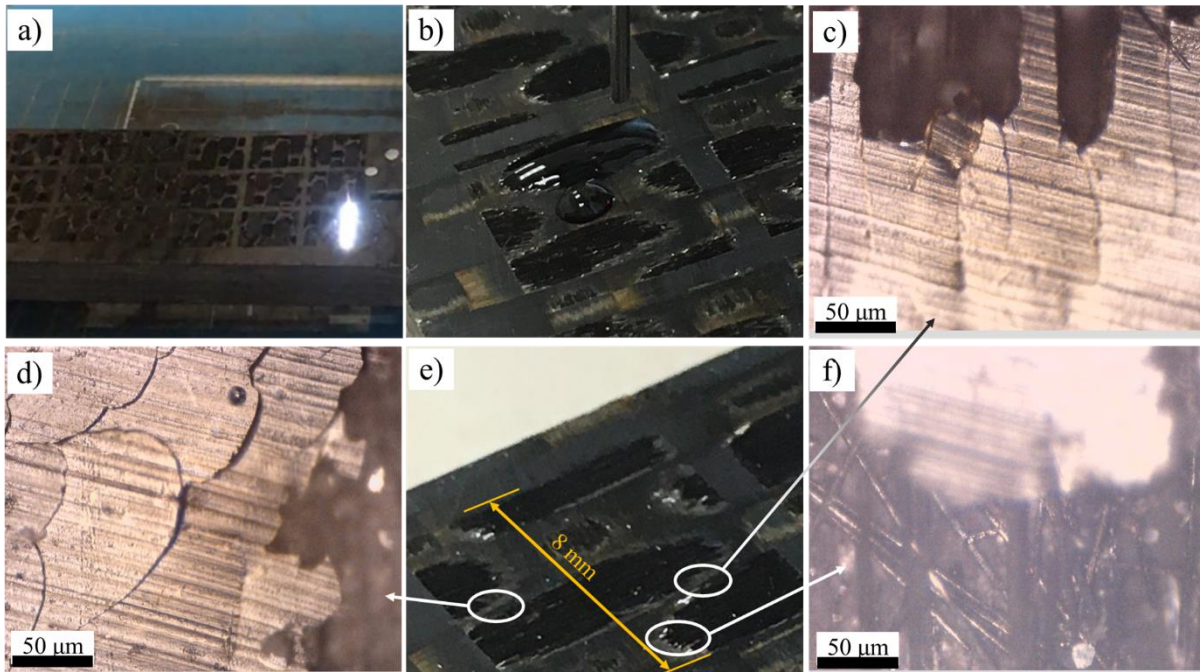


Figure 5.3. (a) macro photograph of the CFRP specimen. (b), (c), (d), and (f) Optical microscopic images highlighting the degraded regions of the matrix or the carbon fibres. (e) Macro photograph indicating the degraded regions with arrows.

Figure 5.4 (a) shows a 3D profilometric image of nine samples processed using a pulse energy of 0.1 mJ and variable scanning speeds and hatch spacings stitched together to illustrate the effects of varying scanning speed and hatch spacing. **Figure 5.4** (b) shows a 3D profilometric image of a sample processed with a pulse energy of 0.1 mJ, a hatch spacing of 30 μm , and a scanning speed of 1000 mm/s. The profilometric images clearly revealed that a significant portion of the outer matrix layer remained intact, with a considerable amount degraded and forming a thin layer above the original surface of the sample.

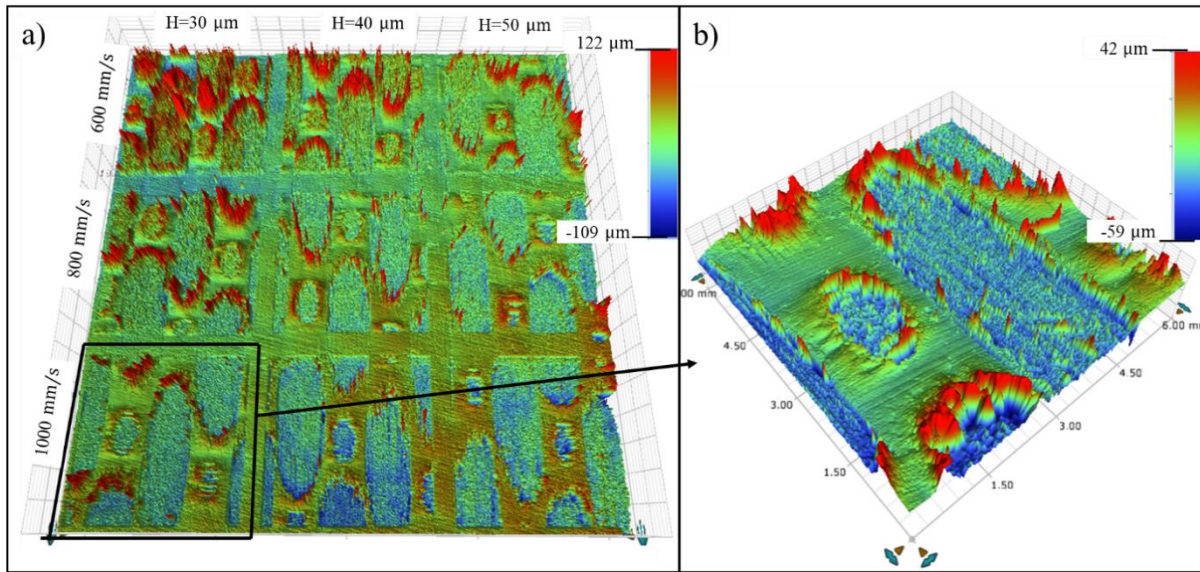


Figure 5.4. (a) 3D profilometric image of nine samples processed with a pulse energy of 0.1 mJ, stitched together. The hatch spacing and scanning speed are indicated at the top and the left side. (b) 3D profilometric image of a sample processed with a pulse energy of 0.1 mJ, a hatch spacing of 30 μm , and a scanning speed of 1000 mm/s.

5.5. The main study, laser surface treatment of woven reinforced CFRPs to improve adhesive bonding using a mask

In this study, a novel technique (partial laser treatment using a mask) is employed for laser texturing of CFRP surfaces with woven outer reinforcement to improve adhesive bonding. using the 20 W SPI ns pulsed fibre laser, the full description is available in **Chapter 3/ Section 3.2.1**.

The previous experimental trials (**Section 5.4**) revealed that laser processing of woven reinforced CFRPs, where the thickness of the outer matrix layer varies significantly due to the wavy nature of the reinforcement, results in a pattern of exposed fibre regions and retained weakened matrix regions. To avoid surface weakening, a partial surface treatment approach using a masking technique was implemented. The masks were made from 0.3 mm cardboard. This method treats CFRPs by exposing the fibres in regions where the outer matrix layer is shallow while preventing laser exposure to regions rich in matrix resin, thereby protecting the latter from being degraded or damaged. Additionally, this technique can introduce a mechanical interlocking feature, enhancing bonding strength by creating surface topography variations between the laser-exposed and masked areas. The bonding strength of partially laser-treated samples was assessed using SLS tests and compared to samples with several other surface conditions, including full laser surface treated, mechanical abraded, and untreated surfaces. The results demonstrated that the partially treated samples exhibited the highest

average failure load, showing over a 10% improvement compared to the fully laser-treated samples. Additionally, they displayed the best repeatability among all the treated samples.

5.5.1. Methods

5.5.1.1. CFRP material

The CFRP material, supplied by Bombardier UK, was 2.8 mm thick and reinforced with 8-Harness Satin (8-HS) weave carbon fibre. At the surface, the warp appeared as rice grains or semi-elliptical shapes, while the weft manifested as small dark semi-rectangular shapes, as depicted in **Figure 5.5** (a and b). A cross-sectional analysis of the CFRP material was carried out to examine the variation in the thickness of the matrix outer layer, providing deeper insights into the material prior to laser processing. For this purpose, a 20 mm x 20 mm sample (**Figure 5.5** c) was embedded vertically in epoxy resin within a mould and polished to a mirror finish, the description of the polishing method is provided in **Chapter 3/ Section 3.4**.

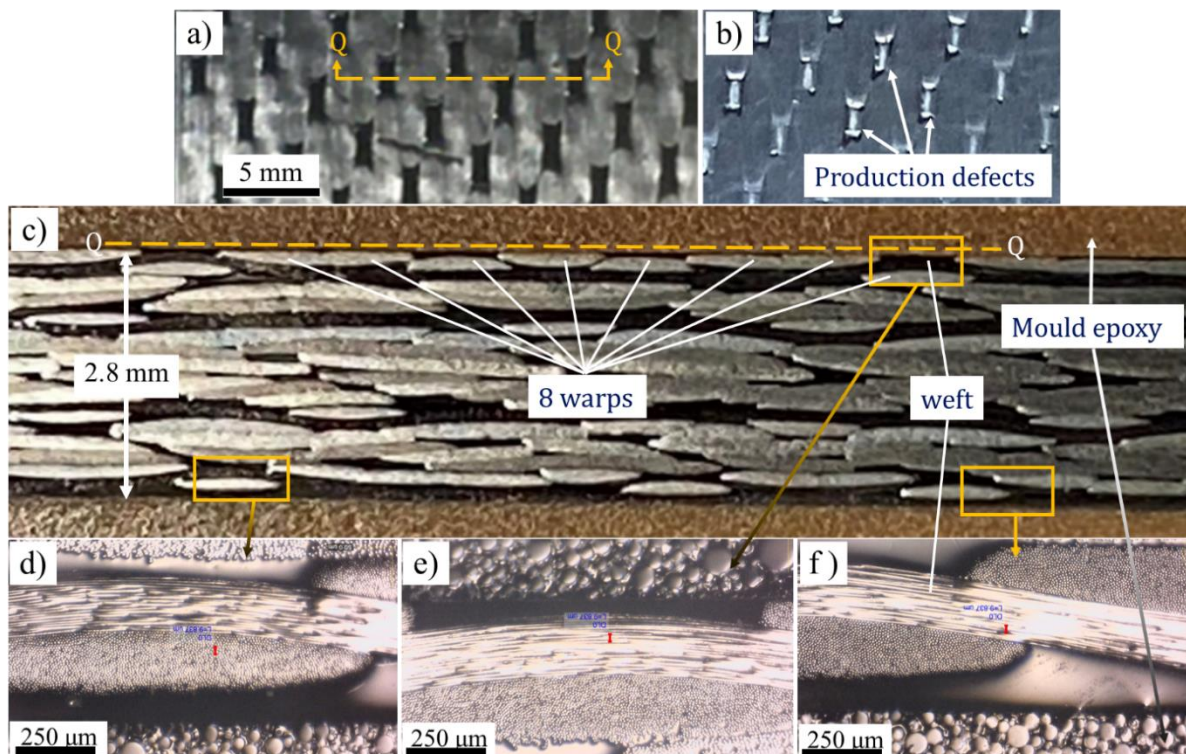


Figure 5.5. (a and b), surface photos of the woven CFRP material captured with two different lighting angles show the carbon fibre weave pattern (8-Harness-Satin) and the production defects, (c) a macro photo shows the cross-section of CFRP sample embedded within epoxy mould, (d, e, and f) optical microscopy images show the variation in the outer layer matrix resin thickness.

It was observed that the matrix outer layer thickness at or near the intersections of fibre tows is up to 200 μm thicker than at the middle of the elliptical shapes belonging to the warp tows, **Figure 5.5** c, d, and f. However, some of the tow intersections were not fully covered with

resin, which are considered as production defects, **Figure 5.5 b**. The warps in **Figure 5.5 c** appear lighter than the wefts due to light interaction with the cut-off fibres.

5.5.1.2 Surface treatment and the optimisation process of the laser variables

The laser processing variables were initially optimised using a factorial experiment. Three variables: pulse energy and scanning speed (varied at three levels each), and hatch spacing (varied at two levels) were examined. The PRF and pulse length (τ) remained fixed throughout the experiments. **Table 5.3** illustrates the factorial experimental design. Notably, the previous experimental trials provide a foundation for determining the current experimental processing variables.

Table 5.3. The factorial experimental design.

| Level | τ (ns) | PRF (kHz) | E_p (mJ) | H (μm) | v (mm/s) |
|-------|----------------|--------------|---------------|------------------------|-------------|
| 1 | 200 | 25 | 0.056 | 25 | 600 |
| 2 | | | 0.092 | 40 | 800 |
| 3 | | | 0.124 | | 1000 |

The laser scanning was uniaxial perpendicular to the dominant fibre tows (the warps). Optical microscopy, digital microscopy, and optical profilometry (Bruker) were used to assess the processed surfaces. The optimization criteria of the laser variables focused on maximising the laser removal of the outer layer matrix while exposing the underlying CFs with minimal damage. To achieve this, ImageJ colour thresholding processes were employed to estimate the percentages of the exposed fibre areas for the various processing conditions based on the digital microscopy images. The optimised laser processing parameters are detailed in **Table 5.4** below. These parameters were used for treating CFRP coupons with both full and partial laser treatment techniques, which were then compared in terms of adhesive bonding using SLS tests. Furthermore, contact angle assessment was conducted with the sessile droplet method using a *CAM 101 from KSV Instruments Ltd (UK)*. However, the results of the assessment were not as informative as expected. All instruments are described in **Chapter 3**.

Table 5.4. The optimised laser parameters.

| τ (ns) | PRF (kHz) | E_p (mJ) | H (μm) | v (mm/s) |
|----------------|--------------|---------------|------------------------|-------------|
| 200 | 25 | 0.092 | 25 | 800 |

For the partial treatment, cardboard masks (0.3 mm thick) were perforated to match the dimensions of the rice grain-shaped (ellipses) corresponding to the warp fibre tows, with tolerances of about 1 mm and 0.2 mm for the major and minor dimensions of the grains, respectively. The purpose of including tolerance in the mask design was to facilitate the alignment of the mask holes with the elliptical shapes on the material surface, see **Figure 5.6**. These masks were then used to shield regions with thicker matrix resin (around/outside the rice grains) during laser processing. Noting that Galvoscaner-based selective scanning was tested prior to using the mask, the processing was uneven, with significant variations such as unintended overlap or underlap in the processed areas, caused by the acceleration and deceleration of the scanner.

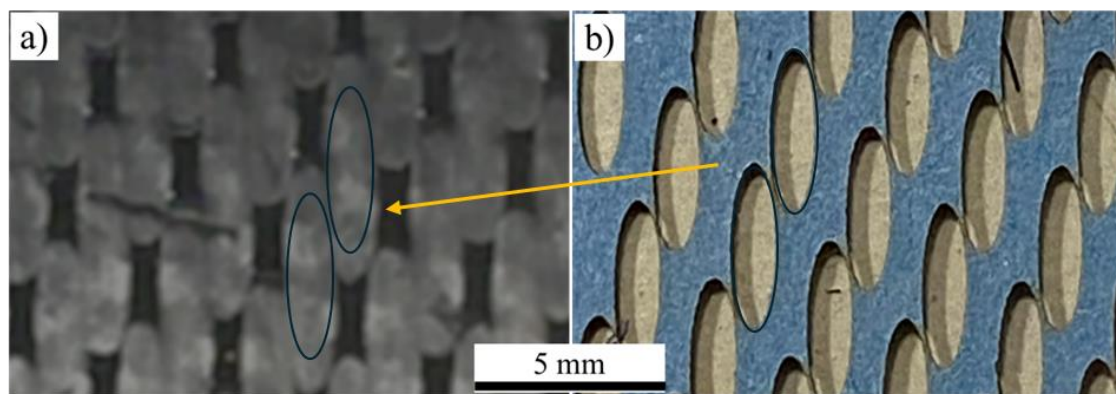


Figure 5.6. Photos of a) the CFRP material and b) the cardboard mask illustrates the alignment of the mask holes within the elliptical shapes at the CFRP surface.

Figure 5.7 (a) depicts a CFRP coupon undergoing laser partial treatment, while **Figures 5.7** (b) and (c) show two CFRP coupons treated using both laser techniques. The perforation of the mask was carried out using the CW CO₂ laser, described in **Chapter 3/ Section 3.2.2**, with a power of 8 W and a scanning speed of 20 mm/s. The selection of 0.3 mm thick cardboard for creating the mask was based on several experimental investigations conducted on various materials. It was found that cardboard with a thickness of 0.3 mm could be machined easily and accurately using a CW CO₂ laser. Additionally, it was observed that this thickness of cardboard was mostly unaffected by the NIR laser parameters range used in this experiment. Furthermore, thicker masks might obstruct or shadow the laser beam.

For the mechanically abraded coupons, a cordless handheld random orbit sander (*Makita DBO180Z*) with paper grit size 320 was used at the slowest speed until the outer glossy layer of the matrix was removed (**Figure 5.7** (d)).

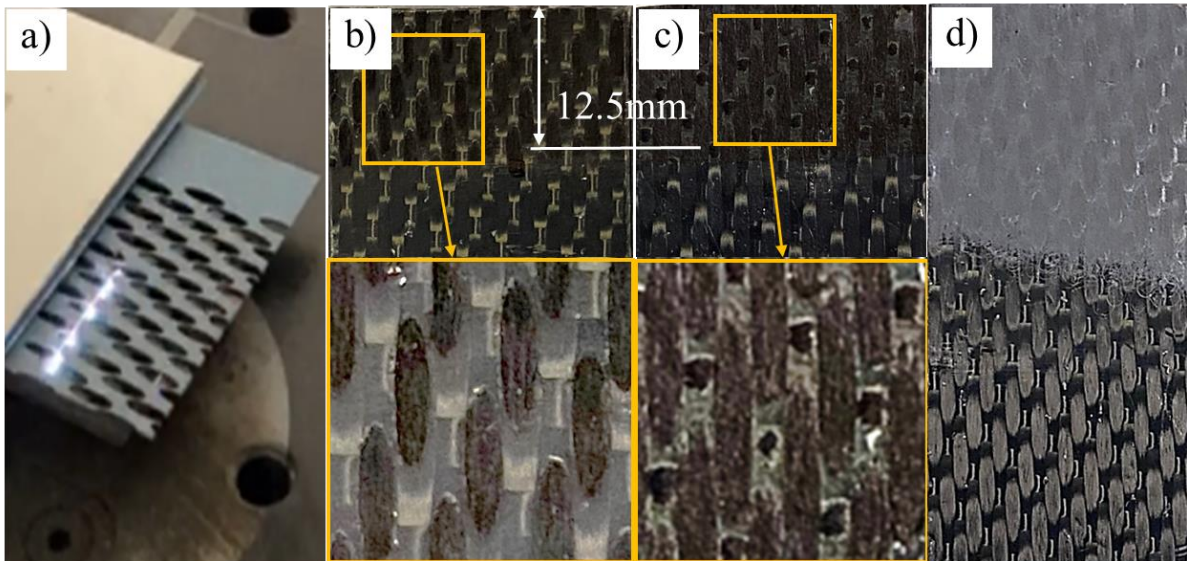


Figure 5.7. Macro photos of (a) a CFRP coupon undergoing laser partial treatment, (b) and (c) two CFRP coupons treated using partial and full laser surface treatment, d). mechanically abraded coupon.

5.5.1.3. Cross-section assessments

In addition to the cross-section assessment provided in the material description (**Section 5.5.1.1**), several other assessments were performed for laser-treated samples and fractured coupons post-mechanical testing. The aim was to evaluate the impact of laser processing on the resin-rich zones. These samples were vertically embedded in mould epoxy and polished. Optical microscopy and SEM were employed to examine the cross-sections. Equipment and polishing methods are described in **Chapter 3/ Section 3.4**.

5.5.1.4. Bonding strength / (SLS) tests

For the mechanical shear tests, coupons were cut using a water-cooled cut-off saw (*Erbauer 750W*) with a diamond cutting blade, resulting in dimensions of approximately 100 ± 1 mm x 25 ± 0.5 mm. Subsequently, all coupons underwent the cleaning procedures outlined in **Chapter 3 Section 3.6**. For both laser treatment techniques, the coupons were cleaned again before undergoing laser treatment. Similarly, coupons subjected to non-laser treatments (mechanical abrasion and non-treated) were also cleaned again using the same procedure before adhesive joining. Five repeated samples were bonded using a special jig for each surface condition and according to BS EN ISO 1465:2009 SLS tests. The adhesive used was Loctite EA9394 AERO Epoxy, and the curing was conducted in an oven for 1 hour at a temperature of 66°C . A tensile testing machine (50 kN *Tinius Olsen*) was employed at a load rate of 1 mm/min. Further details regarding equipment and bonding procedures can be found in **Chapter 3/ Section 3.5**.

5.5.2. Result and discussion

5.5.2.1. Optimisation of the laser variables

Based on colour thresholding estimations (**Figure 5.8**), the laser optimisation processes revealed that processing with the highest specific energy (pulse energy 0.124 mJ, scanning speed 600 mm/s, and hatch spacing of 25 μm) resulted in the highest percentage of fibre-exposed areas (about 93%). However, samples treated with a pulse energy of 0.124 mJ and/or scanning speed of 600 mm/s showed damage (breakage) to the CFs at various locations, mainly at the intersected weft tows, where the scanning is aligned with the orientation of the fibres [26], but also within the elliptical shapes. Conversely, processing with the lowest pulse energy (0.056 mJ) and/or the highest scanning speed (1000 mm/s) produced significant amounts of degraded matrix resin that remained unrecovered (cracked, chipped). The narrow hatch spacing resulted in a reduction in the amount of degraded non-removed matrix chips with no significant effect on the CFs. **Figure 5.9** illustrates the damaged CFs and the degraded, non-removed matrix resulting from varying processing variables.

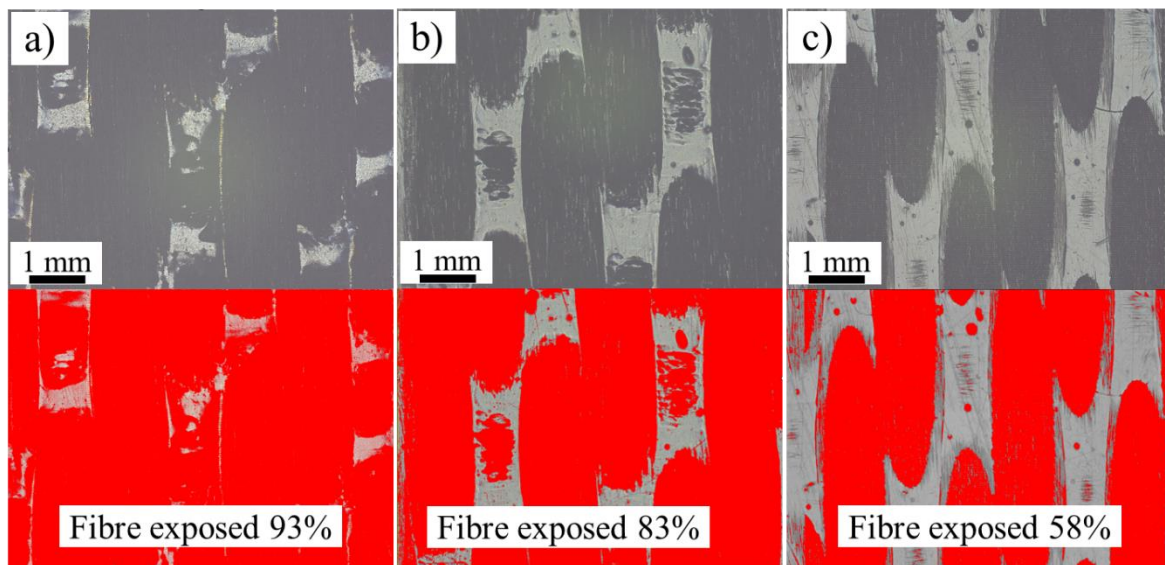


Figure 5.8. Low magnified digital microscopy images and their ImageJ corresponded colour adjusted images of a) fully laser treated sample using $E_p = 0.124$ mJ, $S_{sc} = 600$ mm/s, $H = 25$ μm , b) fully laser treated sample using $E_p = 0.092$ mJ, $S_{sc} = 800$ mm/s, $H = 25$ μm , and c) partially treated samples using $E_p = 0.092$ mJ, $S_{sc} = 800$ mm/s, $H = 25$ μm .

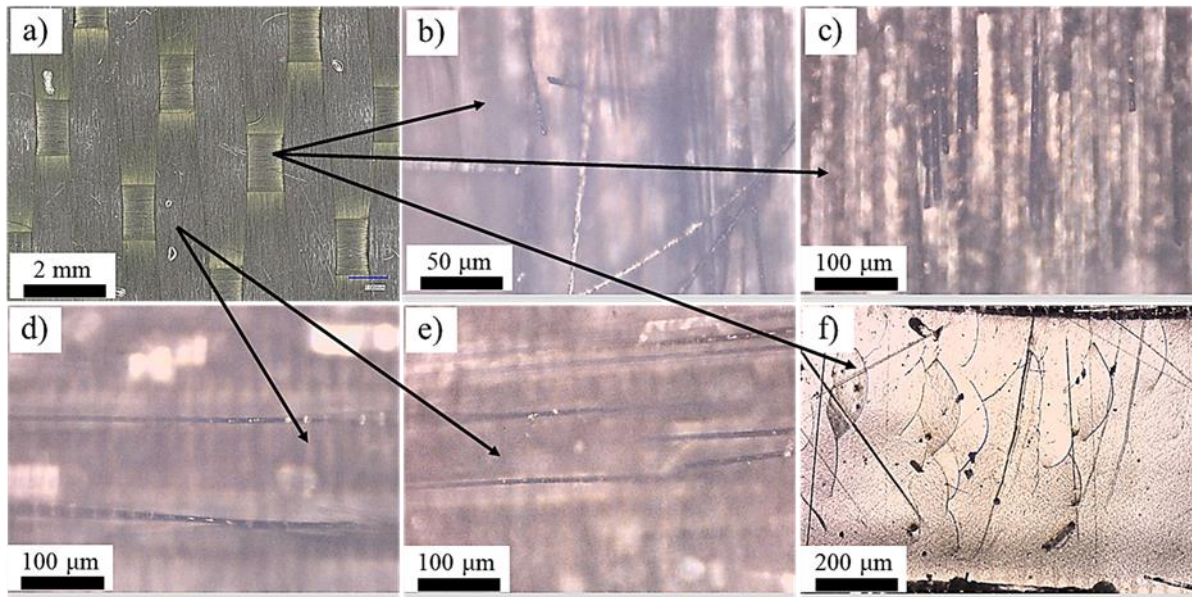


Figure 5.9. a) Low-magnification digital microscopy image of an as-received sample with arrows indicating the positions of the broken CFs and the degraded non-removed matrix on laser-treated samples. b-f) Optical microscopy images of samples treated using different processing parameters: b) $E_p = 0.124$ mJ, $v = 600$ mm/s, $H = 25$ μ m, c) $E_p = 0.092$ mJ, $v = 600$ mm/s, $H = 25$ μ m, d) $E_p = 0.124$ mJ, $v = 600$ mm/s, $H = 25$ μ m, e) $E_p = 0.124$ mJ, $v = 1000$ mm/s, $H = 40$ μ m, f) $E_p = 0.056$ mJ, $v = 1000$ mm/s, $H = 40$ μ m. Note that the optical microscopy images may require to be unfocused to capture damaged fibres.

As the optimization process primarily aimed to increase the percentage of the removed matrix while minimising damage to the CFs, processing with a pulse energy of 0.094 mJ, scanning speed of 800 mm/s, and hatch spacing of 25 μ m achieved the removal of about 83% of the matrix at the surface with minimal CF damage. These parameters which were utilised for full laser treatment, resulting in 58% exposure for the partial laser treatment. Consequently, these optimised laser parameters were applied to process the CFRP coupons for subsequent adhesive bonding tests, **Figure 5.10**. Notably, variations in the processing parameters for the partial laser technique revealed little to no differences in the percentage of fibre-exposed areas.

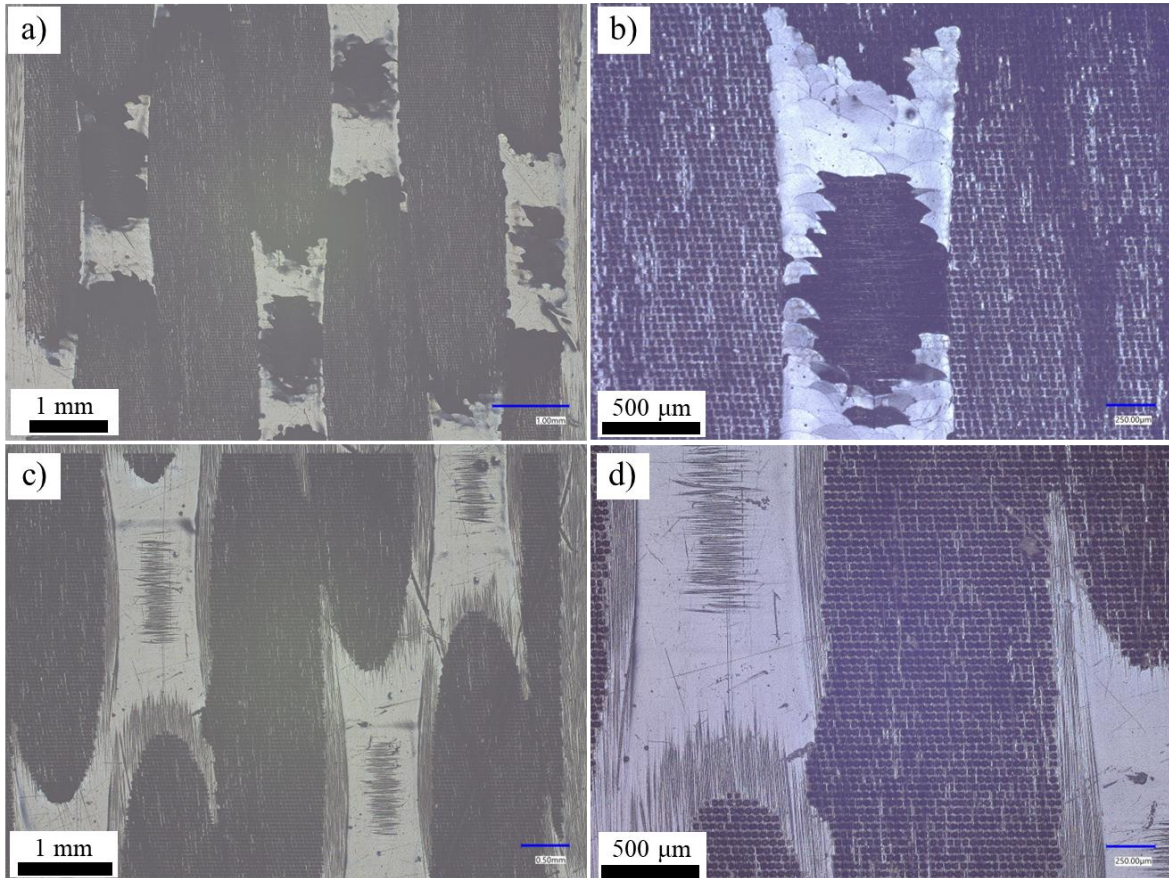


Figure 5.10. Digital microscopy images captured at different magnifications (a and b) for a fully laser-treated sample and (c and d) for a laser partially treated sample, utilising the optimised laser variables.

Regarding the mechanical surface abrasion treatment, optical microscopy assessment shows that the CFs were mostly exposed; however, the CFs were fragmented or damaged. See the optical microscopy images in **Figure 5.11** below.

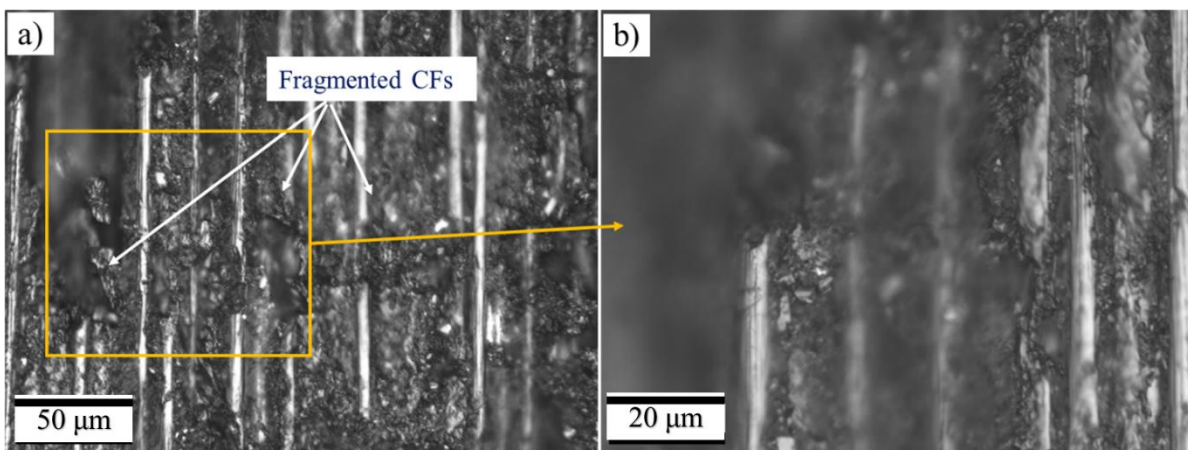


Figure 5.11. Optical microscopy images of a mechanically abraded CFRP sample with two different magnifications showing CF breakage.

5.5.2.2. Optical profilometry assessment

The optical profilometry evaluation of both laser-treated and non-treated CFRP samples revealed notable topographical variations, as depicted in **Figure 5.12**. Specifically, the surface of the non-treated sample, shown in **Figure 5.12** (a), displayed non-flat features that closely resembled the wavy nature of the underlying reinforcement (fibre tows). It predominantly exhibited a pattern of crests and valleys with varying heights, though some regions of the surface appeared relatively flat, indicating areas with a dense matrix resin content. Regarding the optimised laser processing parameters, depicted in **Figure 5.12** (b) and (c) for fully and partially treated samples, respectively, visible differences were observed. However, the irregular surface topography of the non-treated sample limited the depth of insights gained from assessing laser-treated samples, regardless of whether masks were utilised. **Figure 5.12** (d), (e), and (f) further underscored this limitation through the 3D images of laser fully treated samples employing the same scanning speed and hatch spacing but varying pulse energies: 0.124, 0.092, and 0.056 mJ, respectively. The surface height differences seem mostly noticeable with the highest pulse energy, indicating significant delamination of the matrix above the original surface (peeled or separate from the surface but remained partially attached).

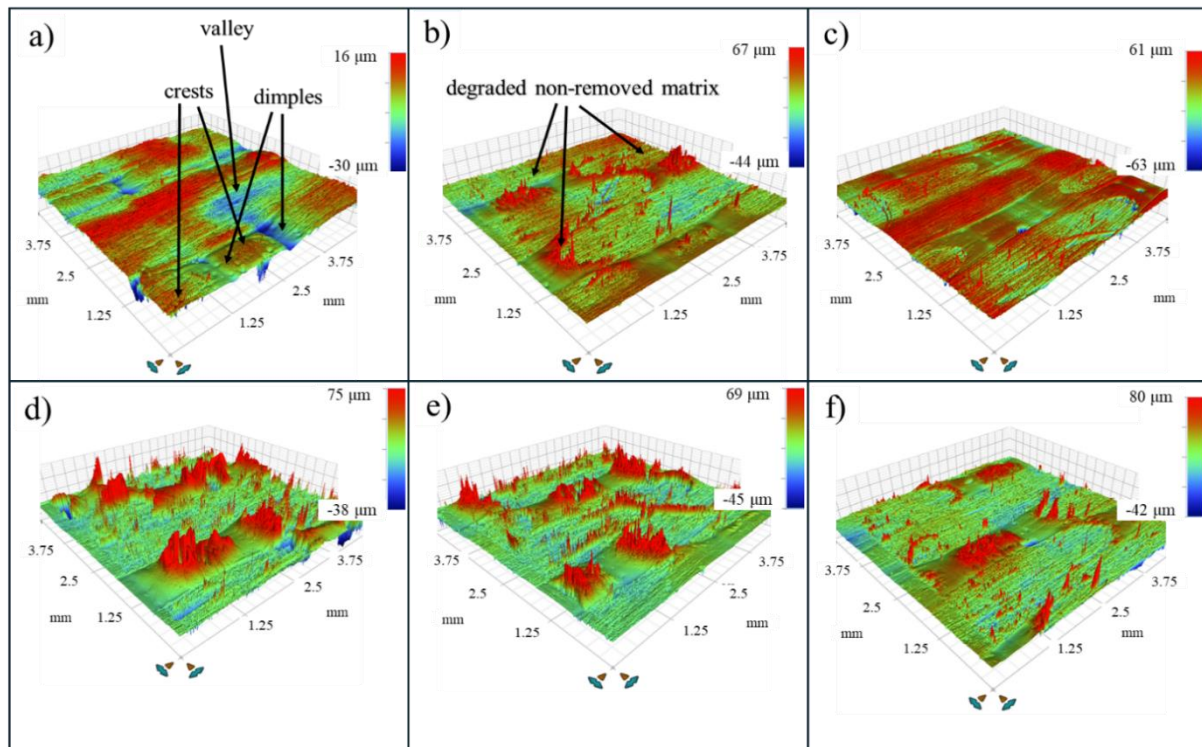


Figure 5.12. 3D optical profilometric images of a) an as-received sample, b) and c) laser fully and partially treated samples, respectively, using $E_p = 0.092$ mJ, $v = 800$ mm/s, $H = 25$ μ m. d), e), and f) laser fully treated sample using the same $v = 600$ mm/s and $H = 25$ μ m but variable $E_p = 0.124$, 0.092, and 0.056 mJ, respectively.

5.5.2.3 Cross-section assessment

Cross-section analysis of the non-treated and laser-treated samples was assessed using optical microscopy and SEM. **Figures 5.13 and 5.14** display images obtained from both techniques, focusing on regions with rich matrix resin and those affected by laser treatment. **Figure 5.13** (a) and (b) show two positions of the cross-section of a non-treated sample with rich matrix zones. **Figure 5.13** (c), (d), (e), and (f) represent optical microscopy images of the laser treated sample. The ablation of the shallow matrix zone, **Figure 5.13** (c), is evident. However, thicker matrix resin zones appear degraded, peeled, and have lost their integrity with the fibres, although they still remain, **Figure 5.13** (c), (d), (e), and (f). The SEM images of the laser-treated sample (**Figure 5.14** b and c) reveal fragmented matrix particles. It is apparent that the large cracks within these fragmented matrix particles have been filled with mould epoxy, which means that they might be re-integrated with the composite when adhesive bonding is applied. However, micro-cracks still exist. It is worth noting that adhesive bonding epoxies generally have higher viscosity than other epoxies; see the properties of different epoxies provided in **Chapter 3/ Sections 3.3.2 and 3.3.3**. Consequently, the presence of fragmented matrix particles is expected to weaken the bonding strength by acting as contaminants, causing the adhesive to bond to them rather than to the underlying fibres.

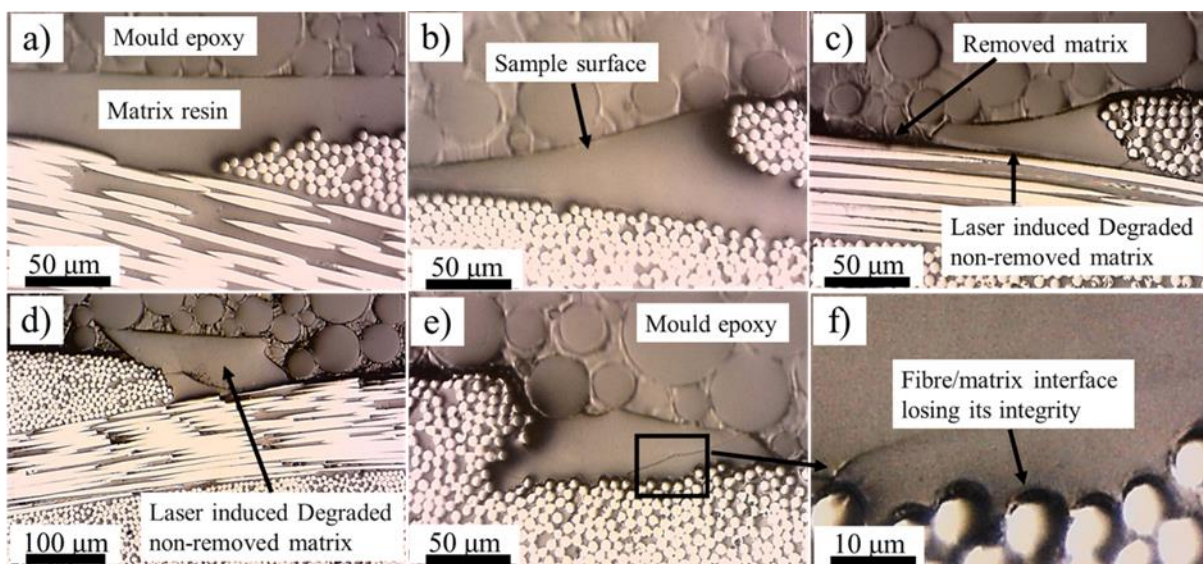


Figure 5.13. Optical microscopy images of cross-section of a) and b) an as-received sample, c), d), e) and f) laser treated sample. The orientations of the samples align with those depicted in the images.

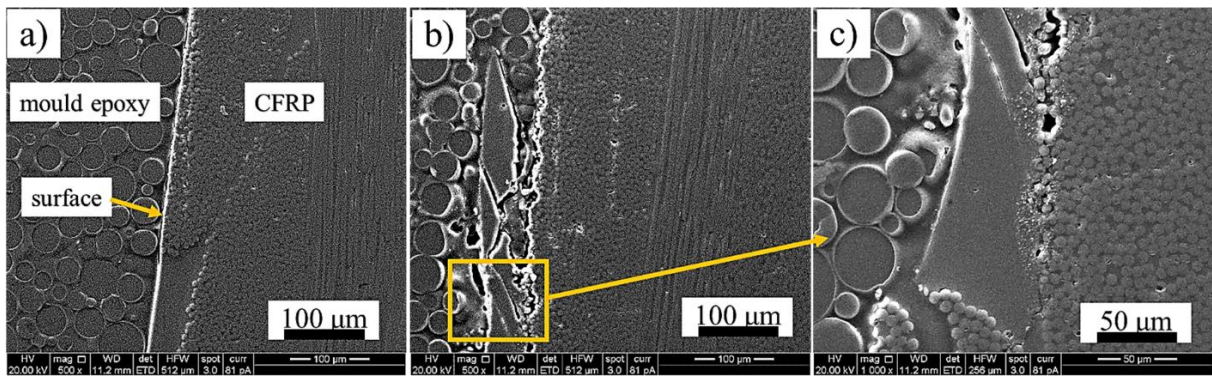


Figure 5.14. SEM image of a) an as-received sample, b) and c) laser treated sample. The tops of the samples are positioned on the left side of the images.

5.5.2.4 Wettability assessment

For this experiment, achieving a reliable comparison of water contact angles among the different processed samples, particularly laser-treated ones, proved challenging. In the case of the non-treated CFRP material, the average contact angles using water and diiodomethane were found to be 57° and 48° , respectively. However, the water contact angles varied widely for the laser-treated samples, ranging between 12° and 70° . This variability was primarily attributed to the presence of large surface variations. The degraded matrix particles constrained the spread of the droplets, resulting in non-circular droplet/sample interfaces. Consequently, the contact angle value was highly dependent on the direction of view of the drop, as illustrated in the photos in **Figure 5.15**. Therefore, it was concluded that obtaining meaningful contact angle values proved to be extremely difficult due to the significant size of the surface heterogeneities [306].

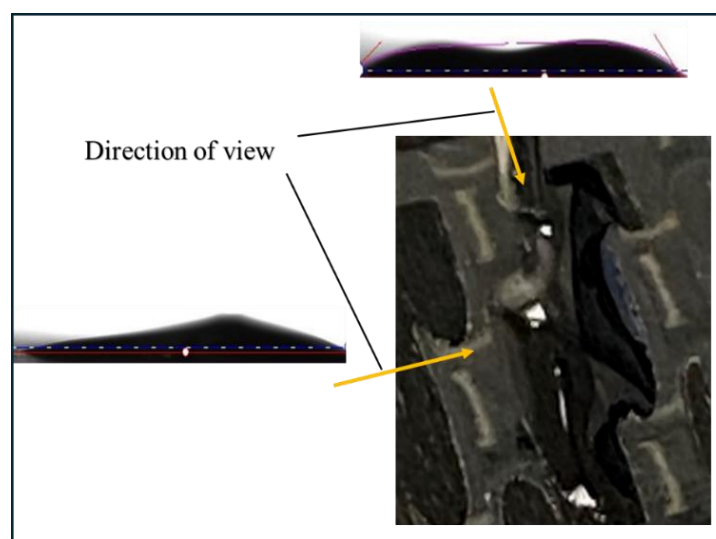


Figure 5.15. A mobile phone photo of a water droplet with two side-view images, captured through the goniometer (contact angle measuring equipment), showing significant variations in droplet shapes and CAs depending on the direction of view.

5.5.2.5 Mechanical test of adhesively bonded coupons

The bar chart in **Figure 5.16** illustrates the averages and SDs of the failure strength of the five repeated samples tested across all treatment conditions. The strength was determined by dividing the failure load by the bonded area (25 mm x 12.5 mm). Notably, the laser partially treated samples (masking technique) demonstrate the highest average failure strength, reaching approximately 21 MPa, with the narrowest range of variation. Conversely, the laser fully surface-treated samples exhibit an average failure strength of around 19 MPa, representing a 10% decrease compared to the partially laser-treated samples. However, their range of variation is notably high, likely attributable to the degraded, non-removed matrix particles believed to act as contaminants. The failure strength for mechanically abraded samples was about 17.3 MPa, and for non-treated samples, it was 13.6 MPa.

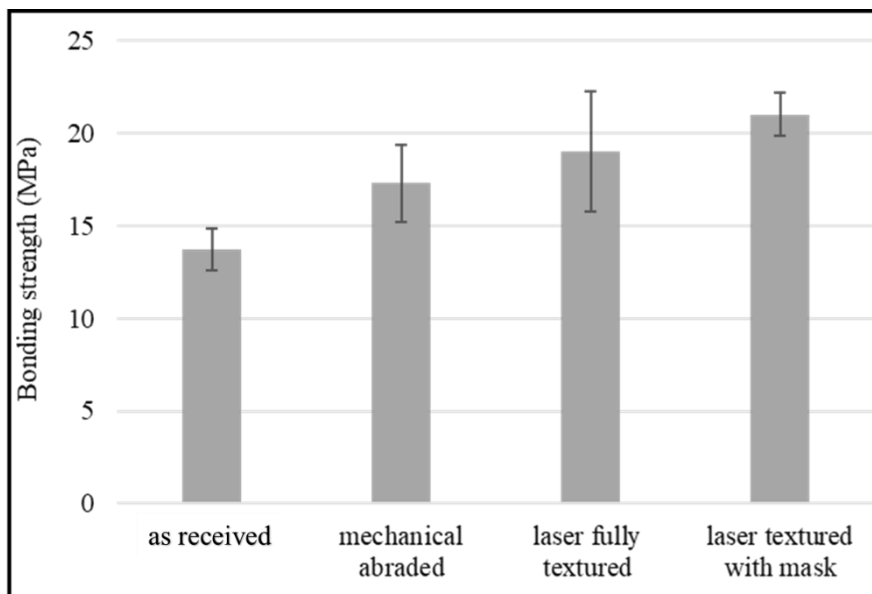


Figure 5.16. The average failure strength and SD across the different treatment conditions.

Figure 5.17 represents the failure modes of different fractured samples. The non-treated samples exhibited 100% Adhesion Failure (AF), occurring at the interface between the bonding adhesive and one of the two coupon surfaces. Mechanically abraded samples also primarily displayed AF failure but with visible broken CF particles within the adhesive layer. These CF particles, chopped during the sanding process, led to a combination of AF and Light Fibre Tear Failure (LFTF). In the laser-treated samples using both techniques, torn fibres were observed, with CFs torn from one coupon and bonded to the adhesive on the other coupon, which indicates LFTF. For laser fully treated samples, degraded or weakened matrix particles were also observed, splattered from one coupon, and adhered to the bonding adhesive on the other

coupon, suggesting a mix of LFTF and Near Surface Substrate Failure (NSSF). Conversely, partial laser treated samples showed a combination of LFTF and AF, with lasered regions exhibiting LFTF and non-lasered regions showing AF.

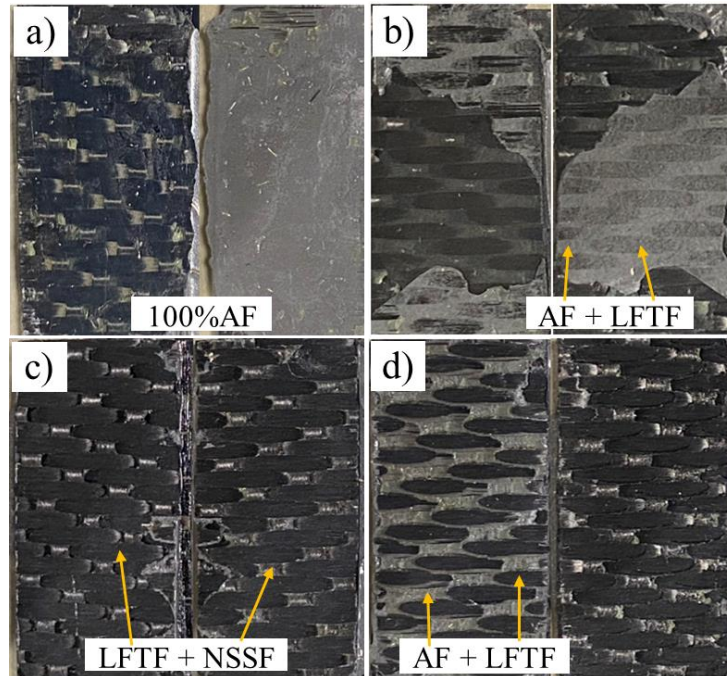


Figure 5.17. Failure modes observed in a) as-received, b) sandpaper-treated, c) fully laser-scanned, and d) laser-treated with mask CFRP samples.

For both laser treatment techniques, the observations mentioned earlier based on failure modes were further verified through fracture analyses of the cross-sections of the failed coupons, as depicted in **Figure 5.18**. The SEM images in **Figure 5.18** (a and b), corresponding to the fully laser-treated sample, reveal that thick matrix resin zones, which lost their integrity with the fibres due to laser irradiation, were torn and remained bonded to the adhesive bonding layer. This suggests that the failure at these regions occurred at the interface between the CFs and the outer layer matrix.

It is believed that the CFs/matrix interface was weakened by the laser treatment. The torn matrix layer is estimated to range between 30-50 μm and was distinguished from the bonding adhesive layer by conducting elemental analysis (**Figure 5.19**), which revealed the presence of aluminium powder within the adhesive. According to literature, metal powder is added to structural adhesives to improve their mechanical or thermal properties [307]. For the partially laser-treated coupon, **Figure 5.18** (c and d), no torn matrix was observed. Instead, the fracture analyses revealed a combination of torn fibre (LFTF) and AF, (matrix/adhesive interface failure).

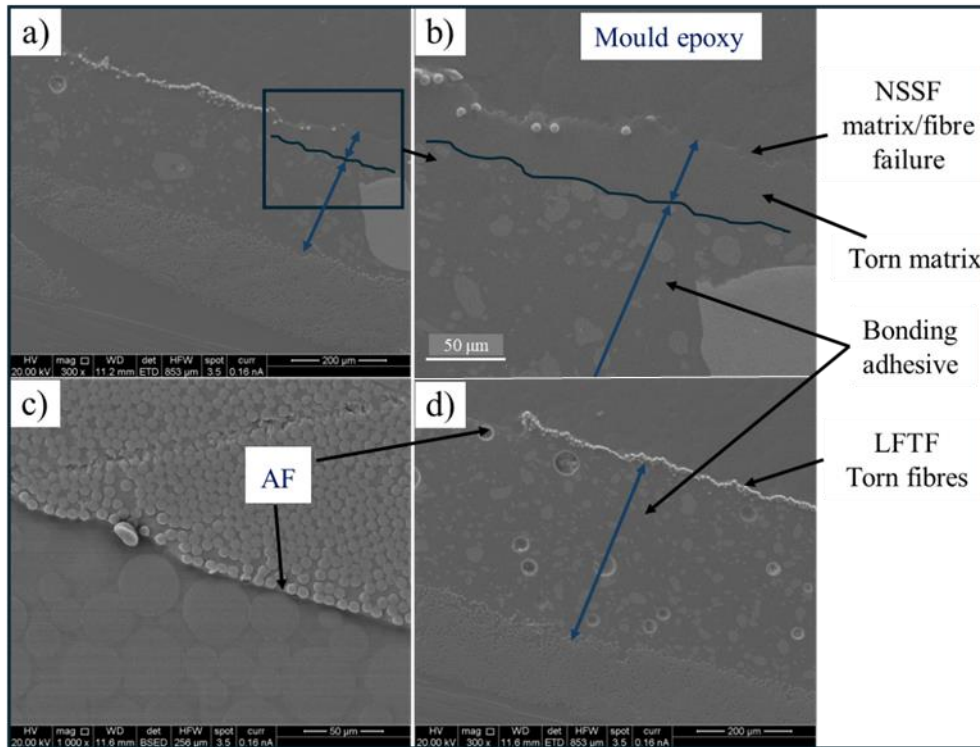


Figure 5.18. Fracture analysis clarifies the different failure modes associated with two laser processing techniques: a) and b) laser fully treated coupon, c) and d) laser partially treated coupon.

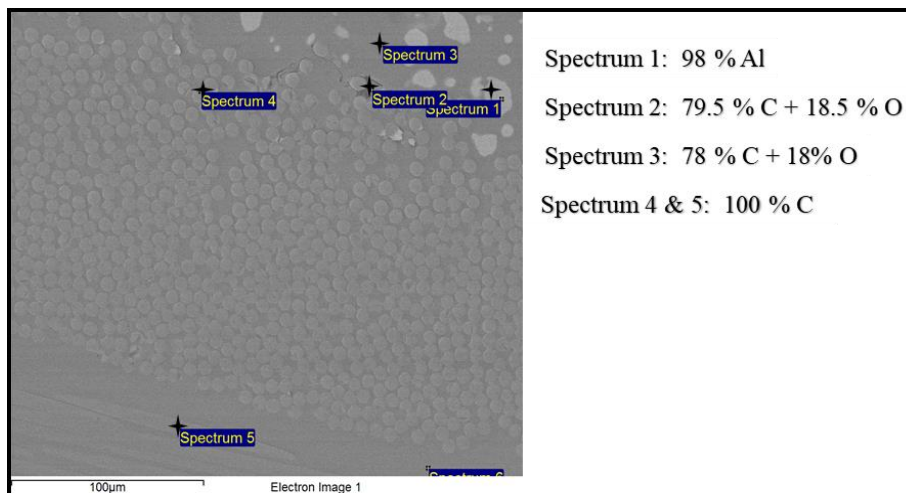


Figure 5.19. Elemental analysis reveals the presence of aluminium powder within the adhesive bonding.

For a deeper insight into the various failure modes observed in this study, considering the adhesive joint as a chain, failure occurs at its weakest link. The schematic diagram in **Figure 5.20** below illustrates the different failure modes based on this concept. It is important to note that the failure modes in this study were mixed, as previously stated.

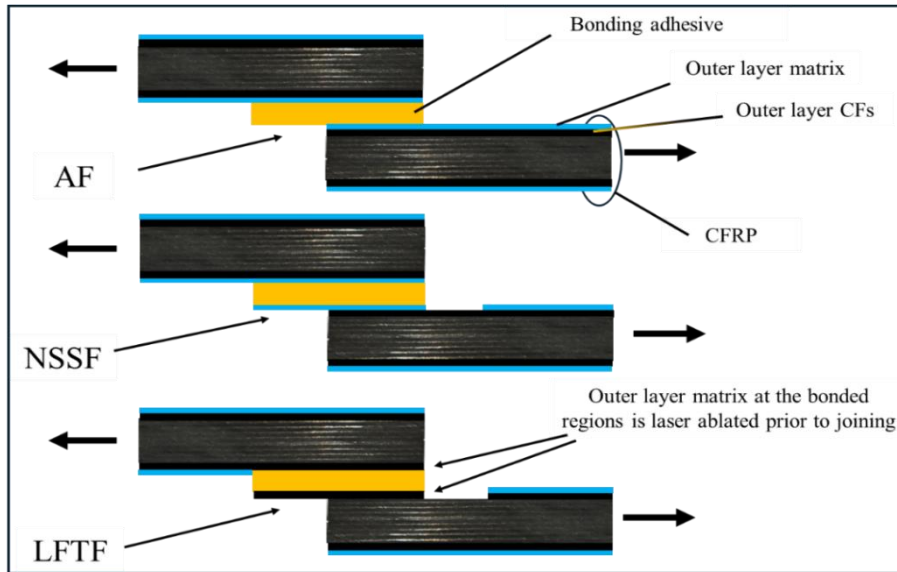


Figure 5.20. Schematic diagram illustrates the different failure modes experienced in the current study.

Comparing the two laser techniques, the mechanisms behind the higher failure loads in partially treated samples suggest that the unaffected matrix regions contribute to the bonding strength in two ways: first, they bear part of the load, and second, they add macro-mechanical key interlocking. In contrast, for fully laser-scanned samples, the degraded, peeled-off matrix fragments are believed to bear no load and instead cause concentrated stresses that reduce bonding strength and lead to less repeatable outcomes. The schematic in **Figure 5.21** illustrates this.

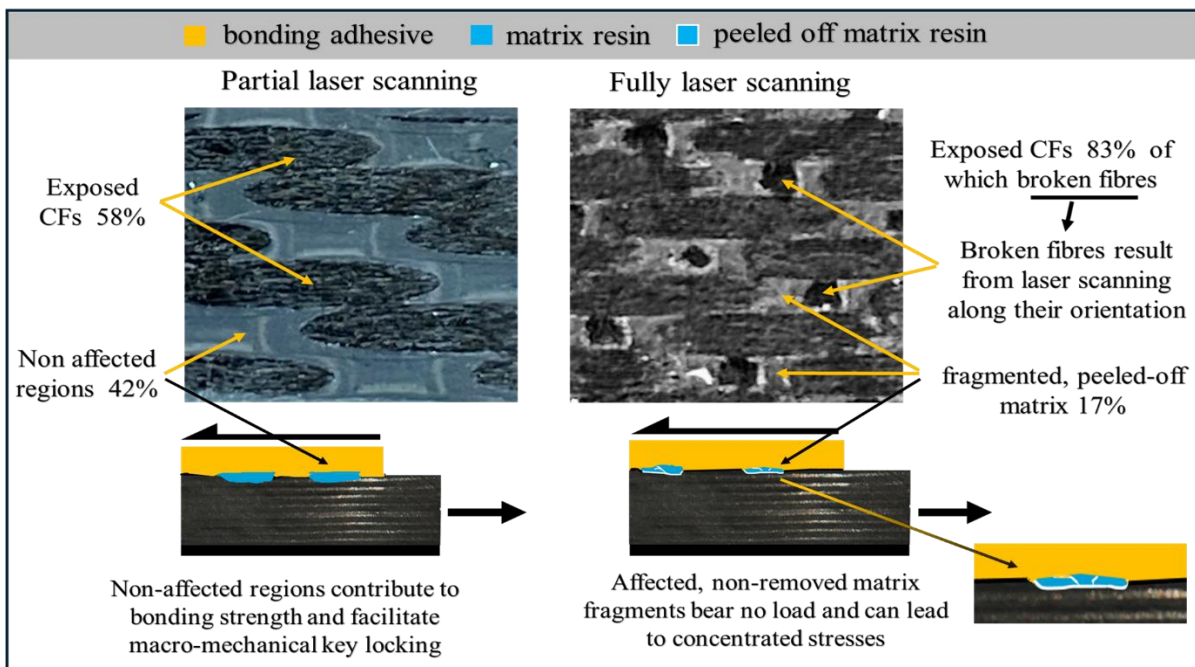


Figure 5.21. Schematic illustration explaining why partially scanned samples exhibit higher strength than fully laser-scanned samples.

5.6 Conclusions

- The effectiveness of NIR laser processing on CFRPs is highly contingent upon the thickness of the outer layer matrix, which refers to the distance from the fibres to the surface. In woven reinforced CFRPs, especially those featuring thick fibre tows as examined in the current study, with fibre tow thicknesses around 200 μm , the outer layer matrix exhibits significant variation. This outer matrix layer thickness can range from a few micrometres at the mid of the warp up to 200 μm near the warp/weft intersections.
- It was concluded that the ablation of regions rich in matrix resin by exposing them to NIR laser presents challenges. Since most of the light is transmitted through the matrix to the underlying CFs, regardless of matrix thickness due to the high transmittance of the matrix to NIR, there is a risk of degrading such rich matrix zones or weakening their integrity with the fibres without effectively removing them. Accordingly, such degraded matrix zones might act as surface contaminants. Utilising high laser intensities, such as higher pulse energy, may increase the percentage of matrix removal. However, it can also lead to the breakage of load-carrying CFs. Therefore, optimising the laser parameters to balance matrix removal with CF preservation is crucial in achieving strong adhesive bonding.
- Laser processing with a mask was observed to prevent the degradation of matrix-rich regions and enhance bonding strength by an additional 10% compared to the fully laser treatment technique. This highlights that exposing 58% of the carbon fibres without affecting the remaining 42% is more advantageous than exposing 83% of the fibres while compromising the integrity of the fibre/matrix interface in the remaining 17%.
- Mechanical abrasion with sandpaper resulted in approximately 25% improvement in bonding strength compared to the as-received samples. The observed failure mode was a mixture of mainly AF and, to a lesser extent, LFTF. The abrasion process caused breakage of CFs. Consequently, broken fibre segments were observed mixed with the adhesive bonding. In fact, during mechanical abrasion, due to the breakage of the carbon fibres at the surface, the latter lost its main feature as the load-carrying constituent of the CFRP composite.

CHAPTER 6: Laser Surface Processing of UD Reinforced CFRP Composites to Improve Adhesive Bonding Using NIR ns Pulsed Fibre Laser.

6.1. Introduction

The previous study on the processing of woven reinforced CFRPs (**Chapter 5**) revealed that due to the high inhomogeneity of the laser-processed material, it was challenging to fully understand the effects of the different laser processing variables on the resultant responses. UD CFs CFRPs are less inhomogeneous, allowing for a better understanding of the effects of these laser processing variables. Accordingly, in this chapter, a UD CFs CFRP material was utilised to be investigated for surface treatment with laser. The influences of various laser processing variables on different responses, including matrix removal and adhesive bonding strength, were examined through separate experiments. The laser equipment used in these studies was the SPI ns pulsed fibre laser, detailed in **Chapter 3/ Section 3.2.1**.

It is well-documented in the literature that concentrated shear and/or peel stresses can cause bond failure before the theoretical maximum joint strength is reached (Banea, 2019). Low modulus adhesives typically have lower strengths, but their ability to distribute stresses uniformly along the overlap and deform plastically can result in a much higher joint strength compared to high modulus adhesives (da Silva et al., 2006). To further understand the effect of the adhesive bonding ductility on the bonding strength of single lap joints, two adhesives were utilised for the bonding strength tests and a simulation study using SolidWorks was conducted to compare the two adhesives.

6.2. Objectives

- Studying and understanding the potential effect of heat accumulated within the material during laser scanning on adjacent scans.
- Studying the influences of laser processing parameters, particularly the pulse energy and pulse length, on the ablation of the matrix, the surface wettability, and the bonding strength.
- Studying the effect of the adhesive modulus of elasticity on the bonding strength.

6.3. Experimental design and workflow

This chapter encompasses four distinct studies: three experimental and one modelling. The first two experiments are single-phase, while the third includes multiple phases. The flowchart in **Figure 6.1** provides a simplified overview of the experimental design and stages for these investigations. The foundation for these studies was built on knowledge acquired from the literature and our previous work. Before delving into the four studies, a detailed presentation of the CFRP used in this chapter, including cross-section assessments, is provided.

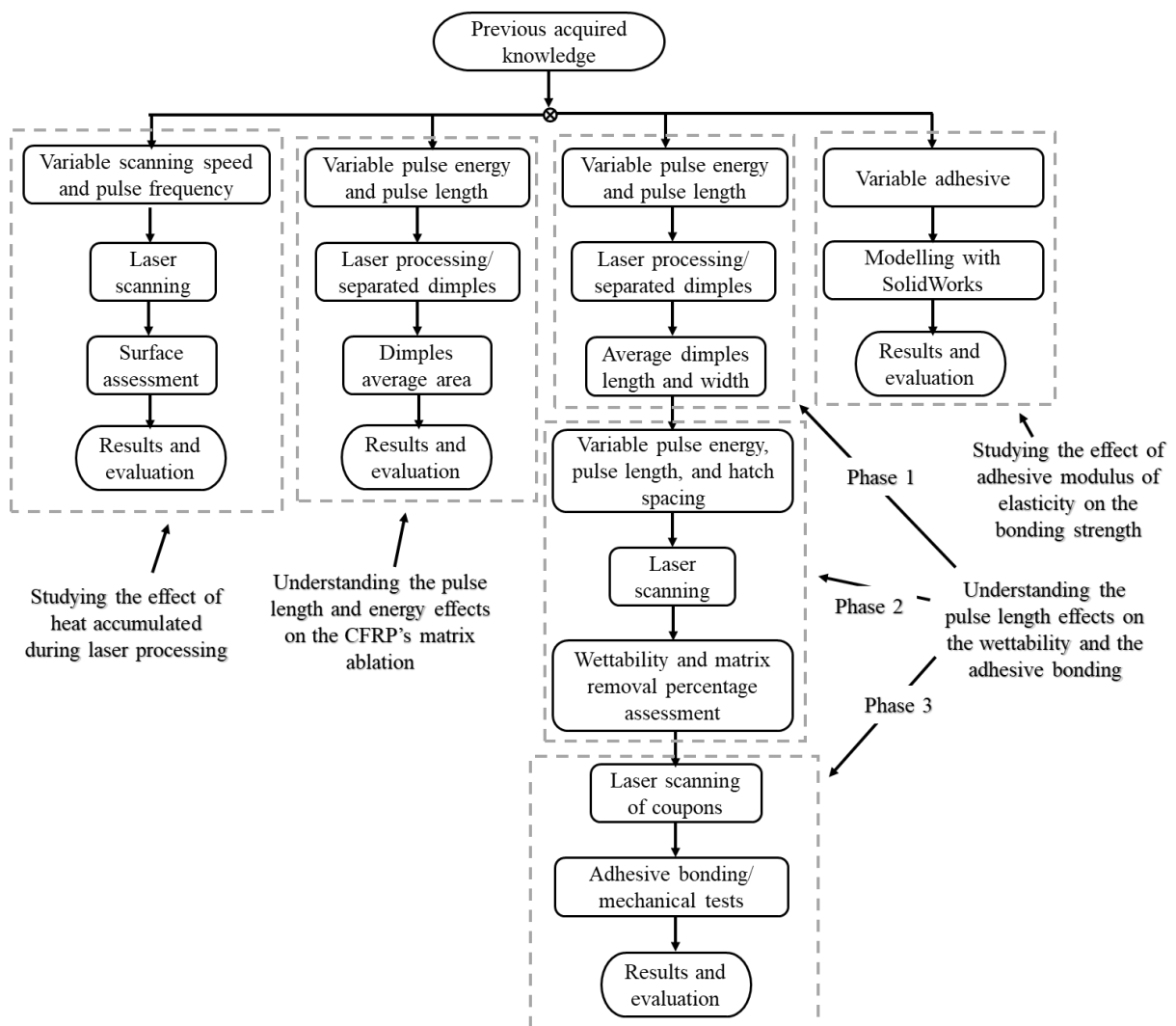


Figure 6.1. Flowchart simplifies the experimental design, steps, and phases.

6.4. CFRP material and laser equipment

CFRP laminates, with a thickness of 1.43 ± 0.02 mm, were produced at Reverie Ltd. (UK) using an autoclave process. These laminates comprised five layers of unidirectional (UD) prepreg (SHD MTC510-UD300-T700-33-35%, 300 mm wide) arranged in alternating orientations ($0^\circ/90^\circ/0^\circ/90^\circ/0^\circ$). The datasheet (**Appendix A**) specifies that the prepreg material possesses a tensile strength of 2300 MPa and a modulus of 119 GPa in the fibre direction, with an interlaminar shear strength of 84 MPa. Destructive tensile tests conducted in-house on the CFRP panels revealed an average tensile strength of 1500 MPa parallel to the direction of the surface CFs. This indicates that a 25 mm wide sample would require a load of approximately 56 kN to fail, which is 5-6 times higher than the anticipated adhesive failure loads. The SPI ns pulsed NIR fibre laser, detailed in **Chapter 3**, was employed for the experimental works involving laser processing in this chapter.

6.4.1 Cross-section assessment of the CFRP material

Similar to the experiment in **Chapter 5**, cross-sections were prepared for an as-received sample by embedding it in mould epoxy and polishing it. This process aimed to examine the distance from the surface to the fibres. Details of the moulding and polishing procedures can be found in **Chapter 3/ Section 3.4**. The polished cross-sections were then analysed using optical microscopy and SEM (Inspect S model, ThermoFisher), employing both backscatter and secondary electron imaging at various magnifications.

SEM and optical microscopy assessments of cross-sections of an as-received CFRP sample revealed variations in the thickness of the outermost epoxy matrix layer (distance from the surface to the fibres). The thickness ranged from approximately 1 to 25 μm , with an average of about 10 μm , as shown in **Figures 6.2** and **6.3**. This non-uniformity in fibre distribution varied from one position to another.

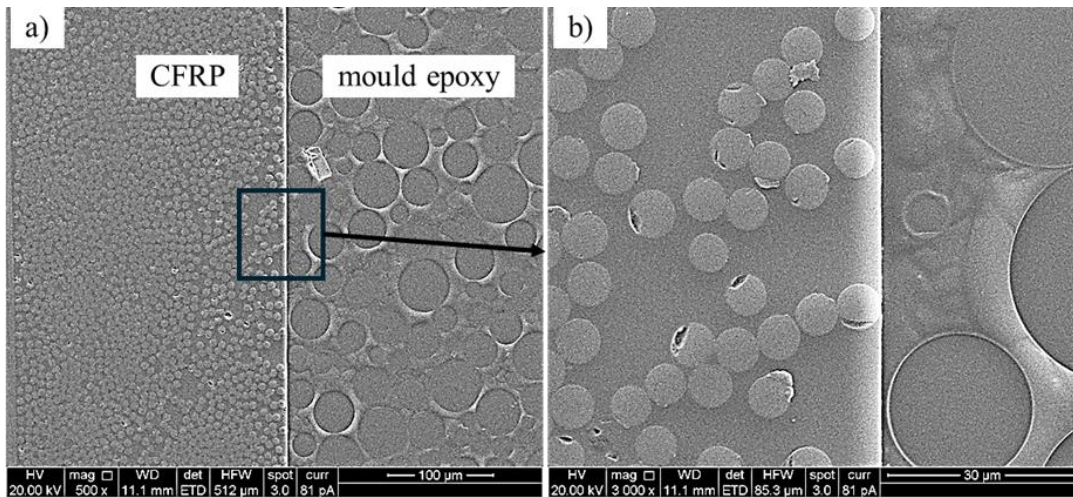


Figure 6.2. (a) and (b) SEM images at two magnifications showing the cross-section of an as-received UD CFs CFRP sample, illustrating the distance from the surface to the fibres (adapted from **Figure 4.11**).

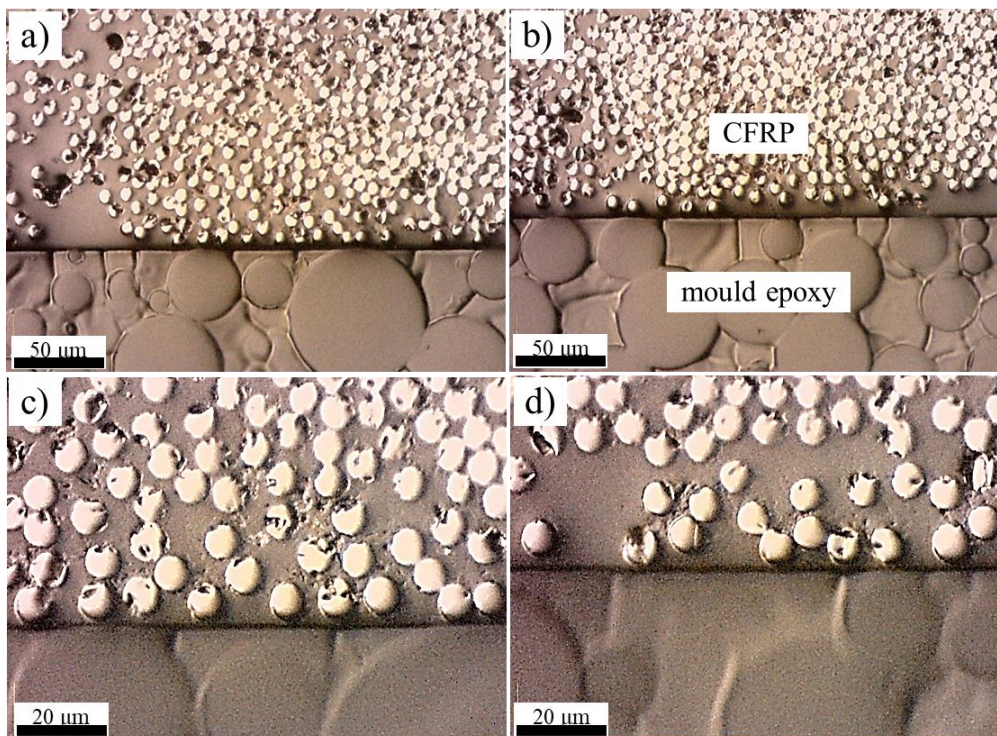


Figure 6.3. Optical microscopy images with different magnification of the cross-section of an as-received UD CFs CFRP sample.

In addition to the as-received sample, the same process was applied to laser-processed samples and samples that had failed after bonding and destructive testing. The third experiment details these latter analyses.

6.5. First study: Investigating the effect of heat accumulated during laser processing.

6.5.1. Methods (First study)

Previous experiments (**Chapter 5**) revealed uncontrollable CF damage when the laser scanning was aligned with the direction of the fibres. This was believed to be due to heat accumulation within the fibres. The short period and distance between two consecutive pulses can lead to high temperatures [308], which might result in fibre breakage due to melting or thermal expansion. The PRF used in those experiments was 25 kHz, and the scanning speed (v) was around 1 m/s, resulting in a period of 0.04 ms and a distance of 40 μm between consecutive pulses. Using lower pulse energies reduced the observed fibre damage but also led to matrix degradation without its removal.

To address this, subsequent experiments avoided laser scanning in the direction of fibre orientation. However, it was unclear whether there would be any effect from the heat accumulated in the fibres when the scanning is perpendicular to the fibre orientation. Therefore, this investigation was conducted. The experimental setup aimed to compare samples processed using the same pulse energy, pulse length, and different overall processing times to assess the impact of the period between adjacent marks (the scanned lines where the laser is on) on the processing. Three sets, each consisting of two samples, were laser scanned. Within each set, the same pulse length, pulse energy, and hatch spacing were applied. The processed areas were 10 mm x 10 mm for each sample, with each set's samples processed on a single, closely positioned piece of CFRP to minimise material inhomogeneity effects. The PRF and the scanning speed (v) were varied, but the ratio of PRF/ v was fixed within each set so that the distances between consecutive and adjacent pulses remained constant while the periods were varied. **Table 6.1** presents the processing variables for the three sets.

Table 6.1. The laser processing variables for the three experimental sets concern studying the effect of heat accumulated within the fibre.

| Set | (τ) (ns) | E_{pulse} (mJ) | (v) (mm/s) | PRF (kHz) | Pulse spacing (μm) | (H) (μm) | Energy /unit area (J/mm^2) | Period (δt) (ms) |
|-----|------------------|----------------------------|-----------------|--------------|------------------------------------|----------------------------|---|-------------------------------|
| 1 | 200 | 0.09 | 80 | 2 | 40 | 50 | 0.045 | 125.5 |
| | 200 | 0.09 | 1000 | 25 | 40 | 50 | 0.045 | 10.5 |
| 2 | 30 | 0.08 | 800 | 25 | 32 | 50 | 0.05 | 13 |
| | 30 | 0.08 | 4000 | 125 | 32 | 50 | 0.05 | 3 |
| 3 | 9 | 0.029 | 5000 | 250 | 20 | 50 | 0.029 | 2.5 |
| | 9 | 0.029 | 10000 | 500 | 20 | 50 | 0.029 | 1.5 |

The "period" represents the time the scanner takes between any two points at two adjacent marks. The scheme in **Figure 6.4** illustrates the scanning pattern for the laser processing experiments conducted within this chapter including this experiment. The jump speed is fixed at 20 m/s. The samples from each set were then compared using optical microscopy.

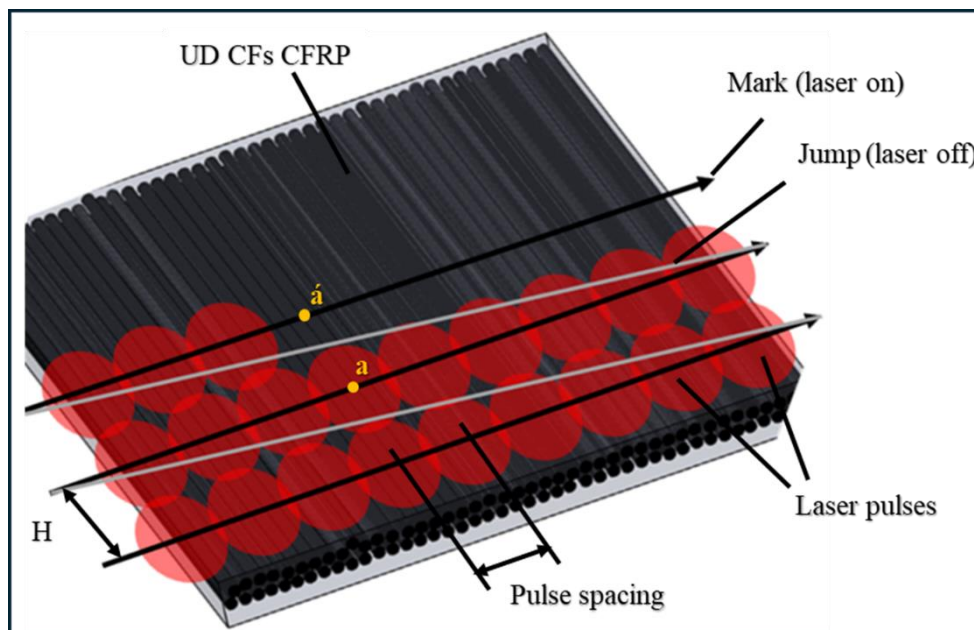


Figure 6.4. Illustration of the scanning pattern, the mark, and the jump, the distance between points a and á is equal to H, while the time the scanner takes to move from a to á is equal to δt .

6.5.2. Results (First study)

Figure 6.5 shows three sets of optical microscopy images. In each set, two samples processed using the same pulse energy and pulse length are presented. The scanning speed and PRF were varied, but the ratio of their values was fixed within each experimental set. For all three experimental sets, the optical microscopy images revealed almost no variations between the

two samples within any of the experimental sets, except for some differences believed to be due to sample inhomogeneity. Noting that the processing variables are depicted on each image.

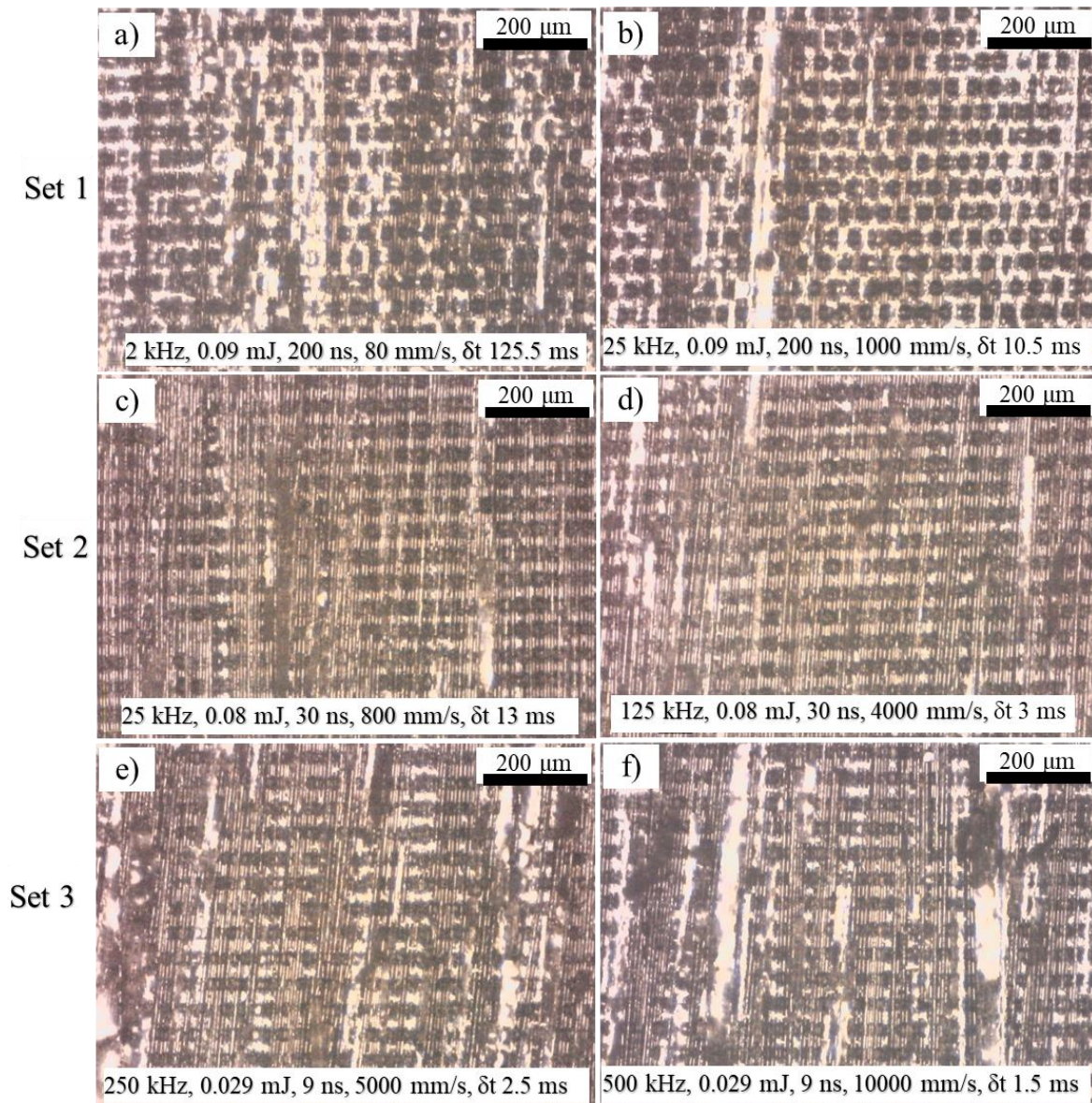


Figure 6.5. Optical microscopy images of samples processed using different processing variables, marked on them, each set of 2 processed with the same pulse length and energy and the same ratio of PRF to the scanning speed (v).

Heat accumulation between subsequent laser pulses leads to an increase in the resulting temperature if the interval between the pulses is too short for the material to completely cool back to its initial temperature [308]. When a laser pulse moves away from a specific spot, the resin at that spot starts to cool down until the subsequent pulse in the neighbouring scanning path reheats the area [309]. Consequently, the scanning frequency ($1/\delta t$) has a direct impact on the resin vaporization effect, which must be considered. The cooling time of the fibre is in the order of a few hundred nanoseconds [308, 310]. However, for the resin to cool down, it takes

about 1 ms [311]. This is because the thermal conductivity of CFs is many times (10s-100s) higher than that of the resin. Note that CFs T700 have a thermal conductivity of 9.4 W/m.K [309], whereas for the epoxy resin matrices, it is typically around 0.2 W/m.K [312, 313].

In the current investigation, the theoretical shortest time interval between consecutive scans (δt) was 1.5 ms (sample in **Figure 6.5** (f)), which was compared with a sample with a time interval (δt) of 2.5 ms (**Figure 6.5** (e)). This interval was somewhat higher than the cooling time reported in the literature [311]; consequently, no significant variation was observed. It is important to note that the theoretical time interval (δt) is shorter than the actual one due to scanner delays caused by acceleration and deceleration of the scanner equipment.

It is also worth noting that variation in the matrix removal within a single sample was observed, which resulted from the material inhomogeneity (see **Figure 6.6**).

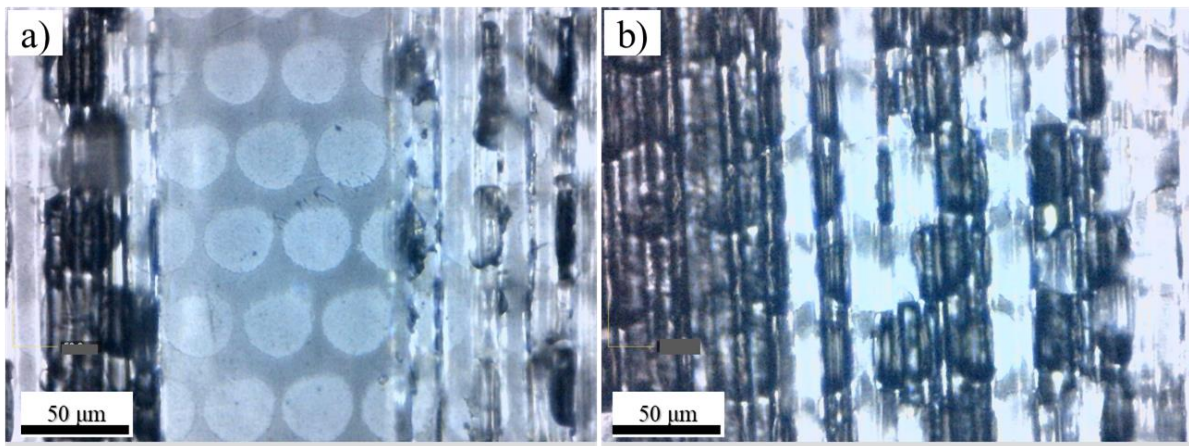


Figure 6.6. Two highly magnified optical microscopic images were taken at different positions of a single sample treated with 25 kHz, 0.09 mJ, 200 ns, and 1000 mm/s.

6.6. Second study: Understanding the pulse length and energy effects on the CFRP matrix ablation.

6.6.1. Methods (Second study)

In this investigation, laser surface processing of CFRP was conducted using two different pulse lengths (30 and 200 ns) and five different pulse energies (30, 41, 52, 65, 78 μ J). The aim was to compare the ablated area and depth of the matrix resin. Separated dimples were created by utilising a relatively high scanning speed (2000 mm/s) compared to the PRF (25 kHz) and a large hatch spacing (100 μ m). The processing involved creating lines of separated dimples, each with a specific combination of pulse energy and length. The 10 lines of dimples were

processed on a single CFRP sample and placed close to each other to reduce the effect of material inhomogeneity.

Optical microscopy images were employed to assess the dimples resulting from each set of the processing variables (single pulse exposed area). The ImageJ software's thresholding tool facilitated the measurement of the average dimple area based on optical microscopy images, with 25 dimples analysed for each processing variable (**Figure 6.7**). Additionally, optical profilometry was employed to assess the depth of the dimples. Furthermore, (SEM) was employed to deepen the understanding of the ablation mechanisms associated with different pulse variables. For the latter, alongside the primary samples, an additional sample was laser processed using both pulse lengths, but only the highest pulse energy (78 μJ) was employed.

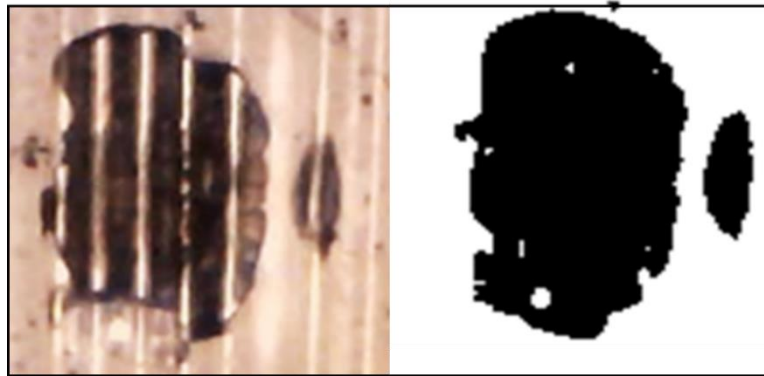


Figure 6.7. Clarification of the colour thresholding process using ImageJ to measure the dimple area.

6.6.2. Results (Second study)

The optical microscopy in **Figure 6.8**, which represents two microscopic images, shows ten lines of separated dimples. Each line of separated dimples was processed using a specific pulse energy (E_p) and pulse length (τ), marked on the side and top of the images. It is obvious that with a 30 ns pulse length, the dimples are larger than those with 200 ns. Moreover, higher pulse energy results in larger dimples.

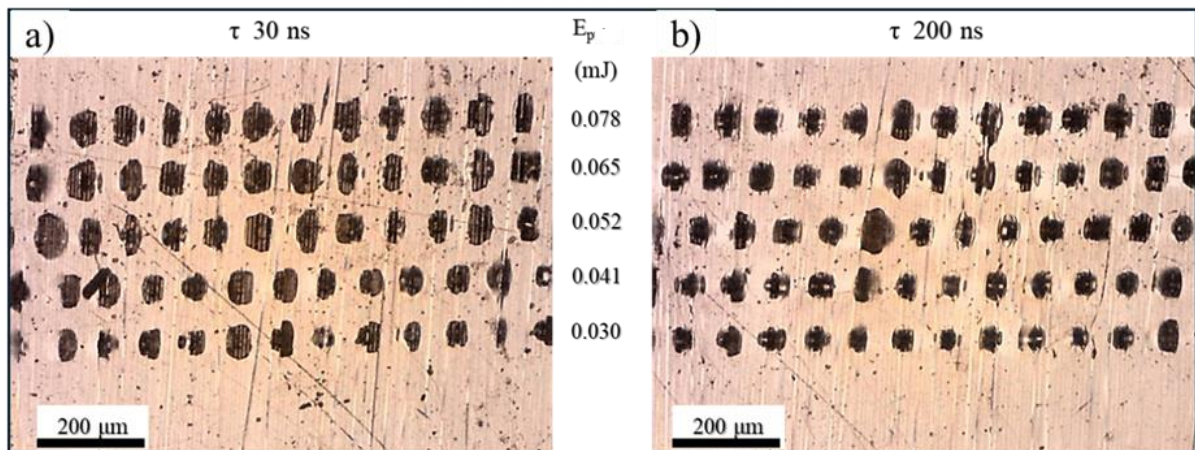


Figure 6.8. Lines of separated dimples with five different pulse energies processed with a) 30 ns, b) 200 ns.

The plots in **Figure 6.9** represent the average dimple areas that were estimated using ImageJ. It appears that the dimple area increased linearly with pulse energy. For the same pulse energy, the average dimple areas created using a 30 ns pulse length are almost double those created using a 200 ns pulse length. With the highest pulse energy, the dimples created using 200 ns pulses are nearly half the laser spot area (A_0). Notably, only degraded (cracked) regions were observed at some processed positions of the sample instead of dimples. This is believed to be due to the high thickness of the outer layer matrix resin at these positions. This phenomenon mostly occurred with the 200 ns pulse length and increased with lower pulse energy, which is logical as the evaporation starts near the fibre-matrix interface, see the SEM images **Figure 6.10**. **Figure 6.11** shows SEM images of two samples, both processed using 0.078 mJ but with two different pulse lengths (30 ns and 200 ns).

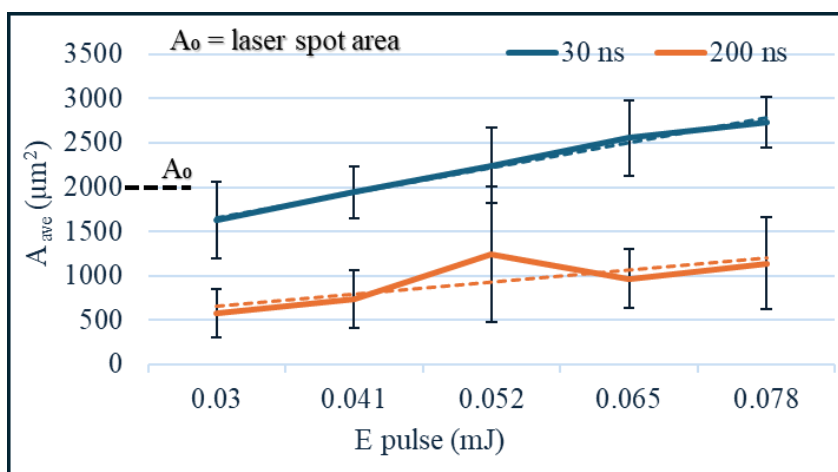


Figure 6.9. The average dimple areas that were created with different pulse energy and pulse length.

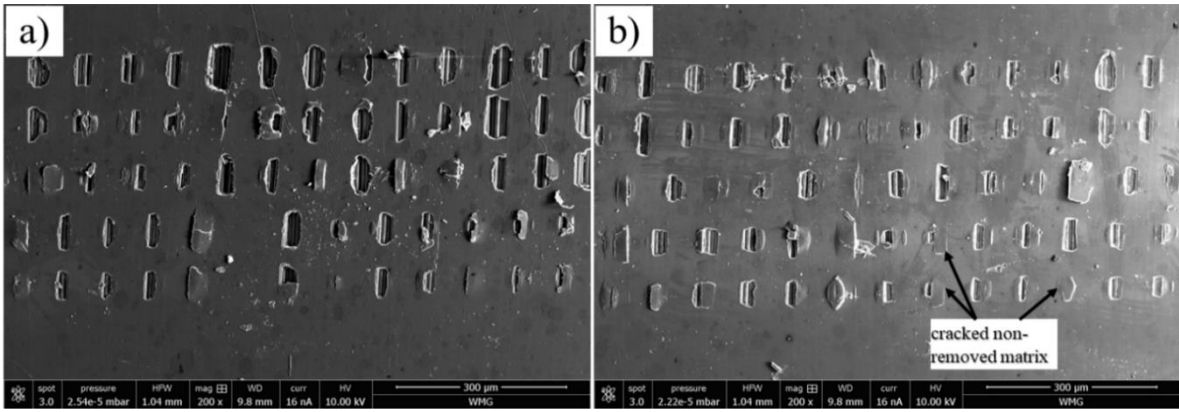


Figure 6.10. SEM images of CFRP samples processed with a) 30 ns and b) 200 ns. For both images, the pulse energy in each line of dimples is as follows: 0.078, 0.065, 0.052, 0.041, 0.03 mJ from top to bottom.

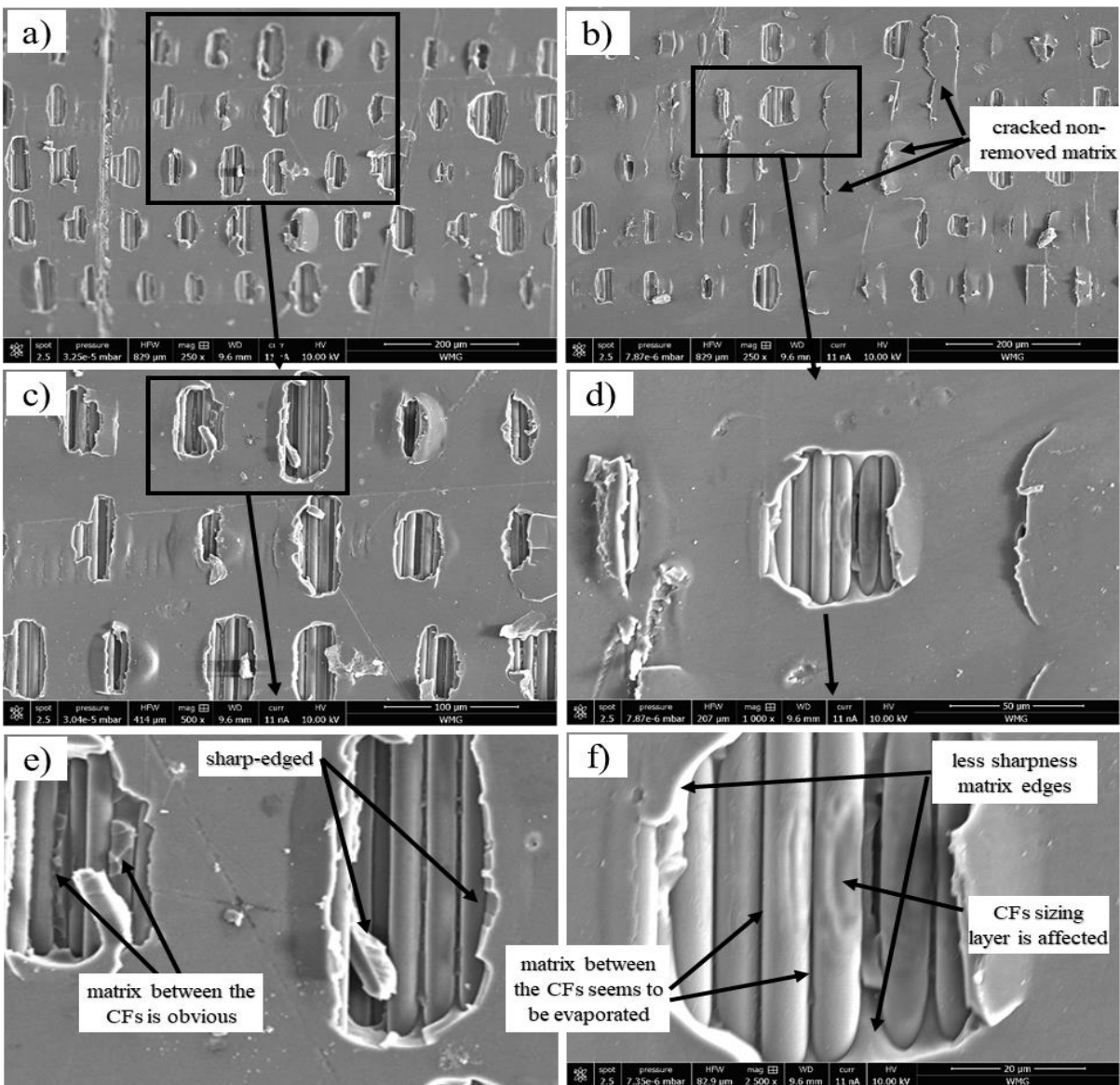


Figure 6.11. SEM images of CFRP samples processed using a), c), and e) 30 ns, and b), d), and f) 200 ns. For all images, the pulse energy is 0.078 mJ.

The variations in dimple size between 30 and 200 ns pulses can be attributed to the high thermal conductivity of the CFs, where the cooling time of fibres is in the range of a few 100s ns. In addition to the variation in dimple sizes, another noticeable difference between the two pulse lengths is that the dimple edges created with 30 ns pulses appear sharper compared to those created with 200 ns pulses. Furthermore, with 200 ns pulses, the matrix between the CFs seems to be evaporated. It seems that the ablation mechanism itself is different. The widely accepted theory among previous researchers regarding the ablation mechanism of the CFRP matrix when using a ns pulsed NIR laser is that the CFs absorb most of the light, where the matrix is mostly transparent to the NIR laser. The laser-induced heating of the fibres leads to partial evaporation of the matrix at the matrix/fibre interface, creating an unintended recoil pressure that blows away portions of the matrix [27, 191]. According to this theory, there are two consecutive phenomena: first, the partial evaporation, and second, the creation of unintended recoil pressure, which causes the spalling and blowing away of the matrix. Longer pulse lengths probably result in a higher amount of heating and evaporation of the matrix compared to shorter pulses, either preceding or following the ablation process, thereby softening the sharpness of the edges. Furthermore, with a 200 ns pulse duration, the sizing layer of carbon fibres appeared to be affected. This suggests that partial evaporation of the sizing may have occurred, leading to the visibility of fibre wrinkles, see **Figure 6.11** (f). This effect occurred even with the lowest pulse energy, as shown in **Figure 6.12**.

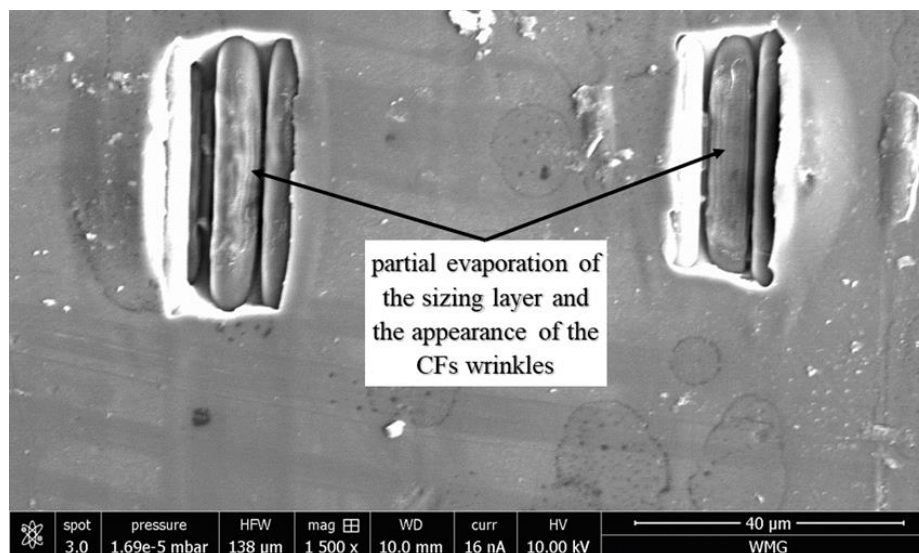


Figure 6.12. SEM images of CFRP samples processed using pulse length of 200 ns and pulse energy of 0.03 mJ. The sizing layer, a thin coating approximately 100 nm thick, is applied to the CFs during the final production stage to cover the surface-folded wrinkles that form during the production

processes and protect the fibre during handling. It is unclear why degradation of the sizing layer occurs when processing with 200 ns pulses. In comparison, no degradation was observed to the sizing layer with 30 ns pulses, despite the latter likely resulting in higher fibre temperatures. The literature lacks detailed information about the optical and thermal properties of sizing agents. Commercially, sizing agents are complex mixtures with confidential formulations applied to CF surfaces [314]. Studies have shown that sizing agents begin to degrade at temperatures above 500°C, with the extent of degradation being a function of exposure time [315], noting that the boiling point of the carbon fibres is approximately 3300°C, whereas the degradation point of the resin matrix is approximately 400°C [311]. In fact, the ablation mechanism with the 200 ns pulse laser appears to be more influenced by chipping and thermal contraction of the matrix's outer layer, rather than spalling, due to the longer laser interaction time. This extended interaction increases the temperature of the matrix and may reduce its brittleness. While this observation might seem to contradict findings from several researchers who stated that thermosetting materials cannot melt, reshape, or soften upon heating [316-318], the latest results from CO₂ laser processing (**Chapter 7, Section 7.5**) provide supporting evidence. These results demonstrate the formation of bubbles around laser-affected fibres, suggesting that the thermosetting matrix can undergo reshaping upon heating under specific conditions. The plots in **Figure 6.13** represent the pulse instantaneous power versus time for the two pulse lengths with the same pulse energy. These plots were created based on the pulse amplitude profile obtained from the SPI laser manual. The area under each of the two curves, which are equal, represents the pulse energy for the specified pulse length. Notably, the actual pulse lengths are slightly longer than stated in the manual. It is also evident from the plots that the pulse power for the 30 ns pulse length is more consistent over time compared to the 200 ns pulse length. The latter shows a significant portion, approximately half, of the energy is likely dissipated at low power, which might not contribute to the ablation process. This may explain several phenomena observed in this study, including the smaller dimples associated with the 200 ns pulse compared to those created with shorter pulses, the softening of the sharp edges, and the degradation of the sizing layer.

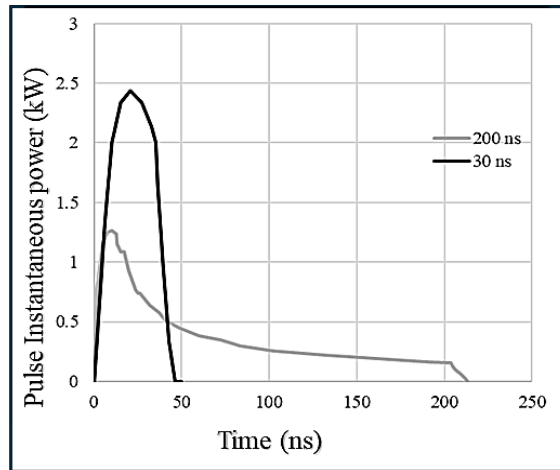


Figure 6.13. The pulse instantaneous power versus time of the 30 and 200 ns pulse lengths was created based on the pulse amplitude profile obtained from the SPI laser manual.

Regarding the depth of the dimples, the optical profilometry assessment shows that the depth is mainly limited by the underlying carbon fibres. However, 200 ns pulses created narrower but deeper dimples. **Figure 6.14** presents 3D profilometric images with profiles of two dimples created with a pulse energy of 0.078 mJ and two different pulse lengths, 30 ns and 200 ns. The base of dimples created using 30 ns pulses appears flatter compared to those created with 200 ns pulses, which seem highly irregular. In line with SEM assessment, it appears that with 200 ns pulses, the matrix between the fibres has been evaporated, creating narrow cavities. Moreover, from **Figure 6.14** (b), it seems that with 200 ns pulses, a larger area around the dimple consists of cracked, non-removed matrix that has certainly lost its integrity.

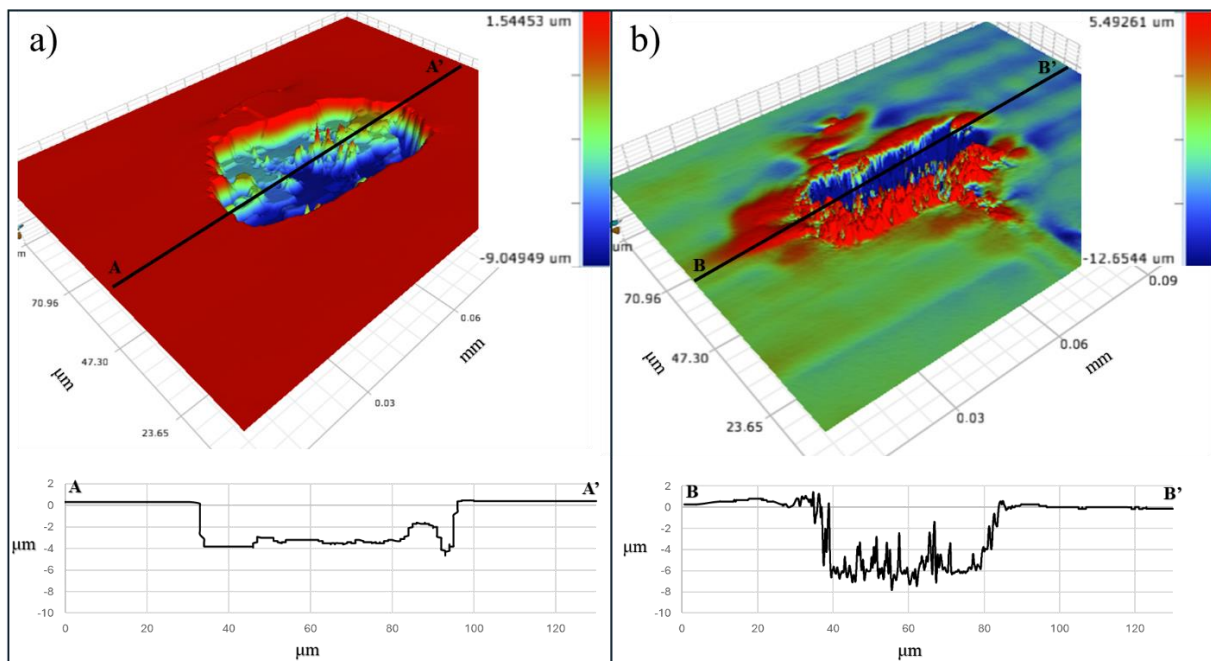


Figure 6.14. 3D profilometric images with profiles of two dimples created with a pulse energy of 0.078 mJ and two different pulse lengths a) 30 ns and b) 200 ns.

It was challenging to quantitatively compare the depth among the different pulse lengths or energies. **Figure 6.15** displays optical profilometric images depicting dimples created with various pulse lengths and energies. Notably, it appears that even at the lowest energy setting, 200 ns pulses result in deeper dimples than 30 ns pulses. This observation suggests that the pulse length has a more significant impact on dimple depth compared to the energy level.

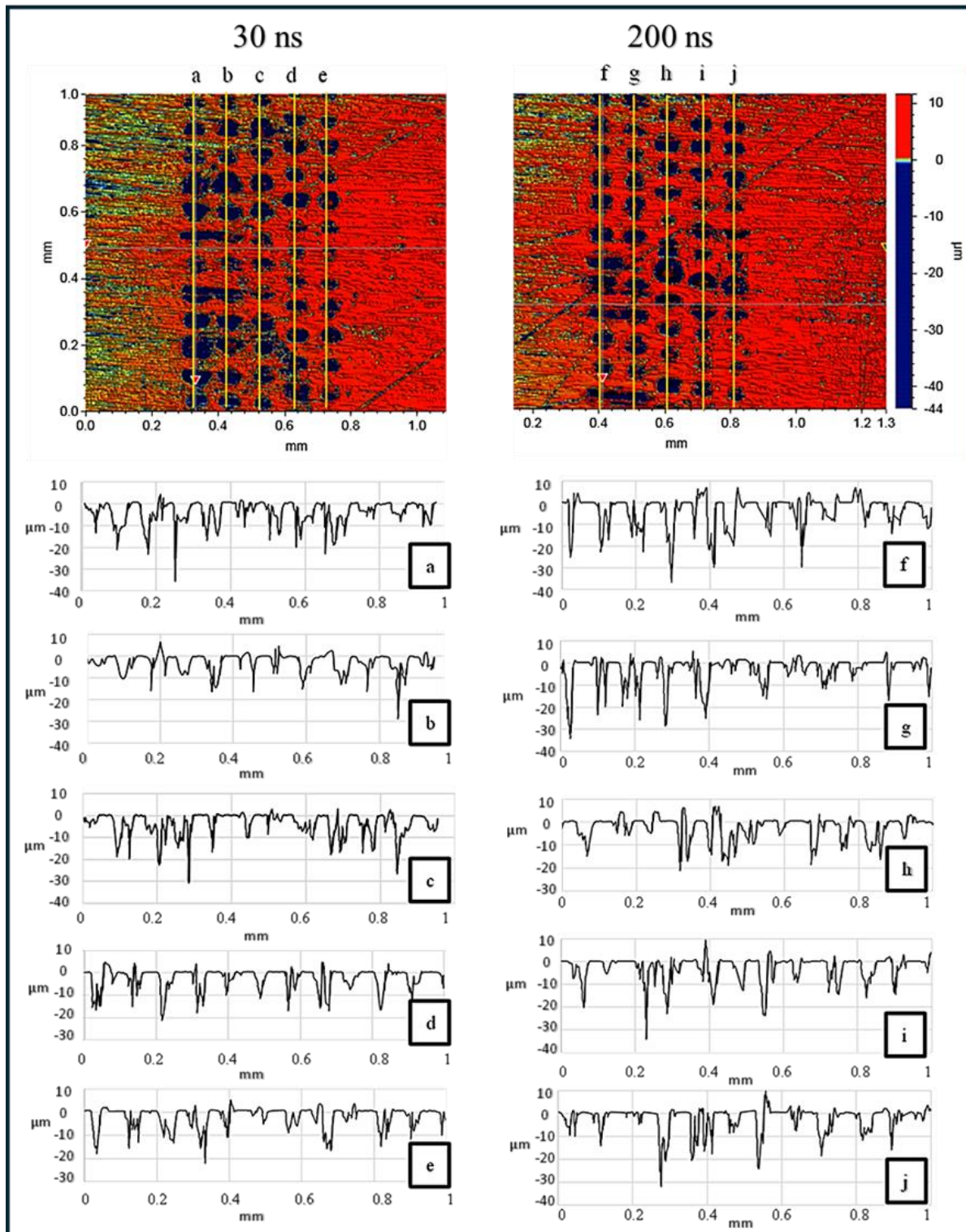


Figure 6.15. Optical profilometric images illustrating dimples and their profiles created with 30 ns (left) and 200 ns pulse length (right). Each profile is labelled with a letter representing each line of pulses, and the latter has specific pulse energy (0.078, 0.065, 0.052, 0.041, 0.03 mJ) from left to right.

6.7. Third study: Understanding the effects of pulse length on wettability and adhesive bonding.

6.7.1. Methods (Third study)

In this study, laser surface processing involving various pulse lengths and pulse energies was compared in terms of wettability and bonding strength. The experiment consisted of multiple stages. Initially, separate dimples were created using three different pulse lengths (30, 80, and 200 ns) and two pulse energies (0.052 and 0.078 mJ). The average length and width of dimples created by each processing variable set were measured using ImageJ. Subsequently, hatch spacings and scanning speeds were determined for fully exposing the fibres. With these values, a factorial experiment was conducted. Wettability was assessed by measuring the WCAs. It was not feasible to determine the SFE accurately due to the absorptive nature of the laser-processed surfaces and the continuous reduction in contact angles. Therefore, the WCAs measured under different processing variables were compared instead. The processing variables that achieved the best wettability and effective matrix removal for each pulse length were selected for adhesive bonding tests. Optical microscopy, profilometry, and SEM were utilised to analyse the samples. Details of all experimental stages related to understanding the effects of pulse length are provided below. Note that outcomes of some experimental stages are presented in subsequent sections as they are utilised in later stages of the experiment.

6.7.1.1. Creation of separated dimples and measurements of the dimple's average lengths and widths.

Separated dimples were created using a high scanning speed (2000 mm/s) relative to the PRF (25 kHz) and a large hatch spacing (100 μm). Three pulse lengths (30, 80, and 200 ns) and two pulse energies (0.052 and 0.078 mJ) were investigated. The processing variables are detailed in **Table 6.2** below. The created dimples were irregular elongated shapes featuring greater depth towards the fibre orientation. The average length and width of 25 dimples created with each processing variable set were measured using ImageJ. This was based on optical profilometry (Bruker) 2D images for each sample. Optical microscopy images of the samples and one profilometric image for illustration are shown in **Figure 6.16**.

Table 6.2. The laser processing variable for dimple creation

| (τ) (ns) | E_p (mJ) | (v) (mm/s) | PRF (kHz) | Hatch (H) (μm) |
|------------------|---------------|-----------------|--------------|--------------------------------|
| 30 | 0.052 | 2000 | 25 | 100 |
| 30 | 0.078 | 2000 | 25 | 100 |
| 80 | 0.052 | 2000 | 25 | 100 |
| 80 | 0.078 | 2000 | 25 | 100 |
| 200 | 0.052 | 2000 | 25 | 100 |
| 200 | 0.078 | 2000 | 25 | 100 |

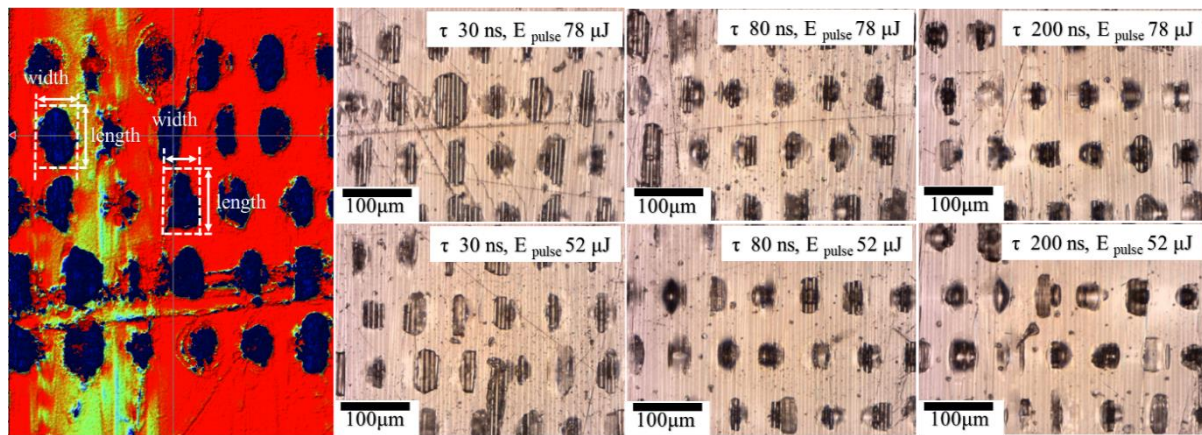


Figure 6.16. The left image is an optical profilometric image illustrating the method used for estimating the dimple length and width. The other six images are optical microscopy images of the samples treated with different pulse lengths and energies, with the specific pulse length and energy marked on each microscopic image.

6.7.1.2. Estimation of the hatch spacings and scanning speeds to be utilised for laser processing to fully expose the CFs for wettability assessment.

A factorial experiment was conducted to determine the best surface wettability for each of three pulse lengths (30, 80, and 200 ns) among different other processing variables. For each set of (pulse length and pulse energy), three hatch spacings were examined based on the measured average dimple lengths along with values 20% lower and 20% greater. The scanning speeds were calculated based on the average width of the dimples (scanning speed = dimple width \times PRF). PRF was fixed at 25 kHz for all processing sets. The full experimental runs are depicted in **Table 6.3** below. The 18 experimental runs were conducted using two CFRP coupons, each measuring 75 mm x 25 mm. Each coupon contained nine samples; each measuring 7 mm x 20 mm. **Figure 6.17** shows a macro photo of a CFRP coupon with the first nine samples.



Figure 6.17. Macro photo of a CFRP coupon with the first nine samples.

Table 6.3. The laser processing variable for the different experimental runs.

| Sample (#) | τ (ns) | E_p (mJ) | v (mm/s) | H (μm) | Pulse spacing (μm) | Energy/ unit area (J/mm^2) |
|------------|-------------|------------|------------|---------------------|---------------------------------|--|
| 1 | 30 | 0.078 | 925 | 65 | 37 | 0.032 |
| 2 | 30 | 0.078 | 925 | 78 | 37 | 0.027 |
| 3 | 30 | 0.078 | 925 | 52 | 37 | 0.041 |
| 4 | 30 | 0.052 | 825 | 56 | 33 | 0.028 |
| 5 | 30 | 0.052 | 825 | 67 | 33 | 0.024 |
| 6 | 30 | 0.052 | 825 | 45 | 33 | 0.035 |
| 7 | 80 | 0.078 | 925 | 61 | 37 | 0.035 |
| 8 | 80 | 0.078 | 925 | 73 | 37 | 0.029 |
| 9 | 80 | 0.078 | 925 | 49 | 37 | 0.043 |
| 10 | 80 | 0.052 | 825 | 49 | 33 | 0.032 |
| 11 | 80 | 0.052 | 825 | 59 | 33 | 0.027 |
| 12 | 80 | 0.052 | 825 | 39 | 33 | 0.040 |
| 13 | 200 | 0.078 | 850 | 44 | 34 | 0.052 |
| 14 | 200 | 0.078 | 850 | 53 | 34 | 0.043 |
| 15 | 200 | 0.078 | 850 | 35 | 34 | 0.066 |
| 16 | 200 | 0.052 | 725 | 40 | 29 | 0.045 |
| 17 | 200 | 0.052 | 725 | 48 | 29 | 0.037 |
| 18 | 200 | 0.052 | 725 | 32 | 29 | 0.056 |

6.7.1.3. Surface wettability

Surface wettability was assessed by measuring the WCAs using the goniometer and sessile droplet method detailed in **Chapter 3/ Section 3.2.4**. Three repeated measurements were performed for each of the 18 laser-processed samples. The assessments were conducted at 2, 5, and 10 days after the laser processing. Prior to each assessment, the samples were cleaned as described in **Chapter 3/ Section 3.6**. The droplet size was 1.5 mm in diameter. For all laser-treated samples, the CAs were continuously decreased over time due to the liquid infiltrating

the pores of the laser-processed samples. Consequently, the goniometer was set up to capture 200 frames (100 at 0.016 s intervals and 100 at 2 s intervals). Where the CAs decreased by approximately over 20 degrees within 200 seconds. The averages of the three measurements for each sample, which varied by up to 10°, were obtained. The reduction in CAs over time was almost linear, with some fluctuation within the first 25 seconds. **Figure 6.18** shows the CA versus time behaviour of two samples, illustrating each of the three WCA measurements and their averages as examples. **Figure 6.19** presents photos extracted from a video recording of sample (3), showing the reduction in water droplet size and contact angle (CA) over time. For some samples, the WCA measurements were disrupted when their values dropped below 15 degrees due to fluffy fibres or loose matrix particles. Consequently, some of the data was refined. For non-treated samples, the wettability assessment was conducted using 25 measurements conducted on three samples, each 20 mm x 20 mm, with both faces of the samples tested to assess the inhomogeneity within the material. For these measurements, the goniometer was set up to capture 200 frames at 0.016-second intervals, with the CA stabilising within the first second.

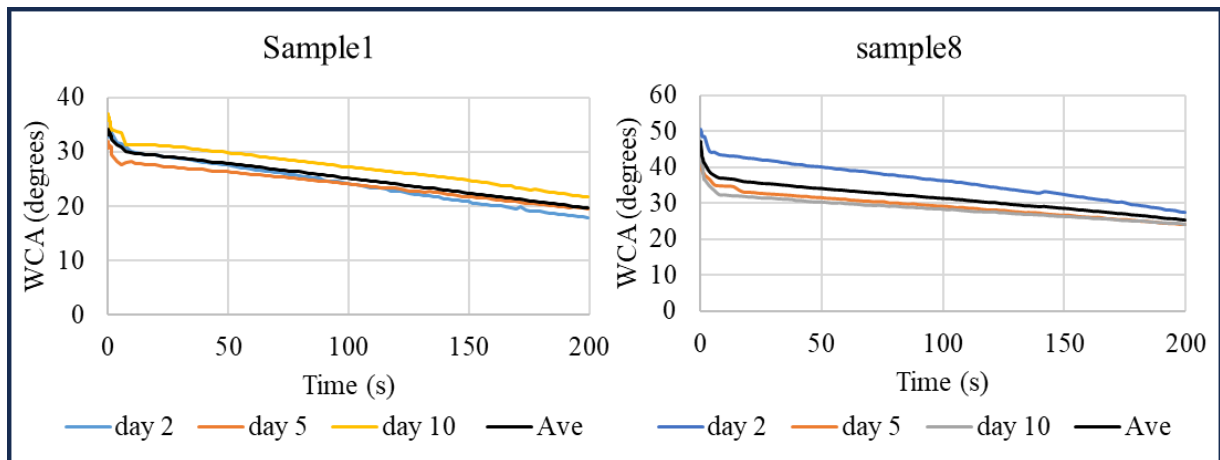


Figure 6.18. The three WCA measurements and their averages for two samples as examples.

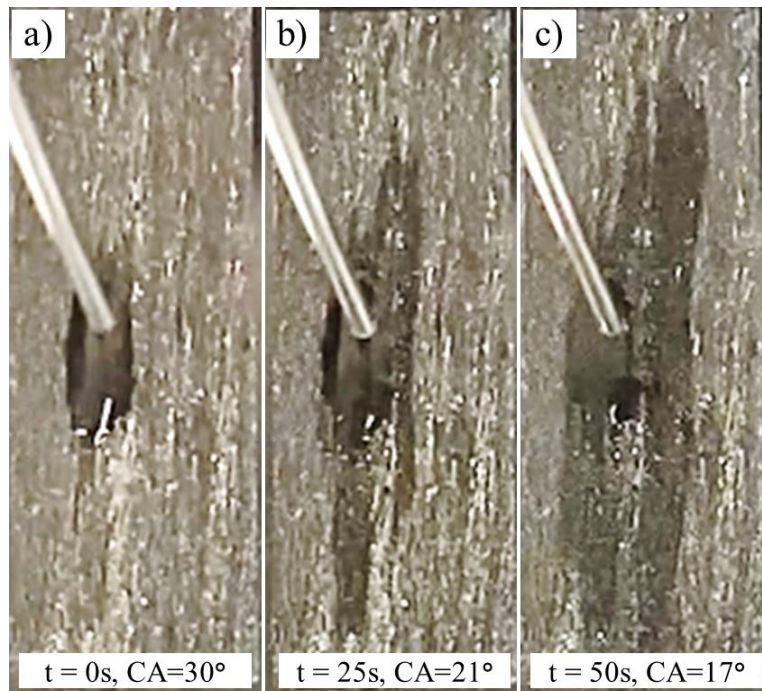


Figure 6.19. Photos extracted from a video record show the absorption of a water droplet with time.

6.7.1.4 Investigating the adhesive bonding strength

Bonding strength was investigated under three different surface conditions using variable laser processing parameters, particularly three different pulse lengths. The processing variables that achieved the best compromise of wettability and matrix removal for each of the three pulse lengths among the 18 tested samples were selected for adhesive bonding tests. The sample numbers that were implemented in the test and their corresponding processing variables are shown in **Table 6.4**. SEM was used to assess matrix removal, with specific samples processed specifically for SEM analysis. Each sample measured 3 mm x 3 mm, and all samples were processed on a single piece of CFRP material.

Table 6.4. The laser processing variables utilised for the adhesive bonding tests. The sample numbers are initials from the previous optimisation step.

| Sample (#) | τ (ns) | E_p (mJ) | v (mm/s) | H (μm) | WCA (degrees) |
|------------|-------------|------------|------------|---------------------|---------------|
| 3 | 30 | 0.078 | 925 | 52 | 21 |
| 9 | 80 | 0.078 | 925 | 49 | 13 |
| 15 | 200 | 0.078 | 850 | 35 | 0 |

The three sets of laser variables were compared in terms of adhesive bonding strength, with non-treated samples serving as a reference. Three repeated samples were tested for each surface

condition. Bonding strength tests were performed using two different adhesives: Loctite EA 9394 AERO Epoxy and Araldite 420. Two investigations were conducted for the Loctite adhesive: oven curing and ambient condition curing. For the Araldite adhesive, only ambient condition curing was investigated. Notably, both adhesives are two-part paste adhesives, but Araldite 420 has different properties, particularly a lower modulus of elasticity compared to Loctite EA 9394, which is believed to influence bonding strength significantly. Moreover, Araldite 420's lower viscosity is thought to better penetrate the porous laser-treated surfaces. Curing was performed according to their data sheets. Loctite was cured in an oven at 66°C for 1 hour or at room temperature (23°C) for 5 days. Araldite adhesive was cured for 14 days at room temperature, though this process can be accelerated in an oven at 120°C for 1 hour. The full specifications of the two bonding adhesives are available in **Chapter 3/ Section 3.3.2**. The overlaps of the joined coupons, designed to be 12.5 mm, were measured after curing using a digital vernier calliper and were within ± 0.25 mm of the designed overlap, which was considered acceptable. **Figure 6.20** shows the laser-treated regions of the coupons using different laser processing variables, the bonding jig, and the samples after curing and ready for the SLS test.

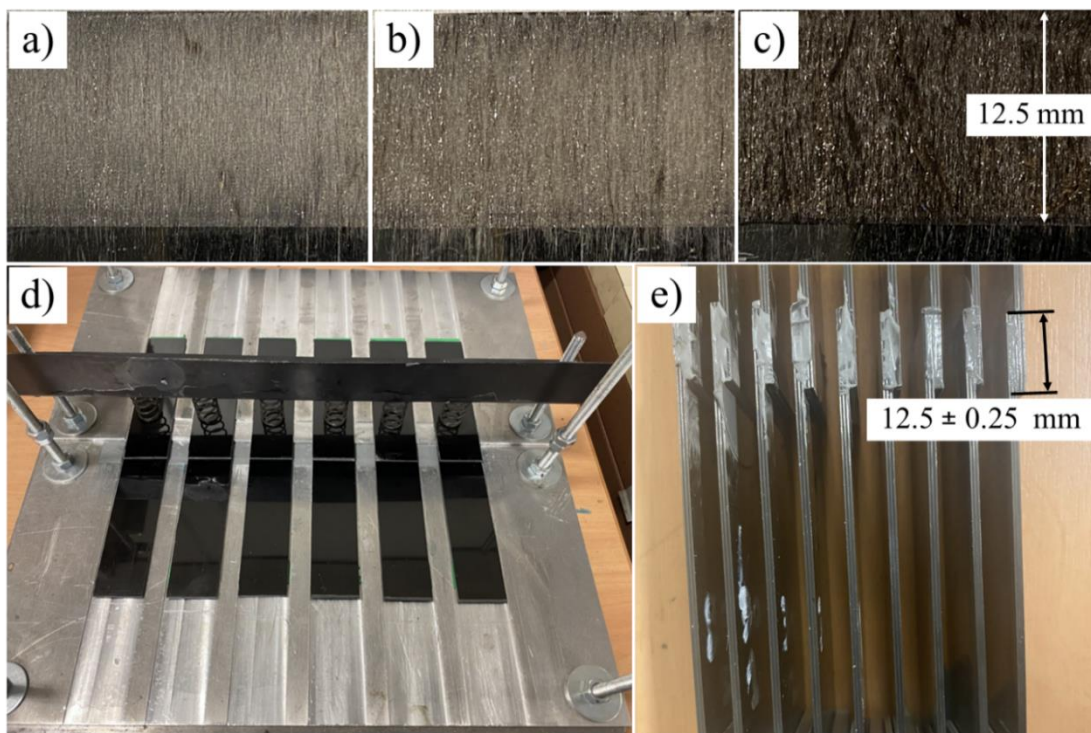


Figure 6.20. (a), (b), and (c) show the laser-treated regions of the coupons with different laser processing sets specified respectively according to the pulse lengths used: 30 ns, 80 ns, and 200 ns; (d) depicts the bonding jig; and (e) presents the samples after curing, ready for the SLS test.

6.7.2. Results (Third study)

As stated in the experimental section, the plan at first was to measure the contact angles (CAs) for water and diiodomethane (polar and non-polar liquids) to determine the SFE. However, the literature review highlighted that the wetting behaviour on porous substrates is notably influenced by the absorption of liquids into the fibre mat of fibre-reinforced composites [319-322]. Measuring a real contact angle on absorbing substrates is feasible only if the liquid absorption does not significantly decrease the drop volume. When the liquid absorption is substantial, it increasingly affects the resulting contact angle value. Additionally, there is no universally established procedure for determining the time point after drop deposition when the real CA should be measured for absorbing substrates [319]. Therefore, instead of comparing the SFE, the WCAs of the different samples at 25 seconds after droplet deposition were compared. At this time point, the reduction in contact angle was almost linearly stable for all samples, except for samples 12, 15, and 18, which showed CAs of less than 10° within the first second of droplet deposition and were considered as 0° . **Figure 6.21** represents the average WCA vs time for the 18 samples that were processed using different processing variables, as depicted in **Table 6.5**. Samples processed with 200 ns and 80 ns pulse lengths generally show lower contact angles than those processed with 30 ns. Furthermore, the hatch spacing has a significant effect on the contact angle, narrower hatch spacing results in lower contact angles.

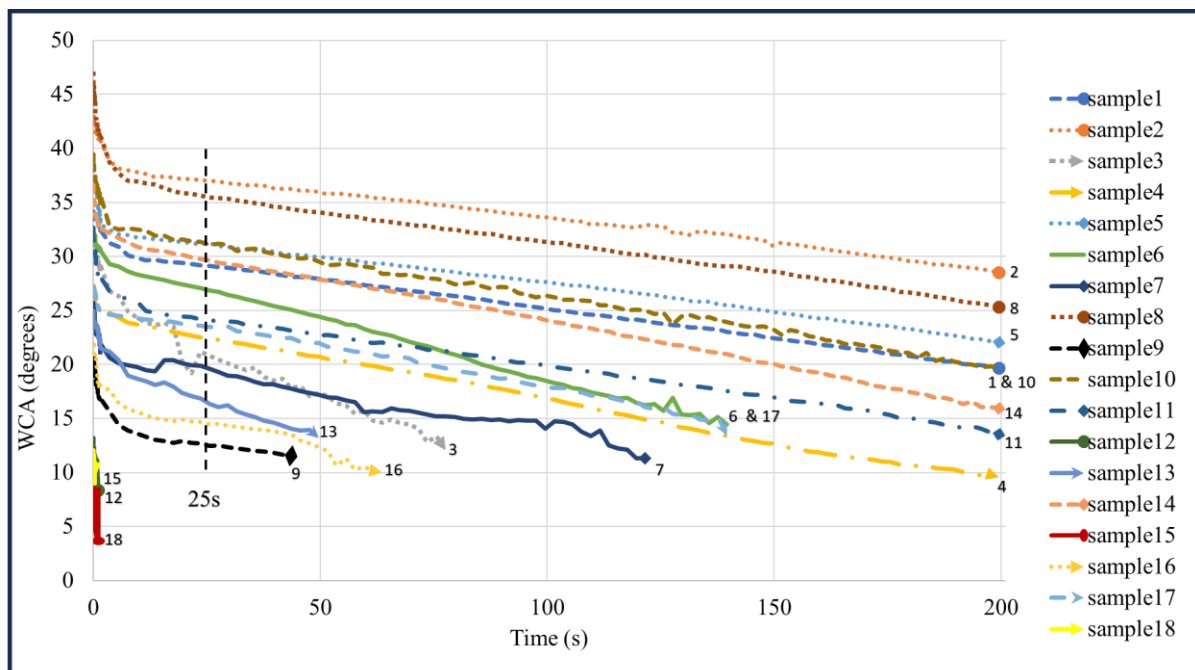


Figure 6.21. The average WCA vs time for the 18 samples which processed using different laser variables. For details on the laser processing variables for the different samples, see **Table 6.3**.

The WCA ranged between 78° and 99° for the as-received CFRP material, with an average of approximately 91°. The significant differences in wettability observed between the two faces of the composite laminate (tool side and bag side) suggest potential variations in surface finish resulting from the CFRP material's manufacturing processes.

Table 6.5. The laser processing variables and the resultant WCAs at 25s after droplet deposition.

| Sample (#) | τ (ns) | E_p (mJ) | v (mm/s) | H (μm) | Pulse spacing (μm) | Energy/ unit area (J/mm^2) | WCA _{ave} at 25s (degrees) |
|------------|-------------|------------|------------|---------------------|---------------------------------|--|-------------------------------------|
| 1 | 30 | 0.078 | 925 | 65 | 37 | 0.032 | 29 |
| 2 | 30 | 0.078 | 925 | 78 | 37 | 0.027 | 37.5 |
| 3 | 30 | 0.078 | 925 | 52 | 37 | 0.041 | 21 |
| 4 | 30 | 0.052 | 825 | 56 | 33 | 0.028 | 23 |
| 5 | 30 | 0.052 | 825 | 67 | 33 | 0.024 | 31.5 |
| 6 | 30 | 0.052 | 825 | 45 | 33 | 0.035 | 27 |
| 7 | 80 | 0.078 | 925 | 61 | 37 | 0.035 | 20 |
| 8 | 80 | 0.078 | 925 | 73 | 37 | 0.029 | 35.5 |
| 9 | 80 | 0.078 | 925 | 49 | 37 | 0.043 | 13 |
| 10 | 80 | 0.052 | 825 | 49 | 33 | 0.032 | 31.5 |
| 11 | 80 | 0.052 | 825 | 59 | 33 | 0.027 | 24 |
| 12 | 80 | 0.052 | 825 | 39 | 33 | 0.040 | 0 |
| 13 | 200 | 0.078 | 850 | 44 | 34 | 0.052 | 17 |
| 14 | 200 | 0.078 | 850 | 53 | 34 | 0.043 | 30 |
| 15 | 200 | 0.078 | 850 | 35 | 34 | 0.066 | 0 |
| 16 | 200 | 0.052 | 725 | 40 | 29 | 0.045 | 14.5 |
| 17 | 200 | 0.052 | 725 | 48 | 29 | 0.037 | 23 |
| 18 | 200 | 0.052 | 725 | 32 | 29 | 0.056 | 0 |

Figure 6.22 presents SEM images comparing laser processed samples numbers 3, 9, 12, and 15. SEM images for all samples can be found in **Appendix B**. From **Figure 6.21**, samples 3, 12, and 15 exhibited the best wettability for their respective pulse lengths. However, SEM images of sample 12 revealed a significant amount of cracked non-removed matrix particles (**Figure 6.22 (c)**), which was processed using the lower pulse energy (0.052 mJ). Consequently, sample 9 (**Figure 6.22 (b)**), which exhibits a WCA of 13°, was chosen for the adhesive bonding test instead of sample 12. Moreover, **Figure 6.22 (a)** and **(b)** indicate that laser processing with 30 ns and 80 ns pulses causes fibre breakage, which is more pronounced with the 30 ns pulse

length. **Figure 6.23** represents a cross-section for a sample treated with 200 ns laser and compared with an as-received sample.

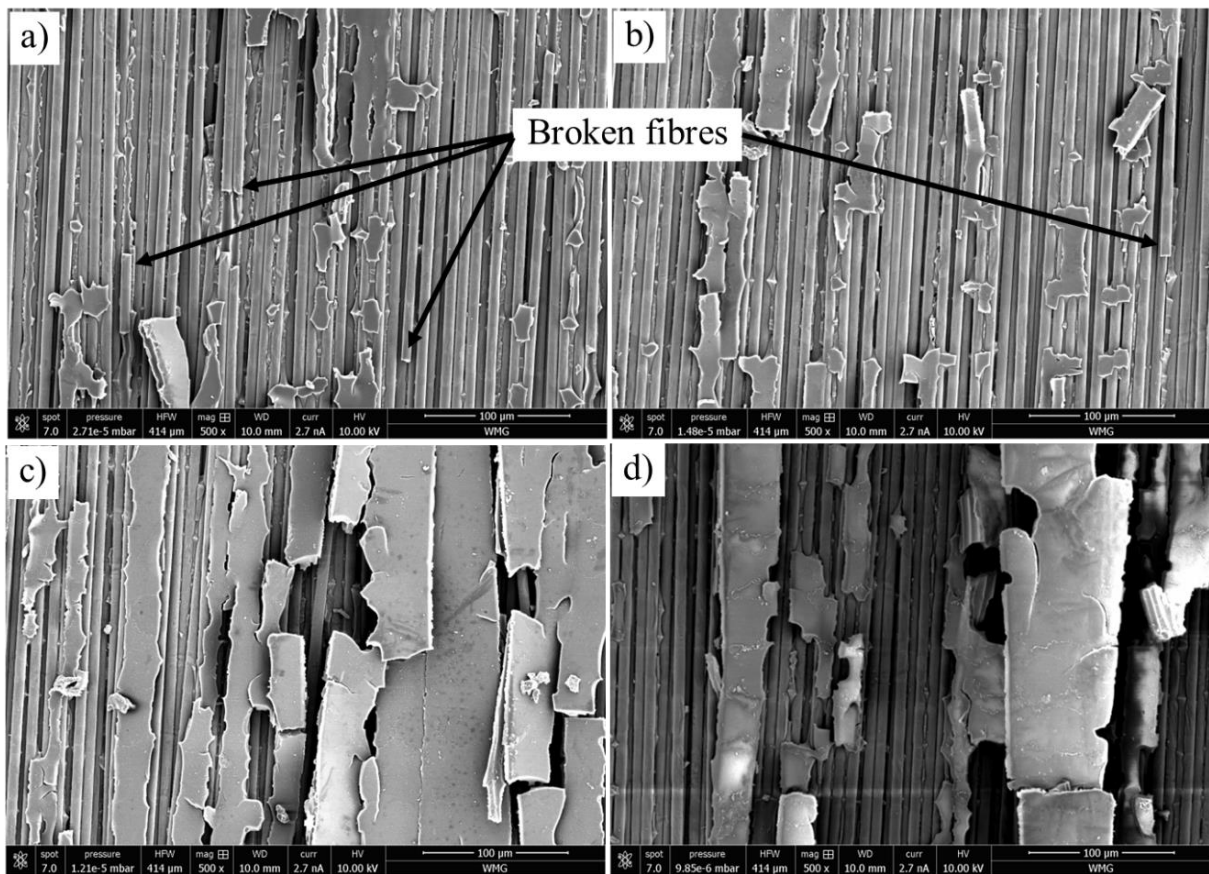


Figure 6.22. SEM images for a) sample 3, b) sample 9, c) sample 12, and d) sample 15.

The SEM assessments (**Figure 6.22** (d)) and the cross-section assessment (**Figure 6.23**) demonstrate that laser treatment using 200 ns pulses efficiently removed most of the outer layer matrix, exposing the CFs without noticeable fibre breakage. However, a considerable amount of chipped but non-removed matrix particles is observed. The distances between these particles and the exposed fibres are unknown, raising uncertainty about whether the adhesive can penetrate through them effectively to adhere to the fibres.

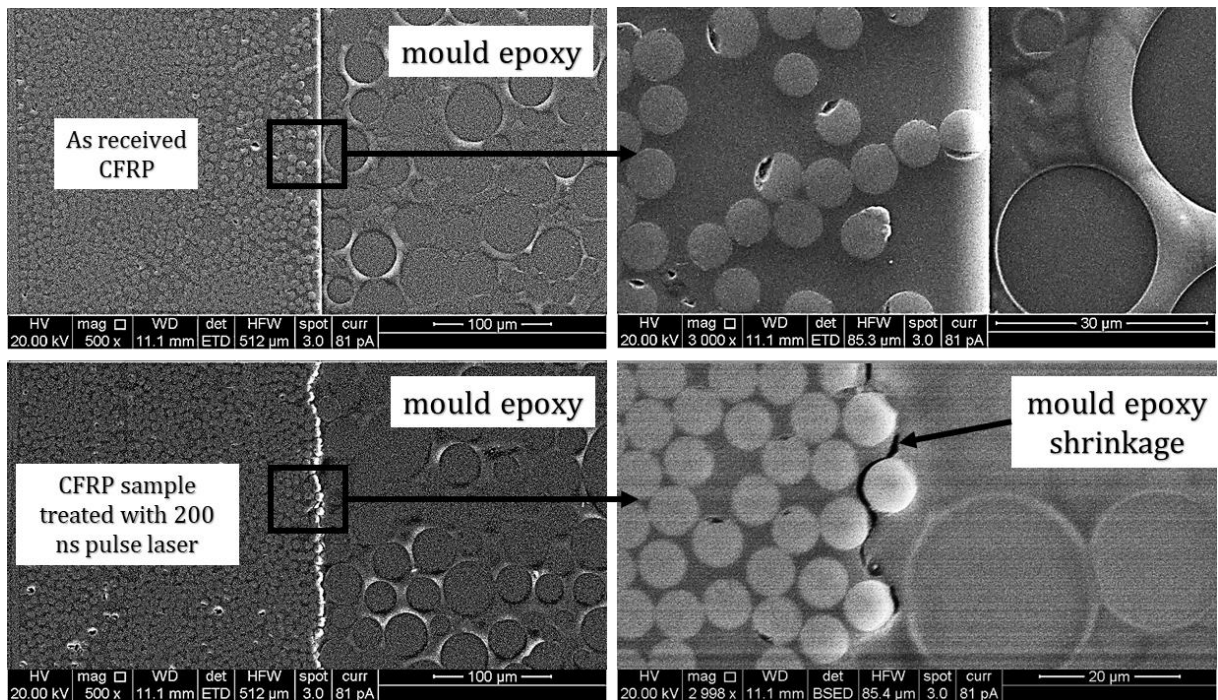


Figure 6.23. SEM images with variable magnification of the cross-section of (on top) an as-received sample and (on bottom) a laser-treated sample with a pulse length of 200 ns.

Regarding adhesive bonding strength, the three different laser processing variables were compared with non-treated samples. An initial test using Loctite EA9394 adhesive with oven curing revealed a reduction in bonding strength for all laser-treated samples compared to non-treated samples, especially those treated with 30 ns pulses. Consequently, further tests were conducted using two adhesives, Loctite EA9394 and Araldite 420, with curing for both adhesives performed under ambient conditions (approximately 23°C). Three repeated samples were tested for each surface condition and curing method. The bar chart in **Figure 6.24** represents the bonding strength of the different surface conditions with the various adhesives and curing methods.

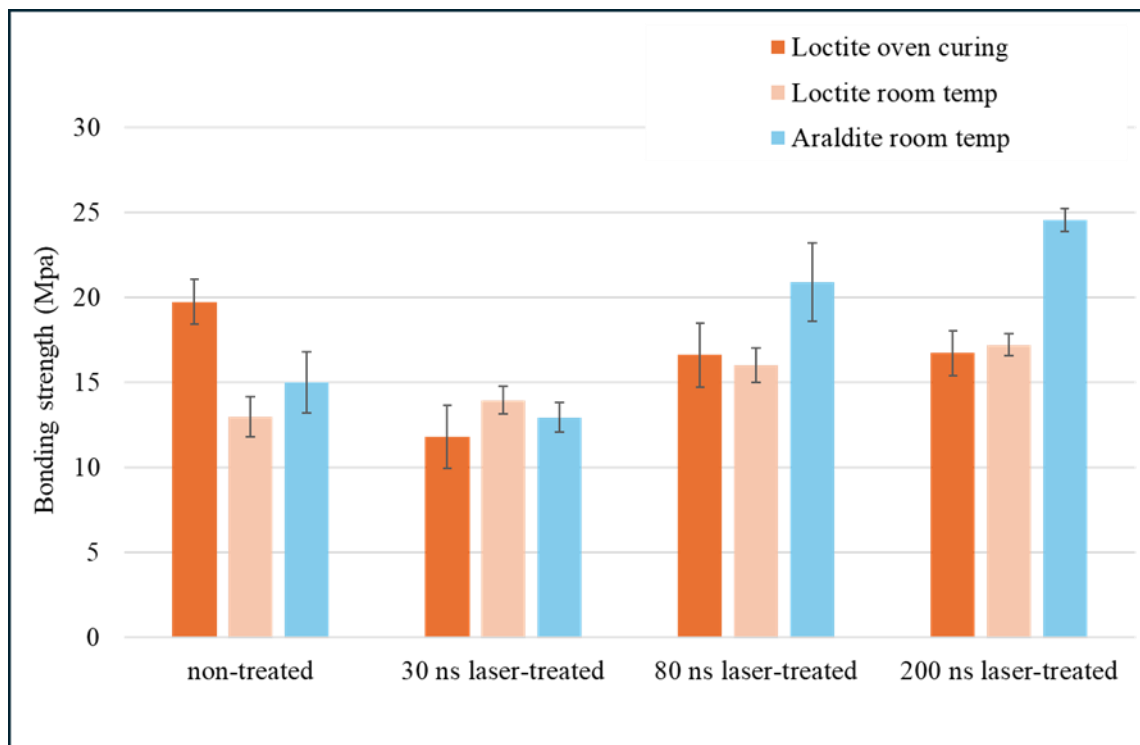


Figure 6.24. Bar chart showing the adhesive bonding strengths of CFRP samples with different surface conditions, adhesives, and curing methods.

Regardless of the adhesive and curing method used, samples treated with the 30 ns pulse laser showed a reduction or no noticeable improvement in bonding strength compared to non-treated samples. In contrast, samples treated with the 200 ns pulse laser demonstrated significant improvement: approximately 60% with Araldite adhesive and about 30% with Loctite adhesive under room temperature curing. Samples treated with the 80 ns pulse laser showed less improvement than those treated with the 200 ns pulse laser. It is suggested that the breakage of the load-carrying fibres has a significant impact on the low bonding strength for samples treated using a 30 ns pulse laser. Where the bonding strength in an adhesively bonded CFRP sample with exposed fibre at the surface contributes to both the fibre-matrix integrity and the tensile strength of the fibres themselves. The scheme presented in **Figure 6.25** elucidates the various forces acting on a single CF when it is exposed at the surface and incorporated into an adhesively bonded joint.

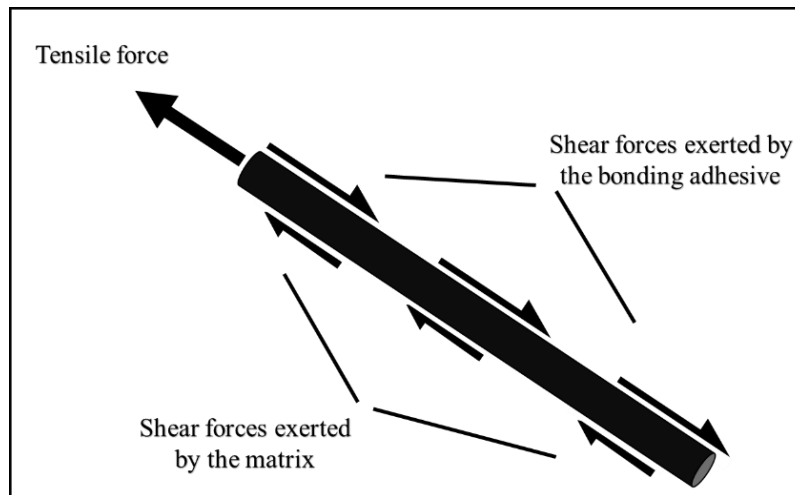


Figure 6.25. A schematic illustration of the various forces acting on a single CF when it is exposed at the surface and incorporated into an adhesively bonded joint.

Moreover, as discussed earlier, processing with a 200 ns pulse laser effectively evaporates the matrix between the fibres, creating significantly wide pores. This allows the adhesive to penetrate deeply, thereby reintegrating the laser-induced weakened fibre-matrix interface and restoring integrity. This hypothesis can be supported by the high bonding strength of samples treated with the 200 ns pulse laser and bonded with Araldite adhesive compared to those bonded with Loctite adhesive, where the Araldite adhesive has a much lower viscosity (40 Pa·s) compared to the Loctite (160 Pa·s).

With regards to the variation in bonding strength between the different curing methods, where Loctite adhesive was cured both in an oven and under ambient conditions according to the producer's datasheet. However, a discrepancy in bonding strength was observed for non-treated samples between the two curing conditions. Non-treated samples bonded with Loctite adhesive and oven-cured exhibited a bonding strength of approximately 19 MPa, which was higher than those of the laser-treated samples bonded with the same adhesive and curing method. Numerous studies have highlighted the significant influence of curing temperature on the bonding performance of some epoxies [323-327]. Elevated temperatures particularly impact the diffusion phenomena in polymer-to-polymer adhesion, as polymer diffusion is temperature-dependent [328, 329]. **Figure 6.26** (a) and (b) illustrate the failure modes of non-treated samples, bonded using Loctite adhesive but cured under different conditions: one in an oven and the other at room temperature. The room temperature-cured samples exhibited a 100% AF mode, whereas the oven-cured samples showed a combination of NSSF and LFTF. This indicates that the adhesion between the bonding adhesive and the matrix at the surface for the oven-cured sample is stronger than the adhesion between the matrix and the carbon fibres (CFs)

within the composite, suggesting that the elevated curing temperature enhanced polymer-polymer adhesion.

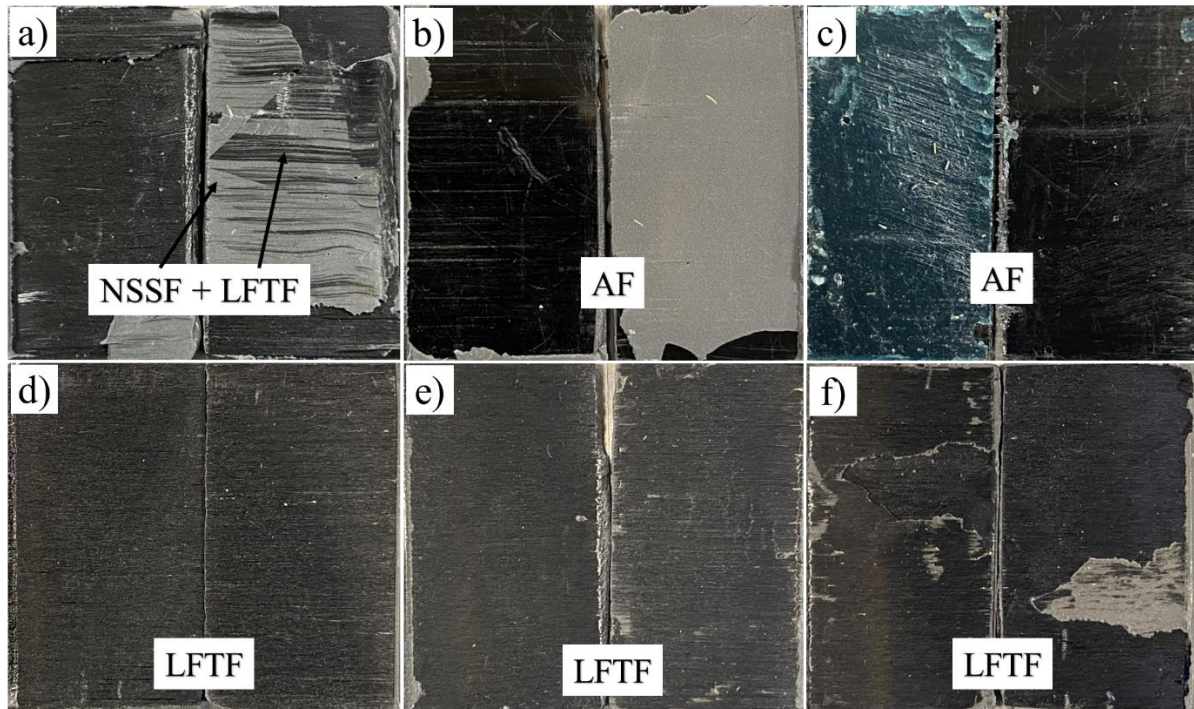


Figure 6.26. Representation of the failure modes of a) and b) non-treated samples bonded using Loctite adhesive cured in an oven and at room temperature, respectively, c) non-treated sample bonded using Araldite adhesive, d), e), and f) samples treated with 30 ns, 80 ns, and 200 ns pulse lasers, respectively, and bonded with Loctite adhesive and cured in an oven.

For laser-treated samples with 30 ns, 80 ns, and 200 ns pulses bonded with Loctite adhesive and oven-cured, the failure modes are depicted in **Figure 6.26** (d), (e), and (f), respectively. The observed failure mode is predominantly LFTF, where rows of fibres were torn from one coupon and stuck to the adhesive on the other coupon. The grey colour in **Figure 6.26** (f), corresponding to the sample treated with the 200 ns laser, is believed to be due to the penetration of the adhesive within a few rows of fibres. For the laser-treated samples bonded using Araldite adhesive, the failure modes are shown in **Figure 6.27**.

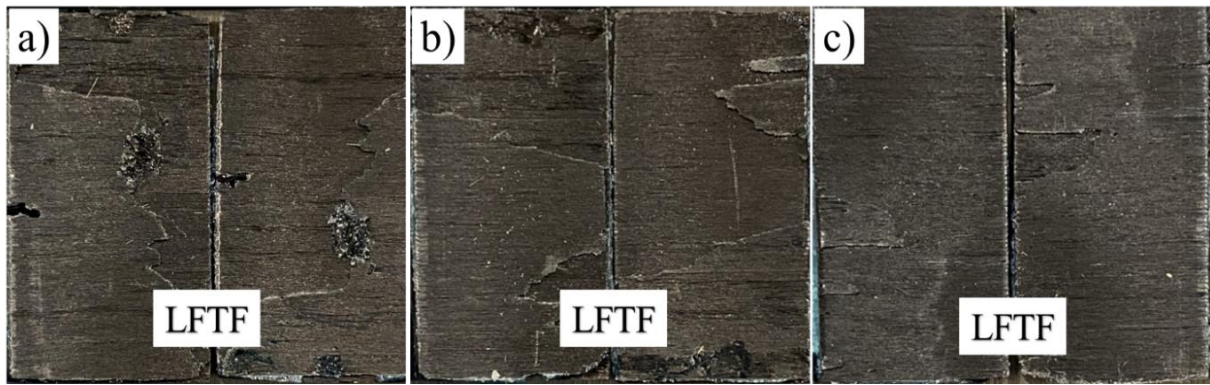


Figure 6.27. Failure modes of laser-treated samples bonded with Araldite adhesive, treated with a) 30 ns, b) 80 ns, and c) 200 ns pulse lengths.

No variations in failure modes were observed among the various laser-treated samples, regardless of the adhesive or curing technique used. Notably, the cured Araldite adhesive is dark blue and transparent, making it difficult to recognise against the black fibres in the macro photos of the failure modes, unlike the cured Loctite adhesive, which appears grey.

In addition to examining the failure modes, fracture analysis using optical microscopy (**Figure 6.28**) and SEM (**Figure 6.29**) was conducted on the cross-sections of some of the failed samples: non-treated samples and laser-treated samples with 30 ns and 200 ns pulses, all bonded using Araldite adhesive. The optical microscopy image of the cross-section of a fractured non-treated sample (**Figure 6.28** (a)) shows the layer of the bonding adhesive adhered to one of the failed coupons, with the failed surface appearing almost flat. **Figures 6.28** (b), (c), and (d) show cross-sections of failed samples treated with 200 ns pulses, where at least a single row of fibres was torn from one coupon and adhered to the adhesive on the other coupon. The SEM images (**Figures 6.29** (a) and (b)) compare the cross-sections of fractured samples treated with 30 ns and 200 ns pulses, respectively. The 30 ns sample predominantly shows a single row of fibres torn and stuck to the adhesive, whereas the 200 ns sample shows predominantly more than a single row of fibres.

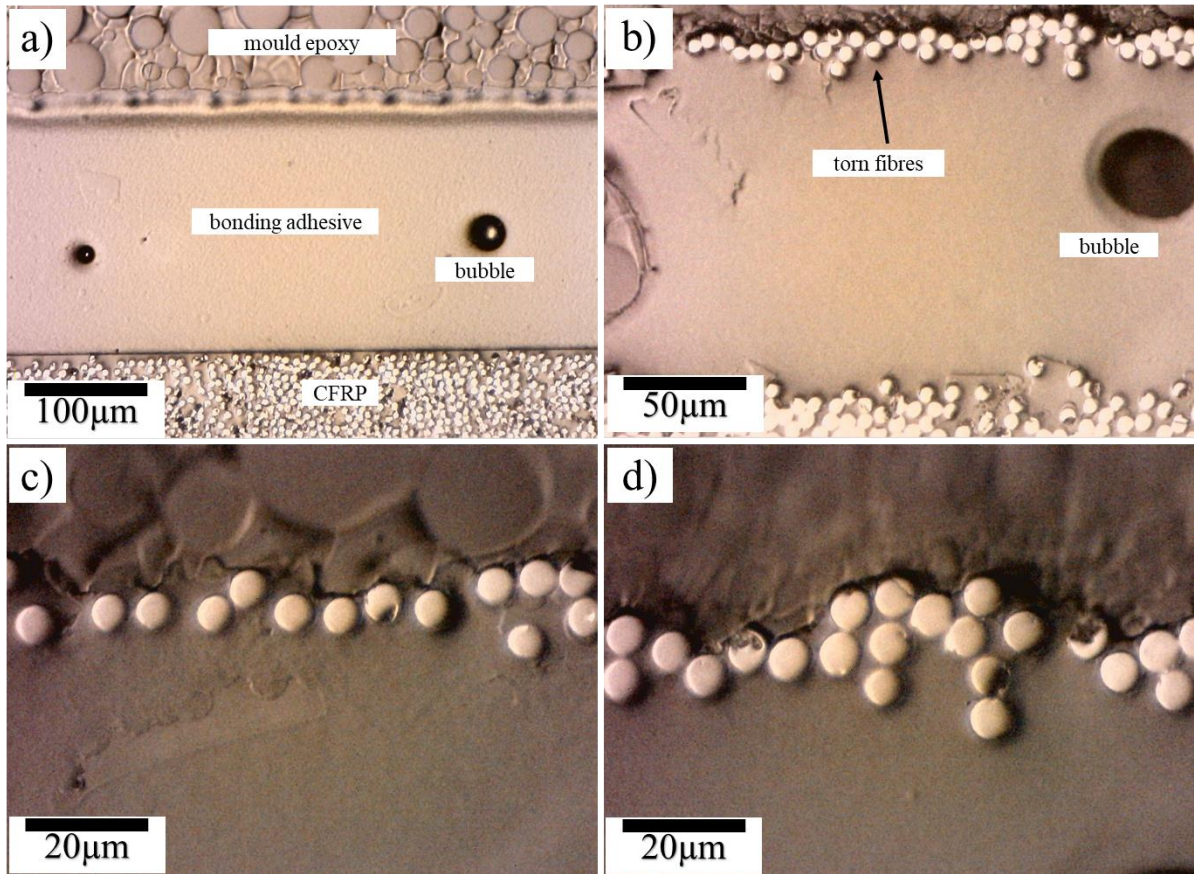


Figure 6.28. Optical microscopy images of cross-section of fractured a) non-treated sample, b), c), and d) laser treated using 200 ns pulse length with different magnifications show fibres was torn from one coupon and adhered to the adhesive on the other coupon.

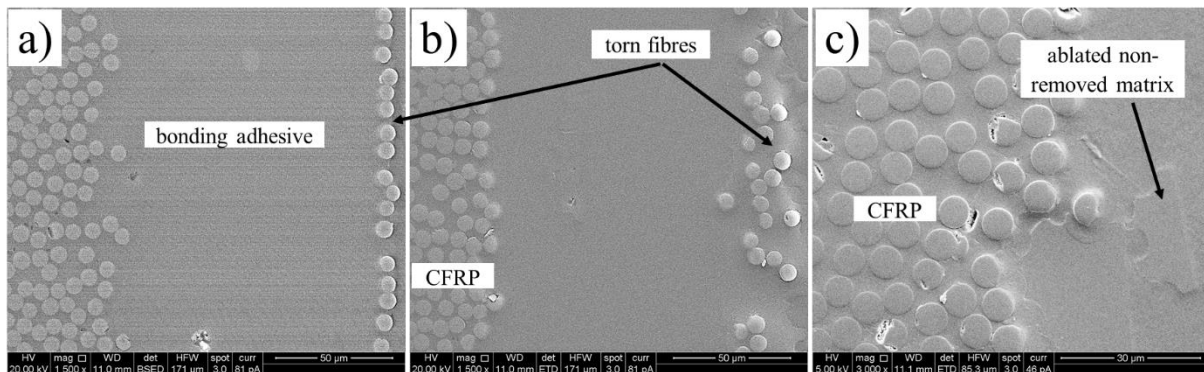


Figure 6.29. SEM images of the cross-sections of fractured laser-treated samples using pulse lengths of (a) 30 ns, (b) 200 ns, and (c) 200 ns, with high magnification focused on the CFRP-adhesive interface.

The SEM image in **Figure 6.29** (c) reveals an ablated non-removed matrix piece within the bonding adhesive, approximately 10 μm thick, which appears to serve merely as filler. Importantly, these matrix pieces seem to have minimal or negligible negative effects on the adhesive bonding strength.

The results of laser-treated samples generally indicated that NIR ns pulsed laser treatment in the range of 30 ns to 200 ns weakens the fibre-matrix integrity. In terms of matrix removal, processing with a 30 ns pulse laser is better than with a 200 ns pulse laser, where shorter pulses resulted in larger fibre-exposed regions with less degradation to the sizing layer of the CF. However, a high number of broken carbon fibres (CFs) were observed, which is believed to have a significant influence on the bonding strength. The fibre breakage can be attributed to the rapid increase in the temperature due to the higher instantaneous power of the short pulses. In contrast, the 200 ns pulse laser shows more effective evaporation of the matrix between and beneath the exposed fibres, allowing the bonding adhesive to penetrate between the fibres, which increases the bonded area, re-integrates the fibre-matrix and adds mechanical interlocking and consequently improves the adhesive strength significantly. The results of this investigation align well with several previous studies concerning the use of NIR ns pulsed lasers for surface treatment of CFRPs [26, 27].

6.8. Fourth study: Understanding the effects of the adhesive's modulus of elasticity on the concentrated stresses in single lap joints.

6.8.1. Methods (Fourth study)

The single lap joint was modelled using the educational version of SolidWorks. The modelling was for SLS test samples according to the standard BS EN ISO 1465:2009 [286], which is used throughout the entire research and specified in **Chapter 3/ Section 3.5**. The aim was to understand the effect of the modulus of elasticity on the concentrated stresses during the SLS test by comparing two adhesives with high and low moduli of elasticity. One end of the specimen was fixed, and a load of 6 kN was applied to the other end, as shown in **Figure 6.30**.

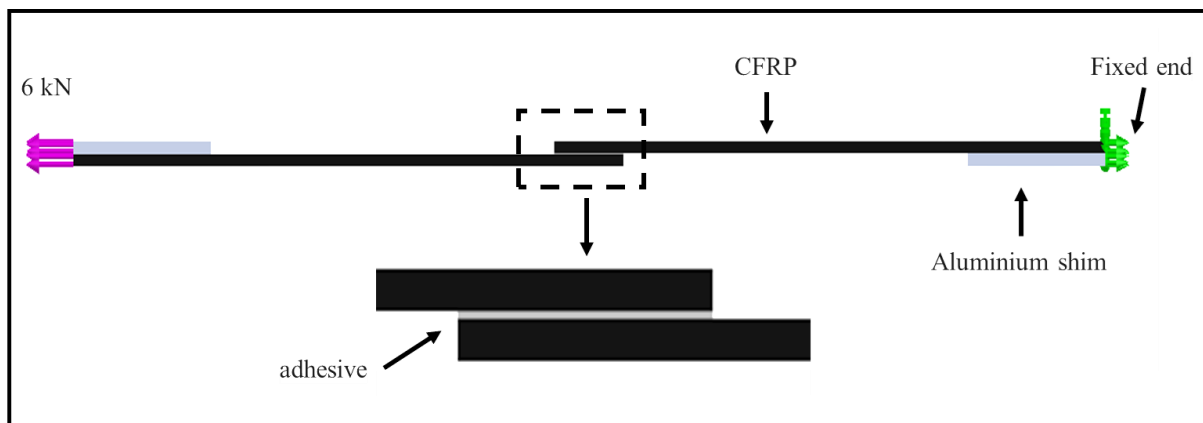


Figure 6.30. Side view of a single lap joint derived from the SolidWorks model.

The adhesive layer, 0.2 mm thick, was attached to the two coupons using the "mate" function with no clearance, ensuring it behaved as if welded or adhesively bonded according to SolidWorks specifications. Each of the adherends (CFRP coupons) was considered a single piece of composite reinforced with UD fibres aligned in the direction of the coupon's length. Two models were created within SolidWorks using two different adhesives: Loctite EA 9394 and Araldite 420. The mechanical properties of the adherend and the adhesives were customised using the SolidWorks material options based on the materials data sheets. For the adhesives, a Linear Elastic Isotropic Model was applied, assuming uniform mechanical properties in all directions, which is a reasonable approximation given the nature of the adhesives used. While for the adherend, it was orthotropic, indicating different mechanical behaviours along different axes including differences in stiffness and strength along the fibre.

The key distinctions in the mechanical properties of the two adhesives were observed in the modulus of elasticity (Loctite 9394 being approximately three times that of Araldite 420) and the shear modulus (Loctite 9394 being double that of Araldite 420), as detailed in **Table 6.6**. Full descriptions of the two adhesives are available in **Chapter 3/Section 3.3.2**. For the CFRP material properties, see **Section 6.4**. For the materials characteristics applied in SolidWorks software, see **Appendix C**. The models were meshed using the "Quick Mesh" option with the finest size for better accuracy.

Table 6.6. The main variations between Loctite EA9394 Aero Epoxy and Araldite 420.

| Property | Loctite EA9394 Aero Epoxy | Araldite 420 |
|-----------------------|--------------------------------|------------------------------------|
| Curing | 5 days @ 25°C or 1 hour @ 66°C | 1 hour @ 120°C or 1-2 weeks @ 25°C |
| Viscosity (Pa.s) | 160 @ 25°C | 35-45 @ 25°C |
| Tensile modulus (MPa) | 4237 | 1450 |
| Shear modulus (MPa) | 1360 | 730 |
| Elongation at break | 1.7% | 4.6% |

6.8.2. Results (Fourth study)

The SolidWorks simulation results, which compare the concentrated stresses between two adhesives (Loctite EA9394 and Araldite 420), are presented in **Figure 6.31**.

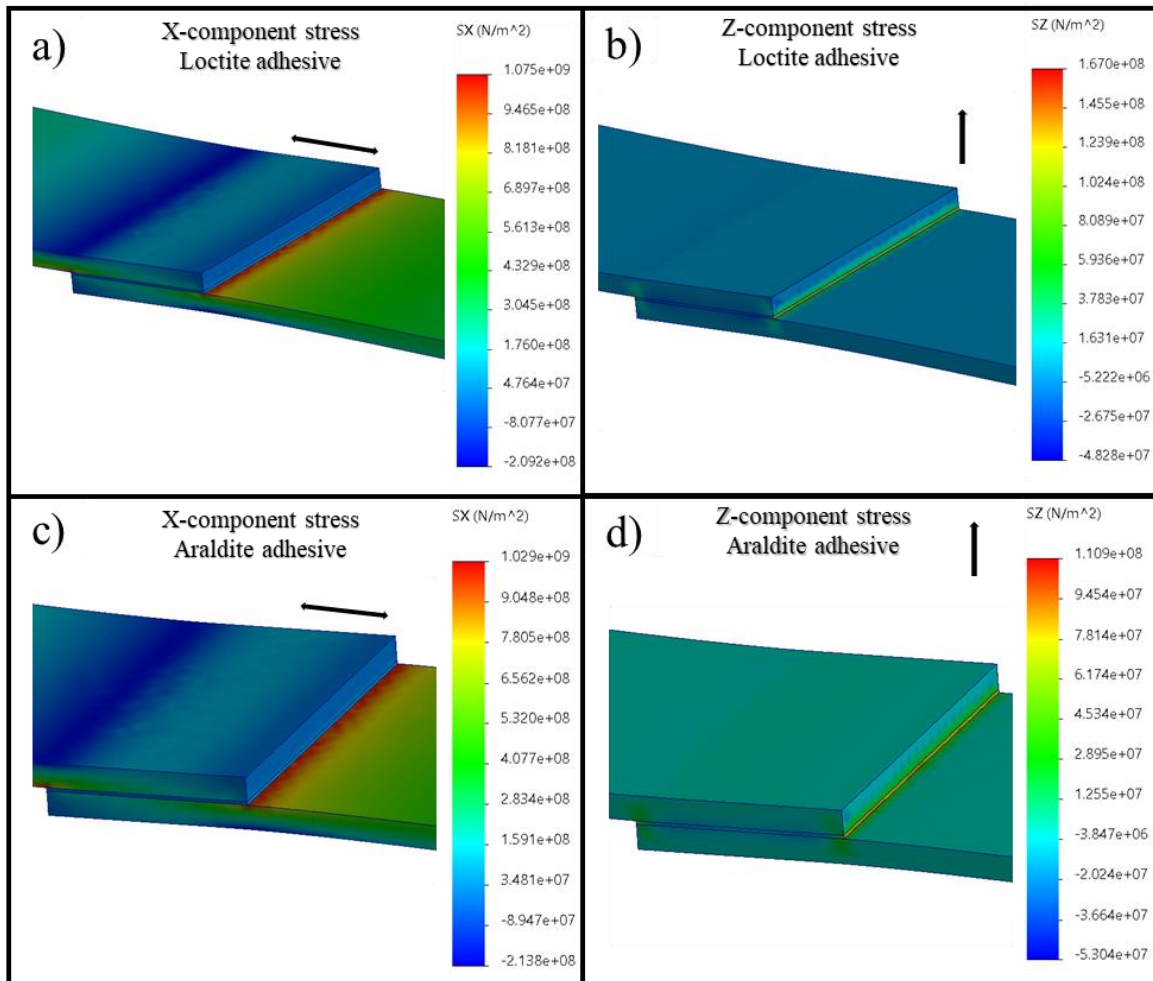


Figure 6.31. SolidWorks simulation results showing the x and z stress components of (a) and (b) the Loctite adhesive model, and (c) and (d) the Araldite adhesive model.

The simulation results indicated that high modulus adhesives result in higher concentrated peeling stresses at the bond line tips. The Loctite adhesive model exhibited a z-component stress of 167 MPa, representing the peeling stress, whereas the Araldite adhesive showed 111 MPa. This aligns with previous research, as shown in **Figure 6.32** [330].

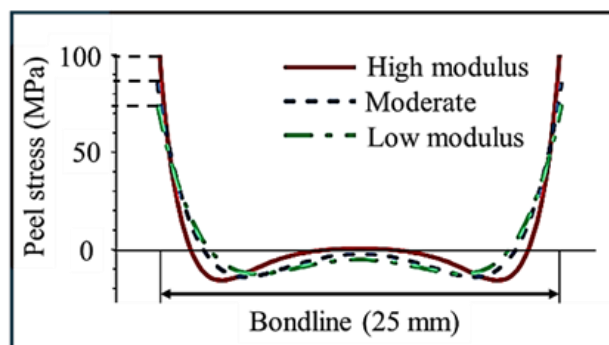


Figure 6.32. Peel stress distribution along the overlap of single lap joint using three different adhesives with variable modulus, adapted from [330]*.

In terms of the x-component stresses (**Figure 6.31** (a) and (c)), which represent shear stresses, no significant difference was observed between the two adhesives. Although several researchers have emphasised the significant impact of adhesive modulus on the maximum shear stress in single lap joints [331, 332], see **Figure 6.33**. However, the substantial difference between the modulus of the adherends and the adhesive can significantly diminish its impact on shear stresses. This latter issue has not been thoroughly documented in the literature.

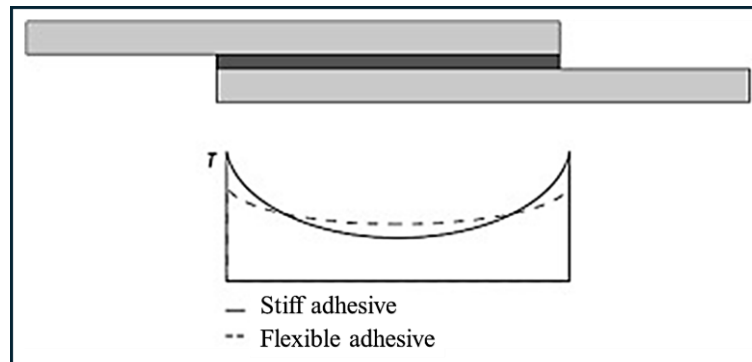


Figure 6.33. Shear stress distribution along the overlap of single lap joint using two different adhesives adapted from [332]*.

Regarding maximum strain, the Loctite 9394 model showed approximately 1.5%, while the Araldite 420 model exhibited about 3.3%.

A variable mesh approach, utilising finer and denser elements in regions near the bondline tips, could enhance both computational efficiency and accuracy, likely revealing areas of higher stress concentration. However, this refinement was not applied in the current model. Instead, the meshing approach relied on the default capabilities of SolidWorks Simulation, aligning with the study's primary objective of assessing whether significant variations in behaviour arise due to the use of adhesives with markedly different moduli.

An examination of existing research on the effect of adhesive modulus of elasticity reveals considerable focus on the influence of concentrated stresses on the failure loads in SLS tests [331, 333, 334], the latter has particular effects when the adherends are composite laminates [335]. The low transverse tensile strength (through the thickness) of composites, which is of the same order or lower than the adhesive strength, can lead to interlaminar failure due to high peel stresses at the ends of the overlap [333]. Additionally, differential adhesive straining along the bonded line leads to non-uniform shear stresses concentrated at the ends of the bonded line. This typically occurs when a non-ductile adhesive is used [331].

The concentrated shear and/or peel stresses can cause bond failure before the theoretical maximum joint strength is attained [336]. In the current study, no significant difference in shear stresses was observed between the two adhesives because, compared to both adhesives, the adherend has a very high modulus of elasticity along the bond line. Consequently, no significant differential straining of the adhesive is expected. Ductile or flexible adhesives generally have lower strengths. However, their ability to distribute stress uniformly along the overlap and deform plastically can result in a joint strength much higher than with seemingly stronger but less ductile adhesives [333].

This modelling study aligns well with the experimental results of the lap joint tests presented in this chapter, which compared the failure loads of adhesively bonded coupons using the same two adhesives. Moreover, the results are highly consistent with the literature, where high-stiffness adhesives create higher concentrated stresses at the bond line ends, leading to failure under lower loads. Full modelling results, including detailed stresses and strains, are available in **Appendix D**.

6.9. Conclusions

- Cross-section assessments revealed significant variation in the thickness of the outermost epoxy matrix layer (distance from the surface to the fibres) in as-received CFRP samples, ranging from 1 to 25 μm , with an average of about 10 μm . Non-uniformity in fibre distribution was observed, varying across different positions within the samples.
- Investigation into heat accumulation between consecutive scans found no observable variations despite comparing pulse intervals of 1.5 ms and 2.5 ms, slightly longer than the reported cooling times for the matrix resin of approximately 1 ms.
- Laser processing with a pulse length of 30 ns led to larger ablated areas (dimples) compared to a 200 ns pulse laser, with higher pulse energies producing larger dimples. The average dimple area increased linearly with pulse energy, and dimples created with 30 ns pulses were nearly double the size of those created with 200 ns pulses at the same energy level. While the depth of the dimples was primarily constrained by the underlying carbon fibres, 200 ns pulses caused the matrix around the CFs to evaporate, resulting in deeper pockets. Additionally, 30 ns pulses produced sharper edges and less matrix evaporation compared to 200 ns pulses. Moreover, 200 ns pulses degraded the sizing layer of carbon fibres, leading to the visibility of fibre wrinkles.

- The water contact angles for laser-processed samples consistently decreased over time due to surface porosity, indicating significant liquid absorption. Initially ranging from 20°-40°, they fell to 0°-30° within 200 seconds, showing linear stability. Notably, samples treated with 200 ns pulses had lower WCAs than those treated with 30 and 80 ns pulses, likely due to matrix evaporation around the fibres.
- Surface treatment of CFRP materials utilising ns pulse laser significantly improved the adhesive bonding strength, with 200 ns pulse laser showing the most notable improvement (over 60%) compared to non-treated samples.
- Shorter pulse lengths (30 ns) offer better matrix ablation but risk damaging or breaking the load-carrying CFs. In contrast, longer pulse lengths (200 ns) enable more effective evaporation of the matrix around the fibres, thereby enhancing adhesive strength.
- Adhesives with lower modulus of elasticity demonstrated lower concentrated peeling stresses and stronger bonding strength.

CHAPTER 7: Surface Treatment of CFRP Composites Using Continues Wave Carbon Dioxide Laser

7.1. Introduction

Due to their easy availability and the low capital and operating costs, CO₂ lasers find extensive applications in processing a wide variety of polymeric materials [337]. However, due to their lower photon energy, CO₂ laser systems deposit more heat into the material, thereby increasing the risk of damage and delamination [15]. In CFRP, the substantial difference in thermal properties between carbon fibres and the resin matrix leads to the creation of a significant heat-affected zone (HAZ). This compromises the integrity of the composite by degrading the interface between the CFs and the matrix [338]. Recently, numerous studies have explored utilising pulsed CO₂ lasers for the surface treatment of CFRPs to enhance adhesive bonding, with many demonstrating effective selective removal of the epoxy matrix material [9, 15, 20, 25]. The high intensities and short interaction times of pulsed lasers generally allow for the processing of CFRPs with very high quality and minimal thermal damage, as only a small fraction of the incident laser energy is converted to residual heat, which does not contribute to the ablation process [339]. CW CO₂ lasers, commonly used in metalworking applications, have been highly investigated for machining of CFRP laminates. However, to the best of available knowledge, only a single study has explored their use for CFRP surface treatment to improve adhesive bonding. In their study, Nattapat et al. [16] have successfully removed the top resin layer, a crucial step before adhesive bonding, without damaging the underlying fibres, resulting in nearly double the adhesive bonding strength compared to the untreated material.

This chapter investigates the use of a CW CO₂ laser to enhance the adhesive bonding of CFRP composites. The study explores the effects of various processing variables on material removal in both CFRP material and bulk resin. It also examines wettability and adhesive bonding strength across different laser parameters. Two different CFRP materials were tested for adhesive strength. The results showed a slight improvement (approximately 30%) in the bonding strength of one material, while the other showed a decrease in bonding strength. In terms of wettability, processing CFRP material with a CO₂ laser increased the WCA, approaching superhydrophobicity. For matrix removal, at high scanning speeds, matrix removal was found to be a function of the Linear Energy Density (LED).

7.2. Objectives

- Investigating the feasibility of utilising CW CO₂ lasers for the surface treatment of CFRP composites to improve adhesive bonding.
- Examining the effects of various laser processing variables on matrix removal and bonding strength.
- Understanding the matrix removal mechanism.

7.3. Experimental design and workflow

This chapter, like the previous ones, involves multiple experiments and phases, either separate or linked. First, two separate experiments were conducted to study the effect of CO₂ laser variables on CFRP material and bulk epoxy resin. These experiments aimed to understand how these variables impact material removal. Along with the previous investigation on matrix transmittance (**Chapter 4/Section 4.4**), these studies provided insights into both the laser variable effects on ablation and the ablation mechanism itself. Second, wettability and bonding strength were assessed and compared across different processing variables. The flowchart in Figure 7.1 illustrates the experimental workflow.

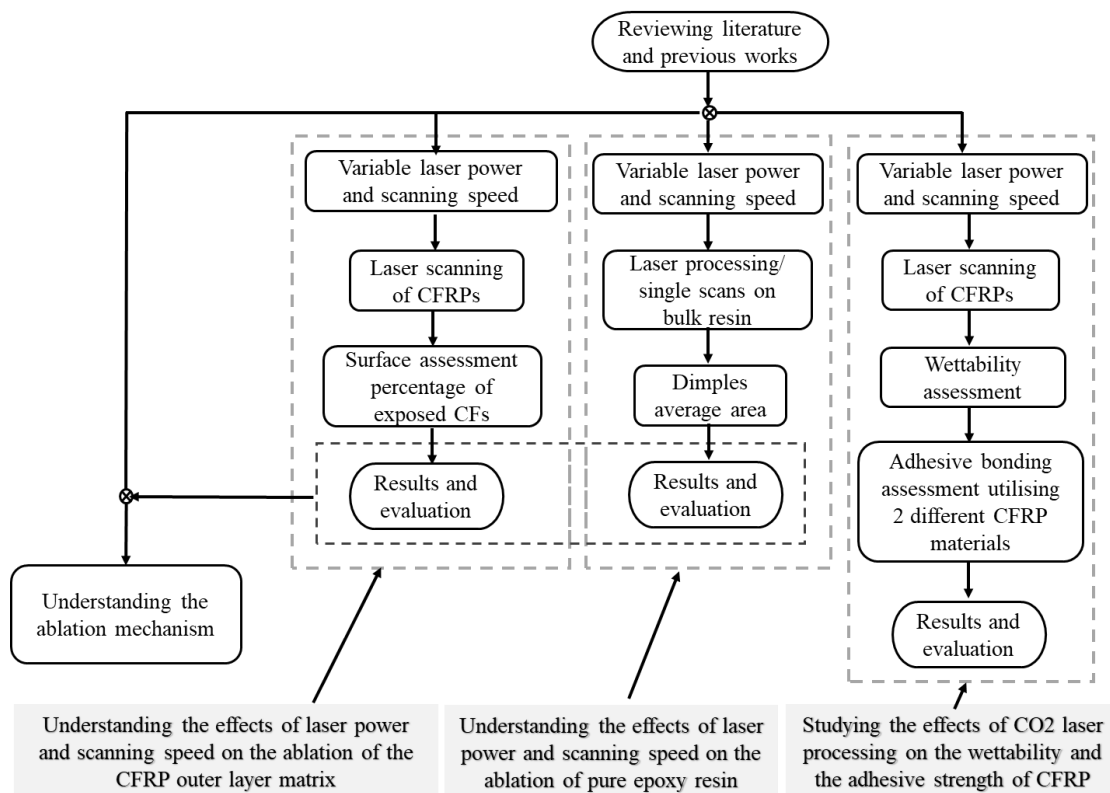


Figure 7.1. Flowchart simplifies the experimental design and workflow.

7.4. Experiments

Three separate experiments were conducted using the CW Lotus CO₂ Laser Systems LL10060, detailed in **Chapter 3/Section 3.2.2**. The methods and results of each experiment are outlined in the subsections as follows. All the surface assessment apparatus that was utilised in this chapter including optical microscopy, digital microscopy, optical profilometry, and goniometer are detailed in **Chapter 3/Section 3.2.4**.

7.4.1 Understanding the effects of laser power and scanning speed on the ablation of the CFRP outer layer matrix.

To understand the effect of laser power and scanning speed on the removal of the outer layer matrix, 15 different laser processing runs (samples), each with specific laser power and scanning speed, were performed on a single CFRP specimen. This approach was taken to minimise the effect of the potential material inhomogeneity arising from variations in position or between sides of the specimens. The material utilised was the UD fibre CFRP, detailed in **Chapter 6/Section 6.4**. The hatch spacing (H) for all runs was 0.2 mm, which is slightly greater than the laser spot diameter (d) at the focus ($d = 0.185$ mm). For all samples, the laser beam was focused on the specimen surface, and the scanning was conducted perpendicular to the direction of the CFs. To avoid possible scanner delay effects during the reversal of direction, a large over-scan distance of 75 mm was employed, see **Figure 7.2**.

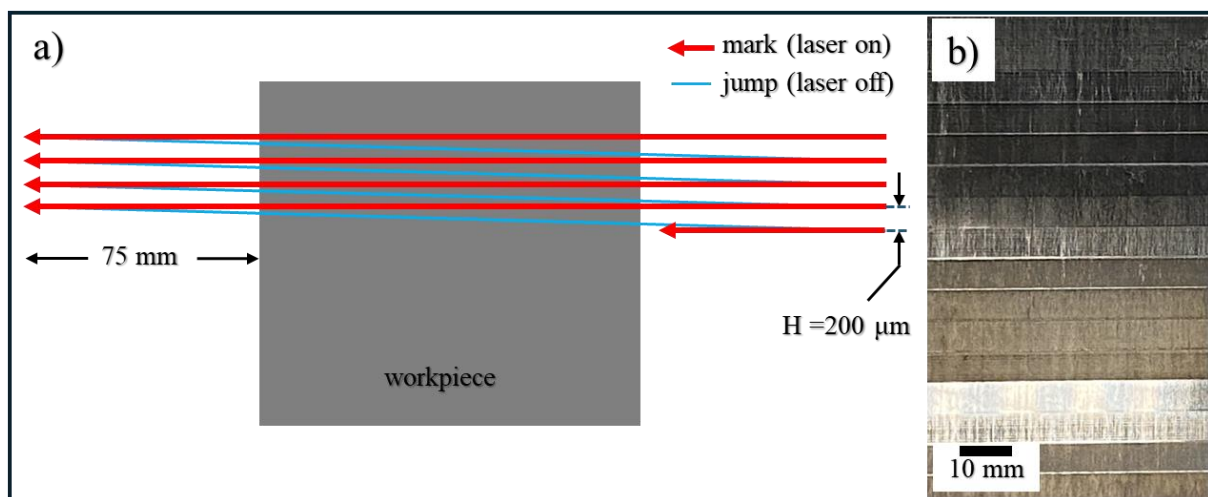


Figure 7.2. a) scheme of the scanning pattern, and b) the laser-processed specimen.

The samples were then assessed using optical microscopy, digital microscopy, and optical profilometry. The LED for each run was calculated using **Equation 7.1** [340].

$$LED = \frac{P}{v} \quad (7.1)$$

Where (P) is the laser power and (v) is the scanning speed.

Additionally, the interaction time (t_i) of the laser scanning for each sample was determined using **Equation 7.2**, [341]. Where (d) is the laser beam diameter.

$$t_i = \frac{d}{v} \quad (7.2)$$

The percentage of fibre-exposed area for each sample was estimated using the ImageJ colour thresholding feature. This analysis was based on the digital microscopy images depicted in **Figure 7.3**. **Table 7.1** presents the processing variables along with the calculated and resultant values for each sample.

Table 7.1. The laser processing variables along with the calculated and resultant values for each sample.

| Sample (#) | P (W) | v (mm/s) | LED (J/cm) | t_i (ms) | Ablation (%) |
|------------|-------|----------|------------|------------|--------------|
| 1 | 2.25 | 50 | 0.45 | 3.7 | 100 |
| 2 | 2.25 | 75 | 0.3 | 2.5 | 95 |
| 3 | 2.25 | 100 | 0.23 | 1.85 | 55 |
| 4 | 2.25 | 150 | 0.15 | 1.2 | 4 |
| 5 | 4 | 50 | 0.8 | 3.7 | 100 |
| 6 | 4 | 75 | 0.53 | 2.5 | 100 |
| 7 | 4 | 100 | 0.4 | 1.85 | 97 |
| 8 | 4 | 150 | 0.27 | 1.2 | 91 |
| 9 | 4 | 200 | 0.2 | 0.9 | 83 |
| 10 | 4 | 250 | 0.16 | 0.74 | 31 |
| 11 | 4 | 300 | 0.13 | 0.62 | 7 |
| 12 | 6 | 150 | 0.4 | 1.2 | 96 |
| 13 | 6 | 200 | 0.3 | 0.9 | 91 |
| 14 | 6 | 250 | 0.24 | 0.74 | 87 |
| 15 | 6 | 300 | 0.2 | 0.62 | 80 |

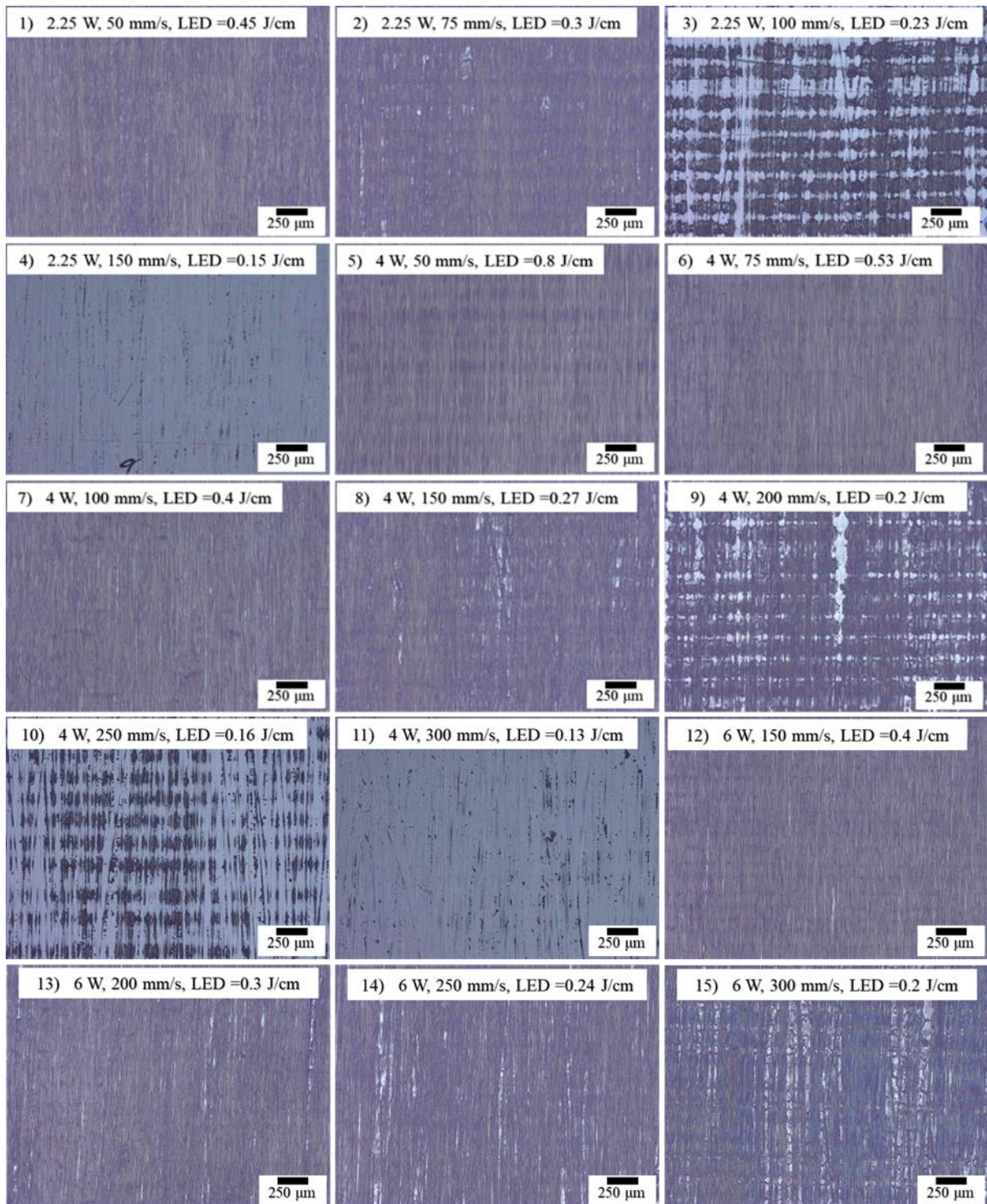


Figure 7.3. Digital microscopy images of the laser processed CFRP samples, the sample number and the processing variables along with the LED are marked on top of each sample.

The plots in **Figure 7.4** represent the percentage of the removed outer layer matrix as a function of the LED for each of the three laser powers used in this experiment. For the 6 W plot, the lowest removal percentage is 80%, achieved with a scanning speed of 300 mm/s. Achieving a

lower removal percentage with 6 W was hindered by the table's maximum scanning speed limit of 300 mm/s, preventing further reduction of the LED.

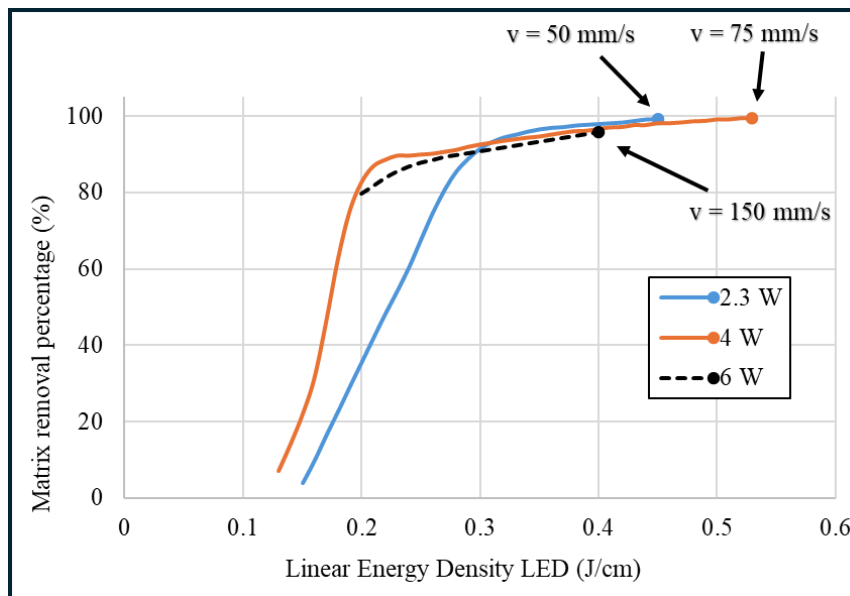


Figure 7.4. The relationship between the LED and the matrix removal percentage.

For the other two laser powers (2.3 W and 4 W), **Figure 7.4** shows that matrix removal initiates at an LED of about 0.15 J/cm for the 2.3 W laser and about 0.12 J/cm for the 4 W power laser. As the LED increases, the matrix removal percentage (exposed fibres) rises rapidly and linearly up to approximately 80%. For the 4 W laser power, an LED of 0.2 J/cm achieves 80% removal, whereas the 2.3 W laser power requires an LED of 0.27 J/cm to achieve the same percentage. In this region (0-80%), representing the removal of the shallow matrix resin, the lower laser power (2.3 W) requires a higher LED to achieve similar removal percentages as the 4 W laser power. This outcome is logical, as the increased interaction time allows more heat to dissipate through the CFRP constituents, particularly the CF. A similar trend was reported in the finite element analysis study conducted by Nattapat et al. [16]. Although the laser power in the mentioned study was applied as surface heat flux, the transmittance was not considered.

Based on previous findings within this thesis regarding the absorption and transmission of the matrix resin to the CO₂ laser (**Chapter 4/ Section 4.4**), the average thickness of the outer matrix layer of the CFRP material used in this investigation was estimated to be about 10 μm. By assuming that the epoxy resin used in that experiment has similar absorption behaviour to the matrix resin of the CFRP material, it means that about 60% of the laser intensity is transmitted through this matrix layer and absorbed by the underlying fibres, while only 25% of the laser

intensity is absorbed by the matrix itself, with the rest being reflected, as illustrated in **Chapter 4 /Figure 4.11**. Accordingly, the removal of such thin matrix zones is highly influenced by the heat conducted from the laser-induced CFs and, to a lesser extent, by the direct matrix absorption of the laser radiation. However, for thicker matrix resin zones such as 30 or 40 μm thick, only a small amount of the laser intensity is transmitted to the underlying fibres, which might not be enough to elevate the fibre temperature to the point where the matrix resin is degraded. Therefore, the removal of such rich matrix zones occurs mostly due to direct matrix absorption of laser radiation. This explains why the three plots for the different laser powers in **Figure 7.4** converge between 90-100% of the matrix removal, which represents the removal of rich matrix zones. In these zones, most of the laser intensity is absorbed by the low-conductive matrix itself, resulting in less influence from the differences in the interaction time, as minimal heat is dissipated via the fibres. It is worth noting that attempting to achieve 100% matrix removal by increasing the laser energy density (LED) while using a 0.2 mm hatch spacing, which is slightly wider than the laser spot diameter, can potentially compromise the fibre-matrix integrity, resulting in loose fibres at the surface. In such cases, a higher LED is required to remove the matrix in regions between adjacent scans, which could lead to excessive matrix removal at the centre of the laser scans.

In addition to the above findings, it was observed that the non-removed matrix expanded due to the formation of bubbles within the matrix. Optical profilometry assessment (**Figure 7.5**) shows that the non-removed, CO₂ laser-treated CFRP matrix expanded by 100-200 nm.

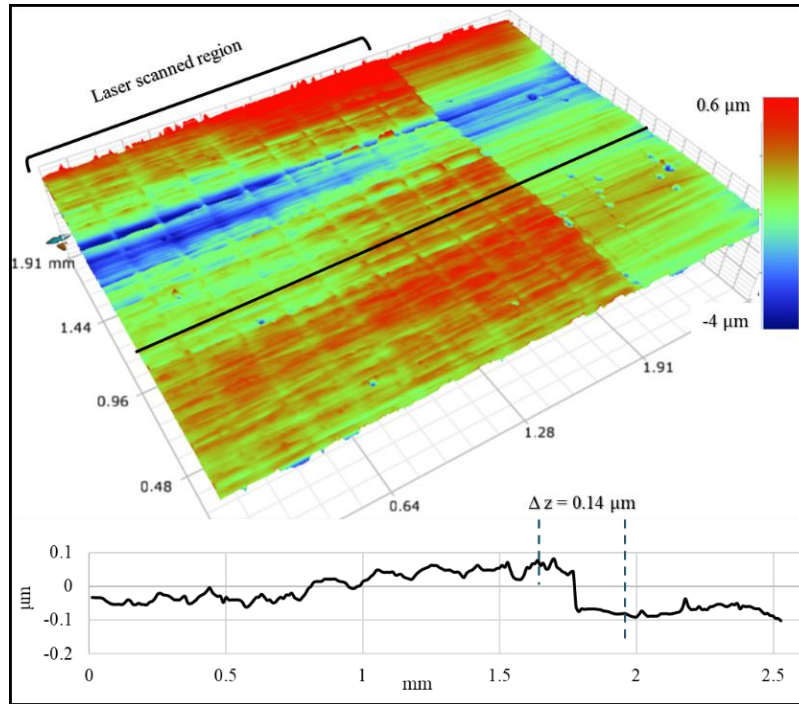


Figure 7.5. An optical profilometry image with a surface profile shows the expansion of the laser-treated region compared to the non-treated region of sample 4, which was treated with a low LED (15 J/cm²) CO₂ laser.

High-magnified optical microscopy images of a CFRP sample treated with a low LED CO₂ laser show sub-micro particles within the matrix, believed to be tiny bubbles (see **Figure 7.6** (b)).

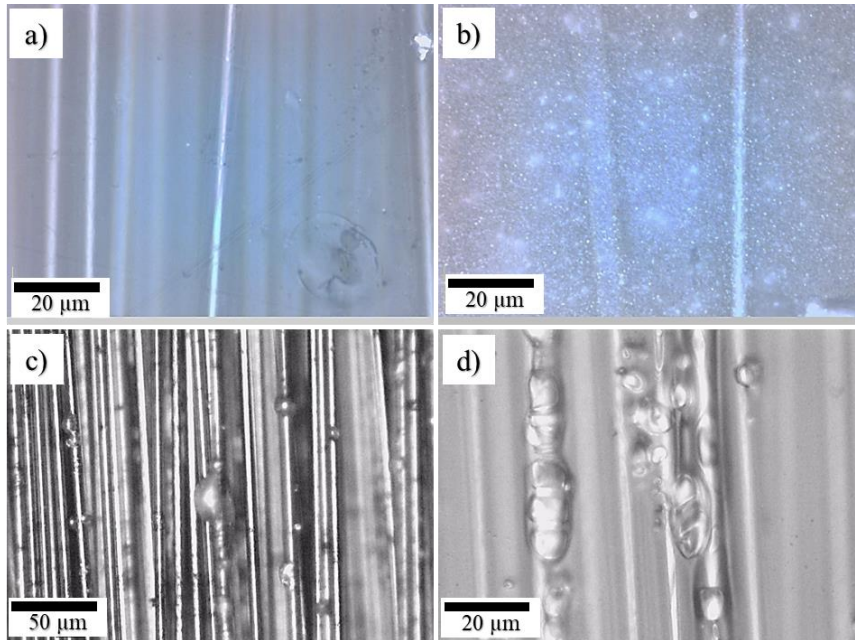


Figure 7.6. Optical microscopy images of (a) as-received CFRP material, (b) laser-treated CFRP with low LED (non-removed matrix), (c) laser-treated with high LED (fully exposed fibres), and (d) laser-treated CFRP with low LED showed inflation of the matrix in regions where the CFs are close to the surface.

Additionally, optical microscopy images of samples treated with high LED, where the fibres are fully exposed, showed bubbles ranging in size from 5-10 μm adhered to the fibres (**Figure 7.6 (c)**). Moreover, optical microscopy images of CFRP samples treated with low LED (**Figure 7.6 (d)**) showed inflation of the matrix in regions where the CFs are close to the surface. These findings are related to the ablation mechanism, which will be discussed later in this chapter.

7.4.2 Understanding the effects of laser power and scanning speed on the ablation of pure epoxy resin.

The effect of both laser power and scanning speed of a CW CO_2 laser on the ablation of pure epoxy resin was investigated. A 2 mm thick epoxy resin sample was created by moulding IN2 resin on a glass laminate. IN2 resin, two parts ultra-low viscosity infusion thermoset epoxy typically used as a matrix in fibre-reinforced composites, was utilised according to its datasheet; full characteristics of the resin are available in **Chapter 3/Section 3.3.3**. A foam tape (2 mm thick) was used as shims, **Figure 7.7**. The glass laminate was wiped with a lint-free cloth soaked in CR1 Easy-Lease, a volatile chemical release agent from Easycomposites UK, and allowed to evaporate for about 60 seconds before applying the resin. The moulds were then left for seven days at room temperature to be fully cured.

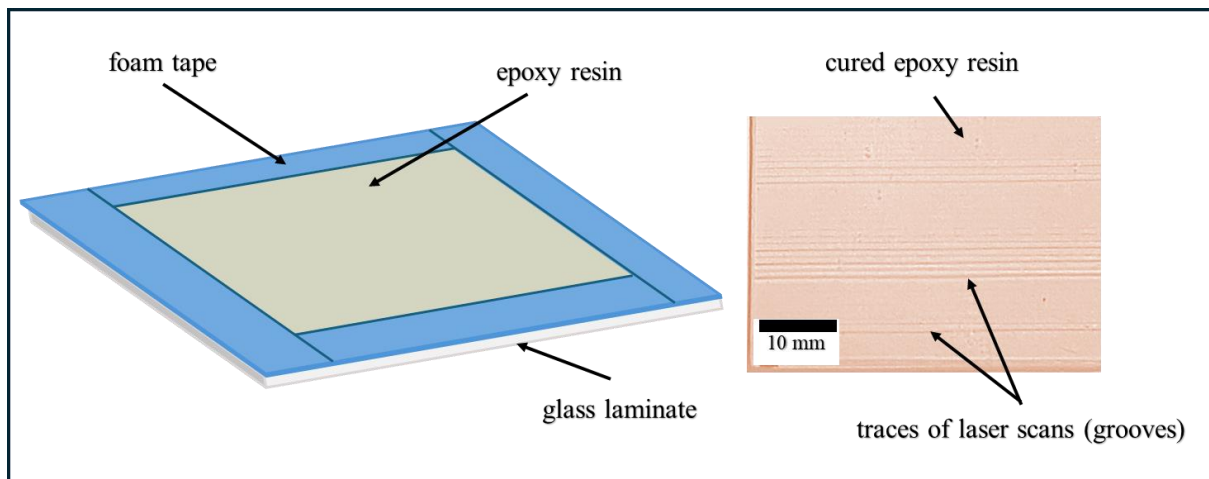


Figure 7.7. Schematic illustration of the epoxy resin moulding process (on the left), photo of the resin sample processed with laser (on the right).

The cured epoxy sample was processed with a laser using 15 different sets of processing variables (laser power and scanning speed). A single scan (mark) was performed for each set to create grooves, which were spaced 1 mm apart. The LED and the interaction time (t_i) were calculated; see **Table 7.2**.

Table 7.2. The laser processing variables along with the calculated and resultant depth and width of each groove.

| groove (#) | P (W) | v (mm/s) | LED (J/cm) | t_i (ms) | depth (μm) | width (μm) |
|------------|-------|----------|------------|------------|-------------------------|-------------------------|
| 1 | 2.25 | 50 | 0.45 | 3.7 | 17 | 165 |
| 2 | 2.25 | 75 | 0.3 | 2.5 | - | - |
| 3 | 2.25 | 100 | 0.23 | 1.85 | - | - |
| 4 | 2.25 | 150 | 0.15 | 1.2 | - | - |
| 5 | 4 | 50 | 0.8 | 3.7 | 58 | 390 |
| 6 | 4 | 75 | 0.53 | 2.5 | 34 | 310 |
| 7 | 4 | 100 | 0.4 | 1.85 | 18 | 190 |
| 8 | 4 | 150 | 0.27 | 1.2 | - | - |
| 9 | 4 | 200 | 0.2 | 0.9 | - | - |
| 10 | 4 | 250 | 0.16 | 0.74 | - | - |
| 11 | 4 | 300 | 0.13 | 0.62 | - | - |
| 12 | 6 | 150 | 0.4 | 1.2 | 18 | 187 |
| 13 | 6 | 200 | 0.3 | 0.9 | 8 | 115 |
| 14 | 6 | 250 | 0.24 | 0.74 | - | - |
| 15 | 6 | 300 | 0.2 | 0.62 | - | - |

The sample was then assessed using optical microscopy and optical profilometry (Bruker) to measure the grooves depth and width. For the Bruker, VXi mode, which is typically used when a transparent material is assessed, and it was challenging to obtain continuous profiles for some of the created grooves accordingly data restore function of the Bruker software were utilised. The optical microscopy images in **Figure 7.8** revealed that grooves created using 2.25 W with a scanned speeds above 50 mm/s showed no significant depth, where only some bubbles are observed on the laser scanned region. Similarly, those treated with 4 W and 6 W exhibited no significant depth when scanned at speeds above 100 mm/s and 200 mm/s, respectively.

Optical profilometry assessment revealed that grooves created with an LED of 0.3 J/cm or less (except for groove 13) have depths of less than 1 μm and are surrounded by expanded regions approximately 600 μm wide. These regions expand up to about 1 μm in height. The presence of bubbles in these areas appears to cause the expansion. **Figure 7.9** represents optical profilometric images of grooves numbers 8 and 14 as examples.

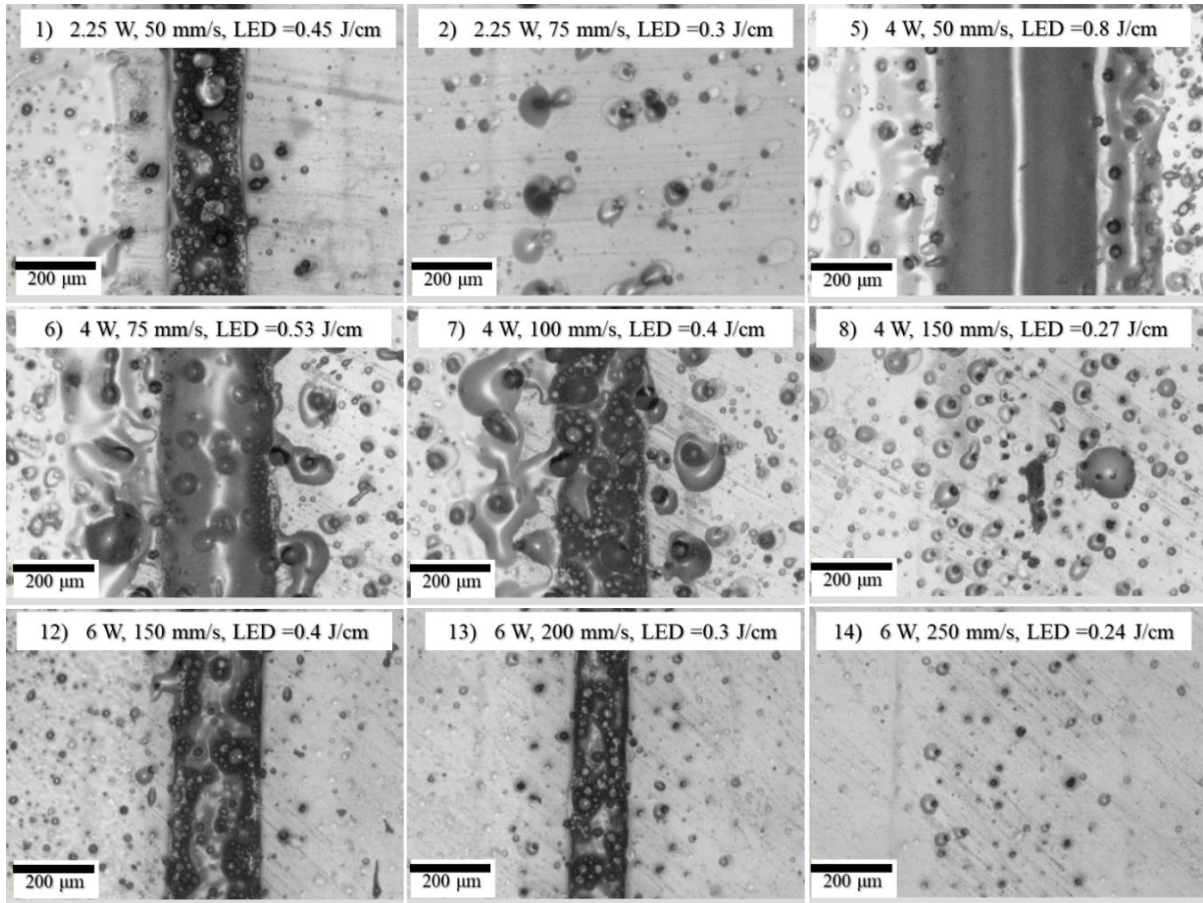


Figure 7.8. Optical microscopy images of pure epoxy resin sample, each processed with a single CO₂ laser scan utilising variable laser power and scanning speeds.

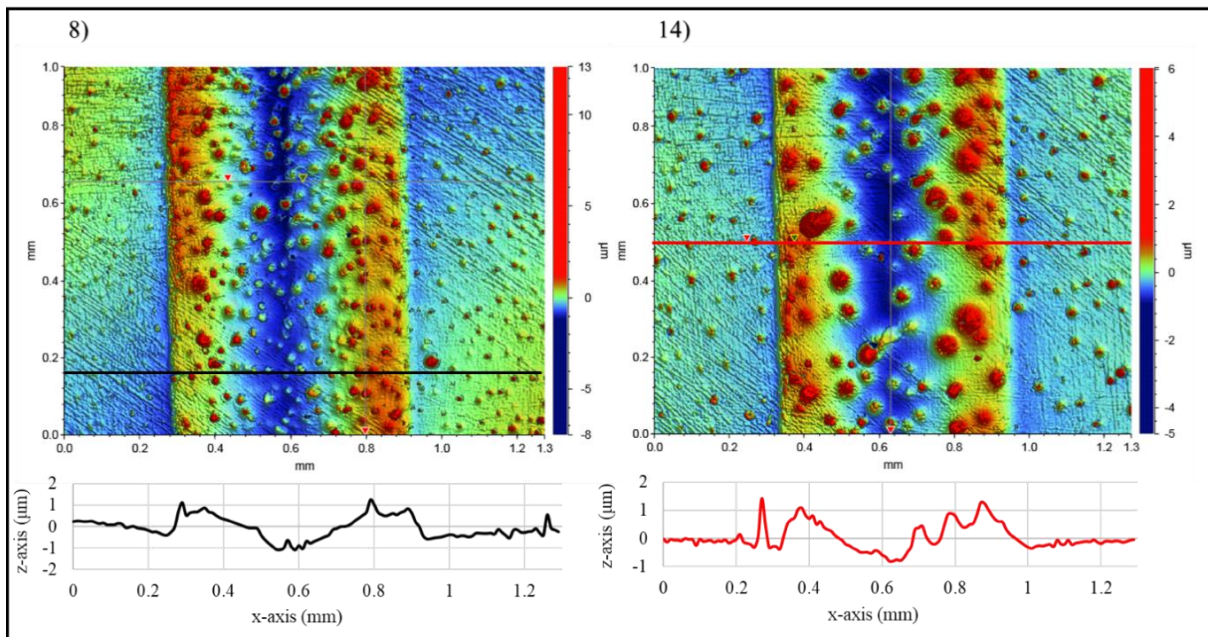


Figure 7.9. 2D optical profilometric images of grooves 8 and 14, along with their profiles represented at the bottom of the figure.

In contrast, grooves created with LED over 0.3 J/cm show significant depth and width, see **Figure 7.10**. Comparing grooves numbers 2 and 13, groove 2 shows no noticeable depth, whereas groove 13 has a depth of about 8 μm . Both grooves were processed using an LED of 0.3 J/cm; however, the interaction time for groove 2 is approximately three times longer than that for groove 13, indicating that heat dissipation plays a significant role. In other words, during the laser processing of groove number 2, the temperature at the laser-exposed area might have remained below the evaporation temperature of the material, which is around 500°C [342].

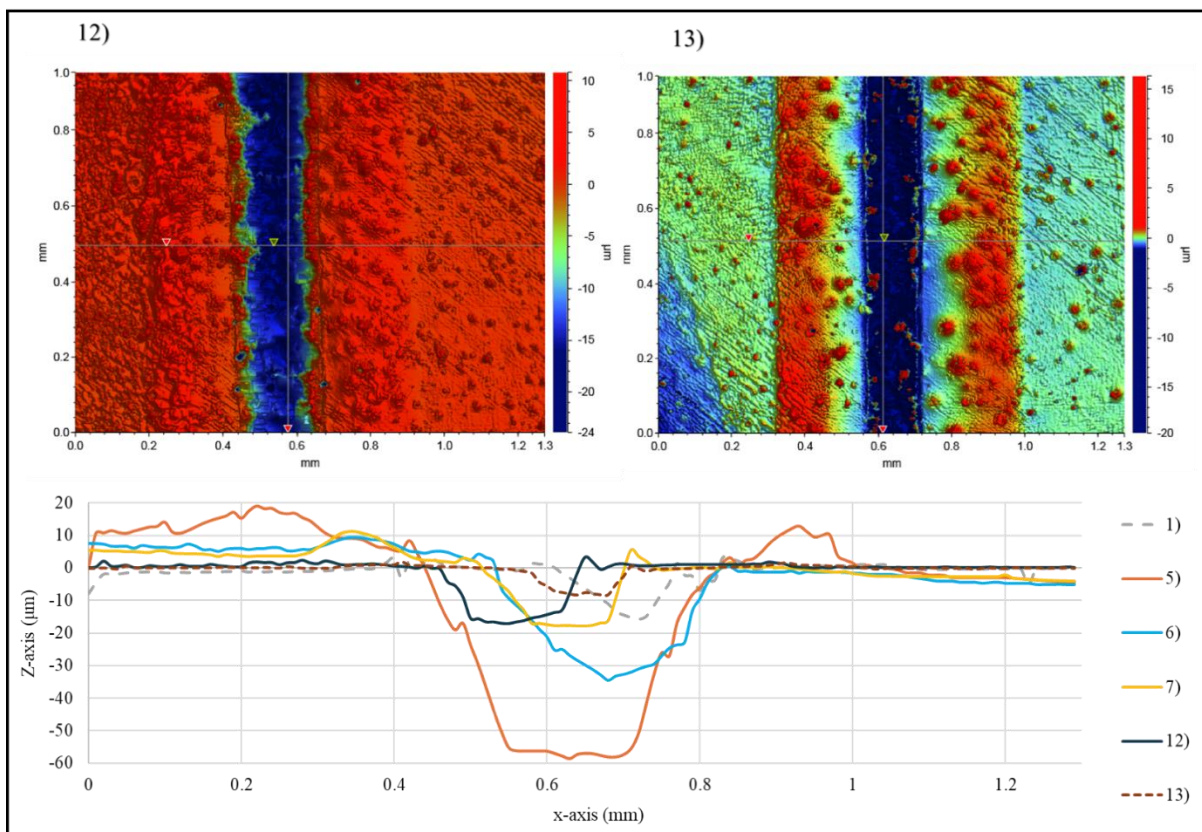


Figure 7.10. Top: 2D optical profilometric images of grooves 12 and 13. Bottom: profiles of grooves 1, 5, 6, 7, 12, and 13.

The plots in **Figure 7.11** represent the influence of the laser LED on the groove depth and width. Despite the varying interaction times, a linear relationship appears to be evident. The trend line of groove depth versus LED indicates that ablation initiates at an LED of approximately 2.5 J/cm². Conversely, for CFRP (**Figure 7.4**), the ablation of the matrix begins at an LED of less than 1.5 J/cm². This difference is attributed to variations in material interactions, where the ablation of the matrix in CFRP is governed by a combination of direct evaporation and heat conduction from the underlying irradiated fibres.

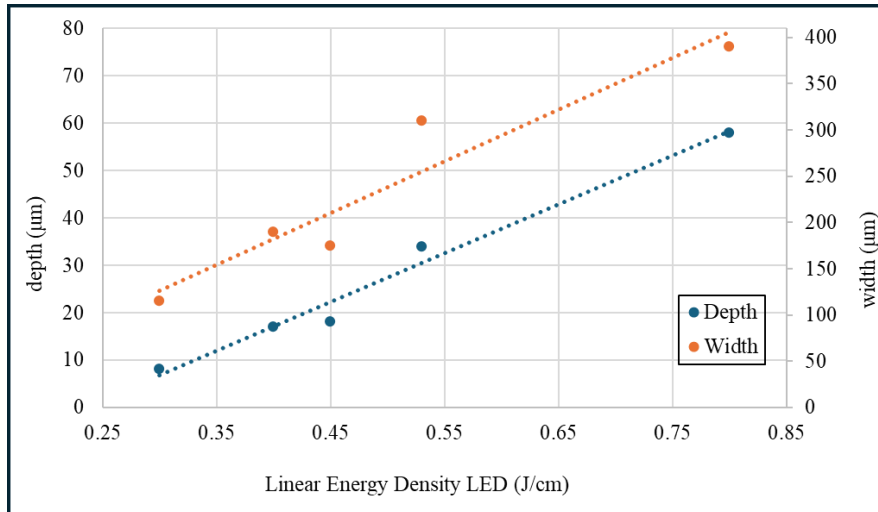


Figure 7.11. The influence of LED on groove depth and width.

7.4.3. Studying the effects of CW CO₂ laser processing on the wettability and the adhesive strength of CFRP composite

In this study, two CFRP materials (referred to as CFRP material 1 and CFRP material 2) were investigated. CFRP material 1 is the same material used in **Section 7.4.1**, which is reinforced with UD CFs, fully described in **Chapter 6/Section 6.4**. The second CFRP material is a 2 mm thick 2/2 twill, 3k woven carbon fibre fabric with a smooth, glossy surface, supplied by Easycomposite UK (see **Figure 7.12**). It has a tensile strength and modulus in the 0/90° directions of approximately 500 MPa and 30 GPa, respectively. The laser used is the CW Lotus CO₂ Laser Systems LL10060, detailed earlier.

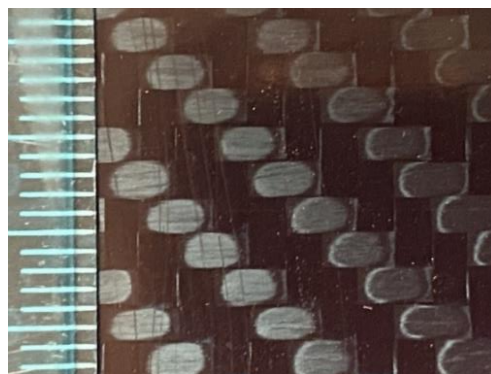


Figure 7.12. A photo showing the surface of CFRP material 2.

7.4.3.1 Surface wettability

Three CFRP samples from each material, each measuring 15 mm x 15 mm, were treated with the CO₂ laser using three different processing conditions. In the initial experiment (**Section**

7.4.1), the hatch spacing was set at 200 μm , with a laser spot size of 185 μm . The laser employed a Gaussian beam profile, characterised by an intensity distribution that varies across its radius. Although complete matrix removal was achieved in certain experimental runs, it is hypothesised that a portion of this removal resulted from heat conduction through the fibres, originating from regions exposed to higher laser intensity. This heat transfer likely led to the evaporation of the matrix material beneath the fibres, subsequently causing fibre-matrix debonding. Accordingly, for all samples in the present study, the hatch spacing was set to 100 μm , with a moderate scanning speed of 150 mm/s. The laser power was set to 2.25 W, 4 W, and 6 W to assess the effects of different power levels (**Table 7.3**).

Table 7.3. The laser variable utilised for wettability assessment.

| run | P (W) | v (mm/s) | H (μm) |
|-----|-------|----------|---------------------|
| 1 | 2.25 | 150 | 100 |
| 2 | 4 | 150 | 100 |
| 3 | 6 | 150 | 100 |

Measurement of WCA utilising the sessile droplet method was conducted for the laser-treated and non-treated samples the same day after the laser processing. Prior to the CA assessment, the samples were cleaned as described in **Chapter 3/Section 3.6**. The droplet size was 1.5 mm in diameter. The goniometer was set up to capture 105 frames (100 at 0.016 s intervals and 5 frames at 2 s intervals).

Figure 7.13 represents the WCA result for material 1. The sample processed with 2.25 W laser power showed no significant effect on the WCA. However, processing with a 4 W laser revealed a slight improvement in surface wettability. Increasing the laser power to 6 W resulted in a significant shift in surface wettability towards superhydrophobicity. This change is attributed to the presence of loose CFs. When a water droplet was deposited on a specific region of the treated sample containing a high number of loose CFs (**Figure 7.14**), it was observed that the water droplet did not adhere to the surface; instead, it remained on the syringe even after two attempts, demonstrating superhydrophobic behaviour.

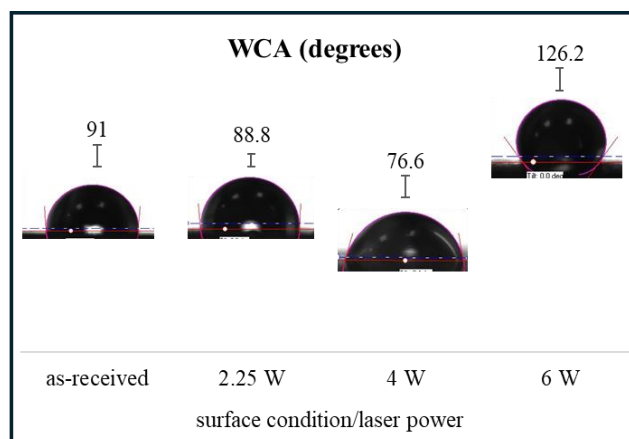


Figure 7.13. WCAs for as received and laser treated samples (material 1).



Figure 7.14. UD-reinforced CFRP sample showing loose CFs after surface treatment using CO₂ laser power of 6 W, scanning speed of 150 mm/s, and hatch spacing of 100 μm. The highlighted region revealed superhydrophobic behaviour.

For CFRP material 2, the large scale of inhomogeneity in the surface of laser treated samples makes the WCA results less informative, as discussed in **Chapter 5/Section 5.5.2.4**. For as-received sample, the average WCA was 85°.

In addition to the WCA measurements, contact angle (CA) assessments using a dispersive liquid (diiodomethane) were conducted for the different surface treatment conditions, utilising the same methodology as for the WCA. For material 1 samples treated with 4 W and 6 W lasers, only a single measurement was conducted because the liquid spread instantaneously over most of the sample surface due to the absorption nature of the porous surfaces [319, 320], resulting in CAs of 0°, which prevented further measurements. For the sample treated with a 2.25 W laser, the dispersive average CA was reduced from 65° (as received) to 46°. For CFRP material 2, the dispersive average CA of the as-received sample was 48°. For laser-treated samples, no informative results for material 2 were obtained, similar to the WCA.

7.4.3.2. Adhesive bonding strength

Two different sets of laser variables were examined for the adhesive bonding strength of the two CFRP materials, with non-treated samples serving as references. For both laser treatment sets, the scanning speed and hatch spacing were fixed at 150 mm/s and 100 μm , respectively, while the power was varied at 4 W and 6 W. Notably, with the hatch spacing set at 100 μm , the removal percentages of the outer layer matrix resin for CFRP material 1 were nearly 100% for both laser powers used, unlike the results when a 200 μm hatch was employed in **Section 7.4.1**. Moreover, loose fibres were observed for the 6 W sample, as depicted in **Figure 7.14**. For CFRP material 2, the rich matrix resin zones at the weft and warp tow intersections were significantly reduced with the 6 W laser power compared to the 4 W, as shown in **Figure 7.15**.

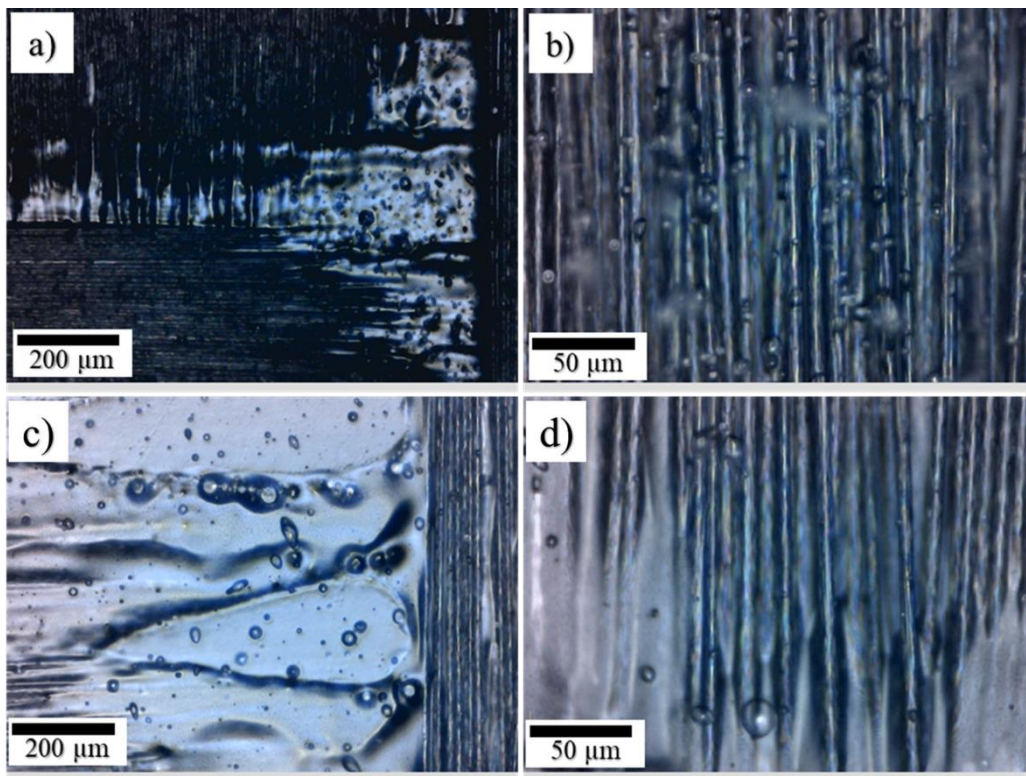


Figure 7.15. Optical microscopy images with different magnifications of CFRP material 2 after laser processing: a) and b) with 6 W CO₂ laser, c) and d) with 4 W CO₂ laser. The scanning speeds and hatch spacing for both samples were 150 mm/s and 100 μm , respectively.

For each surface condition of each material, three bonded pairs were tested using the SLS tests according to the BS EN ISO 1465:2009 standard [286]. The adhesive used was Araldite 420. The coupons were cut, joined, cured, and mechanically tested as described in **Chapter 3**. The laser scanning was uniaxial and parallel to the shortest coupon length, as shown in **Figure 7.16**. The bar chart in **Figure 7.17** shows the bonding strength results. For non-treated material 1, the results were obtained from another experiment outlined in **Chapter 6/Section 6.7**.

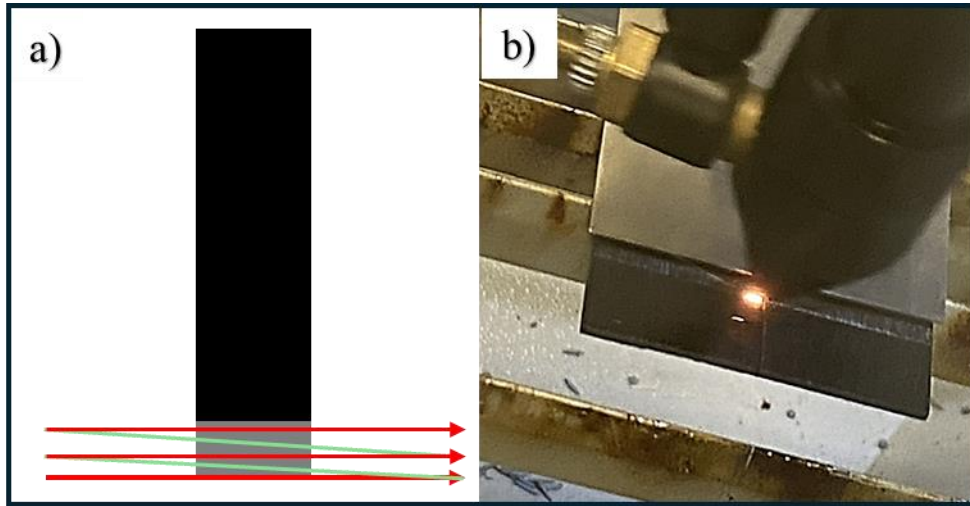


Figure 7.16. a) schematic and b) photo showing the scanning strategy.

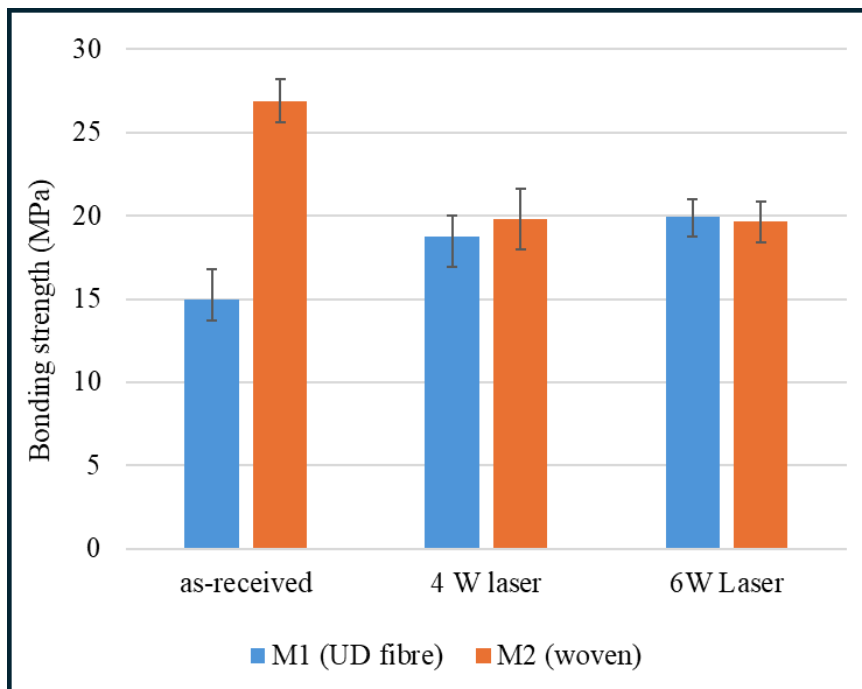


Figure 7.17. The bonding strength for the different materials/surface conditions.

For CFRP material 1 (UD fibres), the results indicate approximately 20% and 30% improvement in bonding strength with laser treatment using 4 W and 6 W, respectively. In contrast, there was a significant reduction in bonding strength for CFRP material 2 (woven fabric). Although the bonding strength results for all laser-treated samples of both materials are comparable, the bonding strength of non-treated CFRP material-2 is much higher than that of material-1. The failure mode, supported by optical microscopy images of non-treated CFRP material-2 (**Figure 7.18**), shows that the outer layer matrix has been torn with the bonding

adhesive, indicating NSSF. This suggests that the bonding between the two epoxies is stronger than that between the matrix and the CFs.

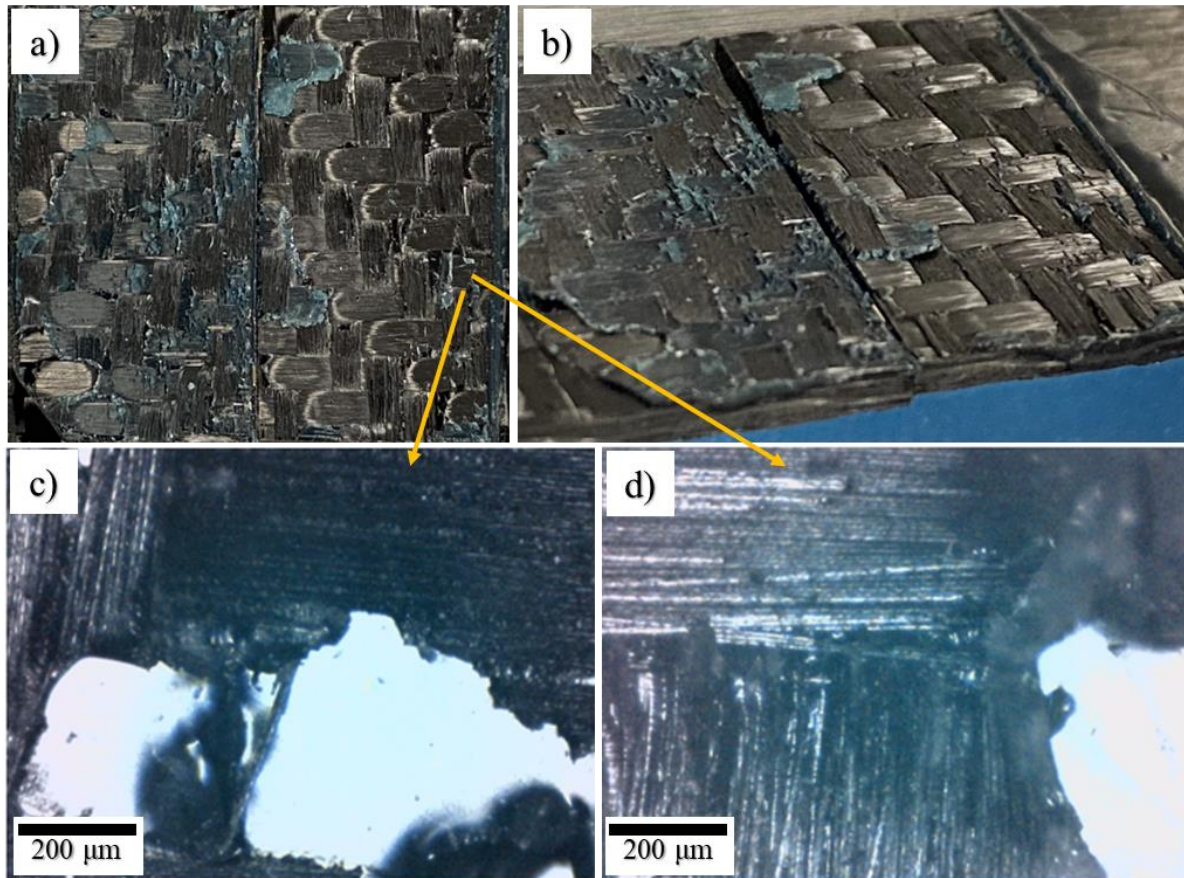


Figure 7.18. a) and b) photos of failed coupons of non-treated CFRP material 2 from two different angles, indicating NSSF. c) and d) optical microscopy images showing torn matrix.

Regarding the failure modes of laser-treated samples, material 1 (**Figure 7.19** (a) and (b)) shows 100% LFTF for both 4 W and 6 W lasers. Rows of fibres were torn from one coupon and adhered to the adhesive on the other coupon. It is possible that the number of torn fibres is higher for samples treated with the 6 W laser, where loose fibres were already observed prior to adhesive joining. Material 2 (**Figure 7.19** (c) and (d)) primarily shows LFTF with a lesser extent of NSSF. Non-removed ablated matrix particles, which belong to rich matrix zones, were observed at different positions on the fractured coupons. The amount of these particles appears to be higher in samples treated with the 4 W laser.

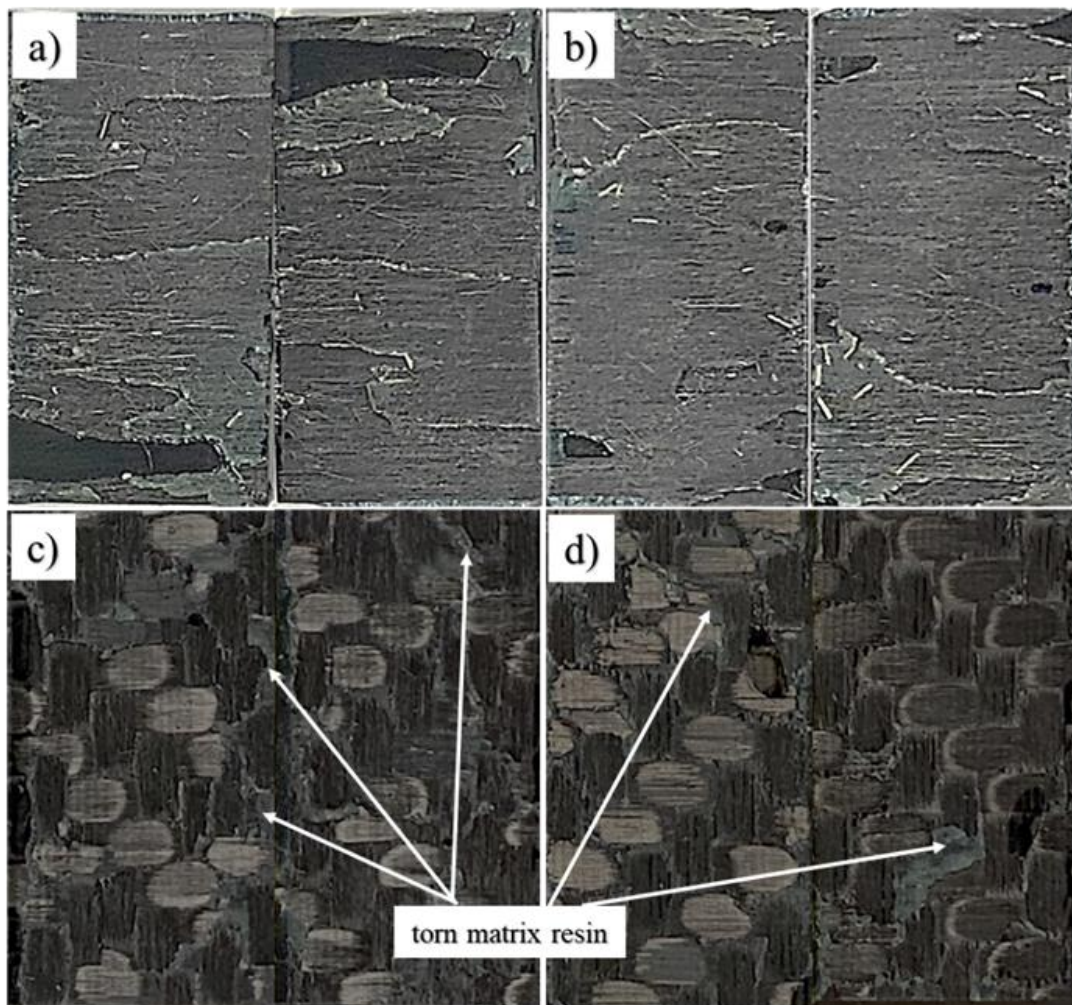


Figure 7.19. Photos of failed coupons of CFRP: a) material 1 processed with 4 W, b) material 1 processed with 6 W, c) material 2 processed with 4 W, and d) material 2 processed with 6 W.

Overall, the results indicated a slight improvement in the bonding strength for material 1, as the bonding strength of the as-received material was initially low. The failure mode of the as-received material was AF, indicating weak adhesion between the adhesive and the matrix resin system of the CFRP material. In contrast, for CFRP material 2, despite having comparable wettability behaviour to material 1, the adhesion between the adhesive and the matrix was very strong, resulting in tearing of the matrix. Similar CFRP behaviour was observed in a previous study [27]. This suggests that the high adhesion strength might be due to the potential interdiffusion of molecules between the adhesive and the matrix. According to the diffusion theory, the nature of the materials and bonding conditions significantly influence the extent to which diffusion occurs [343] and it is primarily applicable when both the adherend and adhesive are polymers [130]. Diffusion theory proposes that due to molecular migration

between the adhesive and the adherend, the interface will eventually diminish or disappear [333].

7.5. The ablation or removal mechanism of epoxy resin using CW CO₂ laser.

Based on optical microscopy images of laser-treated UD CFRP fibres (Figure 7.3) and pure epoxy (Figure 7.8), it appears that CW CO₂ laser treatment leads to the formation of gaseous micro and sub-micro bubbles within the matrix. This observation is further supported by optical microscopy images of CFRP material 2, which showed a notably high number of bubbles surrounding the exposed CFs (Figures 8.15 and 8.20). These bubbles were subsequently eliminated by spraying the sample with isopropanol.

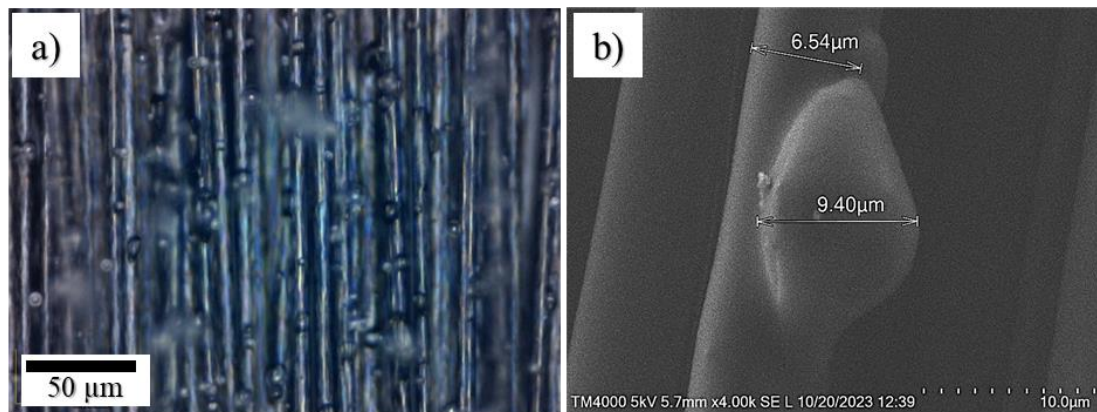


Figure 7.20. a) optical microscopy images of fibre-exposed CFRP material 2 after CO₂ laser treatment with high LED, showing a high number of bubbles surrounding the fibres, b) an SEM image shows a bubble adhere to a CF.

For pure epoxy resin, according to the Beer-Bouguer-Lambert law, described in **Chapter 2/ Section 2.3.6**, the maximum absorption of laser energy occurs at the surface of the processed material. However, when a CW laser is used, the hottest layer is at a certain depth (h) from the surface because the surface is in contact with the heat-conductive medium (air) [344]. This can explain the formation of microbubbles near the surfaces of both the CFRP and the pure epoxy during laser treatment, as the decomposition of the resin releases gases trapped within the material, forming bubbles, see the scheme in **Figure 7.21**.

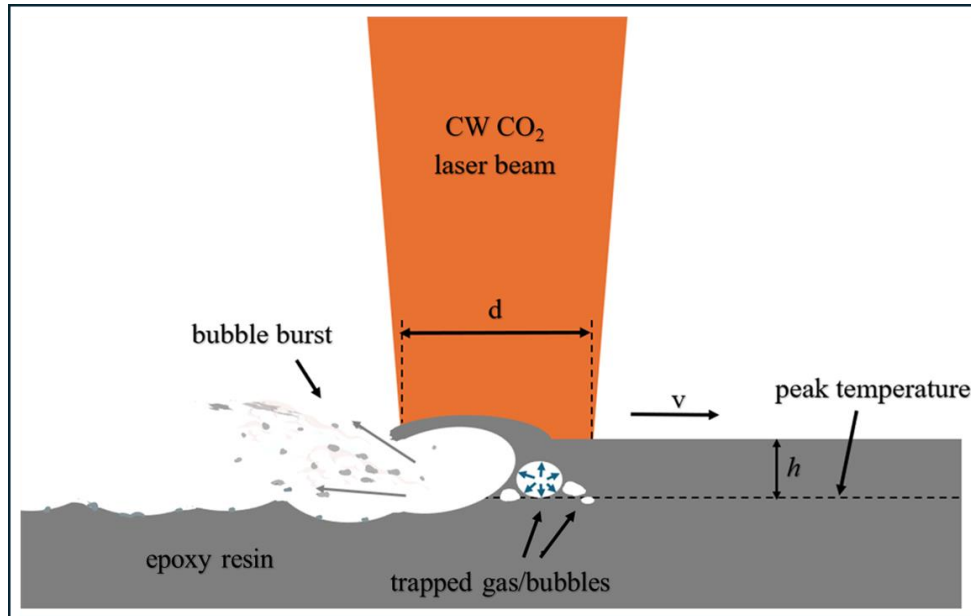


Figure 7.21. Schematic of the CW laser ablation process of polymer material, illustrating bubble formation near the surface due to gas release from resin decomposition.

In CFRP composites with a thin outer layer matrix, hot spots can be formed at the interfaces between the matrix and fibres, primarily due to the high absorptivity of the CFs [15]. This can lead to the formation of non-exploded bubbles at the matrix/fibre interface. The formation of these bubbles may contradict the views of many researchers who argue that thermosetting polymers cannot be reshaped through heating [316-318]. However, it is important to note that many thermosets have a glass transition temperature, indicating that they can soften when heated [345].

7.6. FTIR spectroscopy

The FTIR spectra (**Figure 7.22**) comparing the transmittance of the two different CFRP materials investigated in this chapter revealed slight chemical differences that lead to approximately 5% different in transmittance at 10600 nm. This suggests variations in the resin systems between the two CFRP materials. As discussed in **Chapter 3/Section 3.2.4**, the penetration depth of ATR FTIR is only up to a few micrometres, indicating that for the as-received CFRP material, this depth likely corresponds to the outer matrix layer.

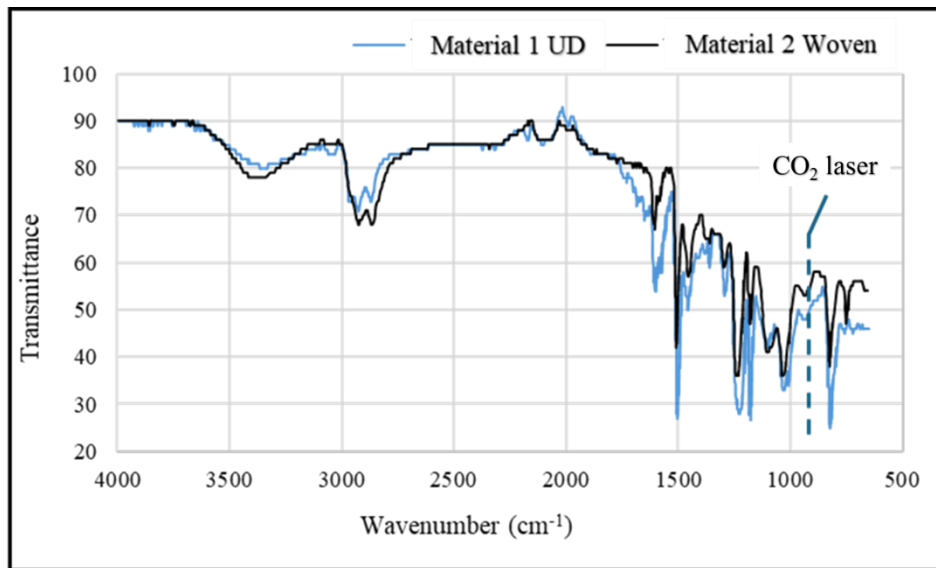


Figure 7.22. Comparison of FTIR spectra between CFRP Material 1 and Material 2.

Figure 7.23 presents a comparison of FTIR spectra between as-received samples and CO₂ laser-treated samples at 4 W and 6 W, all of which are from CFRP Material 1.

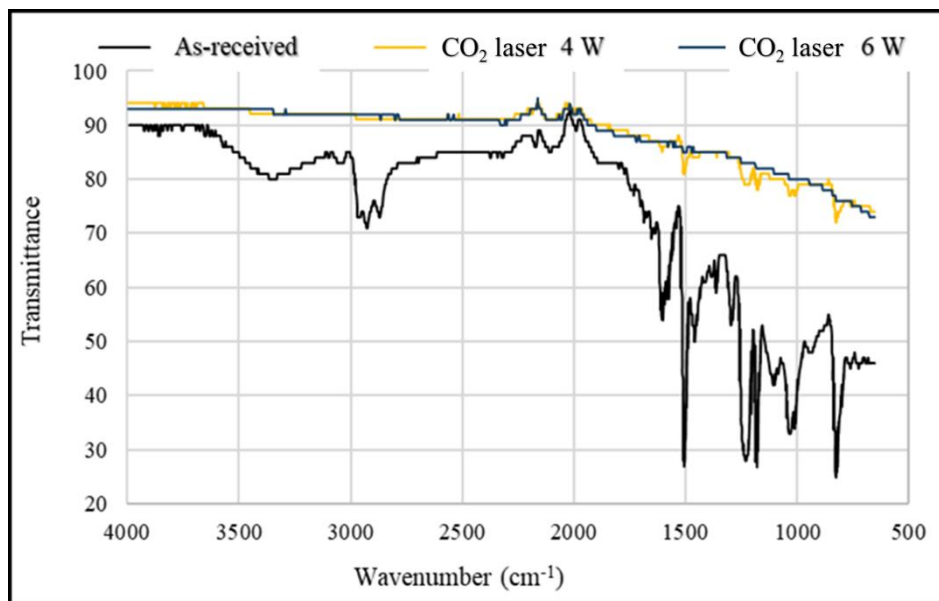


Figure 7.23. Comparison of FTIR spectra among as-received and CO₂ laser-treated samples with 4 W and 6 W. All of which are from CFRP Material 1. The scanning speed and hatch spacing for both laser-treated samples were 150 mm/s and 100 μm, respectively.

Figure 7.23 illustrates the FTIR spectra comparison between as-received CFRP Material 1 and CO₂ laser-treated samples at 4 W and 6 W. The spectra reveal a significant change attributed to the removal of the outer matrix resin layer. Additionally, slight differences between the two laser-treated samples suggest variations in the extent of matrix removal.

7.7. Conclusion

- By optimising processing parameters, a CW CO₂ laser can selectively remove the outer layer matrix resin to expose the underlying carbon fibres. However, this process may compromise the integrity of the fibre/matrix interface. Furthermore, ablating thick matrix resin zones, such as those found at intersections of fibre tows in woven fabric CFRP, may necessitate higher laser power, potentially resulting in the generation of loose fibres on the surface.
- The removal of epoxy resin is believed to occur due to the evaporation of the resin at the hottest point within the material thickness. In regions with thick matrix resin or in pure epoxy samples, evaporation occurs at a distance (h) from the surface, characterised by the formation of bubbles that subsequently explode. In CFRP materials with shallow matrix resin, evaporation is more likely to occur at the fibre/matrix interface, where the fibre is the hottest point in this case. This phenomenon is thought to significantly impact the integrity of the fibre-matrix bond. The removal of matrix resin at high scanning speeds is a function of the LED.
- Contact angle assessment revealed that processing with moderate laser power can slightly reduce the WCA, whereas high-power laser processing leads to increased WCA towards the superhydrophobicity. With diiodomethane, the contact angle was 0° for both moderate and high laser power. It is believed that the slight reduction in WCA for moderate laser power is due to the dispersive part of the surface energy of water. This suggests that processing with a CW CO₂ laser improves the dispersive SFE, while the polar part shows the opposite effect.
- Depending on the bonding strength of non-treated materials, a CW CO₂ laser can enhance the bonding strength of CFRP materials that exhibit low bonding strength with interfacial adhesion failure. Similar to the effects observed with NIR laser processing discussed in **Chapter 6/Section 6.7**, it is believed that the tensile strength of the exposed fibres contributes to increasing the bonding strength by facilitating the tearing of exposed or loose fibres.

CHAPTER 8: Utilising Incoherent UV Light to Augment IR Lasers in Improving CFRP Composite for Adhesive Bonding

8.1. Introduction

Numerous researchers have explored non-laser UV light treatments to enhance the surfaces of polymeric and non-polymeric materials for adhesive bonding [32, 193-201]. These studies often use UV light with ozone, either by applying ozone directly or using UV sources emitting wavelengths below 240 nm to generate ozone in the surrounding atmosphere. UV/ozone treatments have shown effectiveness in improving joint strength across various materials, surpassing methods like grit blasting and primers. However, UV/ozone treatment necessitates facilities with high corrosion resistance to ozone, making it impractical for larger structures. Additionally, ozone is highly toxic [199]. UV light can impact polymer surfaces in two primary ways. First, it can directly cause photo-degradation or photo-crosslinking of the polymer's molecular bonds. Second, when UV light has a wavelength shorter than 240 nm, it indirectly affects the polymer by interacting with atmospheric oxygen to generate ozone, atomic oxygen, and oxygen radicals, which then oxidise and alter the polymer surface [200, 201]. Photodegradation typically occurs at micron or sub-micron depths from the surface, with the most significant effects near the surface, where degraded species can absorb UV light more strongly and limit its penetration into the polymer's interior [202].

This chapter examines the effect of treating CFRP composite with incoherent UV light at a wavelength of 254 nm, emitted by a UV germicidal lamp, on improving CFRP surfaces' wettability and adhesive bonding. The study explores how UV intensity and exposure duration affect the water contact angle (WCA) and investigates the WCA response of various CFRP composites. Additionally, it compares the adhesive bonding strength of CFRP composites treated with UV light to those treated with other surface methods, including ns pulsed NIR lasers and CW CO₂ lasers, both individually and in combination with UV treatment. Mechanically sanded and untreated samples serve as references. The findings suggest that UV exposure is viable and cost-effective for enhancing wettability and adhesive bonding. To the best of current knowledge, no similar research has been published. It is worth noting that the incoherent UV light treatment performed in this study chemically modifies the surface, as it lacks sufficient intensity to induce ablation [346]. In contrast, laser-based treatments, including UV lasers, can texture the surface or completely remove the matrix to expose the underlying fibres through ablation. This ablation requires the high intensity of lasers [347].

8.2. Objectives

- Quantitatively assess the wettability of CFRP surfaces treated with UV light and the influence of the UV intensity and exposure period on the wettability.
- Evaluate the impact of UV light treatment on the adhesive bonding strength of CFRP, comparing it with other techniques such as ns pulsed NIR laser and CW CO₂ laser treatments.

8.3. Experimental design and workflow

This chapter comprises a main experiment, which includes two phases and a supplementary experiment. In the first phase, the surface wettability of CFRP material was assessed after UV exposure at various intensities and durations. The second phase involved comparing the adhesive bonding of UD CFs CFRP material among different surface treatment techniques. Additionally, a supplementary experiment was conducted to evaluate the differences in WCA responses among various CFRP materials exposed to UV light. The flowchart in **Figure 8.1** illustrates the experimental workflow.

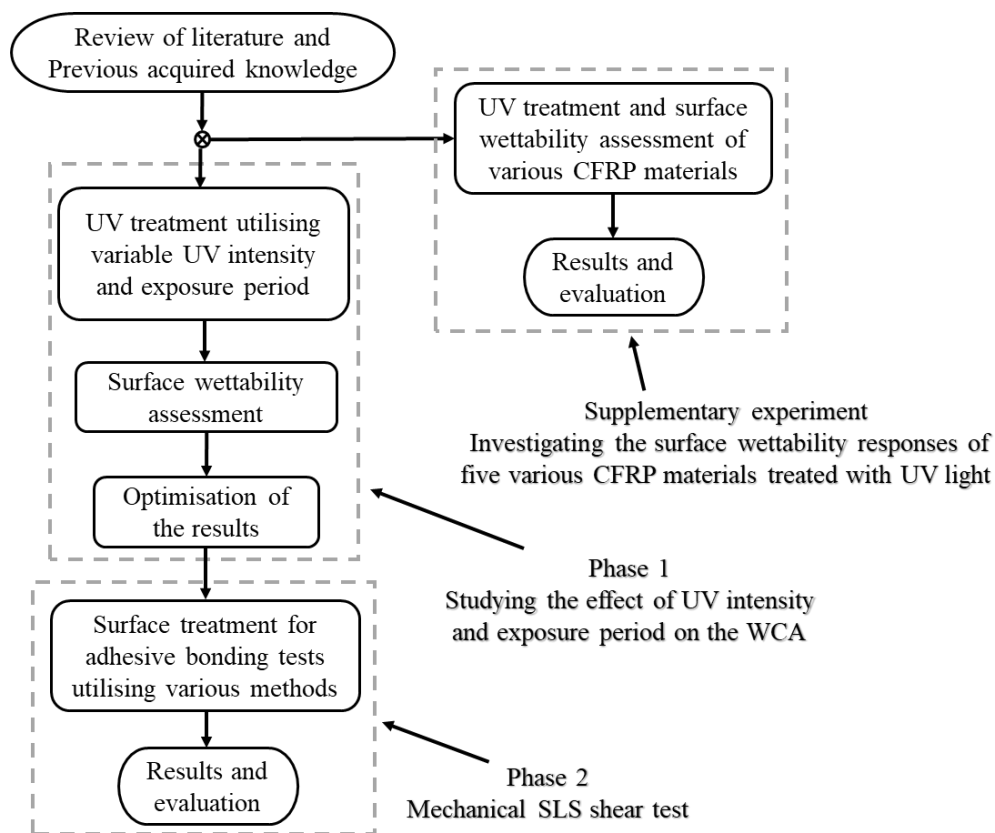


Figure 8.1. Flowchart Simplifies the experimental design and workflow.

8.4. Main experiment

As described earlier, the main experiment consists of two phases. The first phase involves assessing wettability based on UV intensity and exposure period. The second phase compares CFRP bonding strength across different treatment techniques. The CFRP material used was the UD reinforced type from Reverie Ltd. (UK), detailed in **Chapter 6/Section 6.4**. For UV treatment of CFRP surfaces, a Germicidal UV lamp (TUV Amalgam T6 130W XPT SE G10.2q) from Philips UK Ltd was utilised. A full description of the UV lamp is available in **Chapter 3/Section 3.2.3**. The details and results of each phase are presented separately as follows.

8.4.1. Phase 1: Studying the effect of UV intensity and exposure period on the WCA.

8.4.1.1. Methods

UV treatment was conducted with three different UV intensities, calculated based on the distances from the lamp to the exposed surfaces. The lamp's illumination was assumed to be uniform, and the UV intensity at a sample placed at a distance (r) from the centre of the lamp was calculated by dividing the lamp's output power (46 W) by the cylindrical area ($2\pi rL$), where (L) the lamp length (74 cm). The light intensity at a distance (r) from the axis of a long cylindrical source is inversely proportional to (r) [278]. **Table 8.1** (repeated from **Table 3.2/Chapter 3**) presents the UV intensities and the corresponding distances of the samples from the lamp used in the experiment. For each of the three different UV intensities, six CFRP samples, each 25 mm x 15 mm, were exposed for various periods (**Table 8.2**), ranging from 15 minutes to 120 minutes. The samples were centred under the UV lamp with their longest length parallel to the lamp axis, **Figure 8.2** (repeated from **Figure 3.5/Chapter 3**). The mean WCA for each sample was then calculated based on 15 measurements taken immediately after the UV treatment using a goniometer (CAM 101 from KSV Instruments Ltd UK). The diameter of the droplet out at the syringe was 1.5 mm. To capture the initial and the stable WCAs for the different UV-treated surfaces and the non-treated ones, 100 frames were recorded at a time interval of 16 ms, and then 10 frames were recorded at a time interval of 1 s. The cutting and cleaning processes of the samples and the equipment utilised are described in **Chapter 3/Section 3.6**.

Table 8.1. UV intensities and distances from the lamp applied in the project.

| Distance from the lamp centre (mm) | UV intensity (mW/cm ²) |
|------------------------------------|------------------------------------|
| 19.8 | 50 |
| 39.6 | 25 |
| 79.2 | 12.5 |

Table 8.2. UV intensities and exposure periods.

| UV intensity (mW/cm ²) | Exposure periods (min) | | | | | |
|------------------------------------|------------------------|----|----|----|----|-----|
| 12.5 | 15 | 30 | 45 | 60 | 90 | 120 |
| 25 | 15 | 30 | 45 | 60 | 90 | 120 |
| 50 | 15 | 30 | 45 | 60 | 90 | 120 |

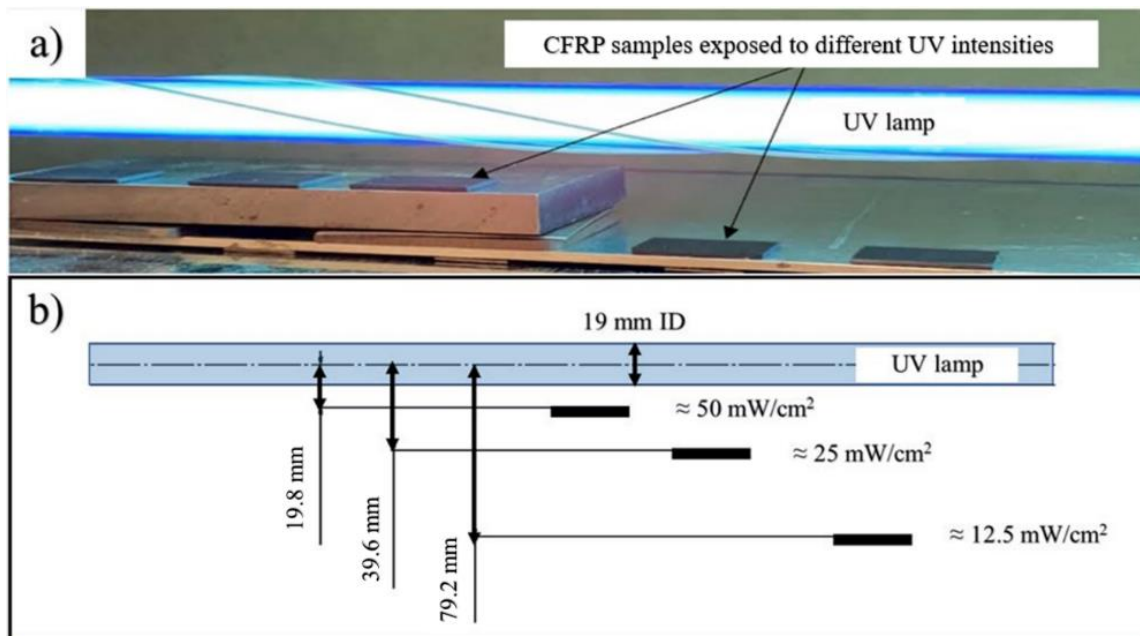


Figure 8.2. UV lamp and the experimental setup: a) photograph and b) schematic drawing, [279]*.

In addition to the WCA assessment, CA measurement using dispersive liquid (diiodomethane) was performed, but no significant differences were recognised. Moreover, FTIR analyses were conducted on an as-received sample and on a sample subjected to the highest UV fluence using the Cary 630 FTIR spectrometer described in **Chapter 3/Section 3.2.4**. For the UV-treated sample, the assessments were performed twice: initially, immediately after the UV treatment, and subsequently, following cleaning with distilled water and an isopropanol bath. The cleaning methodology is comprehensively detailed in **Chapter 3/Section 3.6**.

8.4.1.2. Results and discussion

For each surface condition, the measured WCAs varied by up to $\pm 10^\circ$ around their mean values. This discrepancy is primarily due to surface topography inhomogeneity and potential variations in droplet sizes, which were manually adjusted for each measurement, as well as goniometer error [319].

UV treatment significantly enhanced the wettability of CFRP surfaces. WCAs, **Figure 8.3**, decreased from hydrophobic to nearly super hydrophilic with increased UV fluence, defined as the product of UV intensity and exposure duration.

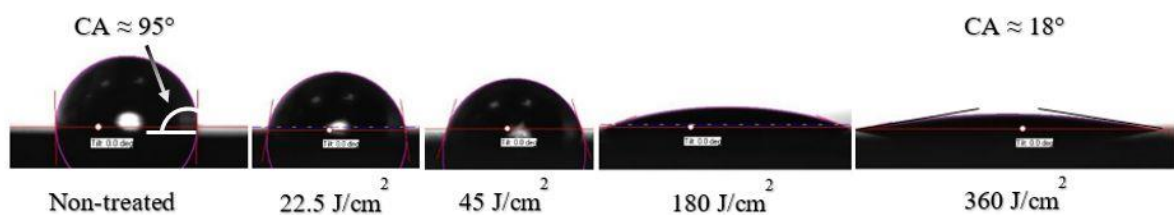


Figure 8.3. Droplet shapes and WCAs at different UV fluence.

The average WCAs from 15 measurements for each of the UV-treated samples were calculated based on the final stable state of the test droplet. For samples treated with the highest UV fluence, the initial average WCA was around 30° and stabilised at approximately 20° in less than 5 seconds. In contrast, for a sample treated with a ns pulsed NIR laser (**Chapter 6**), the WCA continued to decrease as the water droplet spread across the sample. The graphs in **Figure 8.4** illustrate examples of the time dependency of WCA reduction for both a NIR laser-treated sample and a UV-treated sample.

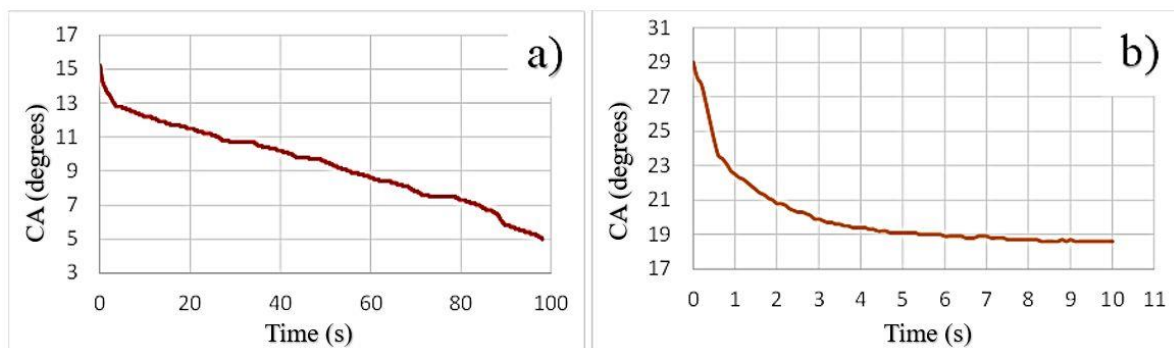


Figure 8.4. Typical time dependency for the reduction or stability of WCA of, a) laser textured, b) UV treated sample highest UV fluence.

Based on the measured stable WCAs, **Figure 8.5** illustrates the reduction in mean WCA across different UV intensities and exposure periods. **Figure 8.6** demonstrates that with different UV intensities, the reduction in CA was dependent on UV fluence; in other words, higher UV intensity required less time to reduce the WCA.

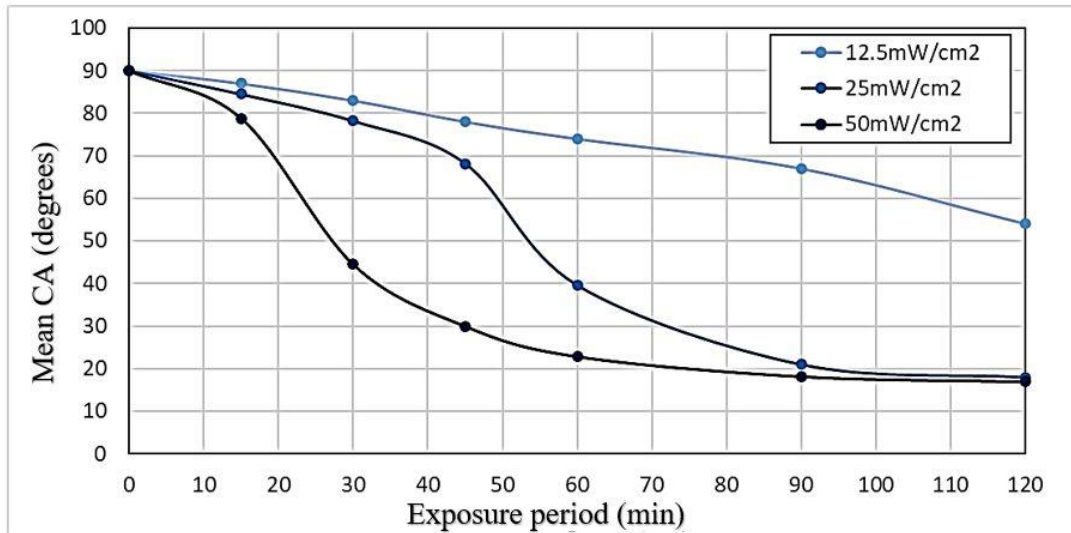


Figure 8.5. Mean WCAs for CFRP samples treated with different UV intensities and exposure periods.

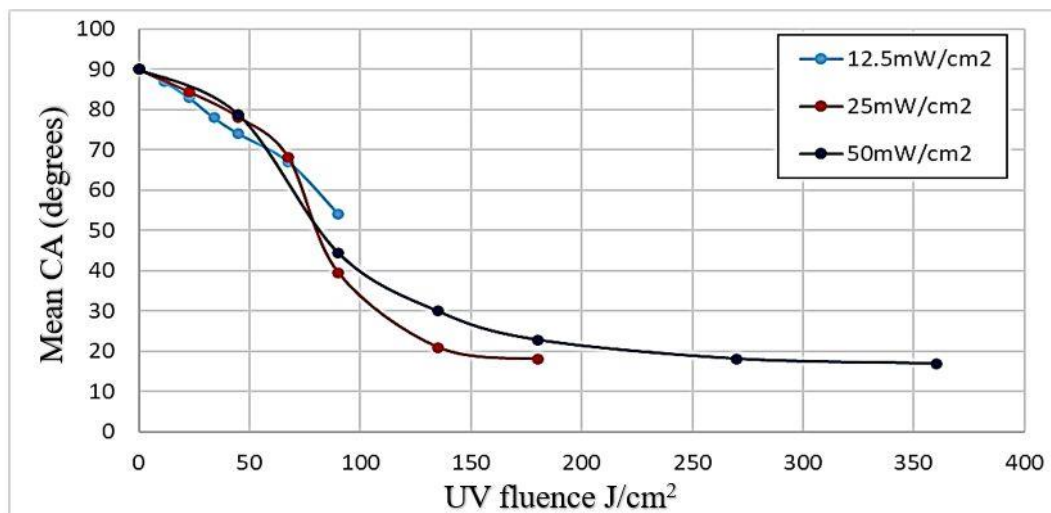


Figure 8.6. Mean WCAs for CFRP samples treated with different UV fluence.

Figures 8.5 and 8.6, depicting the relationship between WCA and the UV exposure period and fluence, show an initial linear change followed by a non-linear variation. The mean WCA initially decreases slightly from 91° to around 70° or 80° within the first 50 J/cm². It then drops significantly to around 30° or 40° with the next 50 J/cm² of UV fluence, with minimal reduction thereafter. At 200 J/cm², the mean WCA is approximately 20° or slightly lower. Similar non-

linear behaviour of WCA versus UV exposure has been observed in the literature for certain polyimide films [140]. UV light at 254 nm interacts with polymeric molecules by breaking molecular bonds with binding energies less than its photon energy (4.88 eV). This interaction causes chain scission, creating unsaturated products in the polymer chains and free radicals on the polymer surface. These free radicals can react with oxygen in the air to form carboxyl and hydroxyl groups. The presence of unsaturated groups, carboxyl, and hydroxyl groups increases the absorbance of the polymeric material to UV-C irradiation. This increased absorbance with more UV exposure can explain the non-linear (rapid) reduction in WCA. [348]. Moreover, it is noticed from **Figure 8.6** that above 80 J/cm^2 the contact angle at 25 mW/cm^2 exposure drops below that at 50 mW/cm^2 . This can be attributed to several factors. Firstly, the duration of exposure plays a role: even with the same UV fluence, longer exposure times allow more free radicals to react with oxygen, leading to a higher formation of oxidative products over time and thereby increasing absorbance, as previously mentioned. However, the literature does not consistently confirm this relationship.

The more probable explanation lies in the distances between the samples and the cylindrical UV lamp. The closer the sample is to the lamp, the less uniform the UV intensity distribution across the sample surface, with the intensity decreasing towards the edges (as illustrated in **Figure 8.7**). Moreover, the incident angle of light at the sample edges, which likely affects reflection, is approximately 70° and 80° for the two intensities. It is important to note that for accuracy, contact angle measurements were primarily taken near the sample edges.

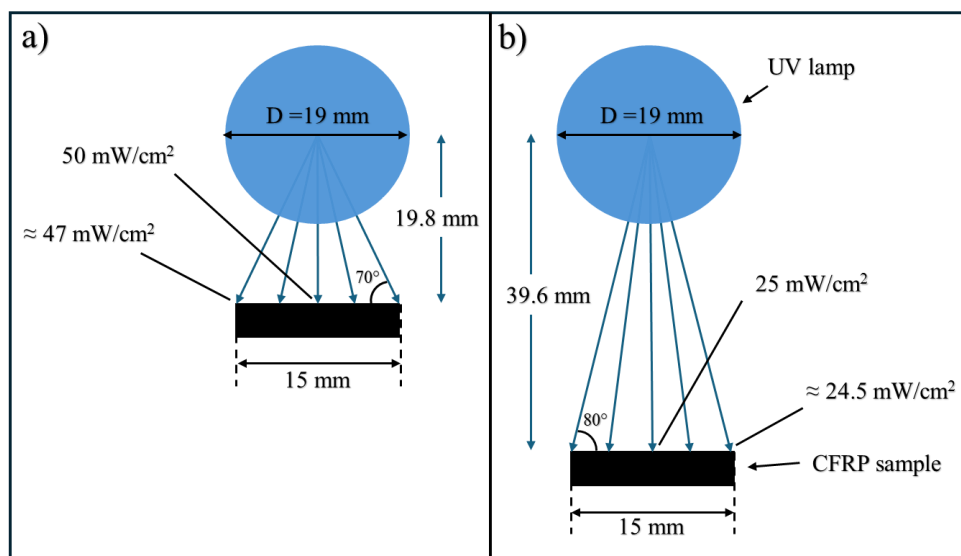


Figure 8.7. Schemes show the UV intensity distribution over the width of samples exposed to a) 50 mW/cm^2 , and b) 25 mW/cm^2 .

With regards the FTIR spectra, both UV treated samples show no significant difference compared to the as-received sample, **Figure 8.8**.

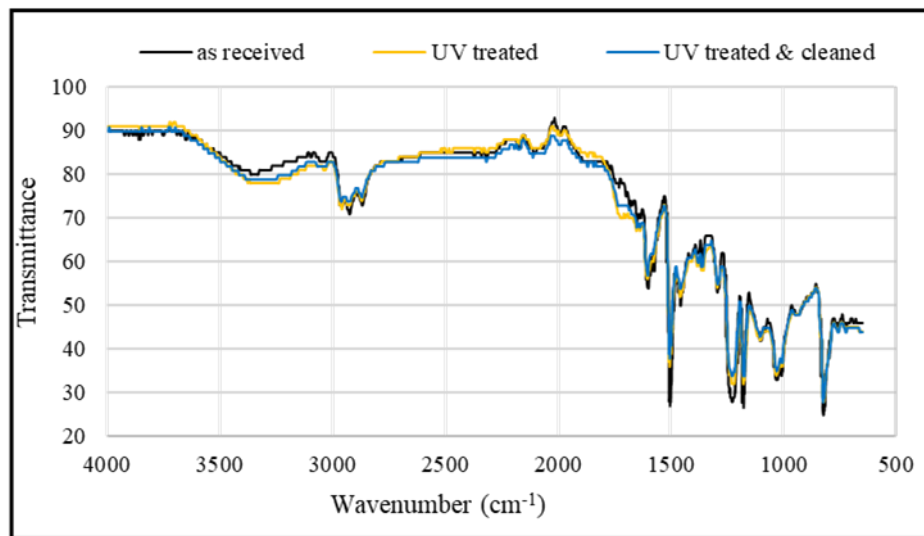


Figure 8.8. FTIR spectra comparison among as-received, UV-treated, and UV-treated and subsequently cleaned samples.

8.4.2. Phase 2: Comparing the adhesive bonding of different surface treatment techniques

8.4.2.1. Methods

For investigating adhesive bonding strength, SLS tests were conducted according to the BS EN ISO 1465:2009 standard [286]. The adhesive bonding used is Araldite 420. The coupling technique, the equipment utilised, and adhesive bonding characteristics are detailed in **Chapter 3**. Various surface treatment techniques were compared, including UV treatments with variable intensities and exposure periods, ns pulsed fibre laser, CW CO₂ laser with both low and high specific energy, mechanical sanding, and untreated samples. Additionally, the comparison included combined treatment techniques involving laser processing before and after UV treatment. A description of all the treatment techniques and their processing variables is presented in **Table 8.3**.

For the mechanically abraded coupons, a cordless handheld random orbit sander (Makita DBO180Z) equipped with 600-grit sandpaper was operated at the slowest speed until the outer glossy layer of the matrix was removed. Optical microscopy was used to assess the mechanically abraded samples. It is worth noting that the same mechanical sanding process was utilised for the woven CFRP material investigated in **Chapter 5/Section 5.5** but was using 320-grit sandpaper. Note that three repeated samples were tested for each surface condition.

Table 8.3. The techniques implemented in the adhesive bonding strength comparison.

| Technique | Description |
|------------------------|---|
| As received | No treatment |
| UV1 | UV treatment (Intensity 50 mW/ cm ² , exposure period 60 min) |
| UV2 | UV treatment (Intensity 25 mW/ cm ² , exposure period 120 min) |
| UV3 | UV treatment (Intensity 50 mW/ cm ² , exposure period 120 min) |
| NIR | Treatment with ns pulsed NIR fibre laser (Pulse energy 0.078 mJ, pulse length 200 ns, PRR 25 kHz, scanning speed 850 mm/s, and hatch 35 µm) |
| NIR + UV1 | Treatment with NIR followed by UV1 |
| UV1 + NIR | Treatment with UV1 followed by NIR |
| L-CO ₂ | Low specific energy CO ₂ laser (Power 4 W, Scanning speed 150 mm/s, hatch 100 µm) |
| H-CO ₂ | High specific energy CO ₂ laser (Power 6 W, Scanning speed 150 mm/s, hatch 100 µm) |
| L-CO ₂ +UV1 | Low specific energy CO ₂ laser treatment followed by treatment with UV1 |
| H-CO ₂ +UV1 | High specific energy CO ₂ laser treatment followed by treatment with UV1 |
| M | Mechanical abrading with sandpaper # 600 followed by cleaning |

Prior to the adhesive bonding comparison, wettability assessments using both water and diiodomethane were conducted for each treatment technique implemented in the adhesive strength tests. For as-received samples and single treatments utilising fibre laser and CO₂ laser, wettability and adhesive bonding data were adopted from previous experiments in **Chapters 6** and **7**. For the combined treatments (NIR + UV1, UV1 + NIR, L-CO₂ + UV1, or H-CO₂ + UV1), the goniometer setup was the same as for the corresponding single laser treatments depicted in **Chapters 6** and **7**. After performing the mechanical tests, a cross-section study was conducted for UV treated fractured coupons using optical microscopy.

8.4.2.2. Results and discussion

Optical microscopy images of mechanically abraded samples revealed partial CF damage, **Figure 8.9**. In a previous experiment (**Chapter 5**), the same sanding method was utilised using coarser sandpaper grits (grit number 320) but instead of the partial damage occur in this experiment, fully breakage of CFs was noticed.

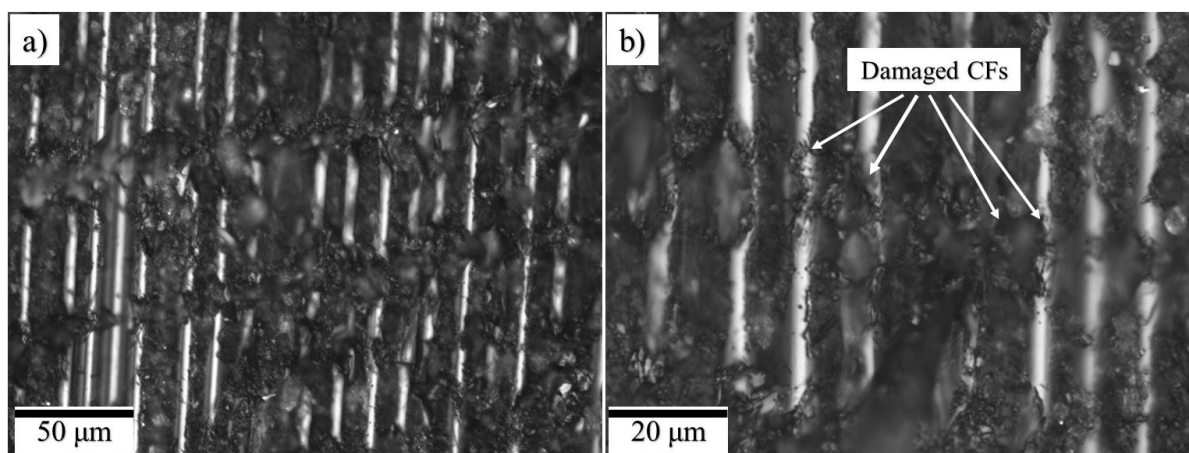


Figure 8.9. a) and b) optical microscopy images for sandpaper treated sample at various magnifications.

For laser treated samples both with NIR fibre and CO₂ lasers, optical microscopy and/or SEM images are available in **Chapter 6** and **7**. The bar chart in **Figure 8.10** shows the comparison in CA for both water and diiodomethane among the different surface treatment techniques utilised. As previously indicated, the results of single treatments with NIR laser were adopted from **Chapter 6**, single CO₂ laser treatments from **Chapter 7**, and single UV treatments from the first phase of this **Chapter**. Treatment with NIR laser led to zero WCA. Low specific energy CO₂ shows only a slight reduction in WCA, whereas high specific energy CO₂ laser showed an increase in WCA towards superhydrophobicity. For samples treated with combined methods (UV and either of the two lasers), no further reduction in WCA is observed beyond the lowest value achieved by the individual treatments. The notable variation in WCAs between samples treated with the two laser techniques can be attributed to differences in their respective ablation mechanisms, as detailed in the preceding chapters. NIR laser treatment leads to the exposure of the fibres, along with alterations to their sizing layer. In contrast, CO₂ laser treatment appears to leave a thin resin layer, potentially at the submicrometer scale, covering the fibres (see Figure 7.20). For all laser treatment methods, whether NIR or CO₂, and whether single or combined with UV light, the CAs of diiodomethane were zero. In contrast, no significant change in the CAs of diiodomethane was observed for any of the single UV treatments. Mechanical abrasion showed a significant reduction in diiodomethane CA (65° to

31°), whereas only a slight reduction was observed for the WCA, likely due to the dispersive component of water.

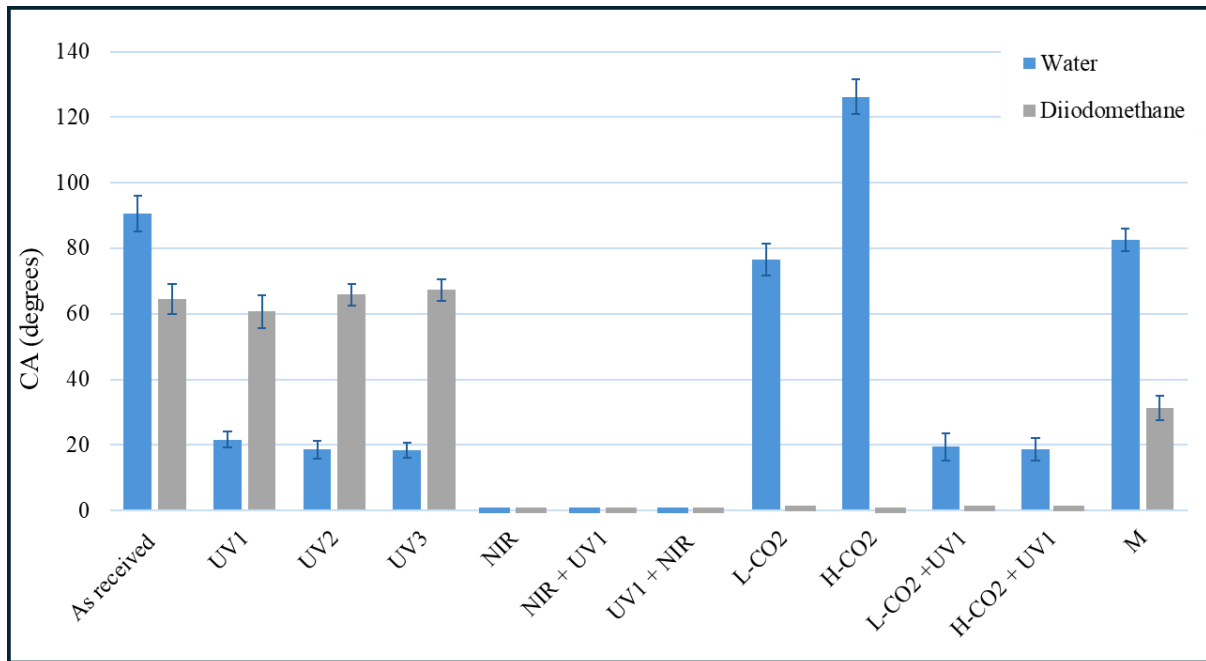


Figure 8.10. Comparison in CA for both water and diiodomethane among various surface treatment techniques. Noting that it was challenging to measure the exact contact angle (CA) when values approached 0°, all CAs reported as 0° in **Figure 8.8** had actual measurements of less than 10°.

With regards the bonding strength, compared to untreated samples, the bonding strength tests (**Figure 8.11**) indicate a substantial (70-80%) increase in bonding strength for single UV light treatments. UV-treated samples demonstrated slightly better strength than those treated only with an NIR laser or in combination with UV light. The average bonding strength was around 27 MPa for UV1 and UV3 and just above 25 MPa for UV2. Samples treated solely with an NIR laser had an average bonding strength of less than 25 MPa. Pre-treatment with UV before laser treatment resulted in a slight decrease in bonding strength, while strength improved when UV treatment followed laser texturing. For combined NIR and UV treatments, the slight variations in strength are not statistically significant. Combining low-specific-energy CO₂ laser treatment with UV light significantly increased bonding strength from 18.8 MPa to 25 MPa. However, combining UV light with high-specific-energy CO₂ laser treatment did not show a significant change. Mechanical abrasion increased bonding strength by about 40% compared to untreated samples.

The failure modes for samples treated using a combination of laser (NIR or CO₂) and UV light were predominantly LFTF, consistent with those treated solely with a laser, as detailed in **Chapters 6 and 7** for UD CFRP coupons.

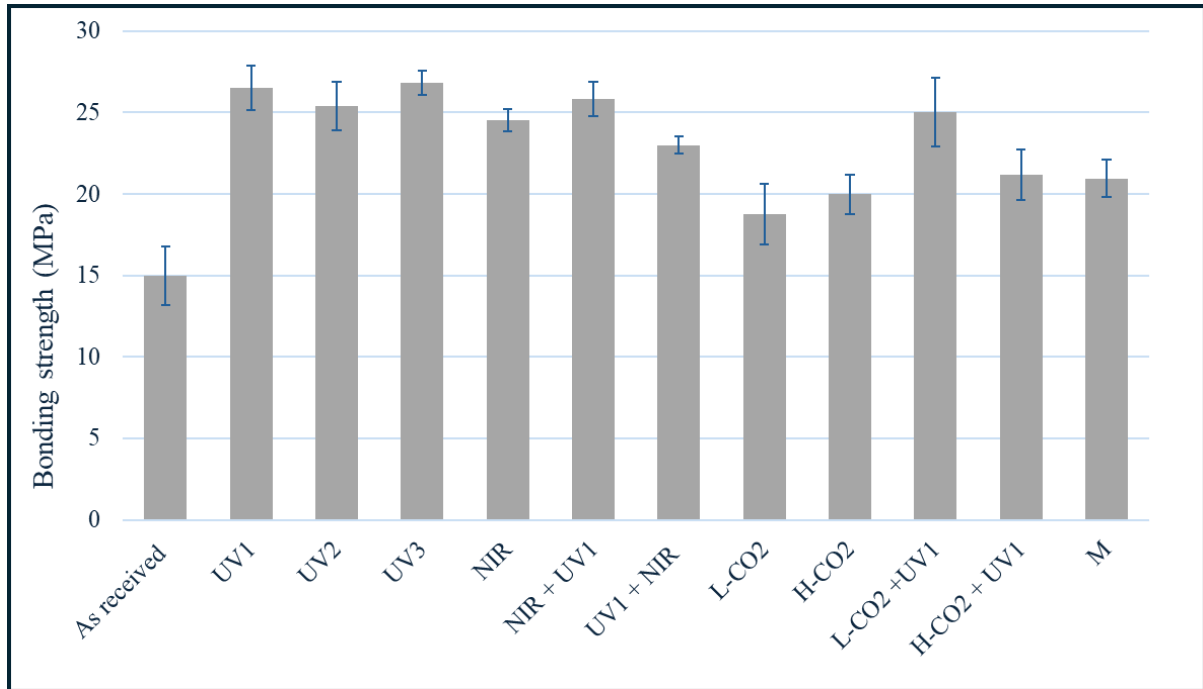


Figure 8.11. Comparison of the bonding strength among different surface conditions.

However, samples treated exclusively with UV light were distinctly different, exhibiting a mix of CSF, where the first prepreg layer was torn completely in some areas, and AF, as shown in **Figure 8.12** (a). Mechanical abrasion resulted in a mix of CSF, LFTF, and Cohesive Failure (CF), with the latter representing failure within the adhesive bonding layer, as illustrated in **Figure 8.12** (b).

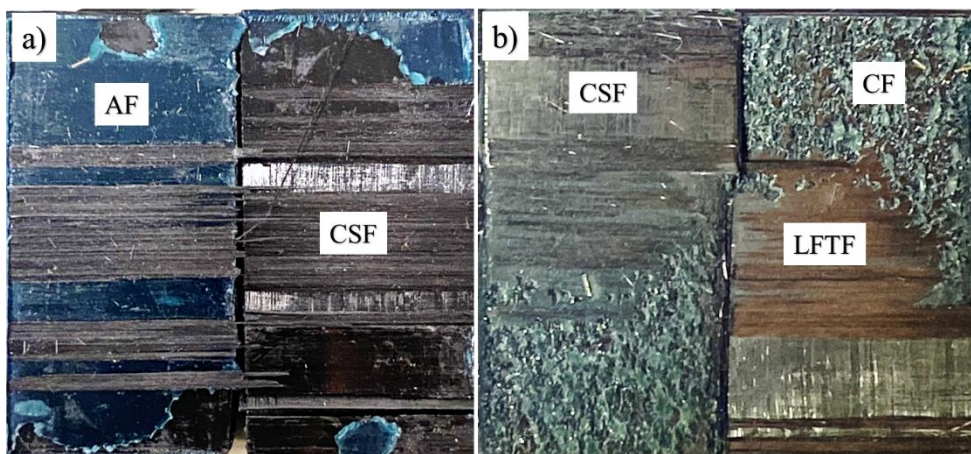


Figure 8.12. The failure modes of a) UV treated, and b) sandpaper treated sample.

The failure modes are categorised according to the classification system provided by Banea and Silva [117]. The CSF of the UV-treated samples occurred mostly at or near the interface between the first and second prepreg layers and was not only within the bonded region but along the whole coupon in some samples (**Figure 8.13**).

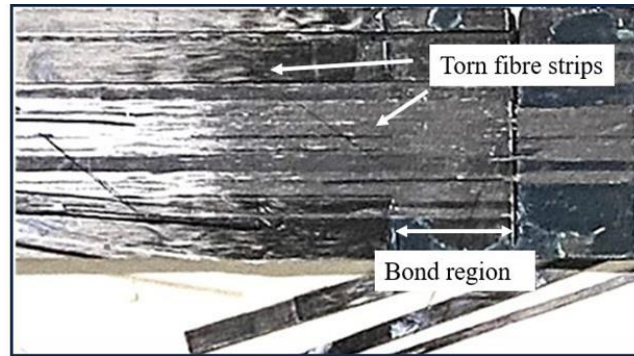


Figure 8.13. A macro photo showing a fractured UV-treated sample shows the fracture along the entire coupon. In addition to the macro photos of the failure modes, further clarification for UV-treated samples is provided by fracture analysis through optical microscopy of the cross-sections of the failed samples (**Figure 8.14**).

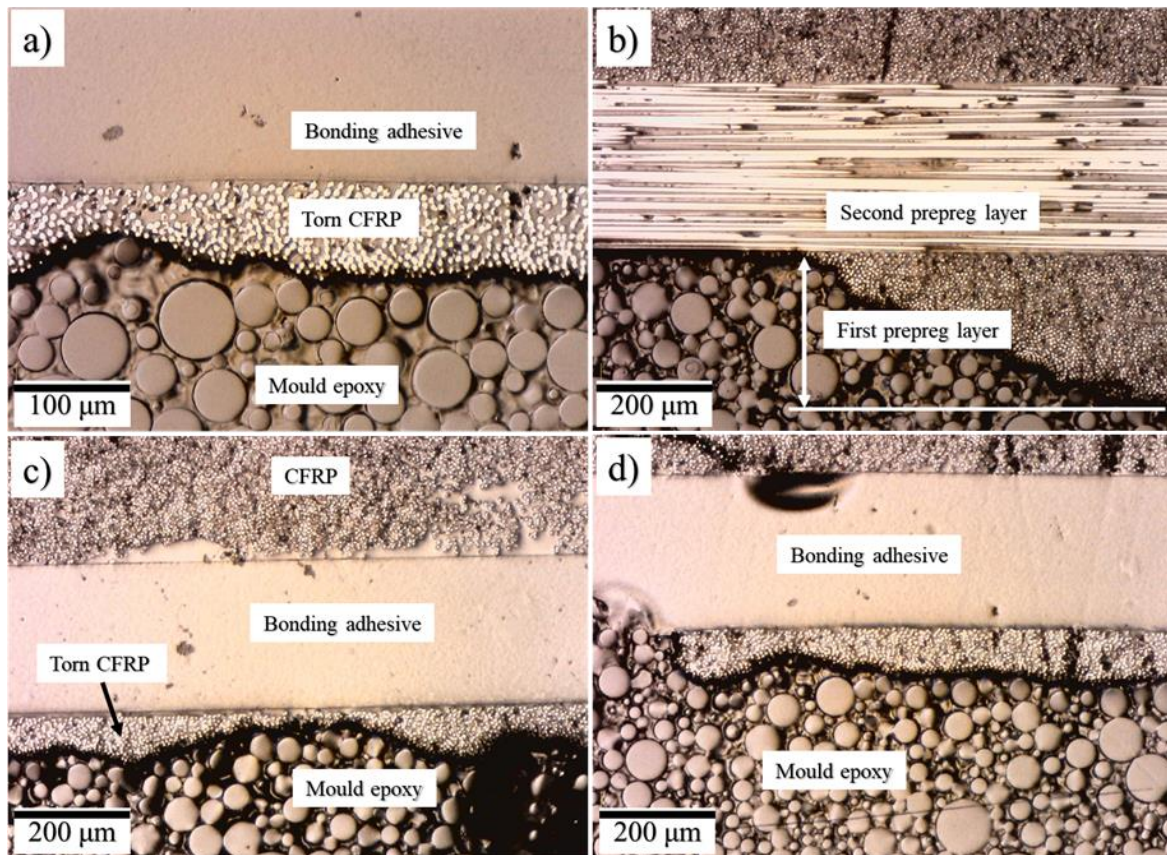


Figure 8.14. Optical microscopy images of cross-sections of CFRP coupons treated with UV light after SLS test.

The failure modes of UV-treated samples predominantly consisted of CSF, with AF to a lesser extent. A torn layer up to 0.25 mm thick from the substrate was observed (**Figure 8.14** (b)), indicating that the failure occurred within the first prepreg layer. In general, CSF is characterised by sections of the composite material tearing away from one coupon and remaining adhered to the opposing coupon. This type of failure indicates strong adhesive bonding, causing the composite material itself to fail [343].

The presence of both shear and peel stresses, discussed in **Chapter 6/Section 6.8**, indicates that fracture in adhesively bonded single lap joints is a mixed-mode problem [349]. Generally, in single lap joints, previous studies have shown that, within the bondline, shear and peel stresses peak at the bonded substrate surface; through the substrate thickness, shear stress decreases progressively with distance from the bonded surface [350-352]. Moreover, with regard to fibre reinforced composites, the literature [350, 353] demonstrates that for adhesively bonded prepreg CFRP structures, the fibre orientation and the prepreg layup sequence determine the stiffness of the composite material and have significant impacts on the joint stresses and the failure load. Previous research demonstrates a consensus that increasing the number of 0° oriented layers near the bonded face can reduce the load path's eccentricity, thereby decreasing the resulting peeling forces and enhancing the failure load [349, 353-356].

For the CFRP material used in this study (layup 0°/90°/0°/90°/0°), there is a notable difference in the modulus of elasticity between the first and second prepreg layers, measured at 119,000 MPa and 8,200 MPa, respectively. This difference is attributed to the fibre orientation in the second layer being at 90° relative to the tensile load. As a result, in the bonded region, most of the load is supported by the first prepreg layer, with minimal load or stress being transferred to the subsequent layers; see the SolidWorks simulation results in **Chapter 6/ Section 6.8.2**. The scheme in **Figure 8.15** illustrates the load distribution in the tested material, derived based on the integration of findings and theories reported in the literature, including the effects of fibre orientation in FRP composites on peeling forces in SLS joints and the overall load distribution.

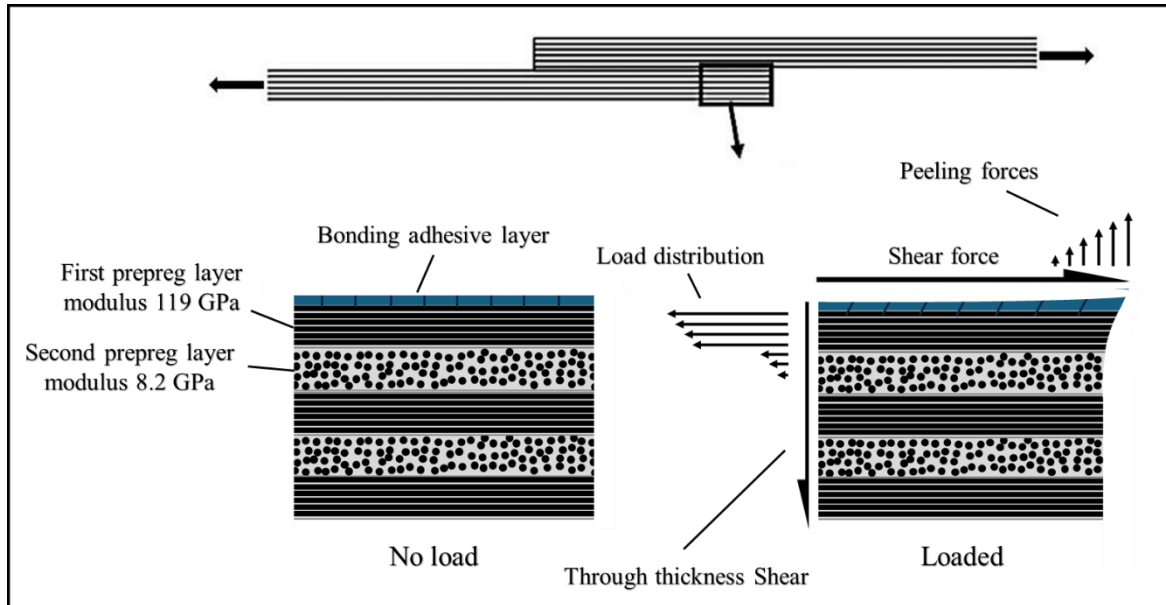


Figure 8.15. Scheme illustrating the load distribution in the tested CFRP material under the SLS test.

Although UV treatment shows a slight improvement (about 10%) over NIR laser treatment, the frequent presence of CSF indicates that the CFRP material tested has nearly achieved its maximum bonding strength with the current joint design. Consequently, it is proposed that using a stronger CFRP material, such as duplicating the 0° fibre layer on the bonded side, could lead to further enhancements with UV treatment.

8.5. Supplementary experiment

In this experiment, UV treatment followed by water contact angle (WCA) assessment was conducted on five CFRP materials, labelled M1 through M5, **Figure 8.16**.

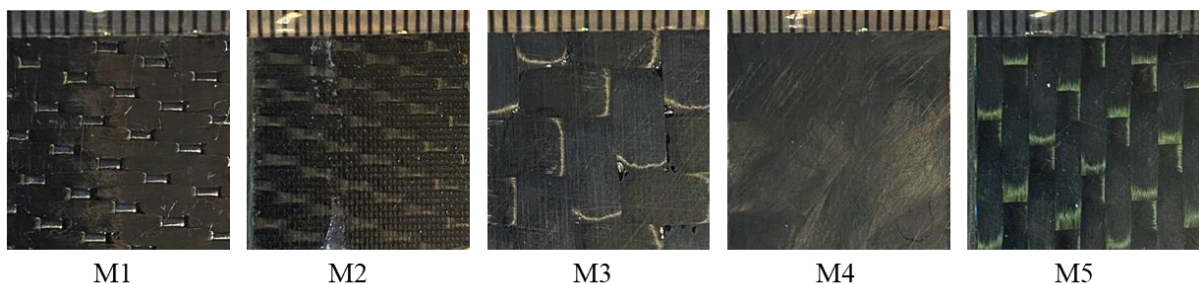


Figure 8.16. Photos of the five different CFRP materials investigated, with labels provided for each.

Two samples, each measuring 25 mm x 15 mm, were prepared from each of the five CFRP materials for this experiment. All samples were first cleaned using the method described in **Chapter 3**, and then one set was exposed to UV light at an intensity of 50 mW/cm² for 60 minutes. The five CFRP materials varied in thickness from 2.5 mm to 3.5 mm. Therefore, pieces of cardboard were used to adjust the distance from the lamp to the top surfaces of the samples to ensure uniform exposure. WCA assessment was then conducted on both sets of samples (UV-treated and non-treated). Ten WCA measurements were taken for each sample, and the averages and the SDs were calculated. For the goniometer setup, the droplet size was 1.5 mm, with 50 frames recorded at 0.016 seconds per frame and an additional 10 frames at 1 second per frame. **Figure 8.17** below displays the obtained results.

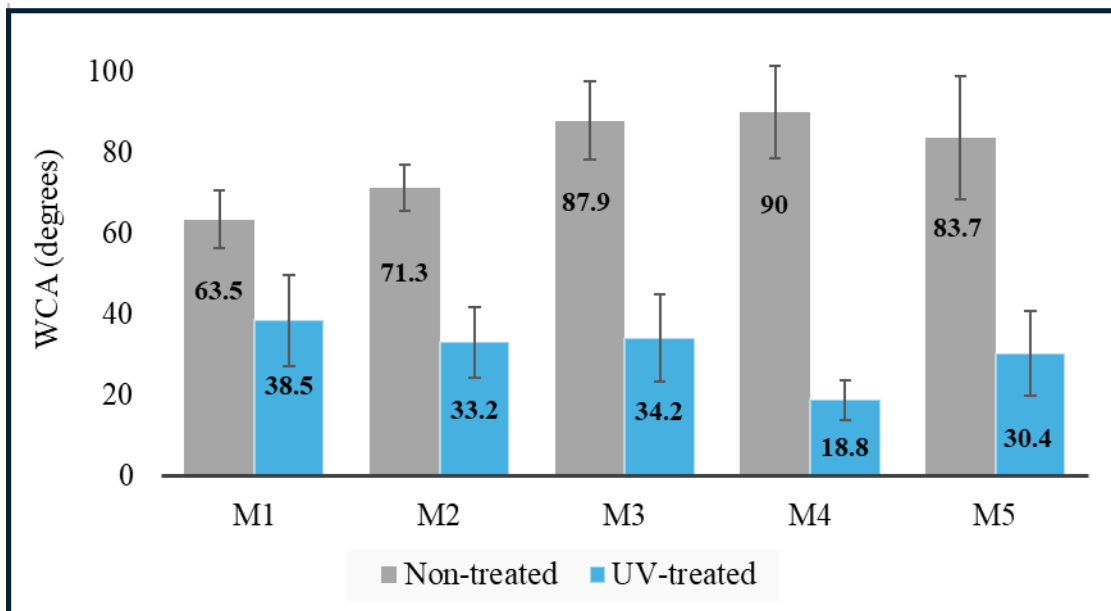


Figure 8.17. Comparison of WCA between non-treated and UV-treated samples of five different CFRP materials. From the results, it is apparent that each of the five CFRP materials exhibits specific surface wettability, likely attributable to its unique resin system and surface topography. Variable contact angle (CA) results for different CFRP materials have been documented in the literature [357]. Furthermore, each material responded differently to UV light treatment. These differences are particularly significant between CFRP M1 and CFRP M4.

UV light can induce chemical changes on the CFRP surface, potentially leading to the formation of new functional groups or the degradation of existing ones [202, 348, 358]. Since different CFRP materials possibly use various matrix resins, this can result in the development of different hydroxyl or carboxyl groups on their surfaces when exposed to UV light [348],

thereby affecting wettability in varying degrees. Consequently, the inherent properties of these resins influence their reaction to UV light, which in turn impacts the resulting surface wettability. Moreover, some fibre-reinforced polymer materials are coated or filled with UV-resistant substances [359, 360], which can affect how the material responds to UV light. These polymer composites are increasingly utilised in applications such as the aerospace industry [360].

8.6. Conclusions

In this chapter, CFRP materials were surface treated using incoherent UV light emitted by a germicidal UV lamp with a wavelength of 254 nm. The surface wettability of the treated CFRP samples was qualitatively characterised under different UV intensities and exposure periods, as well as for different CFRP materials. Additionally, the bonding strength of the UV-treated CFRP material was studied and compared with various surface treatment techniques, including an ns pulsed NIR laser, a CW CO₂ laser, combinations of either laser with UV light, and mechanical sanding. The following conclusions were obtained:

- UV light treatments significantly improved the wettability of CFRP surfaces. With a UV treatment fluence of approximately 180 J/cm², the water contact angle was reduced from 91° to about 20°. Increasing the UV fluence beyond 180 J/cm² did not result in further improvement.
- In comparison to the NIR laser treatment discussed in Chapter 6, NIR laser treatment achieved a greater reduction in the water contact angle, lowering it to under 10°. While both UV light and NIR laser treatments significantly enhance surface wettability, NIR laser treatment demonstrated slightly better performance. However, the absorption behaviour of the exposed fibre surfaces, attributed to their surface porosity, contributed to this effect.
- The response of different CFRP materials to UV light varied, with each material showing distinct improvements in surface wettability.
- The UV light treatment technique for CFRP demonstrated a significant (75%) improvement in bonding strength compared to non-treated samples, and approximately 10% higher improvement than the IR laser texturing technique. The dominant CSF mode observed in UV-treated samples suggests that the adhesion strength exceeded the material's interlaminar shear strength.

- The combination treatments of UV light with NIR laser do not appear to provide any noticeable advantage over the individual treatments. However, treating with UV light following low specific energy CO₂ laser treatment showed significant improvement over the single CO₂ laser treatment
- In terms of treatment duration, NIR laser processing of a single coupon with a bonded area of 25 mm x 12.5 mm took approximately 11 seconds, while UV treatment required about one hour. However, UV treatment can handle multiple samples simultaneously (over 100). Moreover, the duration of UV treatment can be reduced by using reflectors, such as semi-cylindrical or parabolic types, to increase light intensity. A diffuser can also be employed to achieve more uniform light distribution.
- The results from UV treatment are highly promising, indicating substantial potential for improving the joint performance of CFRP composites by enhancing adhesive bonding without altering the surface topography. Additionally, UV treatment is more cost-effective compared to laser methods.

CHAPTER 9: Conclusions and Future Works

Aiming to identify an optimal surface pre-treatment technique for enhancing the adhesive joining of CFRP composites, this thesis explores the use of incoherent UV light combined with IR lasers. This pioneering study assesses the effectiveness of incoherent UV light, both independently and in combination with two types of IR lasers: a ns pulsed NIR fibre laser and a CW CO₂ laser. The research also features a comprehensive analysis of the transmittance and absorption characteristics of epoxy resin in relation to NIR and MIR lasers. The following conclusions and recommendations arise from this work:

9.1. Conclusions

This study has conducted a number of experimental evaluations of aspects relating to the overall investigation of the potential for incoherent UV light to assist IR laser texturing in improving the adhesive joining of CFRPs.

A summary of the conclusions of these individual studies follows:

- The experimental results for epoxy resin transmittance to NIR laser (1064 nm) revealed penetration depths ranging from 90 to 140 μm across three different epoxies, with reflection fractions between 11.5% and 13.6%. These findings align with previous research, which proposed that nearly all NIR light penetrates the outer matrix layer and is absorbed by the underlying carbon fibres.
- For the epoxy resin transmittance to the MIR laser (10600 nm), the penetration depth is approximately 29 μm , with a reflectivity of 15%. An epoxy resin film with a thickness of 15 μm transmitted approximately 55% of the laser power.
- The effectiveness of NIR laser on surface processing of CFRPs to improve the adhesive bonding is highly dependent on the thickness of the outer layer matrix. In woven reinforced CFRPs, the outer layer matrix exhibits significant variation in thickness.
- Laser processing using a masking technique to shield thick matrix regions from NIR laser exposure was observed to prevent delamination and weakening of matrix-rich areas, enhancing bonding strength by an additional 10% compared with the fully laser-treated technique.
- Investigating the impact of scanning speed with ns pulsed NIR laser on heat accumulation between consecutive scans revealed no significant variation, even when

comparing scan intervals of 1.5 ms to 2.5 ms, noting that the reported cooling time of matrix resin is approximately 1 ms.

- Laser processing with a pulse length of 30 ns resulted in larger ablated areas (dimples) than those produced with a 200 ns pulse laser, with higher pulse energies creating larger dimples. Shorter pulse lengths (30 ns) showed fibre breakage. The depth of the dimples was limited by the underlying fibres. Samples treated with 200 ns pulses exhibited lower water contact angles and higher bonding strength than those treated with 30 and 80 ns pulses.
- A CW CO₂ laser, with optimised processing parameters, can effectively remove the outer matrix resin layer and expose the underlying CFs. However, this method may compromise the integrity of the fibre/matrix interface. A CW CO₂ laser can improve the bonding strength of CFRP materials that initially show low adhesion and interfacial failure.
- The UV light treatment technique for CFRP resulted in a substantial 75% increase in bonding strength compared to untreated samples and about 10% higher than the IR laser texturing technique. Combining UV light with NIR laser treatments offers no significant advantage over using each treatment individually. However, applying UV light after low-specific-energy CO₂ laser treatment resulted in a notable improvement compared to using CO₂ laser alone.

The overall conclusion is that incoherent UV lamp treatment used in conjunction with NIR laser texturing (either pre or post laser treatment) does not appear to produce any significant benefit to the strength of adhesive bonded CFRP. Some benefit was found in using incoherent UV light in conjunction with low specific energy CO₂ laser texturing.

The incoherent UV light treatment alone gives results that are highly promising, showing considerable potential for improving the joint performance of CFRP composites. This method enhances adhesive bonding while preserving the surface topography. Additionally, UV treatment proves to be more cost-effective than laser methods.

9.2. Future works

- Laser surface treatment with both NIR and MIR lasers generally improves bonding strength. The predominant failure modes observed were light fibre tear failure, indicating a separation or loss of fibre-matrix integrity. Further investigation into the

use of low-viscosity adhesives or diluted resin will potentially re-integrate the fibre/matrix, leading to additional improvements in bonding strength.

- UV light surface treatment for 1 hour at an intensity of 50 mW/cm² resulted in approximately 70% improvement in bonding strength, with a predominantly cohesive substrate failure mode. These results, supported by the SolidWorks modelling results and literature review, suggest that the bonding strength exceeded the material strength due to low interlaminar strength, layup sequence, and high peeling forces. Therefore, it is believed that further investigation into UV treatment using different CFRP materials with improved layup sequences and enhanced interlaminar strength will yield additional improvements in bonding strength.
- UV light treatment induces chemical changes on the CFRP surface, leading to the formation of new functional groups or the degradation of existing ones. Further investigation into UV treatment of CFRP materials using higher UV intensities, achieved through a reflector or a higher-power UV lamp, is essential not only to reduce the treatment period but also to enhance understanding of the time dependency of the chemical interaction and the effects on surface wettability and bonding strength.
- Utilising the data from matrix resin transmittance investigations, particularly regarding MIR lasers, in finite element modelling analyses can enhance the understanding of the removal mechanism of the outer layer matrix when using a CO₂ laser. Thus, in future works, a finite element model of this process will be developed.
- This project has explored the transmittance of thermoset epoxy resin to both NIR and MIR lasers. To further investigate NIR laser transmittance, it will be necessary to create samples ranging from a few millimetres to several hundred millimetres in thickness. However, during the curing process, gas bubbles tend to form and become trapped within thick (above 10 mm) moulded samples, which can significantly impact the accuracy of the results. To address this issue, specialised moulding equipment capable of applying high pressure will be essential to minimise and displace the formed bubbles. Notably, among the three different types of thermoset resins tested, only one achieved a thickness of up to 43 mm without noticeable bubbles. Additionally, an automatic polishing machine will be developed to achieve even surface roughness across the different samples.
- Since FTIR shows no significant variations between UV-treated and non-treated samples, it is important to explore and identify an alternative method for analysing the

chemical changes after UV treatment. One potential method to consider is X-ray Photoelectron Spectroscopy, as it could provide more detailed insights into the chemical changes at the surface level.

References

1. Karbhari, V., *Fabrication, quality and service-life issues for composites in civil engineering*, in *Durability of composites for civil structural applications*. 2007, Elsevier. p. 13-30.
2. Carey, J., *Introduction to braided composites*, in *Handbook of Advances in Braided Composite Materials*. 2017, Elsevier. p. 1-21.
3. Campbell, F.C., *Structural composite materials*. 2010: ASM international.
4. Daniel, I.M., et al., *Engineering mechanics of composite materials*. Vol. 3. 1994: Oxford university press New York.
5. French, P.W., et al., *New laser machine tools for processing carbon fibre reinforced plastic (CFRP)*. *Key Engineering Materials*, 2011. **1521**(496): p. 30.
6. Masuelli, M., *Fiber reinforced polymers: the technology applied for concrete repair*. 2013: BoD–Books on Demand.
7. Korkees, F., *Moisture absorption behavior and diffusion characteristics of continuous carbon fiber reinforced epoxy composites: a review*. *Polymer-Plastics Technology and Materials*, 2023. **62**(14): p. 1789-1822.
8. Lima, M., et al., *Laser processing of carbon fiber reinforced polymer composite for optical fiber guidelines*. *Physics Procedia*, 2013. **41**: p. 572-580.
9. Akman, E., et al., *Investigation of the differences between photochemical and photothermal laser ablation on the shear strength of CFRP/CFRP adhesive joints*. *International Journal of Adhesion and Adhesives*, 2020. **98**: p. 102548.
10. Ledesma, R., et al., *Surface characterization of carbon fiber reinforced polymers by picosecond laser induced breakdown spectroscopy*. *Spectrochimica Acta Part B: Atomic Spectroscopy*, 2018. **140**: p. 5-12.
11. Fekete, J. and J. Hall, *Design of auto body: Materials perspective*. *Automotive Steels*, 2017: p. 1-18.
12. Thoppul, S.D., J. Finegan, and R.F. Gibson, *Mechanics of mechanically fastened joints in polymer–matrix composite structures—a review*. *Composites science and technology*, 2009. **69**(3-4): p. 301-329.
13. Teti, R., et al., *Smart multi-sensor monitoring in drilling of CFRP/CFRP composite material stacks for aerospace assembly applications*. *Applied Sciences*, 2020. **10**(3): p. 758.
14. Fischer, F., S. Kreling, and K. Dilger, *Surface structuring of CFRP by using modern excimer laser sources*. *Physics procedia*, 2012. **39**: p. 154-160.
15. Fischer, F., et al., *Laser surface pre-treatment of CFRP for adhesive bonding in consideration of the absorption behaviour*. *The Journal of Adhesion*, 2012. **88**(4-6): p. 350-363.
16. Nattapat, M., et al., *Laser surface modification of carbon fiber reinforced composites*. *Materials and Manufacturing Processes*, 2015. **30**(12): p. 1450-1456.
17. Oliveira, V., et al., *Surface treatment of CFRP composites using femtosecond laser radiation*. *Optics and Lasers in Engineering*, 2017. **94**: p. 37-43.
18. Ebnesajjad, S. and C. Ebnesajjad, *Surface treatment of materials for adhesive bonding*. 2013: William Andrew.
19. Baldan, A., *Adhesion phenomena in bonded joints*. *International Journal of Adhesion and Adhesives*, 2012. **38**: p. 95-116.
20. Çoban, O., et al., *Laser surface treatment of CFRP composites for a better adhesive bonding owing to the mechanical interlocking mechanism*. *Polymer Composites*, 2019. **40**(9): p. 3611-3622.

21. Holtmannspötter, J., et al., *The use of peel ply as a method to create reproduceable but contaminated surfaces for structural adhesive bonding of carbon fiber reinforced plastics*. The Journal of Adhesion, 2013. **89**(2): p. 96-110.
22. Budhe, S., et al., *An updated review of adhesively bonded joints in composite materials*. International Journal of Adhesion and Adhesives, 2017. **72**: p. 30-42.
23. Wu, G., et al., *Oxygen plasma processing and improved interfacial adhesion in PBO fiber reinforced epoxy composites*. Vacuum, 2009. **83**: p. S271-S274.
24. Palmieri, F.L., et al., *Laser ablation surface preparation for adhesive bonding of carbon fiber reinforced epoxy composites*. International Journal of Adhesion and Adhesives, 2016. **68**: p. 95-101.
25. Yokozeki, T., et al., *Evaluation of adhesively bonded joint strength of CFRP with laser treatment*. Advanced Composite Materials, 2016. **25**(4): p. 317-327.
26. Schweizer, M., et al., *Adhesive bonding of CFRP: a comparison of different surface pre-treatment strategies and their effect on the bonding shear strength*. Journal of Adhesion Science and Technology, 2017. **31**(23): p. 2581-2591.
27. Reitz, V., et al., *A comparison of IR-and UV-laser pretreatment to increase the bonding strength of adhesively joined aluminum/CFRP components*. Composites Part A: Applied Science and Manufacturing, 2017. **96**: p. 18-27.
28. Rauh, B., et al., *UV-laser cleaning and surface characterization of an aerospace carbon fibre reinforced polymer*. International Journal of Adhesion and Adhesives, 2018. **82**: p. 50-59.
29. Li, Y., et al., *Comparative study of infrared laser surface treatment and ultraviolet laser surface treatment of CFRP laminates*. The International Journal of Advanced Manufacturing Technology, 2019. **102**: p. 4059-4071.
30. Pagano, N., et al., *Laser interaction with carbon fibre reinforced polymers*. Procedia Cirp, 2015. **33**: p. 423-427.
31. Leone, C., et al., *Investigation of CFRP laser milling using a 30 W Q-switched Yb: YAG fiber laser: Effect of process parameters on removal mechanisms and HAZ formation*. CompoSiteS Part a: applied science and manufacturing, 2013. **55**: p. 129-142.
32. Arikan, E., et al., *The role of chemical surface modification for structural adhesive bonding on polymers-Washability of chemical functionalization without reducing adhesion*. International Journal of Adhesion and Adhesives, 2019. **95**: p. 102409.
33. Tabuchi, M., et al., *UV Light-Generated Superhydrophilicity of a Titanium Surface Enhances the Transfer, Diffusion and Adsorption of Osteogenic Factors from a Collagen Sponge*. International Journal of Molecular Sciences, 2021. **22**(13): p. 6811.
34. Gebauer, J., et al., *On the ablation behavior of carbon fiber-reinforced plastics during laser surface treatment using pulsed lasers*. Materials, 2020. **13**(24): p. 5682.
35. Blass, D., et al., *Composite bonding pre-treatment with laser radiation of 3 μ m Wavelength: Comparison with conventional laser sources*. Materials, 2018. **11**(7): p. 1216.
36. Kumar, M., et al., *Epoxy-paint stripping using TEA CO2 laser: Determination of threshold fluence and the process parameters*. Optics & Laser Technology, 2013. **46**: p. 29-36.
37. McKie, A.D. and R.C. Addison Jr, *Rapid inspection of composites using laser-based ultrasound*, in *Review of Progress in Quantitative Nondestructive Evaluation: Volumes 12A and 12B*. 1993, Springer. p. 507-516.
38. Harris, B., *Engineering composite materials*. 1999.
39. Nijssen, R., *Composite materials: an introduction*. 2015: Inholland University of Applied Sciences Netherlands.
40. Young-Pyo Jeon, R.A.-C., Marlon Morales and Amod A. Ogale, *Handbook of Advanced Ceramics*. 2013.

41. Vasiliev, V.V. and E.V. Morozov, *Advanced mechanics of composite materials and structural elements*. 2013: Newnes.
42. Mahendran, M., *The modulus of elasticity of steel-is it 200 gpa?* 1996.
43. Ahmad, M.H.I.I. and N.H.M.N. Murtadhahadi. *Moulding parameter optimisation for the best sintered density*. in *Proceedings of the world congress on engineering*. 2009.
44. Ozkan, D., M.S. Gok, and A.C. Karaoglanli, *Carbon fiber reinforced polymer (CFRP) composite materials, their characteristic properties, industrial application areas and their machinability*. *Engineering Design Applications III: Structures, Materials and Processes*, 2020: p. 235-253.
45. Shirvanimoghaddam, K., et al., *Carbon fiber reinforced metal matrix composites: Fabrication processes and properties*. *Composites Part A: Applied Science and Manufacturing*, 2017. **92**: p. 70-96.
46. Tang, S. and C. Hu, *Design, preparation and properties of carbon fiber reinforced ultra-high temperature ceramic composites for aerospace applications: a review*. *Journal of Materials Science & Technology*, 2017. **33**(2): p. 117-130.
47. Khan, N.I. and S. Halder, *Self-healing fiber-reinforced polymer composites for their potential structural applications*, in *Self-healing polymer-based systems*. 2020, Elsevier. p. 455-472.
48. Jang, D., et al., *Strategies for the production of PAN-Based carbon fibers with high tensile strength*. *Carbon*, 2022. **186**: p. 644-677.
49. Zhang, J., et al., *Past, present and future prospective of global carbon fibre composite developments and applications*. *Composites Part B: Engineering*, 2022: p. 110463.
50. Carrasco-Baltasar, D., et al., *Modelling of woven CFRP plates subjected to oblique high-velocity impact and membrane loads*. *Composite Structures*, 2023. **303**: p. 116344.
51. Morgan, P., *Carbon fibers and their composites*. 2005: CRC press.
52. Deeraj, B.D.S., et al., *EMI shielding materials based on thermosetting polymers*, in *Materials for Potential EMI Shielding Applications*. 2020, Elsevier. p. 101-110.
53. Somiya, S., *Handbook of advanced ceramics: materials, applications, processing, and properties*. 2nd ed. 2013: Academic press. 11.
54. SHIRASU, K., C. NAGAI, and K. NAITO, *Mechanical anisotropy of PAN-based and pitch-based carbon fibers*. *Mechanical Engineering Journal*, 2020. **7**(4): p. 19-00599-19-00599.
55. Zhang, X. and Q. Li, *Carbon fiber spinning*, in *Activated carbon fiber and textiles*. 2017, Elsevier. p. 39-60.
56. Inagaki, M., *New carbons-control of structure and functions*. 2000: Elsevier.
57. Fitzer, F. and M. Heine, *Carbon fibre manufacture and surface treatment*. Elsevier Science Publishers B. V., *Fiber Reinforcements for Composite Materials.*, 1988. **2**: p. 73-148.
58. Manocha, L., *Carbon fibers*. *Encyclopedia of materials: Science and technology*, 2001: p. 906-916.
59. Newcomb, B.A., *Processing, structure, and properties of carbon fibers*. *Composites Part A: Applied Science and Manufacturing*, 2016. **91**: p. 262-282.
60. Chen, J.Y., *Activated carbon fiber and textiles*. 2016: Woodhead Publishing.
61. Khayyam, H., et al., *PAN precursor fabrication, applications and thermal stabilization process in carbon fiber production: Experimental and mathematical modelling*. *Progress in Materials Science*, 2020. **107**: p. 100575.
62. Somiya, S., *Handbook of advanced ceramics: materials, applications, processing, and properties*. 2013: Academic press.
63. Nunna, S., et al., *Development of a cost model for the production of carbon fibres*. *Heliyon*, 2019. **5**(10).

64. Yang, T., et al., *Effect of Sizing Agents on Surface Properties of Carbon Fibers and Interfacial Adhesion of Carbon Fiber/Bismaleimide Composites*. ACS omega, 2021. **6**(36): p. 23028-23037.
65. Downey, M.A. and L.T. Drzal, *Toughening of carbon fiber-reinforced epoxy polymer composites utilizing fiber surface treatment and sizing*. Composites Part A: Applied Science and Manufacturing, 2016. **90**: p. 687-698.
66. Eyckens, D.J., et al., *Carbon fibre surface chemistry and its role in fibre-to-matrix adhesion*. Journal of Materials Chemistry A, 2021. **9**(47): p. 26528-26572.
67. Sharma, M., et al., *Carbon fiber surfaces and composite interphases*. Composites Science and Technology, 2014. **102**: p. 35-50.
68. Wu, Q., et al., *Effect of sizing on interfacial adhesion of commercial high strength carbon fiber-reinforced resin composites*. Polymer Composites, 2016. **37**(1): p. 254-261.
69. Bascom, W.D. and L. Drzal, *The surface properties of carbon fibers and their adhesion to organic polymers*. 1987, NASA.
70. Dilsiz, N. and J. Wightman, *Effect of acid–base properties of unsized and sized carbon fibers on fiber/epoxy matrix adhesion*. Colloids and Surfaces A: Physicochemical and Engineering Aspects, 2000. **164**(2-3): p. 325-336.
71. Stojcevski, F., et al., *Effect of carbon fiber oxidization parameters and sizing deposition levels on the fiber-matrix interfacial shear strength*. Composites Part A: Applied Science and Manufacturing, 2018. **114**: p. 212-224.
72. Fernandez, B., et al., *A comparative study on the influence of epoxy sizings on the mechanical performance of woven carbon fiber-epoxy composites*. Polymer composites, 2004. **25**(3): p. 319-330.
73. Kausar, A., *Advances in carbon fiber reinforced polyamide-based composite materials*. Advances in materials science, 2019. **19**(4): p. 67-82.
74. Balasubramanian, M., *Composite materials and processing*. 2013: CRC press.
75. Mirdehghan, S.A., *Fibrous polymeric composites*, in *Engineered Polymeric Fibrous Materials*. 2021, Elsevier. p. 1-58.
76. Sauder, C., J. Lamon, and R. Pailler, *The tensile behavior of carbon fibers at high temperatures up to 2400 C*. Carbon, 2004. **42**(4): p. 715-725.
77. *Toray Composite Materials America/ data sheets*. [cited 2024 8 September]; Available from: https://www.cf-composites.toray/resources/data_sheets/.
78. *Solvay THORNEL® P-25 Pitch-Based Fiber/ material property data*. [cited 2024 8 September]; Available from: <https://www.matweb.com/search/DataSheet.aspx?MatGUID=36772f241b654d6a8f6a1b0c322485ce>.
79. *Solvay Thornel® P-100 2K Carbon Fiber, Pitch Precursor/ material property data*. [cited 2024 8 September]; Available from: <https://www.matweb.com/search/datasheet.aspx?matguid=dd21d18e267044a79df3e8d09de9a420>.
80. Ohsawa, T., et al., *Axial compressive strength of carbon fiber*. Journal of applied polymer science, 1990. **39**(8): p. 1733-1743.
81. Nunna, S., et al., *A review of the structural factors which control compression in carbon fibres and their composites*. Composite Structures, 2023. **303**: p. 116293.
82. Park, S.-J. and M.-K. Seo, *Composite characterization*, in *Interface science and technology*. 2011, Elsevier. p. 631-738.
83. Ahmed, A., et al. *Study of thermal expansion in carbon fiber-reinforced polymer composites*. in *SAMPE international symposium proceedings*. 2012. SAMPE Charleston (SC), USA.

84. Islam, M.S., et al., *Toughening carbon fibre composites at cryogenic temperatures using low-thermal expansion nanoparticles*. Composites Part A: Applied Science and Manufacturing, 2021. **150**: p. 106613.
85. Diefendorf, R.J., *1.02 - Pitch Precursor Carbon Fibers*, in *Comprehensive Composite Materials*, A. Kelly and C. Zweben, Editors. 2000, Pergamon: Oxford. p. 35-83.
86. Tao, Z., et al., *Graphite fiber/copper composites with near-zero thermal expansion*. Materials & Design, 2012. **33**: p. 372-375.
87. Mallick, P.K., *Fiber-reinforced composites: materials, manufacturing, and design*. 2007: CRC press.
88. Peijs, A., R. Venderbosch, and P. Lemstra, *Hybrid composites based on polyethylene and carbon fibres Part 3: Impact resistant structural composites through damage management*. Composites, 1990. **21**(6): p. 522-530.
89. Westwood, M., et al., *Oxidation protection for carbon fibre composites*. Journal of materials science, 1996. **31**: p. 1389-1397.
90. Daniel, I.M., et al., *Engineering mechanics of composite materials*. Vol. 1994. 2006: Oxford university press New York.
91. Jabbar, M. and A. Nasreen, *Composite fabrication and joining*, in *Composite Solutions for Ballistics*. 2021, Elsevier. p. 177-197.
92. Jang, B.Z., *Advanced polymer composites*. (No Title), 1994.
93. Bergant, Z., A. Savin, and J. Grum, *Effects of manufacturing technology on static, multi-frequency dynamic mechanical analysis and fracture energy of cross-ply and quasi-isotropic carbon/epoxy laminates*. Polymers and Polymer Composites, 2018. **26**(5-6): p. 358-370.
94. Abdellaoui, H., M. Raji, and R. Bouhfid, *Investigation of the deformation behavior of epoxy-based composite materials*, in *Failure analysis in biocomposites, fibre-reinforced composites and hybrid composites*. 2019, Elsevier. p. 29-49.
95. Sprenger, S., M.H. Kothmann, and V. Altstaedt, *Carbon fiber-reinforced composites using an epoxy resin matrix modified with reactive liquid rubber and silica nanoparticles*. Composites science and technology, 2014. **105**: p. 86-95.
96. Wu, J., et al., *Carbon fiber-reinforced epoxy with 100% fiber recycling by transesterification reactions*. Frontiers in Materials, 2022. **9**: p. 1045372.
97. Pimenta, S. and S.T. Pinho, *Recycling of carbon fibers*, in *Handbook of recycling*. 2014, Elsevier. p. 269-283.
98. Meyer, L.O., K. Schulte, and E. Grove-Nielsen, *CFRP-recycling following a pyrolysis route: process optimization and potentials*. Journal of composite materials, 2009. **43**(9): p. 1121-1132.
99. Sukanto, H., et al. *Carbon fibers recovery from CFRP recycling process and their usage: A review*. in *IOP Conference Series: Materials Science and Engineering*. 2021. IOP Publishing.
100. Nakagawa, K.S.M., *CFRP recycling technology using depolymerization under ordinary pressure*. No. 56 I March 2014, 2014: p. 6.
101. Keith, M.J., A. Ingram, and G.A. Leeke. *Catalytic degradation of a carbon fibre reinforced epoxy resin with an acetone/water solvent*. in *Proceedings of the 18th European Conference on Composite Materials (ECCM18)*. 2018.
102. Karuppanan Gopalraj, S. and T. Kärki, *A review on the recycling of waste carbon fibre/glass fibre-reinforced composites: Fibre recovery, properties and life-cycle analysis*. SN Applied Sciences, 2020. **2**(3): p. 433.
103. Kouparitsas, C., et al., *Recycling of the fibrous fraction of reinforced thermoset composites*. Polymer composites, 2002. **23**(4): p. 682-689.
104. Palmer, J., et al., *Sheet moulding compound (SMC) from carbon fibre recycle*. Composites Part A: Applied Science and Manufacturing, 2010. **41**(9): p. 1232-1237.

105. Conroy, A., S. Halliwell, and T. Reynolds, *Composite recycling in the construction industry*. Composites Part A: Applied Science and Manufacturing, 2006. **37**(8): p. 1216-1222.
106. Pakdel, E., et al., *Recent progress in recycling carbon fibre reinforced composites and dry carbon fibre wastes*. Resources, Conservation and Recycling, 2021. **166**: p. 105340.
107. Yangjie, Z., et al., *Bolt insertion damage and mechanical behaviors investigation of CFRP/CFRP interference fit bolted joints*. Chinese Journal of Aeronautics, 2022. **35**(9): p. 354-365.
108. Worrall, C., E. Kellar, and C. Vacogne, *Joining of fibre-reinforced polymer composites. A good practice guide*. Composites UK Audley House, Northbridge Road, Berkhamsted, Hertfordshire, 2020: p. 1-77.
109. Pramanik, A., et al., *Joining of carbon fibre reinforced polymer (CFRP) composites and aluminium alloys—A review*. Composites Part A: Applied Science and Manufacturing, 2017. **101**: p. 1-29.
110. Ding, Y., et al., *Enhancement of interfacial strength of overmolded hybrid structures of short fiber reinforced polyamide 6 on continuous fiber reinforced epoxy composites under various surface pretreatments*. Polymer Composites, 2022. **43**(2): p. 1038-1047.
111. Mehrabian, M. and R. Boukhili, *3D-DIC strain field measurements in bolted and hybrid bolted-bonded joints of woven carbon-epoxy composites*. Composites Part B: Engineering, 2021. **218**: p. 108875.
112. Martínez-Landeros, V., et al., *Studies on the influence of surface treatment type, in the effectiveness of structural adhesive bonding, for carbon fiber reinforced composites*. Journal of Manufacturing Processes, 2019. **39**: p. 160-166.
113. Murakami, Y., *Metal fatigue: effects of small defects and nonmetallic inclusions*. 2019: Academic Press.
114. Gray, P., R. O'Higgins, and C. McCarthy, *Effect of thickness and laminate taper on the stiffness, strength and secondary bending of single-lap, single-bolt countersunk composite joints*. Composite structures, 2014. **107**: p. 315-324.
115. Viandier, A., et al., *Hybridisation as an efficient joining, electrochemical corrosion study as a need*. Journal for electrochemistry and plating technology, 2017.
116. Abdel Wahab, M., *Fatigue in adhesively bonded joints: a review*. International Scholarly Research Notices, 2012. **2012**.
117. Banea, M.D. and L.F. da Silva, *Adhesively bonded joints in composite materials: an overview*. Proceedings of the Institution of Mechanical Engineers, Part L: Journal of Materials: Design and Applications, 2009. **223**(1): p. 1-18.
118. Campbell, F.C., *Structural composite materials, Chapter 8, adhesive Bonding*. 2010: ASM international.
119. Sathiyamurthy, R. and M. Duraiselvam, *Selective laser ablation of CFRP composite to enhance adhesive bonding*. Materials and Manufacturing Processes, 2019. **34**(11): p. 1296-1305.
120. Cruz González, C.E., et al., *Influence of the roughening method, joint configuration and adhesive thickness on the shear strength of ferritic stainless steel surfaces joined by methyl methacrylate*. Revista de Metalurgia, 2018. **54**(2): p. 1-14.
121. Wingfield, J., *Treatment of composite surfaces for adhesive bonding*. International journal of adhesion and adhesives, 1993. **13**(3): p. 151-156.
122. Ebnesajjad, S. and A.H. Landrock, *Adhesives technology handbook*. 2014: William Andrew.
123. Campbell, F., *Adhesive bonding and integrally cocured structure: a way to reduce assembly costs through parts integration*. Manufacturing Processes for Advanced Composites; Elsevier Science: Amsterdam, The Netherlands, 2004: p. 241-301.

124. Kinloch, A., *Adhesives in engineering*. Proceedings of the Institution of Mechanical Engineers, Part G: Journal of Aerospace Engineering, 1997. **211**(5): p. 307-335.
125. Miller, J.D. and H. Ishida, *Adhesive—Adherent Interface and Interphase*, in *Fundamentals of adhesion*. 1991, Springer. p. 291-324.
126. Cognard, J., *The metal/polymer interphase in adhesive joints*. International journal of adhesion and adhesives, 1991. **11**(2): p. 114-116.
127. Mittal, K. and S. Panigrahi, *Structural Adhesives: Properties, Characterization and Applications*. 2023: John Wiley & Sons.
128. Carolan, D., S. He, and A.C. Taylor, *Advances in toughening strategies for structural adhesives*, in *Advances in Structural Adhesive Bonding*. 2023, Elsevier. p. 251-286.
129. Mouritz, A.P., *Introduction to aerospace materials*. 2012: Elsevier.
130. Petrie, E., *Adhesive bonding of textiles: principles, types of adhesive and methods of use*. Joining textiles, 2013: p. 225-274.
131. Pocius, A.V., *Adhesion and adhesives technology: an introduction*. 2021: Carl Hanser Verlag GmbH Co KG.
132. Schultz, J. and M. Nardin, *Theories and mechanisms of adhesion*. MATERIALS ENGINEERING-NEW YORK-, 1999. **14**: p. 1-26.
133. Pocius, A., *The relationship of surface science and adhesion science*. Adhesion and Adhesives Technology, 2012: p. 145-179.
134. Selvakumar, N., H.C. Barshilia, and K. Rajam, *Effect of substrate roughness on the apparent surface free energy of sputter deposited superhydrophobic polytetrafluoroethylene coatings: A comparison of experimental data with different theoretical models*. Journal of Applied Physics, 2010. **108**(1).
135. Mahadik, D., et al., *Effect of surface composition and roughness on the apparent surface free energy of silica aerogel materials*. Applied Physics Letters, 2011. **99**(10).
136. Pukánszky, B. and E. Fekete, *Adhesion and surface modification*. Mineral Fillers in Thermoplastics I: Raw Materials and Processing, 1999: p. 109-153.
137. Comyn, J., *Theories of adhesion*, in *Handbook of adhesives and sealants*. 2006, Elsevier. p. 1-50.
138. See, T.L., et al., *Laser abrading of carbon fibre reinforced composite for improving paint adhesion*. Applied Physics A, 2014. **117**: p. 1045-1054.
139. Liu, L., et al., *Effect of laser surface treatment on surface and bonding properties of carbon fiber reinforced composites*. International Journal of Material Forming, 2020. **13**: p. 885-895.
140. Tsuda, Y., *Surface wettability controllable polyimides by UV light irradiation for printed electronics*. Journal of Photopolymer Science and Technology, 2016. **29**(3): p. 383-390.
141. Broughton, W. and M. Lodeiro, *Review of surface characterisation techniques for adhesive bonding*. 2002.
142. Abdelbary, A. and L. Chang, *Principles of Engineering Tribology: Fundamentals and Applications*. 2023: Elsevier.
143. Zisman, W.A., *Relation of the equilibrium contact angle to liquid and solid constitution*. 1964, ACS Publications.
144. Anderson, W., *Wettability literature survey-part 2: Wettability measurement*. Journal of petroleum technology, 1986. **38**(11): p. 1246-1262.
145. Gu, H., et al., *Investigation on contact angle measurement methods and wettability transition of porous surfaces*. Surface and Coatings Technology, 2016. **292**: p. 72-77.
146. Law, K.-Y., *Water–surface interactions and definitions for hydrophilicity, hydrophobicity and superhydrophobicity*. Pure and Applied Chemistry, 2015. **87**(8): p. 759-765.
147. Young, T., *Phil. Trans. R. Soc. London*95, 1805. **65**.
148. Barrio-Zhang, H., et al., *Contact-angle hysteresis and contact-line friction on slippery liquid-like surfaces*. Langmuir, 2020. **36**(49): p. 15094-15101.

149. Kung, C.H., et al., *Assessment and interpretation of surface wettability based on sessile droplet contact angle measurement: challenges and opportunities*. *Advanced Materials Interfaces*, 2019. **6**(18): p. 1900839.
150. Law, K.-Y., *Definitions for hydrophilicity, hydrophobicity, and superhydrophobicity: getting the basics right*. 2014, ACS Publications. p. 686-688.
151. Drelich, J. and E. Chibowski, *Superhydrophilic and superwetting surfaces: definition and mechanisms of control*. *Langmuir*, 2010. **26**(24): p. 18621-18623.
152. Hornyak, G. and A. Rao, *Fundamentals of nanoscience (and nanotechnology)*, in *Nanoscience in Dermatology*. 2016, Elsevier. p. 15-29.
153. Roach, P., N.J. Shirtcliffe, and M.I. Newton, *Progress in superhydrophobic surface development*. *Soft matter*, 2008. **4**(2): p. 224-240.
154. Quéré, D., *Non-sticking drops*. *Reports on Progress in Physics*, 2005. **68**(11): p. 2495.
155. Fernández-Blázquez, J.P., et al., *Superhydrophilic and superhydrophobic nanostructured surfaces via plasma treatment*. *Journal of colloid and interface science*, 2011. **357**(1): p. 234-238.
156. Marmur, A., et al., *Contact angles and wettability: Towards common and accurate terminology*. *Surface Innovations*, 2017. **5**(1): p. 3-8.
157. Gao, L. and T.J. McCarthy, *Teflon is hydrophilic. Comments on definitions of hydrophobic, shear versus tensile hydrophobicity, and wettability characterization*. *Langmuir*, 2008. **24**(17): p. 9183-9188.
158. Bhasin, A., et al., *Surface free energy to identify moisture sensitivity of materials for asphalt mixes*. *Transportation Research Record*, 2007. **2001**(1): p. 37-45.
159. Ebnesajjad, S., *Surface tension and its measurement*, in *Handbook of adhesives and surface preparation*. 2011, Elsevier. p. 21-30.
160. Park, S.-J. and M.-K. Seo, *Interface science and composites*. Vol. 18. 2011: Academic Press.
161. Kinloch, A. and A. Kinloch, *Interfacial contact*. *Adhesion and adhesives: science and technology*, 1987: p. 18-55.
162. Zhao, Q., Y. Liu, and E. Abel, *Effect of temperature on the surface free energy of amorphous carbon films*. *Journal of Colloid and Interface Science*, 2004. **280**(1): p. 174-183.
163. Żenkiewicz, M., *Methods for the calculation of surface free energy of solids*. *Journal of Achievements in Materials and Manufacturing Engineering*, 2007. **24**(1): p. 137-145.
164. Fernández, V. and M. Khayet, *Evaluation of the surface free energy of plant surfaces: toward standardizing the procedure*. *Frontiers in plant science*, 2015. **6**: p. 510.
165. Fowkes, F.M. *The relation of the attractive forces at interfaces to wetting, spreading, adsorption, and long-range attractive forces*. in *Fundamental Phenomena in the Materials Sciences: Volume 2 Surface Phenomena Proceedings of the Second Symposium on Fundamental Phenomena in the Materials Sciences Held January 27-28, 1964, at Boston, Mass.* 1966. Springer.
166. Owens, D.K. and R. Wendt, *Estimation of the surface free energy of polymers*. *Journal of applied polymer science*, 1969. **13**(8): p. 1741-1747.
167. Baldan, A., *Adhesively-bonded joints and repairs in metallic alloys, polymers and composite materials: Adhesives, adhesion theories and surface pretreatment*. *Journal of materials science*, 2004. **39**: p. 1-49.
168. Molitor, P., V. Barron, and T. Young, *Surface treatment of titanium for adhesive bonding to polymer composites: a review*. *International Journal of Adhesion and Adhesives*, 2001. **21**(2): p. 129-136.
169. Kodokian, G. and A. Kinloch, *Surface pretreatment and adhesion of thermoplastic fibre-composites*. *Journal of Materials Science Letters*, 1988. **7**: p. 625-627.

170. Tao, R., M. Alfano, and G. Lubineau, *Laser-based surface patterning of composite plates for improved secondary adhesive bonding*. Composites Part A: Applied Science and Manufacturing, 2018. **109**: p. 84-94.
171. Bénard, Q., M. Fois, and M. Grisel, *Peel ply surface treatment for composite assemblies: chemistry and morphology effects*. Composites Part A: Applied Science and Manufacturing, 2005. **36**(11): p. 1562-1568.
172. Kanerva, M. and O. Saarela, *The peel ply surface treatment for adhesive bonding of composites: A review*. International Journal of Adhesion and Adhesives, 2013. **43**: p. 60-69.
173. Ehrhart, B., et al. *Methods for the quality assessment of adhesive bonded CFRP structures-a resumé*. in *2nd International Symposium on NDT in Aerospace*. 2010.
174. Malinowski, P.H., et al. *Characterisation of CFRP surface contamination by laser induced fluorescence*. in *Health Monitoring of Structural and Biological Systems 2014*. 2014. SPIE.
175. Roizard, X., M. Wery, and J. Kirmann, *Effects of alkaline etching on the surface roughness of a fibre-reinforced epoxy composite*. Composite structures, 2002. **56**(3): p. 223-228.
176. Kirmann, J., et al., *Effects of the alkaline permanganate etching of epoxy on the peel adhesion of electrolessly plated copper on a fibre-reinforced epoxy composite*. Journal of adhesion science and technology, 1998. **12**(4): p. 383-397.
177. Wang, D., et al., *Increasing strength and fracture toughness of carbon fibre-reinforced plastic adhesively bonded joints by combining peel-ply and oxygen plasma treatments*. Applied Surface Science, 2023. **612**: p. 155768.
178. De lorio, I., et al., *Plasma treatments of polymeric materials and Al alloy for adhesive bonding*. Journal of Materials Processing Technology, 1997. **68**(2): p. 179-183.
179. Li, R., L. Ye, and Y.-W. Mai, *Application of plasma technologies in fibre-reinforced polymer composites: a review of recent developments*. Composites Part A: Applied Science and Manufacturing, 1997. **28**(1): p. 73-86.
180. Chung, H., et al., *Effect of oxygen plasma treatment on the bonding strength of CFRP/aluminum foam composite*. Journal of Alloys and Compounds, 2009. **481**(1-2): p. 214-219.
181. Pizzorni, M., et al., *Low-pressure plasma treatment of CFRP substrates for epoxy-adhesive bonding: an investigation of the effect of various process gases*. The International Journal of Advanced Manufacturing Technology, 2019. **102**: p. 3021-3035.
182. Kim, J., et al., *Mechanism study of atmospheric-pressure plasma treatment of carbon fiber reinforced polymers for adhesion improvement*. Surface and Coatings Technology, 2020. **393**: p. 125841.
183. Rafailović, L., et al., *Impact of atmospheric pressure plasma treatment on surface metallization of CFRP composites*. Surface and Coatings Technology, 2021. **412**: p. 127046.
184. Sun, C., et al., *Effect of atmospheric pressure plasma treatment on adhesive bonding of carbon fiber reinforced polymer*. Polymers, 2019. **11**(1): p. 139.
185. Ebnesajjad, S., *Material surface preparation techniques*, in *Handbook of adhesives and surface preparation*. 2011, Elsevier. p. 49-81.
186. Dhayal, M., M.R. Alexander, and J.W. Bradley, *The surface chemistry resulting from low-pressure plasma treatment of polystyrene: The effect of residual vessel bound oxygen*. Applied surface science, 2006. **252**(22): p. 7957-7963.
187. Lin, J., et al., *Effect of atmospheric pressure plasma treatment on surface physicochemical properties of carbon fiber reinforced polymer and its interfacial bonding strength with adhesive*. Composites Part B: Engineering, 2020. **199**: p. 108237.

188. Li, S., et al., *A study of laser surface treatment in bonded repair of composite aircraft structures*. Royal Society open science, 2018. **5**(3): p. 171272.
189. Kusano, Y., et al., *Atmospheric pressure plasma treatment of glassy carbon for adhesion improvement*. International journal of adhesion and adhesives, 2007. **27**(5): p. 402-408.
190. Gude, M., S. Prolongo, and A. Ureña, *Adhesive bonding of carbon fibre/epoxy laminates: correlation between surface and mechanical properties*. Surface and Coatings Technology, 2012. **207**: p. 602-607.
191. Leone, C. and S. Genna, *Effects of surface laser treatment on direct co-bonding strength of CFRP laminates*. Composite Structures, 2018. **194**: p. 240-251.
192. Köckritz, T., et al., *Improving the bond strength at hybrid-yarn textile thermoplastic composites for high-technology applications by laser radiation*. International Journal of Adhesion and Adhesives, 2013. **46**: p. 85-94.
193. Askeland, P.A., et al., *UV Ozone Surface Modification of Carbon Based Reinforcements for Composite Materials*. Composite Materials and Structures Center, Michigan State University: East Lansing, MI, USA, 2004: p. 9.
194. Rich, M., et al. *Novel carbon fiber surface treatment with ultraviolet light in ozone to promote composite mechanical properties*. in *Proceedings of ICCM-17th conference, Edinburgh*. 2009.
195. Kamae, T. and L.T. Drzal, *Mechanical and thermal properties of high volume-fraction carbon nanotube/epoxy composites, and property enhancement by UV ozone treatment of carbon nanotubes*. Polymer Composites, 2023. **44**(11): p. 7855-7864.
196. Rich, M., et al. *Surface treatment of carbon fibers by ultraviolet light+ ozone: its effect on fiber surface area and topography*. in *The 19th international conference on composite materials*. 2013.
197. Kawasaki, S., Y. Ishida, and T. Ogasawara, *Effect of vacuum-ultraviolet irradiation in a nitrogen gas atmosphere on the adhesive bonding of carbon-fiber-reinforced polyphenylene sulfide composites*. The Journal of Adhesion, 2022. **98**(1): p. 90-104.
198. Hamdi, M., M.N. Saleh, and J.A. Poulis, *Improving the adhesion strength of polymers: effect of surface treatments*. Journal of Adhesion Science and Technology, 2020. **34**(17): p. 1853-1870.
199. Vig, J.R., *UV/ozone cleaning of surfaces*. Journal of Vacuum Science & Technology A: Vacuum, Surfaces, and Films, 1985. **3**(3): p. 1027-1034.
200. Romero-Sánchez, M.D., et al., *Addition of ozone in the UV radiation treatment of a synthetic styrene-butadiene-styrene (SBS) rubber*. International journal of adhesion and adhesives, 2005. **25**(4): p. 358-370.
201. Øiseth, S.K., et al., *Ultraviolet light treatment of thin high-density polyethylene films monitored with a quartz crystal microbalance*. Journal of Applied Polymer Science, 2004. **92**(5): p. 2833-2839.
202. Nagai, N., T. Matsunobe, and T. Imai, *Infrared analysis of depth profiles in UV-photochemical degradation of polymers*. Polymer degradation and stability, 2005. **88**(2): p. 224-233.
203. Sliney, D., *What is light? The visible spectrum and beyond*. Eye, 2016. **30**(2): p. 222-229.
204. Hitz, C.B., J.J. Ewing, and J. Hecht, *Introduction to laser technology*. 2012: John Wiley & Sons.
205. Kannatey-Asibu Jr, E., *Principles of Laser Materials Processing: Developments and Applications*. 2023: John Wiley & Sons.
206. Weinstein, L., *Electromagnetic waves*. Radio i svyaz', Moscow, 1988.
207. Csele, M., *Fundamentals of light sources and lasers*. 2011: John Wiley & Sons.
208. *The electromagnetic spectrum*. 2013 2013; Available from: <https://imagine.gsfc.nasa.gov/science/toolbox/emspectrum1.html>.

209. Andrews, D.L., *Encyclopedia of applied spectroscopy*. 2009: Wiley Online Library.
210. Dutta Majumdar, J. and I. Manna, *Laser material processing*. International materials reviews, 2011. **56**(5-6): p. 341-388.
211. Maini, A.K., *Lasers and optoelectronics: fundamentals, devices and applications*. 2013: John Wiley & Sons.
212. Schawlow, A.L., *Lasers: The intense, monochromatic, coherent light from these new sources shows many unfamiliar properties*. Science, 1965. **149**(3679): p. 13-22.
213. Ben-Ari, M. and F. Mondada, *Elements of robotics*. 2017: Springer Nature.
214. Ion, J., *Laser processing of engineering materials: principles, procedure and industrial application*. 2005: Elsevier.
215. Brown, M.S. and C.B. Arnold, *Fundamentals of laser-material interaction and application to multiscale surface modification*, in *Laser precision microfabrication*. 2010, Springer. p. 91-120.
216. Saleh, B., *The laser*. Optics in Our Time, 2016. **4**: p. 71.
217. Bogachev, A.V., et al., *Diode-pumped caesium vapour laser with closed-cycle laser-active medium circulation*. Quantum Electronics, 2012. **42**(2): p. 95.
218. Convissar, R.A., *Principles and Practice of Laser Dentistry: Principles and Practice of Laser Dentistry-E-Book*. 2022: Elsevier Health Sciences.
219. Weber, M.J., *Handbook of laser wavelengths*. 2018: CRC press.
220. Arieli, R., *The Laser Adventure*. Versión en español por Requena A., Cruz C., Bastida A. y Zúñiga J. Universidad de Murcia. España, 2005.
221. Goyer, G.G. and R. Watson, *The laser and its application to meteorology*. Bulletin of the American Meteorological Society, 1963. **44**(9): p. 564-570.
222. Silfvast, W.T., *Fundamentals of Photonics*. University of Connecticut, 2003.
223. Eichler, H., et al., *Laser physics and applications*. Landolt-Börnstein: Numerical Data and Functional Relationships in Science and Technology, 2005.
224. Csele, M., *Fundamentals of light sources and lasers chapter 6*. 2011: John Wiley & Sons.
225. Hauer, P., et al., *Spot size engineering in microscope-based laser spectroscopy*. The Journal of Physical Chemistry C, 2016. **120**(37): p. 21104-21113.
226. Bonnett Del Alamo, M., et al., *Laser spot measurement using simple devices*. AIP Advances, 2021. **11**(7).
227. Vainos, N., *Laser growth and processing of photonic structures: an overview of fundamentals, interaction phenomena and operations*. Laser growth and processing of photonic devices, 2012: p. 1-52.
228. Steen, W.M. and J. Mazumder, *Laser material processing chapter 2*. 2010: springer science & business media.
229. Steen, W.M. and J. Mazumder, *Laser material processing*. 2010: springer science & business media.
230. Malíčková, I., et al., *Laser effect in the optical luminescence of oxides containing Cr*. Acta Geologica Slovaca, 2018. **10**(1).
231. Clement, T.S., S. Diddams, and D.J. Jones, *Lasers, ultrafast pulse technology*. 2001.
232. Black, S. and L. Jobling, *Physical principles of LASER*. Anaesthesia & Intensive Care Medicine, 2014. **15**(11): p. 530-532.
233. Haley, D. and O. Pratt, *Basic principles of lasers*. Anaesthesia & Intensive Care Medicine, 2017. **18**(12): p. 648-650.
234. Larimian, T., et al., *Effect of laser spot size, scanning strategy, scanning speed, and laser power on microstructure and mechanical behavior of 316L stainless steel fabricated via selective laser melting*. Journal of Materials Engineering and Performance, 2021: p. 1-20.

235. Siegman, A.E., *Defining, measuring, and optimizing laser beam quality*. Laser Resonators and Coherent Optics: Modeling, Technology, and Applications, 1993. **1868**: p. 2-12.
236. Voisey, K., *Laser drilling of metallic and nonmetallic materials and quality assessment*. 2014.
237. Joignant, A.N., Y. Xi, and D.C. Muddiman, *Impact of wavelength and spot size on laser depth of focus: Considerations for mass spectrometry imaging of non-flat samples*. Journal of Mass Spectrometry, 2023. **58**(5): p. e4914.
238. Bernath, P.F., *Spectra of atoms and molecules*. 2005: Oxford University Press.
239. Eichler, H.J., et al., *Laser beam propagation in free space*. Lasers: Basics, Advances and Applications, 2018: p. 207-229.
240. Bachmann, F. *High-power laser sources for industry and their applications*. in *International Conference on Lasers, Applications, and Technologies 2007: High-Power Lasers and Applications*. 2007. SPIE.
241. Shepelin, N.A., et al., *A practical guide to pulsed laser deposition*. Chemical Society Reviews, 2023.
242. Han, J., et al., *Comparison of Laser Power and Scan Speed in SLM*. ISIJ International, 2022. **62**(1): p. 200-208.
243. Vogel, M., *Principles of Lasers, 5th edn., by O. Svelto: Scope: monograph. Level: advanced undergraduate and above*. 2012, Taylor & Francis. p. 150-160.
244. Kovalev, M., et al., *Reconstructing the spatial parameters of a laser beam using the transport-of-intensity equation*. Sensors, 2022. **22**(5): p. 1765.
245. Jagadeesh, B., et al., *Effect of laser micromachining and laser shock peening on the performance of Inconel alloy parts for aerospace application*. 2023.
246. Eichler, H.J., J. Eichler, and O. Lux, *Lasers: basics, advances and applications*. 2018.
247. Elliott, D.L., *Ultraviolet laser technology and applications Chapter 9*. 2014: Academic press.
248. Brown, M.S. and C.B. Arnold, *Fundamentals of laser-material interaction and application to multiscale surface modification Chapter 4.*, in *Laser precision microfabrication*. 2010, Springer. p. 91-120.
249. Nath, A., *Laser drilling of metallic and nonmetallic substrates*. 2014.
250. Donges, A. and R. Noll, *Laser measurement technology: fundamentals and applications, chapter 3*. Vol. 188. 2014: Springer.
251. Hecht, E., *Optics, 4th editio ed*. Addison-Wesley, San Francisco, 2002. **2**: p. 3.
252. Mayerhöfer, T.G., S. Pahlow, and J. Popp, *The Bouguer-Beer-Lambert law: Shining light on the obscure*. ChemPhysChem, 2020. **21**(18): p. 2029-2046.
253. Chen, M., G. Zak, and P.J. Bates, *Effect of carbon black on light transmission in laser welding of thermoplastics*. Journal of Materials Processing Technology, 2011. **211**(1): p. 43-47.
254. Lippert, T., *Laser application of polymers*. Polymers and Light, 2004: p. 51-246.
255. Zohuri, B., *Thermal effects of high power laser energy on materials*. 2021: Springer.
256. Chichkov, B.N., et al., *Femtosecond, picosecond and nanosecond laser ablation of solids*. Applied physics A, 1996. **63**: p. 109-115.
257. Satta, M., et al., *Time-resolved studies of electron-phonon relaxation in metals using a free-electron laser*. Applied surface science, 2000. **154**: p. 172-178.
258. Chrisey, D.B. and G.K. Hubler, *Pulsed laser deposition of thin films*. 1994.
259. Bulgakova, N.M., et al., *Fast electronic transport and coulomb explosion in materials irradiated with ultrashort laser pulses*. Laser ablation and its applications, 2007: p. 17-36.
260. Sharma, P. and R. Vatsa, *Nanoclusters Under Extreme Ionization Conditions chapter 5*, in *Materials Under Extreme Conditions*. 2017, Elsevier. p. 575-613.

261. Stoian, R., et al., *Surface charging and impulsive ion ejection during ultrashort pulsed laser ablation*. Physical review letters, 2002. **88**(9): p. 097603.
262. Garrison, B.J. and R. Srinivasan, *Laser ablation of organic polymers: Microscopic models for photochemical and thermal processes*. Journal of Applied Physics, 1985. **57**(8): p. 2909-2914.
263. Ehrhart, B., et al. *Extended NDT for the quality assessment of adhesive bonded CFRP structures*. in *Smart Material, Structures & NDT in Aerospace Conference*. Montreal, Canada, November. 2011.
264. Yalukova, O. and I. Sarady, *Investigation of interaction mechanisms in laser drilling of thermoplastic and thermoset polymers using different wavelengths*. Composites science and technology, 2006. **66**(10): p. 1289-1296.
265. Fischer, F., L. Romoli, and R. Kling, *Laser-based repair of carbon fiber reinforced plastics*. CIRP annals, 2010. **59**(1): p. 203-206.
266. Feng, Y., Z. Liu, and X.-S. Yi, *Co-occurrence of photochemical and thermal effects during laser polymer ablation via a 248-nm excimer laser*. Applied Surface Science, 2000. **156**(1-4): p. 177-182.
267. French, P.W., et al., *New Laser Machine Tools for Processing Carbon Fibre Reinforced Plastic (CFRP)*. Key Engineering Materials, 2012. **496**: p. 30-35.
268. Blass, D., et al. *CFRP bonding pre-treatment with laser radiation of 3 μm wavelength: Laser/material interaction*. in *Laser-based Micro-and Nanoprocessing X*. 2016. SPIE.
269. Gao, Q., et al., *Effect of scanning speed with UV laser cleaning on adhesive bonding tensile properties of CFRP*. Applied Composite Materials, 2019. **26**: p. 1087-1099.
270. Bora, M.Ö., et al., *The Effect of CO₂ Laser-Induced Microhole Formations on Adhesive Bonding Strength of CFRP/CFRP Joints*. Polymer Composites, 2019. **40**(7): p. 2891-2900.
271. Sorrentino, L., G. Parodo, and S. Turchetta, *CFRP laser texturing to increase the adhesive bonding: morphological analysis of treated surfaces*. The Journal of Adhesion, 2021. **97**(14): p. 1322-1335.
272. Loutas, T., et al., *Investigation of a pulsed laser ablation process for bonded repair purposes of CFRP composites via peel testing and a design-of-experiments approach*. International Journal of Adhesion and Adhesives, 2019. **95**: p. 102407.
273. Sola, D., et al., *Microstructural and wear behavior characterization of porous layers produced by pulsed laser irradiation in glass-ceramics substrates*. Materials, 2013. **6**(9): p. 3963-3977.
274. Wlodarczyk, K.L., et al., *Laser microsculpting for the generation of robust diffractive security markings on the surface of metals*. Journal of Materials Processing Technology, 2015. **222**: p. 206-218.
275. Yang, P.-K. and J.-Y. Liu, *Determining the waist radius of a focused Gaussian laser beam using a millimeter-scale ruler*. European Journal of Physics, 2017. **38**(2): p. 025302.
276. Jiang, D., et al., *Numerical and experimental studies on the effect of varied beam diameter, average power and pulse energy in Nd: YAG laser welding of Ti6Al4V*. Infrared Physics & Technology, 2019. **101**: p. 180-188.
277. lighting, P. *TUV Amalgam T6 130W XPT SE G10.2q Philips UK*. [cited 2024 13 September]; Available from: https://www.lighting.philips.com/api/assets/v1/file/Signify/content/928101805112_EU_en_AA.PROF.FP/Localized_commercial_leaflet_928101805112_en_AA.pdf.
278. Singh, J., *IIT JEE Physics (1978 to 2018: 41 Years) Topic-wise Complete Solutions*. 3rd ed. 2018.
279. Al-Mahdy, A., et al., *An investigation into the use of incoherent UV light to augment IR nanosecond pulsed laser texturing of CFRP composites for improved adhesion*. Optics & Laser Technology, 2025. **181**: p. 111626.

280. Schumacher, H., U. Künzelmann, and J.W. Bartha, *Characterisation of Surface Processes during Oxide CMP by in situ FTIR Spectroscopy with Microstructured Reflection Elements at Silicon Wafers*. MRS Online Proceedings Library, 2010. **1249**: p. 1-6.
281. Huntsman, *Advanced Materials, Araldite 420A/B*. 2009 [cited 2024 09 September]; Available from: https://vitrochem.com/wordpress/wp-content/uploads/2021/04/Araldite-420-AB_TDS.pdf.
282. Henkel Corporation Aerospace *LOCTITE EA 9394 AERO*. 2013 [cited 2024 09 September]; Available from: https://www.heatcon.com/wp-content/uploads/2015/08/HCS2407-141_Henkel-Resin-Kit-LOCTITE-EA-9394-AERO.pdf.
283. Gurit Services AG, *Zurich SP 115 - Clear Epoxy Laminating System, data sheet*. [cited 2024 8 September]; Available from: <https://pdf.nauticexpo.com/pdf/gurit/sp-115-clear-epoxy-laminating-system-v11/27794-107151.html>.
284. Easycomposite UK, *EL2 EPOXY LAMINATING RESIN*. [cited 2024 8 September]; Available from: <https://media.easycomposites.co.uk/datasheets/EC-TDS-EL2-Epoxy-Laminating-Resin.pdf>.
285. Easycomposite Ltd UK, *IN2 EPOXY INFUSION RESIN*. 2024 [cited 2024 8 September]; Available from: <https://media.easycomposites.co.uk/datasheets/EC-TDS-IN2-Infusion-Resin.pdf>.
286. British Standards Institute, *BS EN 1465:2009 "Adhesives. Determination of tensile lap-shear strength of bonded assemblies"*, 2009, London, BSI. 2009.
287. Duncan, B., *Developments in testing adhesive joints*, in *Advances in structural adhesive bonding*. 2010, Elsevier. p. 389-436.
288. Zheng, G., et al., *Effect of spew fillet on adhesively bonded single lap joints with CFRP and aluminum-alloy immersed in distilled water*. International Journal of Adhesion and Adhesives, 2020. **99**: p. 102590.
289. Bregar, T., et al., *Carbon nanotube embedded adhesives for real-time monitoring of adhesion failure in high performance adhesively bonded joints*. Scientific Reports, 2020. **10**(1): p. 1-20.
290. Zarei, A. and S. Pilla, *Laser ultrasonics for nondestructive testing of composite materials and structures: a review*. Ultrasonics, 2023: p. 107163.
291. Kalms, M., et al., *Beam shaping using liquid crystal-on-silicon spatial light modulators for laser ultrasound generation*. Optical Engineering, 2014. **53**(4): p. 044110-044110.
292. Firbank, M., et al., *An investigation of light transport through scattering bodies with non-scattering regions*. Physics in Medicine & Biology, 1996. **41**(4): p. 767.
293. Azhikannikal, E., P.J. Bates, and G. Zak, *Use of thermal imaging to characterize laser light reflection from thermoplastics as a function of thickness, laser incidence angle and surface roughness*. Optics & Laser Technology, 2012. **44**(5): p. 1491-1496.
294. Church, E., *The measurement of surface texture and topography by differential light scattering*. Wear, 1979. **57**(1): p. 93-105.
295. Saleh, B.E. and M.C. Teich, *Fundamentals of photonics*. NASA STI/Recon Technical Report A, 1991. **92**: p. 35987.
296. Marszalec, J.A. and E.A. Marszalec, *Integration of lasers and fiber optics into robotic systems*. Vol. 10. 1994: SPIE Press.
297. Amaral, I., et al., *Improving the cut surface quality by optimizing parameters in the fibre laser cutting process*. Procedia Manufacturing, 2019. **38**: p. 1111-1120.
298. Li, S., et al., *Layer ablation and surface textured of Carbon fiber reinforced plastics by infrared pulsed laser*. Polymer Composites, 2024. **45**(1): p. 763-776.
299. Piscitelli, F., R. De Palo, and A. Volpe, *Enhancing coating adhesion on fibre-reinforced composite by femtosecond laser texturing*. Coatings, 2023. **13**(5): p. 928.

300. Liu, Y., et al., *Achievement of high-strength Al/CFRP hybrid joint via high-speed friction stir lap joining and laser texturing pretreatment parameters variation*. *Thin-Walled Structures*, 2024. **199**: p. 111762.
301. Jiang, G. and X. Zhou, *Effect of laser surface texture on the adhesion performance of CFRP/Mg laminates*. *The Journal of Adhesion*, 2024. **100**(6): p. 426-445.
302. See, T.L., *Laser surface texturing-Fundamental study and applications*. 2015.
303. Mao, B., et al., *Laser surface texturing and related techniques for enhancing tribological performance of engineering materials: A review*. *Journal of Manufacturing Processes*, 2020. **53**: p. 153-173.
304. Kumar, V., et al., *Recent progresses and applications in laser-based surface texturing systems*. *Materials Today Communications*, 2021. **26**: p. 101736.
305. De Oliveira, M., et al., *Experimental planning factorial: a brief review*. *International Journal of Advanced Engineering Research and Science*, 2018. **5**(6): p. 264164.
306. Chau, T., et al., *A review of factors that affect contact angle and implications for flotation practice*. *Advances in colloid and interface science*, 2009. **150**(2): p. 106-115.
307. Kahraman, R., M. Sunar, and B. Yilbas, *Influence of adhesive thickness and filler content on the mechanical performance of aluminum single-lap joints bonded with aluminum powder filled epoxy adhesive*. *Journal of materials processing technology*, 2008. **205**(1-3): p. 183-189.
308. Freitag, C., et al., *Influence of pulse repetition rate and pulse energy on the heat accumulation between subsequent laser pulses during laser processing of CFRP with ps pulses*. *Applied Physics A*, 2018. **124**: p. 1-9.
309. Xie, Y., et al., *Shear strength of bonded joints of carbon fiber reinforced plastic (CFRP) laminates enhanced by a two-step laser surface treatment*. *Composite Structures*, 2020. **232**: p. 111559.
310. Weber, R., et al., *Minimum damage in CFRP laser processing*. *Physics Procedia*, 2011. **12**: p. 302-307.
311. Takahashi, K., et al., *Heat conduction analysis of laser CFRP processing with IR and UV laser light*. *Composites Part A: Applied Science and Manufacturing*, 2016. **84**: p. 114-122.
312. Zhou, M.-H., G.-Z. Yin, and S.G. Prolongo, *Review of thermal conductivity in epoxy thermosets and composites: mechanisms, parameters, and filler influences*. *Advanced Industrial and Engineering Polymer Research*, 2024. **7**(3): p. 295-308.
313. Fu, Y.-X., et al., *Thermal conductivity enhancement with different fillers for epoxy resin adhesives*. *Applied Thermal Engineering*, 2014. **66**(1-2): p. 493-498.
314. Pawar, S.S., et al., *Carbon fiber sizing agents based on renewable terpenes*. *Composites science and technology*, 2022. **220**: p. 109280.
315. Feih, S. and A. Mouritz, *Tensile properties of carbon fibres and carbon fibre-polymer composites in fire*. *Composites Part A: Applied Science and Manufacturing*, 2012. **43**(5): p. 765-772.
316. Pascault, J.P. and R.J. Williams, *Thermosetting polymers*. *Handbook of polymer synthesis, characterization, and processing*, 2013: p. 519-533.
317. Dodiuk, H., *Handbook of thermoset plastics*. 2021: William Andrew.
318. Guo, Q., *Thermosets: structure, properties, and applications*. 2017: Woodhead Publishing.
319. Krainer, S. and U. Hirn, *Contact angle measurement on porous substrates: Effect of liquid absorption and drop size*. *Colloids and Surfaces A: Physicochemical and Engineering Aspects*, 2021. **619**: p. 126503.
320. André, V. and A. Zosel, *Dynamic wetting on porous and non porous substrates. Influence of surface tension, viscosity and porosity*. *Berichte der Bunsengesellschaft für physikalische Chemie*, 1994. **98**(3): p. 429-434.

321. Kumar, S.M. and A.P. Deshpande, *Dynamics of drop spreading on fibrous porous media*. Colloids and Surfaces A: Physicochemical and Engineering Aspects, 2006. **277**(1-3): p. 157-163.
322. Pezron, I., G. Bourgain, and D. Quéré, *Imbibition of a fabric*. Journal of Colloid and Interface Science, 1995. **173**(2): p. 319-327.
323. Kotynia, R., et al., *Effect of accelerated curing conditions on shear strength and glass transition temperature of epoxy adhesives*. Procedia engineering, 2017. **193**: p. 423-430.
324. Christopher, W., D. Wayne, and A. Andy, *Chemico-diffusion kinetics epoxy-amine resins*. Polymer, 1997. **38**(13): p. 3251-3261.
325. Sahagun, C.M. and S.E. Morgan, *Thermal control of nanostructure and molecular network development in epoxy-amine thermosets*. ACS applied materials & interfaces, 2012. **4**(2): p. 564-572.
326. Deng, Y. and G.C. Martin, *Diffusion and diffusion-controlled kinetics during epoxy-amine cure*. Macromolecules, 1994. **27**(18): p. 5147-5153.
327. Dodiuk, H., S. Kenig, and I. Liran, *Room temperature curing epoxy adhesives for elevated temperature service*. The Journal of Adhesion, 1987. **22**(3): p. 227-251.
328. Voyutskii, S. and V. Vakula, *The role of diffusion phenomena in polymer-to-polymer adhesion*. Journal of Applied Polymer Science, 1963. **7**(2): p. 475-491.
329. Mumby, S.J., et al., *Temperature dependence of the diffusion coefficient of poly (propylene oxide) in the undiluted state*. Polymer, 1986. **27**(11): p. 1826-1828.
330. Redmann, A., et al., *Evaluation of single-lap and block shear test methods in adhesively bonded composite joints*. Journal of Composites Science, 2021. **5**(1): p. 27.
331. Loureiro, A., et al., *Comparison of the mechanical behaviour between stiff and flexible adhesive joints for the automotive industry*. The Journal of Adhesion, 2010. **86**(7): p. 765-787.
332. Carbas, R.J., et al., *Manufacture and testing*, in *Advanced Joining Processes*. 2021, Elsevier. p. 271-317.
333. Da Silva, L.F., A. Öchsner, and R.D. Adams, *Handbook of adhesion technology*. 2011: Springer Science & Business Media.
334. Karachalios, E., R. Adams, and L.F. da Silva, *Strength of single lap joints with artificial defects*. International journal of adhesion and adhesives, 2013. **45**: p. 69-76.
335. Adams, R., *Prediction of the strength of adhesive lap joints. An investigative review*. International Journal of Adhesion and Adhesives, 2024. **129**: p. 103576.
336. Banea, M.D., *Influence of adherend properties on the strength of adhesively bonded joints*. MRS Bulletin, 2019. **44**(8): p. 625-629.
337. Mushtaq, R.T., et al., *State-of-the-art and trends in CO2 laser cutting of polymeric materials—a review*. Materials, 2020. **13**(17): p. 3839.
338. Herzog, D., et al., *Investigations on the thermal effect caused by laser cutting with respect to static strength of CFRP*. International journal of machine tools and manufacture, 2008. **48**(12-13): p. 1464-1473.
339. Weber, R., et al., *Short-pulse laser processing of CFRP*. Physics Procedia, 2012. **39**: p. 137-146.
340. Wang, W.-h. and X.-y. Liu. *Effect of linear energy density on pores of 316L stainless steel by selective laser melting*. in *IOP Conference Series: Earth and Environmental Science*. 2019. IOP Publishing.
341. Suder, W. and S. Williams, *Investigation of the effects of basic laser material interaction parameters in laser welding*. Journal of laser applications, 2012. **24**(3).
342. Wang, Z., et al., *Development of laser processing carbon-fiber-reinforced plastic*. Sensors, 2023. **23**(7): p. 3659.
343. Ebnesajjad, S., *Introduction and adhesion theories*, in *Handbook of Adhesives and Surface Preparation*. 2011, Elsevier. p. 3-13.

344. Rybaltovskii, A., et al., *Laser-induced microstructuring of polymers in gaseous, liquid and supercritical media*. *Polymers*, 2021. **13**(20): p. 3525.
345. Odegard, G.M., et al., *Accurate predictions of thermoset resin glass transition temperatures from all-atom molecular dynamics simulation*. *Soft Matter*, 2022. **18**(39): p. 7550-7558.
346. NIINO, H., et al., *Polymer Ablation Upon Exposure to Vacuum Ultra-Violet Light*. *Journal of Photopolymer Science and Technology*, 1992. **5**(2): p. 301-306.
347. Lippert, T. and J.T. Dickinson, *Chemical and spectroscopic aspects of polymer ablation: Special features and novel directions*. *Chemical Reviews*, 2003. **103**(2): p. 453-486.
348. Akkamma, M. and B. Lobo, *Optical properties of UV-C irradiated polyvinylidene chloride films*. *Radiation Physics and Chemistry*, 2023. **212**: p. 111182.
349. Aydın, M.D., *3-D nonlinear stress analysis on adhesively bonded single lap composite joints with different ply stacking sequences*. *The Journal of Adhesion*, 2008. **84**(1): p. 15-36.
350. Rodríguez, R.Q., et al. *Stress analysis and failure criteria of adhesive bonded single lap joints*. in *21st international congress of mechanical engineering*. 2011.
351. Adams, R. and B. Drinkwater, *Nondestructive testing of adhesively-bonded joints*. *NDT & E International*, 1997. **30**(2): p. 93-98.
352. Özer, H., *Introductory chapter: Structural adhesive bonded joints*. *Applied Adhesive Bonding in Science and Technology*, 2018.
353. Kupski, J., et al., *Composite layup effect on the failure mechanism of single lap bonded joints*. *Composite Structures*, 2019. **217**: p. 14-26.
354. Hart-Smith, L.J., *Adhesive-bonded single-lap joints*. 1973.
355. Ozel, A., et al., *A study on the strength of adhesively bonded joints with different adherends*. *Composites Part B: Engineering*, 2014. **62**: p. 167-174.
356. Purimpat, S., R. Jérôme, and A. Shahram, *Effect of fiber angle orientation on a laminated composite single-lap adhesive joint*. *Advanced Composite Materials*, 2013. **22**(3): p. 139-149.
357. Li, C., et al., *Effect of CFRP surface topography on the adhesion and strength of composite-composite and composite-metal joints*. *Composites Part A: Applied Science and Manufacturing*, 2023. **164**: p. 107275.
358. Rånby, B., *Photodegradation and photo-oxidation of synthetic polymers*. *Journal of Analytical and Applied Pyrolysis*, 1989. **15**: p. 237-247.
359. Chennareddy, R., et al., *UV-resistant GFRP composite using carbon nanotubes*. *Construction and Building Materials*, 2019. **220**: p. 679-689.
360. Ching, Y.C., et al., *Effects of high temperature and ultraviolet radiation on polymer composites*, in *Durability and life prediction in biocomposites, fibre-reinforced composites and hybrid composites*. 2019, Elsevier. p. 407-426.

Appendices

Appendix A, The UD reinforced prepreg datasheet



Pol. Indust. A Granxa, C/Cies 190
36400 O Porriño – Pontevedra (España)
Tfno. 986 342 953
shop@castrocomposites.com
www.castrocompositeshop.com

MTC510

Epoxy Component Prepreg

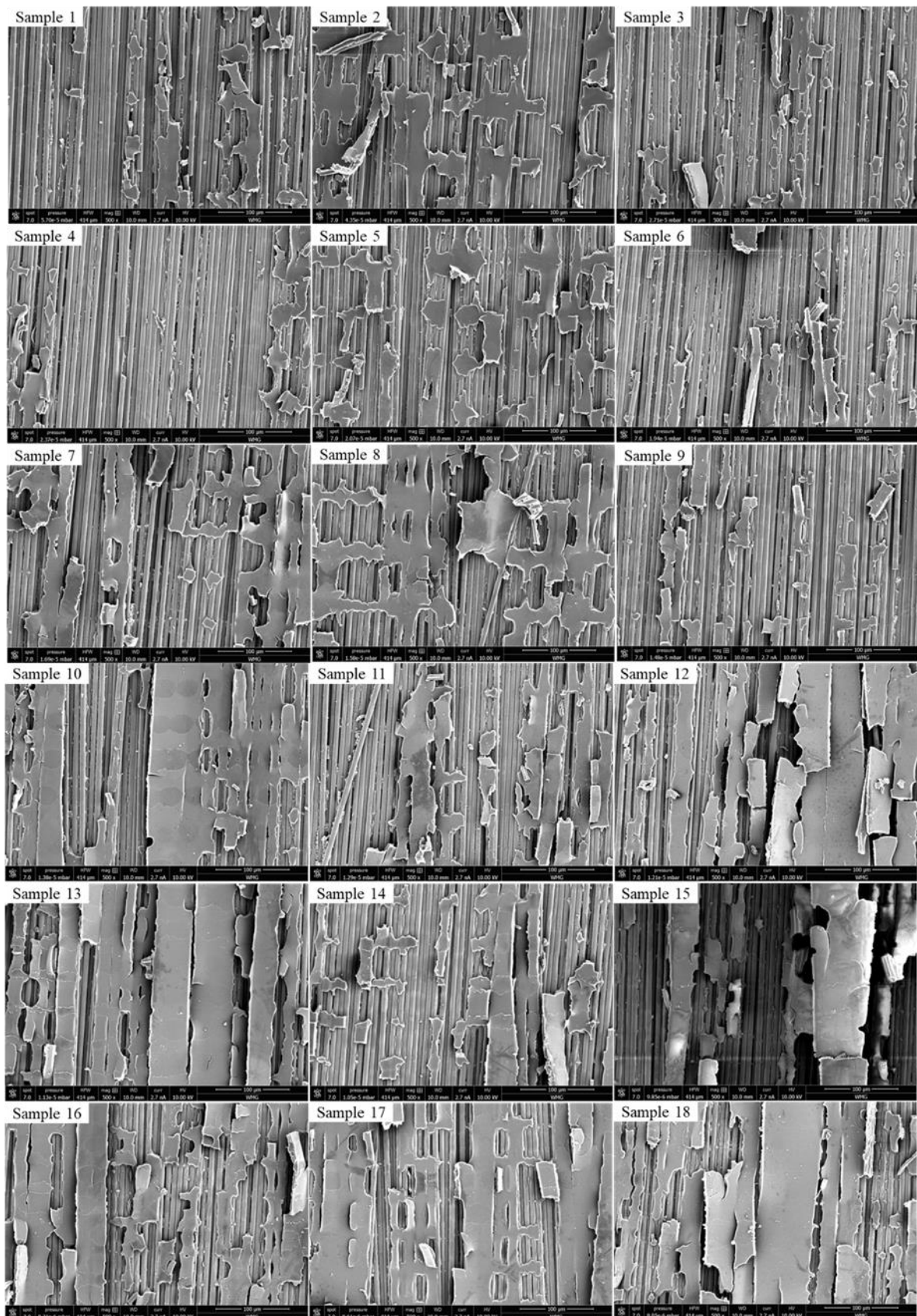
Mechanical Properties

Material: **MTC510-UD300-HS-33%RW (SHD0373-300P)**
Initial cure: 2 hrs @ 110°C, 2°C/min ramp (solid release, caul-plated, 6 bar)
Testing: Performed at room temperature conditions (J15)

| Test | Results | | | Standard |
|--------------------------------|-----------------------------|-------|-----|---|
| Fibre volume fraction (VF) | Measured | 60.20 | % | N/A* |
| | Theoretical | 57.71 | % | |
| Cured Ply Thickness (CPT) | Measured | 0.286 | mm | N/A* |
| | Theoretical | 0.289 | mm | |
| Tension 0° | Tensile strength | 2282 | MPa | BS EN ISO 527-5 |
| | Tensile modulus | 119.3 | GPa | |
| | Poisson's Ratio | 0.34 | | |
| Tension 90° | Tensile strength | 54 | MPa | |
| | Tensile modulus | 8.2 | GPa | |
| | Poisson's Ratio | 0.01 | | |
| Compression 0° | Compressive strength | 1067 | MPa | EN 2850 Type B |
| | Compressive modulus | 113.6 | GPa | |
| Compression 90° | Compressive strength | 200 | MPa | |
| | Compressive modulus | 9.3 | GPa | |
| In-Plane Shear ±45° | In-Plane shear strength | 99 | MPa | ASTM D3518 |
| | In-Plane shear modulus | 3.60 | GPa | |
| Interlaminar Shear Strength 0° | Interlaminar shear strength | 84.8 | MPa | BS EN ISO 14130 |
| DMA | Tg Onset | 123 | °C | Modified ASTM D7028* (Single Cantilever) |
| | Peak Tan Delta | 133 | °C | |

All tests marked * were completed at SHD Composites laboratories on non-condition specimens. Complete test reports can be supplied independently upon request.

Appendix B, SEM images for UD CFRP material processed with different laser variables, see Table 7.3 or Table 7.6.



Appendix C, material properties and model types applied in SolidWorks.

Material properties
Materials in the default library can not be edited. You must first copy the material to a custom library to edit it.

Model Type: Save model type in library

Units:

Category:

Name:

Default failure criterion:

Description:

Source:

Sustainability:

| Property | Value | Units |
|------------------------------------|--------|-------------------|
| Elastic Modulus in X | 119000 | N/mm ² |
| Elastic Modulus in Y | 8200 | N/mm ² |
| Elastic Modulus in Z | 8200 | N/mm ² |
| Poisson's Ratio in XY | 0.34 | N/A |
| Poisson's Ratio in YZ | 0.01 | N/A |
| Poisson's Ratio in XZ | 0.34 | N/A |
| Shear Modulus in XY | 3600 | N/mm ² |
| Shear Modulus in YZ | 3600 | N/mm ² |
| Shear Modulus in XZ | 3600 | N/mm ² |
| Mass Density | 1020 | kg/m ³ |
| Tensile Strength in X | 2282 | N/mm ² |
| Tensile Strength in Y | 54 | N/mm ² |
| Compressive Strength in X | 1097 | N/mm ² |
| Compressive Strength in Y | 200 | N/mm ² |
| Shear Strength in XY | 85 | N/mm ² |
| Yield Strength | 2000 | N/mm ² |
| Thermal Expansion Coefficient in X | -3e-06 | /K |

Material properties
Materials in the default library can not be edited. You must first copy the material to a custom library to edit it.

Model Type: Save model type in library

Units:

Category:

Name:

Default failure criterion:

Description:

Source:

Sustainability:

| Property | Value | Units |
|-------------------------------|--------|-------------------|
| Elastic Modulus | 4237 | N/mm ² |
| Poisson's Ratio | 0.3 | N/A |
| Shear Modulus | 1461 | N/mm ² |
| Mass Density | 1360 | kg/m ³ |
| Tensile Strength | 46 | N/mm ² |
| Compressive Strength | | N/mm ² |
| Yield Strength | | N/mm ² |
| Thermal Expansion Coefficient | | /K |
| Thermal Conductivity | 0.2256 | W/(m·K) |

Material properties
Materials in the default library can not be edited. You must first copy the material to a custom library to edit it.

Model Type: Save model type in library

Units:

Category:

Name:

Default failure criterion:

Description:

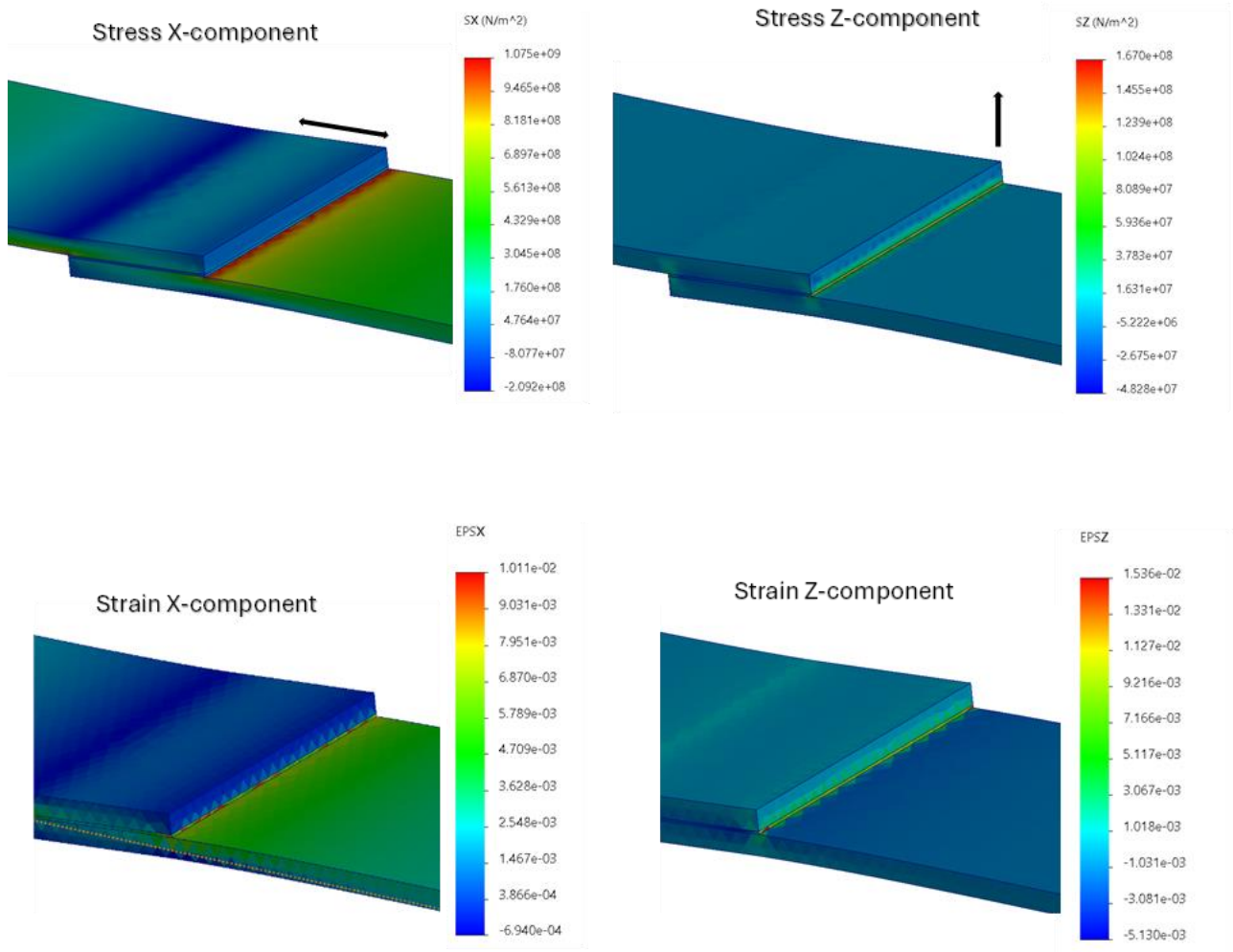
Source:

Sustainability:

| Property | Value | Units |
|-------------------------------|--------|-------------------|
| Elastic Modulus | 1450 | N/mm ² |
| Poisson's Ratio | 0.3 | N/A |
| Shear Modulus | 730 | N/mm ² |
| Mass Density | 1360 | kg/m ³ |
| Tensile Strength | 29 | N/mm ² |
| Compressive Strength | | N/mm ² |
| Yield Strength | 15 | N/mm ² |
| Thermal Expansion Coefficient | | /K |
| Thermal Conductivity | 0.2256 | W/(m·K) |

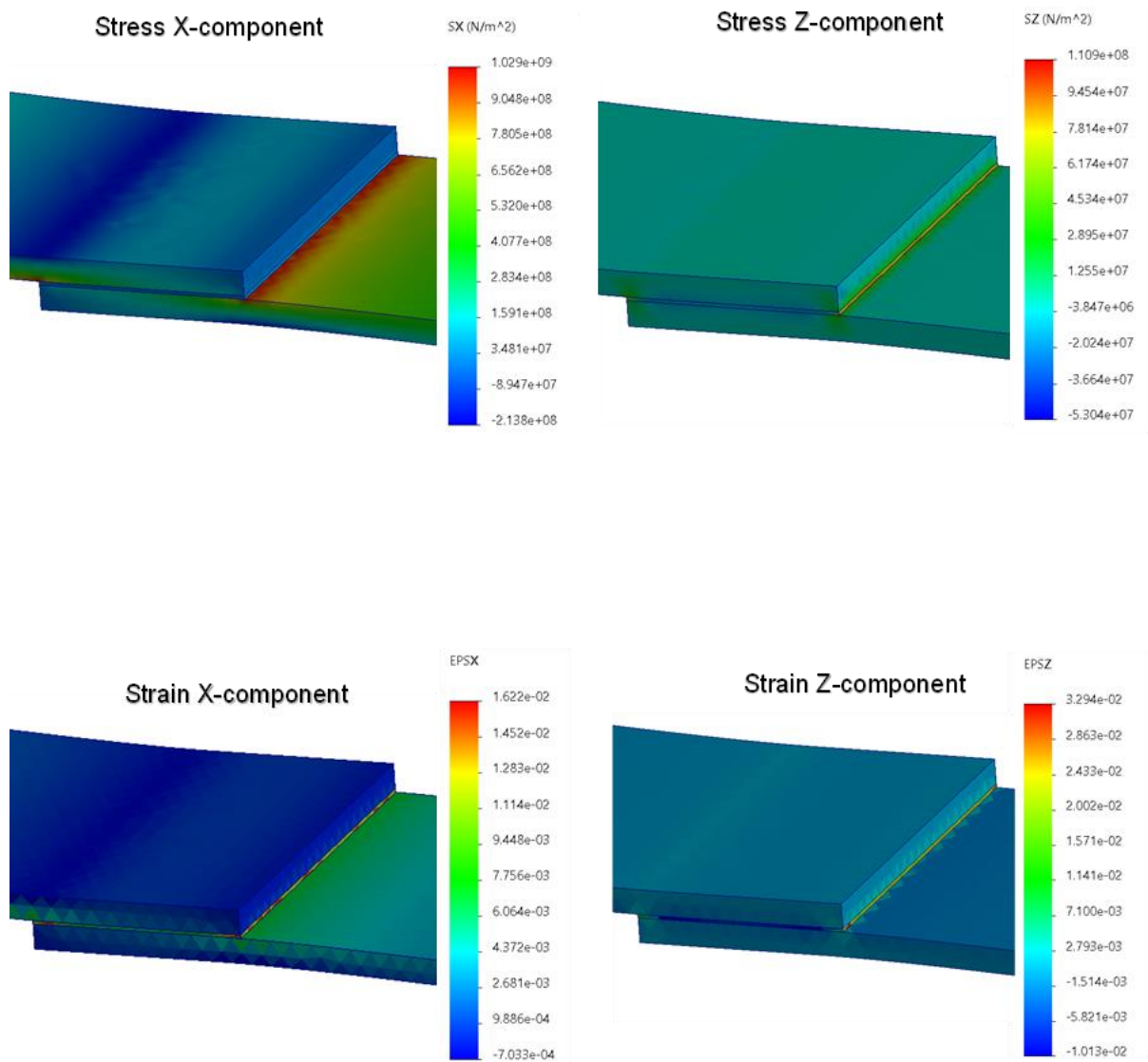
Appendix D, full SolidWorks modelling results of the two adhesives

1. Loctite 9394 Model



Loctite 9394 model stress and strain

2. Araldite 420 Model



Araldite 420 model stress and strain